Structure et propagation d'un rift magmatique en bordure de craton : approche intégrée de la divergence Nord-Tanzanienne par analyse des populations de failles et du réseau de drainage

Remigius Gama

THESE DE DOCTORAT EN CO-TUTELLE DE

L'UNIVERSITE DE BRETAGNE OCCIDENTALE
COMUE UNIVERSITE BRETAGNE LOIRE
ECOLE DOCTORALE N° 598
Sciences de la Mer et du littoral
Spécialité : *Géosciences marines*

AVEC L'UNIVERSITE DE DAR ES SALAAM (TANZANIE)

Par

Remigius GAMA

« Structure et propagation d'un rift magmatique en bordure de craton : Approche intégrée de la Divergence Nord-Tanzanienne par analyse des populations de failles et du réseau de drainage»

Thèse présentée et soutenue à Plouzané le 21 septembre 2018
Unité de recherche : Laboratoire Géosciences Ocean

Rapporteurs avant soutenance :

Charles AUBOURG Professeur, Université de Pau et des Pays de l'Adour

Christophe BASILE Professeur, Université de Grenoble

Composition du Jury :

Laurent GEOFFROY	Professeur, UBO, Président du Jury
Charles AUBOURG	Professeur, Université de Pau et des Pays de l'Adour
Christophe BASILE	Professeur, Université de Grenoble
Christine AUTHEMAYOU	Maître de Conférences, UBO
Christel TIBERI	Chargée de Recherche CNRS, Géosciences Montpellier, UMR 5243
Erwan HALLOT	Maître de Conférences, Université Rennes 1
Pascal TARITS	Professeur, UBO / Directeur de thèse
Bernard LE GALL	Chargé de Recherche CNRS, UBO, UMR 6538 / Co-directeur de thèse
Nelson BONIFACE	Maître de Conférences, Université de Dar es Salaam, Tanzanie / Co-directeur de thèse

Remerciements

Exprimer des remerciements n'est pas si facile, je voudrais donc tout d'abord m'excuser si jamais j'oublie certaines personnes, ce n'est pas mon intention de ne pas remercier quelqu'un. Je voudrais sincèrement tenir à exprimer mes remerciements à toutes les personnes qui m'ont soutenu et aidé pendant la réalisation de ce travail.

Je voudrais tout d'abord dire merci à mon directeur Pascal Tarits de m'avoir fait rêver d'un retour à Brest lorsque nous avons repris contact pendant la préparation de la campagne de magnétotellurique. Merci pour m'avoir dirigé vers la géophysique et aidé à comprendre les structures en profondeur. Ma bourse de l'ambassade de France en Tanzanie était vraiment courte (9 mois au total) mais tu as fait beaucoup d'efforts pour m'aider à avoir un financement du laboratoire pour que je puisse rester plus longtemps et travailler dans un environnement tranquille et pour la mission de terrain. Asante sana kwa wema wako Pascal.

Maintenant je tiens à remercier mon encadrant géologique, c'est toi Bernard Le Gall. Merci beaucoup de m'avoir dirigé vers la compréhension de la tectonique du rift. Tu m'as fait découvrir et comprendre ce qu'est le Rift Est Africain, notamment le rift sud Kenya et la Divergence Nord Tanzanienne. Tu m'as beaucoup apporté pendant cette thèse que ce soit pendant la mission de terrain à Natron et dans les bureaux ici à Brest. J'ai beaucoup apprécié ce que tu as fait scientifiquement et socialement pour moi. Permets-moi de dire brièvement 'usengwile sana va Bambu veve'.

Je voudrais aussi remercier mon deuxième co-directeur de l'université de Dar es Salaam, Nelson Boniface. Merci pour tes aides scientifiques et administratives. Wakola sana kaka.

Grâce à toi Nicolas Loget, j'ai pu étudier les mouvements verticaux par traitement et interprétation de réseaux de drainage. Merci de m'accueillir pendant mon séjour de deux semaines dans votre laboatoire à ISTeP (Paris) et des outils des traitements. J'apprécie beaucoup ton aide dans cette étude.

Pour l'équipe de géochimie du laboratoire, merci à Gilles Chazot d'avoir accepté de nous accompagner dans notre mission à Natron ainsi que pour la réalisation de nos échantillons.

Cette thèse a été partiellement financée par l'ambassade de France en Tanzanie, donc je voudrais exprimer un énorme remerciement à toutes les personnes responsables, notamment les attachés scientifiques et les responsables à Campus France. Je voudrais aussi remercier Christel Tiberi d'avoir financièrement participé à notre campagne de terrain ainsi qu'au salaire m'ayant permis de rester plusieurs mois de plus sur Brest.

Je voudrais aussi remercier toutes les gestionnaires du Laboratoire Géosciences Océan, qui sont Margot, Carole, Charlotte, Audrey et Véronique.

Merci à Christophe Martin et Frédéric Talbourdet ainsi que les autres membres de l'équipe de l'assistance informatique d'avoir résolu les problèmes informatiques qui sont apparus, notamment pendant la rédaction de mon manuscrit.

Sophie Hautot, je te remercie de m'avoir fait découvrir la magnétotellurique. Merci aussi pour les résultats 3D de MT.

Je tiens à remercier Charles Aubourg, Christophe Basile et Erwan Hallot d'avoir accepté d'être les rapporteurs de cette thèse. Je dis merci aux membres du jury, Laurent Geoffroy, Christel Tiberi et Christine Authemayou d'avoir accepté d'examiner mon manuscrit.

Merci à mes collègues thésards de l'IUEM, les anciens et les nouveaux (Marie, Huixin et les autres). Ici je voudrais dire un grand merci à Matthieu Plasman (maintenant en post doc à Montpellier) pour tes aides informatiques pendant le traitement des données MT ainsi que les corrections de français dans quelques parties de mon manuscrit. Mes collègues de l'université de Dar es Salaam sont aussi à remercier. À toi Saitabau je te dire 'ashe naleng '. Mon collègue avec qui je partage le bureau, Kazimoto, merci pour ton soutien moral et 'chai'. Merci Olipa pour me depagner quand j'avais des soucis avec mon ArcGIS.

Maintenant c'est toi 'mdala wangu' Régina, merci pour tout, d'avoir pris mes responsabilités pendant mon absence, de m'avoir encouragé pendant les périodes dures, bien 'hongisa sana'. Merci à mes enfants Francisco, Raul et Khwezi de votre compréhension quand je vous ai demandé de ne pas me déranger (watoto msinipigie kelele !! Shhhhh !!! Baba hataki kelele anafanya kazi !!). Et pour ma famille, merci à mes parents même si vous n'êtes plus là vous me guidez toujours dans l'esprit. Merci à Veremunda (ma tante) et Yasinta Chale (ma belle-mère). Mes frères Abel et Petiri, mes sœurs Apronia et Imani, merci. Merci à tous les autres membres de ma grande famille.

Résumé

Tout modèle cinématique appliqué à la propagation du rift sud kenyan (RSK) et à sa divergence vers l'ouest au nord de la Tanzanie (DNT) doit nécessairement intégré la vallée axiale Magadi-Natron (études antérieures), mais aussi le bloc soulevé Oldoinyo Ogol (OOB) à l'ouest (ce travail). Notre étude, basée pour l'essentiel sur l'interprétation d'imagerie satellitale SRTM 30 m, nous permet (1) de préciser l'organisation morphostructurale de l'ensemble du RSK, (2) d'identifier 2 systèmes successifs de failles bordières, (3) d'affirmer le rôle majeur de celle d'OlDoinyo Ogol, (4) d'élaborer un modèle de rifting en 2 étapes (7-3 Ma et <3 Ma) et (5) d'attribuer le « shift » latéral du domaine rifté (OOB), puis sa divergence le long de la branche d'Eyasi (DNT) à la présence d'une discontinuité transverse protérozoïque, à laquelle on rapporte aussi le développement précoce et 'hors axe' du segment magmatique des « Crater Highlands », démontrant ainsi l'importance de l'héritage structural sur la cinématique du rifting.

L'analyse quantitative des populations de failles démontre le caractère « restricted » des failles intra-rift et aboutit aussi à préciser l'évolution, dans l'espace et le temps, du taux d'extension, depuis un stade précoce à déformation localisée jusqu'à un stade récent à déformation diffuse (<3 Ma).

L'analyse des réseaux de drainage identifiés sur le compartiment de socle bordant à l'ouest le dispositif RSK-NTD démontre (1) leur contrôle étroit par le dispositif lithologique et tectonique du socle, (2) la nature polyphasée du soulèvement lié aux failles bordières, et (3) le caractère déséquilibré du réseau actuel en cours de soulèvement.

Abstract

Any kinematic model applied to the southerly-propagating and diverging South Kenya rift (SKR) should necessarily integrate the structure of the Magadi-Natron axial trough (previous studies), but also those of the Oldoinyo Ogol (OOB) offset block to the west. Our work is chiefly based on SRTM 30 m satellite imagery analysis, and allows us (1) to precise the morphostructural arrangement of the entire SKR, (2) to identify 2 successive border faults systems, (3) to emphasize the role of the Ol Doinyo Ogol master fault, (4) to elaborate a 2-stage rift model (7-3 Ma et <3 Ma), and (5) to attribute a key-role to a transverse Proterozoic discontinuity on the lateral shift of the OOB, as well as on the split of the rift into the Eyasi rift arm and on the off-axis location of the early Crater Highlands magmatic segment, hence demonstrating the importance of basement structural inheritance on rift kinematics.

The quantitative analysis of fault populations shows the restricted nature of most intra-rift faults, and leads us to precise the spatio-temporal evolution of extension from a stage of localized strain (border faults) to a stage of diffuse extension (<3 Ma).

From the analysis of the river drainage extracted from the basement uplifted block bounding the rift system to the west, it is assumed that (1) lithological and tectonic basement features exerted a strong control on the river network, (2) fault-related basement uplift is polyphased, and (3) the unsteady nature of the present-day river drainage is due to still active rift-flank uplift in the southern portion of the rift system.

Table des matières

Liste de Figures

Liste de tableaux

Chapitre 1
Introduction et Problématiques

Ce chapitre presente l'introduction du sujet traité dans la thèse. Il est divisé en deux parties, le premièr partie présente le notion globale du rifting continentale (en anglais) et la seconde partie est la problèmatique (en française).

Chapitre 1

1.1 General notions about continental rifting

1.1.1 Continental rifting

Continental rifting is a thermo-mechanical process in which a complex rheological multi-layer is affected by temperature-dependent processes such as changes in rheological properties or magma-related thermal weakening of the extending lithosphere (Corti, 2012). Continental rifts are complex manifestation of lithospheric break-up that result from diverse extensional mechanisms (Albaric, 2009, Plasman, 2017 and references therein). Continuous continental break-up leads into transition into sea floor spreading as well as continental passive margins (e.g., Fletcher et al., 2018 and references therein). Classification and nomenclature of rifts are based on either extension characteristics or causative mechanisms such as: slow or rapid rifts; narrow or wide rifts; magmatic or amagmatic rifts; symmetric or asymmetric rifts and active or passive rifts (Corti et al., 2003; Albaric, 2009 and references therein). Generally rifting is controlled by several physical parameters, among them are thermal energy, mechanical energy, rheological contrasts, kinematics and dynamic constrains (Ruppel 1995; Corti et al., 2003).

Two end-member models, numerical (Buck, 1991) and analog (Brun, 1999) have shown that continental extension can occur as narrow rift valley or wide rift valley. Narrow rift valleys have lower width usually in the range between 50 and 100 km, example, the East African rift or the Cenozoic European rift system (Corti, 2012) while wide rifting takes place when extension is accommodated by the development of horsts and grabens that are distributed over a wider area than lithospheric thickness, up to 1000 km, e.g., Basin and Range region (Corti, 2012). The two end-members are due to differences of strength of the lithosphere where wide rifts are due to extension of weak lithosphere (absence of a strong upper mantle) while narrow rifts are thought to have developed in strong lithosphere (Brun, 1999; Buck, 1991; Corti, 2012).

The evolution of continental rifts is mainly controlled by volume of magma body existing which weakens the strong lithosphere thermal mechanically and so generating magma-assisted rifts (Buck, 2004, 2006), crustal or lithospheric resistance and pre-existing structures (Corti et al., 2003a; Buck 2006).

It has been established that extensional stresses are not applied to a uniform, isotropic continental lithosphere, but rather to pre-deformed, anisotropic lithosphere which contains pre-existing, inherited weaknesses (Corti et al., 2003a). These weaknesses underlying thinner, thermally and mechanically weaker lithosphere are responsible for strain localization during rift initiation (e.g., Corti et al., 2013; Leseane et al., 2015; Sarafian et al., 2018; Fletcher et al., 2018). During rifting, the weakening of the inherited regional fabrics is enhanced by hot material rising from mantle plumes (e.g., Ebinger and Sleep, 1998). This is one of the reasons continental rifts are not randomly distributed, rather they tend to follow pre-existing weaknesses such as ancient orogenic belts while avoiding stronger regions such as cratons (e.g., Corti et al., 2003a; Dunbar and Sawyer, 1989; Morley, 1999b; Petit and Ebinger, 2000; Tommasi and Vauchez, 2001, Versfelt and Rosendahl, 1989; Ziegler and Cloetingh, 2004). These mobile belts and suture zones are believed to be weaker than the surrounding areas (Petit and Ebinger, 2000), and they are able to localize the extension deformation. One of the conditions for the reactivation of inherited structures is the relationship between orientation of pre-existing structures and the direction of extension, it is generally accepted that rifting reactivates structures at high angles to the direction of anisotropies, that is structures that are parallel to the extension are important in influencing rift architecture since they can block the propagation or fits segments and therefore control the location of transfer zones (Corti, 2012).

1.1.2 Influence of magma on rifting processes

For a long time, it has been considered that stretching of continental lithosphere is a result of two major processes, passive and active rifting. Passive rifting is due to regional stress field which causes diapiric rise of the asthenosphere through the lithosphere whereas active rifting results from thermal upwelling through which the lithosphere is thinned by an ascending mantle plume (Corti et al., 2003; Morgan and Baker, 1983; Turcotte and Emermen, 1983; Keen, 1985; Ziegler and Cloetingh, 2003) (Fig. 1.1). Many rifts are either passive or active though both processes may interchange in the cause of evolution, i.e., an initially passive rift may evolve into active rift (e.g., Wilson, 1993; Merle and Michon, 2001; Ziegler and Cloetingh, 2003).

Passive rifting is synonymous to pure magmatic rifting in which thinning of lithosphere is due to boundary forces which induces adiabatic decompression and rising of asthenosphere (McKenzie, 1978; Wernicke, 1985; Lister et al., 1986; Albaric, 2009). Active rifting is due to the impact of mantle plume at the base of the lithosphere which brings about both, thermal erosion and thinning by isostatic compensation (Turcotte and Emermen, 1983; Corti et al., 2003).

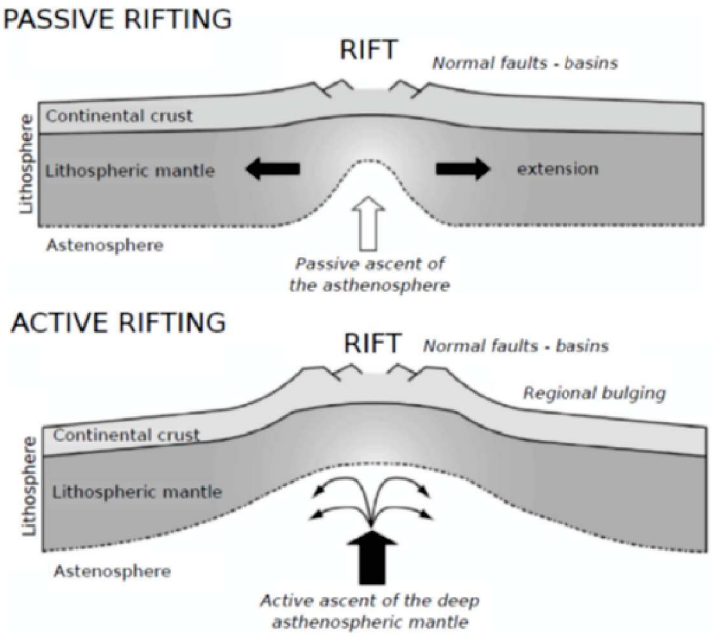

Fig.1.1. Models presenting passive and active rifting models (modified after Stab et al., 2015).

When magmatic bodies are emplaced within the continental lithosphere, they tend to modify initial thermal and mechanical properties leading into both magmatic and tectonic extension (Corti et al., 2003). During tectonic rifting, deformation is essentially accommodated by faults (Fig.1.2) forming a wide deformation domain (Buck, 2006; Albaric, 2009). Contrary to tectonic stretching, magmatic rifting is one of major players of active rifting where extension is due to magmatic intrusion essentially dykes which initiate extension of continental lithosphere (Geoffroy, 1998; Buck, 2006) (Fig.1.2). It should be noted that magmatism often precedes rifting (e.g., Courtillot and Renne 2003 and references therein) and a relatively small amount of hot basalt intruded into lithosphere could significantly heat (e.g., Royden et al., 1980) and weaken that lithosphere (e.g. Buck 2004) resulting into extension.

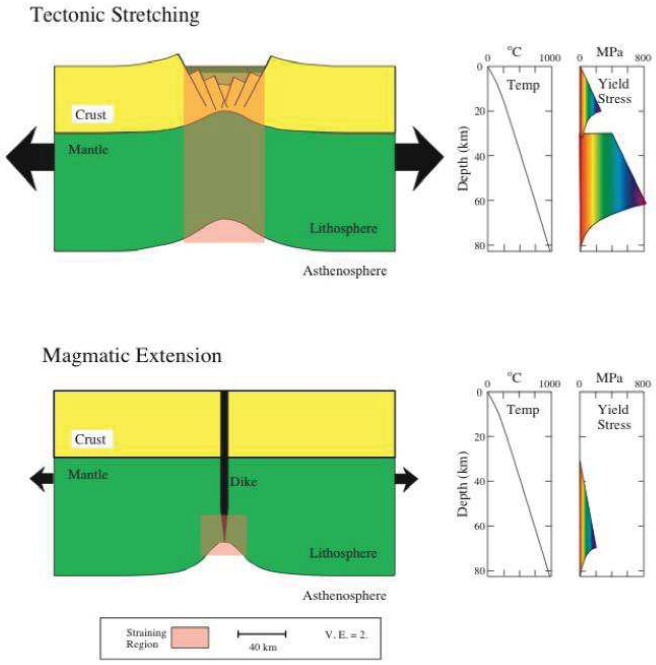

Fig. 1.2. Extension models, pure mechanical extension (on top) and magmatic extension on bottom). Black arrows' sizes indicate the minimum force needed to initiate rifting, it is small or magma (dyke) assisted rifting. (Modified from Albaric (2009).

1.1.3 The East African Rift System

One of the major reference structures for the study of continental rifts is the East African Rift System (EARS) which runs for over 4000 km from the Afar depression at the Red Sea-Gulf of Aden junction up to gulf of Mozambique along which the extension rates vary between 2 and 6.5 mm/yr (Stamps et al., 2008). It is made up of fault-bounded depressions which mark the divergent boundary between two tectonic plates, Somalian and Nubian plates (Calais et al., 2006). EARS is a well-known natural laboratory for the study of active continental rifts because it has recorded different stages of continental extension from rift initiation in the North Tanzanian Divergence (NTD) to beginning of oceanic spreading in the Afar (Ebinger, 2005; Corti, 2012; Philippon et al, 2014).

The evolution of EARS is influenced by one or two mantle plume, one placed in the Kenyan dome and the Ethiopian dome which are said to be implaced prior or synchronously to rifting process (Ebinger and Sleep, 1998; Rogers et al., 2000; Plasman et al, 2017). Also, it is generally accepted that continental rifts nucleate within orogenic mobile belts at the craton margin (e.g., Corti et al., 2013; Fletcher et al., 2018). Mobile

orogenic belts and suture zones are known to be weaker than the surrounding areas (Petit and Ebinger, 2000) and therefore can easily localize the extensional deformation. The EARS is a typical example of a rift development controlled by inherited fabrics, as both the Eastern and Western branch of this rift system would follow pre-existing mobile belts and branch around the Archean Tanzanian Craton (e.g., McConnel, 1972), (Fig. 1.3).

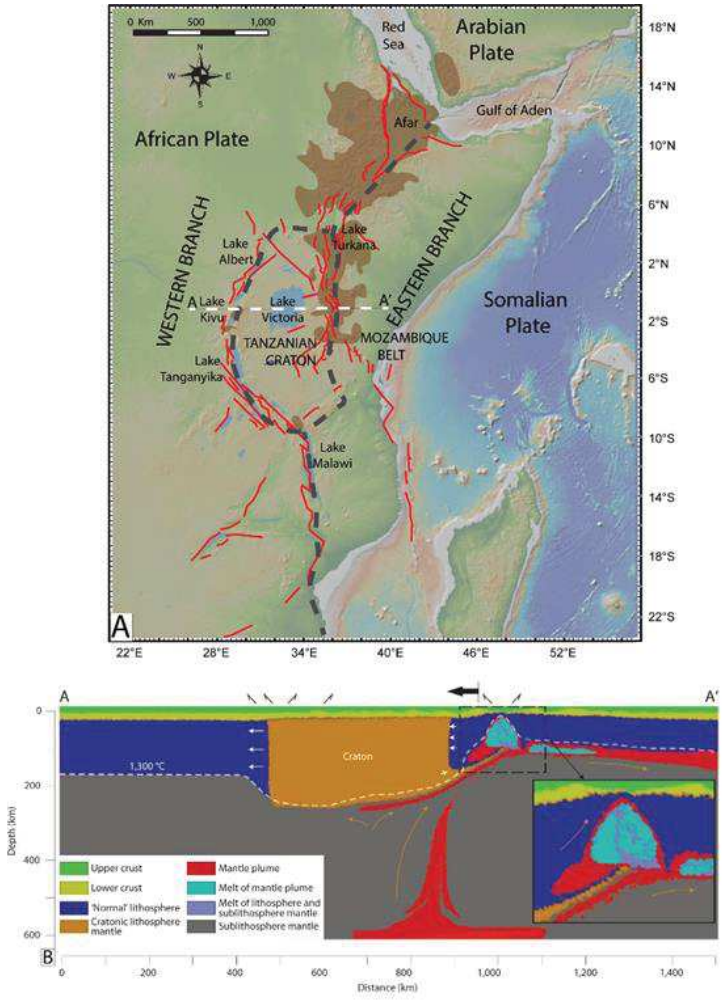

Fig. 1.3. The map of East African Rift system a) (modified from Mana et al., 2015) showing the extent of magmatism (brown) in the two rift branches (red lines) and b) the deflection of the mantle plume materials to the eastern side of the Tanzanian craton (Koptev et al., 2015).

In the eastern branch, where this stud is focused, rifting initiated in the Turkana more than 25 Ma while faulting and magmatism in the south Kenya rift is less than 7 Ma (Baker, 1986; Mana et al., 2012; Plasman et al;, 2017). In this branch, the N-S trending rift segments follow the Neoproterozoic Mozambique belt which is located just at the edge of Tanzanian craton (Fletcher et al., 2018 and references therein). The same has been recorded in the western branch where by the NW-trending Neogene Rukwa rift is

localized in the granulite Proterozoic mobile belt (Fletcher et al., 2018). Despite the acceptance that rifts develop within inherited fabrics, it has also been shown by geological and geophysical investigations that continental rifts can develop and hence propagate within cratons for example in the Albertine-Rhino graben of the north eastern Congo craton (Katumwehe et al., 2015) or the Eyasi basin in Tanzanian craton (Foster et al., 1997; Fletcher et al., 2018). The two branches of the EARS are differentiated by the presence of magma, the western is non-magmatic while the eastern branch is magmatic (Koptev et al., 2015 and references therein). On both branches faults are localized within mobile belts i.e. Kibaran, Ubendian, Ruwenzori and Mozambique belts in the western branch and along the edge of the Tanzanian craton for the eastern branch (McConnel,1972; Corti, 2012). The important volume of magma in the eastern branch is attributed to events such as dyking which are common in magmatic rifts (Calais et al., 2008; Wright et al., 2006). In EARS, rift basin segmentation and orientation are also controlled by ductile and brittle shear zones in basement rocks e.g., N to NW-trending basement shear zones such as the Aswa shear in South Kenya rift (Muirhead & Kattenhorn, 2018; Chorowicz, 1989; Katumwehe et al., 2015). Further in the north, the Main Ethiopian Rift (MER) localization was also controlled by NE-SW trending pre-existing weaknesses (Bastow et al., 2008; Corti, 2008; Keranen et al., 2009; Keranen and Klemperer, 2008).

1.1.4 The North Tanzanian Divergence

In the Kenyan rift sector of the eastern branch of the EARS, rifting and faulting initiated above Kenya dome near Lake Turkana at about 25 Ma (Morley et al., 1992; Ebinger et al., 2000; Muirhead and Kattenhorn, 2018). From Turkana, the rift propagates southwards forming several rift basins, e.g., Naivasha in central Kenya (Smith, 1994; Spiegel et al., 2007; Acosta et al., 2015) and Magadi in southern Kenya (Crossley, 1979), these basins are either comprised of volcanic or sedimentary sequences that date between 23 Ma to Present (Muirhead and Kattenhorn, 2018) overlying Mozambique Belt basement rocks (Baker, 1958, 1963; Baker and Mitchell, 1976; Crossley, 1979; Nyamai et al., 2004). Extension in south Kenya rift is mainly accommodated by both border faults in its western margin and intra-rift faults which accumulate between hundreds to thousands meters of throw in its centre (Muirhead and Kattenhorn, 2018).

As the south Kenya rift propagates southward it forms the Magadi-Natron trough which is bounded by the Nguruman, Sambu and Natron faults to the west making it a hemi-graben. Initial strain in this trough is accommodated by the Nguruman escarpment from ~ 7 Ma and later migrates eastward towards the centre of the rift where strain is accommodated by magmatism and volcanism (Muirhead et al., 2016; 2019) which in fact is marked by the eruption of Lengitoto trachytes lavas along the western margin between 6.9 and 5 Ma (Muirhead et al., 2019; Crossley, 1979). As the rift approaches Lake Natron, it splays out into three main branches, Eyasi in the west, Manyara in the centre and Pangani in the eastern arm forming the North Tanzanian divergence (NTD) (Le Gall et al., 2008), (Fig.1.7). Eyasi and Manyara branches are hemi-graben structures whose depth is less than 3 km (Ebinger et al., 1997). The NTD structure is marked by changes in rift width, it increases from a straight 50 km-wide south Kenya rift (Macdonald et al., 1994) to a more than 200 km in northern Tanzania (Dawson, 1992). Morphological and structural changes between the south Kenya and the north Tanzanian rifts are also marked by the presence of lavas in the south Kenya rift while lavas are scarce in the northern Tanzania rift (Ebinger et al., 1997; Le Gall et al., 2004). Geophysical investigations in southern Kenya show that Moho depth is ~40 km in rift shoulders and decreases to ~35 km in the axial valley (Last et al., 1997). It has been indicated by crust and mantle xenolith data that the thin-skinned thrusts of the Pan-African orogeny are underlined by the Archean mantle lithosphere and that much of the Natron-Manyara rifted zone is formed above this Archean mantle lithosphere (Vauchez et al., 2005; Aulbach et al., 2008; Baptiste et al., 2015; Plasman et al., 2017).

The NTD is comprised of two volcanic axes each having a different orientation; the east-west (Tarosero-Kilimanjaro) axis is comprised of Tarosero, Monduli Juu, Burko, Meru and Kilimanjaro volcanoes whose age is decreasing E-W while the second chain is an off-axis NE-SW-oriented axis, known as Ngorongoro volcanic highland is composed of Ngorongoro, Embagai, Olmoti, Olsirwa, Sadiman, Oldeani, Kerimasi and Lolmalasin volcanoes whose age is decreasing in a north east direction. The main volcanic phase in this rift sector lasts between 2.5 and 1 Ma (Le Gall et al., 2008; Mana et al., 2015) while intense tectonic activities have taken place before 1.2 Ma (Foster et al., 1997).

High seismic activities have also been recorded in the NTD (Nyblade et al., 1996), some of these seismic activities have relatively elevated magnitude as compared to other

rift. The strongest events were recorded south of Lake Eyasi in 1964 (mb=6.3) and in 2007 south of Lake Natron Mw=5.9, Albaric, 2009). Spatially seismic activities are concentrated into two clusters both located in the centre of the NTD (Fig.1.4), the first cluster is located south of Lake Natron, it is related to volcanic activities taking place at Oldoinyo Lengai, Gelai and dykes propagation (Calais et al., 2008; Biggs et al., 2009) and the second cluster is located at the south of Lake Manyara at about 150 km from the northern cluster (Albaric et al., 2009; Craig et al., 2011). Albaric et al. (2014) indicated that volatile fluids have played an important role in localizing earthquake swarms in the NTD. One of interesting features of seismic activities in this region is the existence of seismicity at an anomalous depth of more than 35 km (Nyblade et Langston, 1995; Brazier et al., 2005) which is indicative of rift propagation within the Mozambique mobile belt (Doser and Yarwood, 1994) as a result of reactivation of steep north east trending Precambrian shear zones (Albaric et al., 2010).

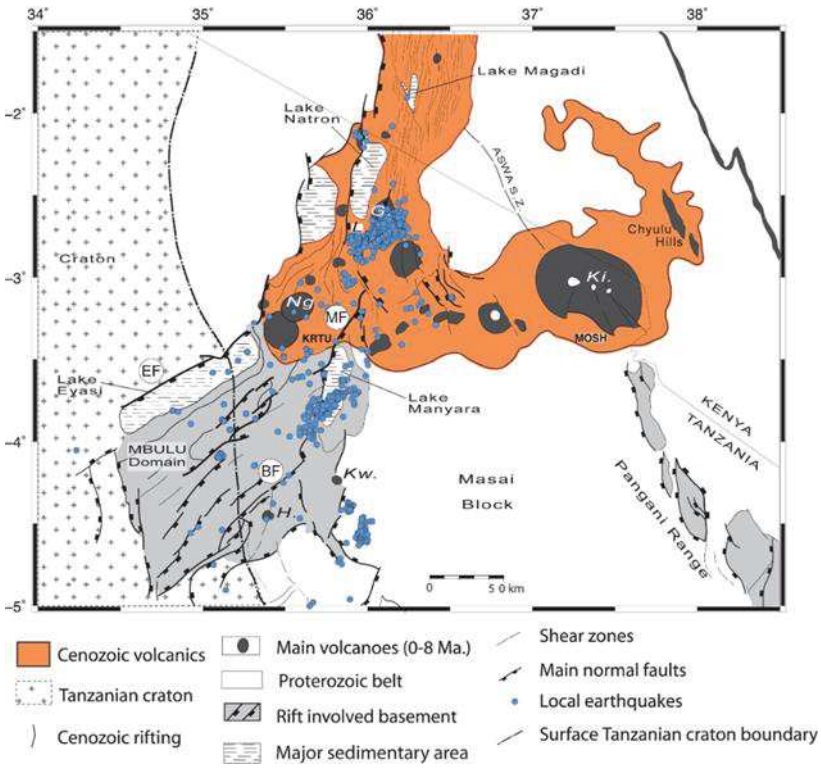

Fig. 1.4. Structural sketch of the NTD demonstrating two major seismic clusters of the NTD (modified from Le Gall et al., 2008 and Albaric et al., 2009).

The concept of structural inheritance evoked above is important on both contexts (extension or compression), whereby any anisotropic material when submitted to forces of any kind, its deformation is more or less controlled by pre-existing discontinuities. In

the EARS, this concept has already been used on both large and small scales. In large scale, it is indicated by the fact that the rift forms two branches which surround the Tanzanian Craton and propagate along the Proterozoic belts. The same craton seems to control the distribution of magma to the extent that the western branch has recorded very little magmatic activities while the eastern branch is magmatic. Moreover, tectonically the eastern branch is strongly influenced by structural inheritance which can be observed from the Ethiopian rift where the extension is E-W but its orientation is oblique following the direction of pre-existing oblique structures but also the existence of internal en-echelon rift segments (Corti, 2008).

In Kenyan rift, structural inheritance is also responsible on both, its segmented form and its zig-zag shape where newly formed segments are N-S while inherited structures are transverse in a NW-SE direction for most part of Kenyan rift. To the contrary in south Kenya and north Tanzania transverse structures are NE-SW, this NE-SW structure is very particular at the scale of EARS making part of the NTD which has drawn a lot of attention from the scientific communities particularly on the origin of its magma and its structure at depth (e.g. Albaric, 2009; Plasman et al., 2017; Weinstein et al., 2018). Such NE-SW structures are also observed in most parts of the NTD, as for example in the Eyasi basin and Mbulu several authors have indicated that dykes (Albaric et al., 2014) and faults have developed within the suture zone which itself is a result of collision between the Tanzanian craton and Proterozoic Mozambique basements blocks (e.g., Fletcher et al., 2018). Moreover, the boundary between these two basement formations have been marked by lithospheric thinning and weakening at the edge of the craton (Fletcher et al., 2018). To date, a comprehensive structural model which explains the origin of the NTD is missing, it is the objective of this study to propose a structural model which provide details about the origin of NTD by integrating two arms of the NTD (Eyasi and Manyara) and the South Kenya rift.

1.2 Introduction et problématiques

La notion d'héritage structural est un concept communément appliqué à tout matériau soumis à des contraintes tectoniques, qu'elles soient de natures compressive ou extensive. Dans tous les cas de figures, il s'agit de matériau anisotrope renfermant des

discontinuités, de natures et géométries diverses, qui peuvent se comporter de deux façons antagonistes vis-à-vis des contraintes principales. Elles peuvent, soit faciliter la déformation du matériau par réactivation de fabriques pré-existantes dont l'obliquité vis-à-vis des contraintes va déterminer en partie la cinématique de la déformation, soit inhiber, voire bloquer la déformation. Dans le premier cas de figure, les structures héritées se combinent à celles néoformées, directement contrôlées par les champs de contraintes, tandis que l'état thermique du matériau déformé intervient également dans le bilan respectif des deux types de déformation (Kirby & Kronenberg, 1987).

En contexte extensif, l'un des dispositifs de référence pour les processus de rifting continental est le rift Est-Africain (Fig. 1.5) au sujet duquel le concept d'héritage structural a été appliqué précocement et à diverses échelles. C'est ainsi que la division du REA en deux branches, de part et d'autre du craton tanzanien, et l'allure arquée de sa branche occidentale, sont classiquement attribuées au comportement rigide de la lithosphère archéenne vis-à-vis de l'extension, celle-ci se focalisant de manière préférentielle au niveau du socle protérozoïque qui ceinture le craton (Rosendahl, 1987 ; Daly et al., 1989). À l'échelle de la branche orientale du REA, typique d'un rift magmatique, l'héritage structural s'exprime de façon contrastée entre (1) le rift éthiopien, au nord, sécant sur le dôme lié au panache Afar, et (2) le rift kenyan, au sud, sécant sur le dôme Est-Africain (Fig. 1.5). L'organisation du rift éthiopien, en segments linéaires subméridiens, disposés en échelon dextre au sein d'un domaine rifté d'allure cartographique arquée, globalement N20°E, est classiquement attribuée à un processus de rifting oblique résultant d'une extension EW appliquée à une discontinuité crustale pré-existante N20°E (Corti, 2009, et références).

Vers le sud, au-delà de la grande dépression transverse du Turkana, le rift kenyan présente une allure cartographique plus 'anguleuse', due à l'interférence de deux familles de segments de rift de directions obliques, soit subméridienne (néoformée), soit transverse et à dominante NW-SE (héritée) contrôlée par des zones de cisaillement protérozoïques (direction ASWA) (Smith & Mosley & 1993; Chorowicz, 1989). Celles-ci se comportent souvent comme des zones de transfert (Le Turdu et al., 1999; Morley, 1999) et sont responsables de la trajectoire en zig-zag du rift kenyan. Parmi les plus significatives, on peut citer celles d'Anza-Soudan au niveau du segment Turkana (Vétel et Le Gall, 2006 ; Le Gall et al., 2005), d'Aswa au niveau du segment Baringo-

Bogoria (Le Turdu et al., 1999; Hautot et al., 2000), ou de Kordjya au niveau du segment Sud Kenya (Atmaoui & Hollnack, 2003; Muirhead et al., 2016).

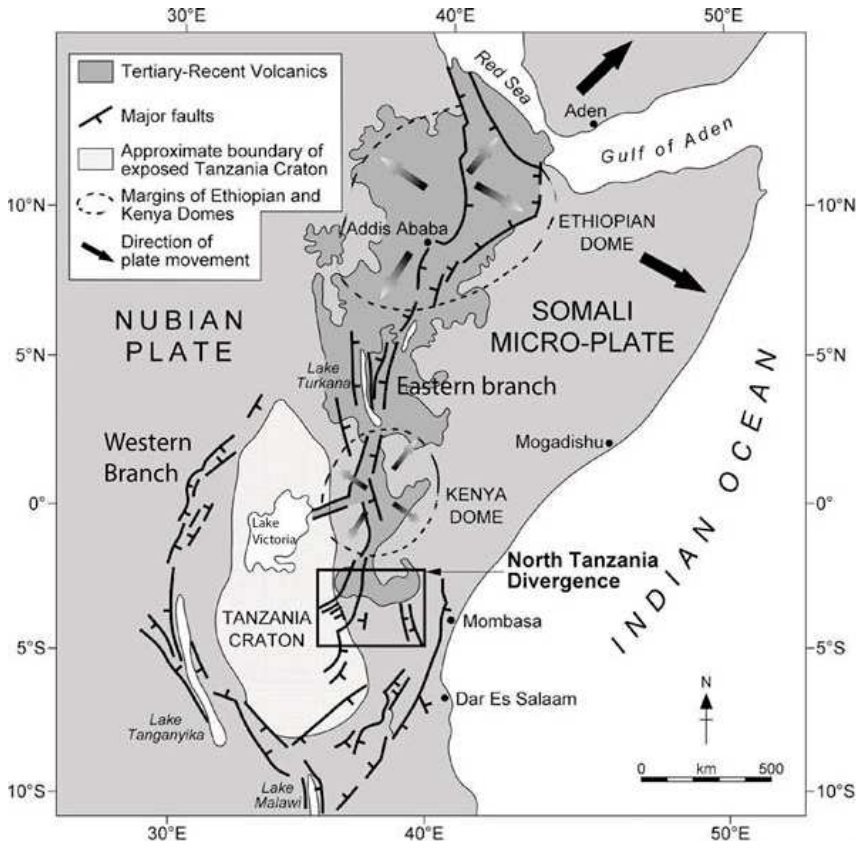

Fig. 1.5. Carte schématique du Rift Est Africain montrant les structures majeures de l'ensemble du REA, il s'agit des dômes Ethiopie et Kenya, des branches Est et Ouest, du Craton Tanzanien et de la Divergence Nord Tanzanienne, d''après Dawson, 2008.

Démontrer l'origine héritée de structures tectoniques ne repose, dans la plupart des cas, que sur de simples arguments cartographiques. L'utilisation de critères rhéologiques peut-être aussi pratiquée à l'échelle lithosphérique, comme à propos du rift cénozoïque du Turkana dont la trace recoupe en oblique celle du rift plus ancien d'Anza, orienté NW-SE et d'âge Crétacé-Paléogène (Fig.1.6).

Il a été suggéré par Vétel & Le Gall (2006) que la trajectoire subméridienne du premier, qui coïncide avec une portion de lithosphère épargnée par l'extension crétacée, était la conséquence d'un processus de 'strain hardening' (Kusznir & Park 1987 ; Ziegler & Cloetingh 2004) ; la lithosphère initialement intacte (non étirée au Crétacé) étant a priori plus facilement déformable car épargnée par les processus de substitution

(matériel infra-lithosphérique *versus* manteau asthénosphérique riche en olivine et plus rigide une fois refroidi), intervenant lors de l'amincissement lithosphérique.

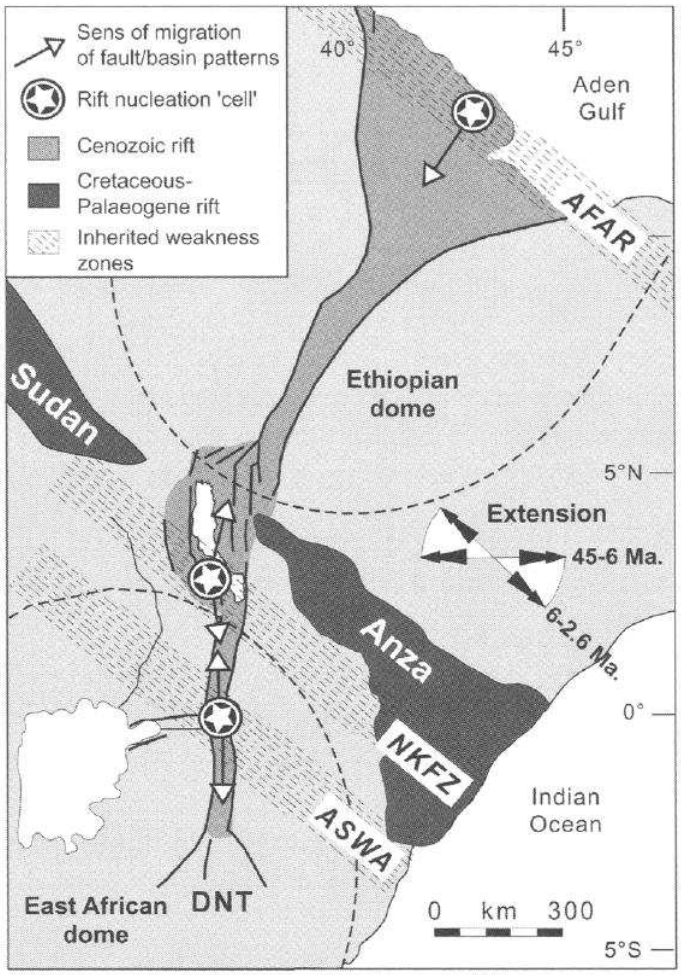

Fig. 1.6. Modèle de propagation du rift le long de la branche est du REA montrant la nucléation du rift Turkana en relation avec le dispositif rifté antérieur d'Anza (crétacé), d'après Vétel et Le Gall, 2006.

L'un des thèmes de cette thèse est de discuter le concept d'héritage structural à propos de l'un des dispositifs les plus atypiques de l'ensemble du REA, situé à l'extrémité sud du rift kenyan (RSK). Dans ce secteur, la vallée axiale des segments Magadi-Natron passe vers le sud à trois branches divergentes, celles d'Eyasi (W), de Manyara (Central) et de Pangani (E), qui déterminent ainsi un domaine rifté hétérogène et anormalement large (>200 km), la Divergence Nord Tanzanienne (Fig. 1.7). Ces variations tectoniques de premier ordre coïncident avec (1) la transition brutale entre un rift magmatique (Sud Kenya) et un rift amagmatique (DNT), par l'intermédiaire de deux chaînes volcaniques

transverses, celles du Kilimanjaro et du 'Crater Highlands', et (2) la proximité de la bordure orientale du craton tanzanien. Compte tenu de ce contexte géodynamique exceptionnel, la DNT a fait l'objet de nombreux programmes de recherche focalisés pour l'essentiel sur sa structure profonde et son comportement rhéologique lors du rifting (Albaric, 2009; Albaric et al., 2009; Weinstein et al., 2017; Plasman, 2017; Plasman et al., 2017), ainsi que sur la nature des sources du magmatisme synrift (Nonnotte, 2007; Nonnotte et al., 2008; Mana et al., 2015). Paradoxalement, très peu d'études structurales lui ont été consacrées et les quelques modèles proposés ne rendent pas compte de façon convaincante de l'origine de la DNT. Ceux de Foster et al. (1997) ou d'Ebinger et al. (1997), basés sur des données géophysiques (gravimétrie, aéromagnétisme, ..) et des datations du volcanisme synrift, accordent un rôle majeur aux structures du socle archéen qui auraient contrôlé l'orientation oblique (NE-SW) du système de failles d'Eyasi. Celui de Le Gall et al. (2008), basé sur des données morphostructurales et des datations du magmatisme, propose un modèle de distribution spatio-temporelle de l'extension au cours des 7 derniers Ma, âge du début du rifting dans l'ensemble du système RSK-DNT.

L'une des limitations de l'ensemble des modèles proposés à ce jour est de ne pas prendre en compte le dispositif synrift du RSK qui jouxte la DNT au nord et présente également des anomalies structurales par rapport à la configuration 'classique' du rift kenyan-éthiopien. En effet, le dispositif du RSK se démarque par un élargissement anormal (>110 km entre 2° et 2°52'S) qui résulte de la juxtaposition (1) du fossé axial Magadi-Natron, de largeur normale (60 km) et dans le prolongement sud de l'hémigraben kenyan, et (2) d'un bloc losangique (80 x 40 km), celui d'Ol Doinyo Ogol (ODO), dont les séries synrift (volcaniques et sédimentaires) forment l'épaulement occidental du fossé Magadi-Natron (Fig. 1.7). Bien que cité dans la littérature et ayant fait l'objet d'études à finalités volcano-sédimentaires (Isaac & Curtis, 1974; McHenry et al., 2008) et géochronologiques/géochimiques (Manega, 1993 ; Foster et al. 1997), le bloc ODO n'a jamais fait l'objet d'études structurales spécifiques, limitant ainsi la portée des modèles de rifting appliqués au système RSK (Muirhead et al., 2016 ; Lee et al., 2017).

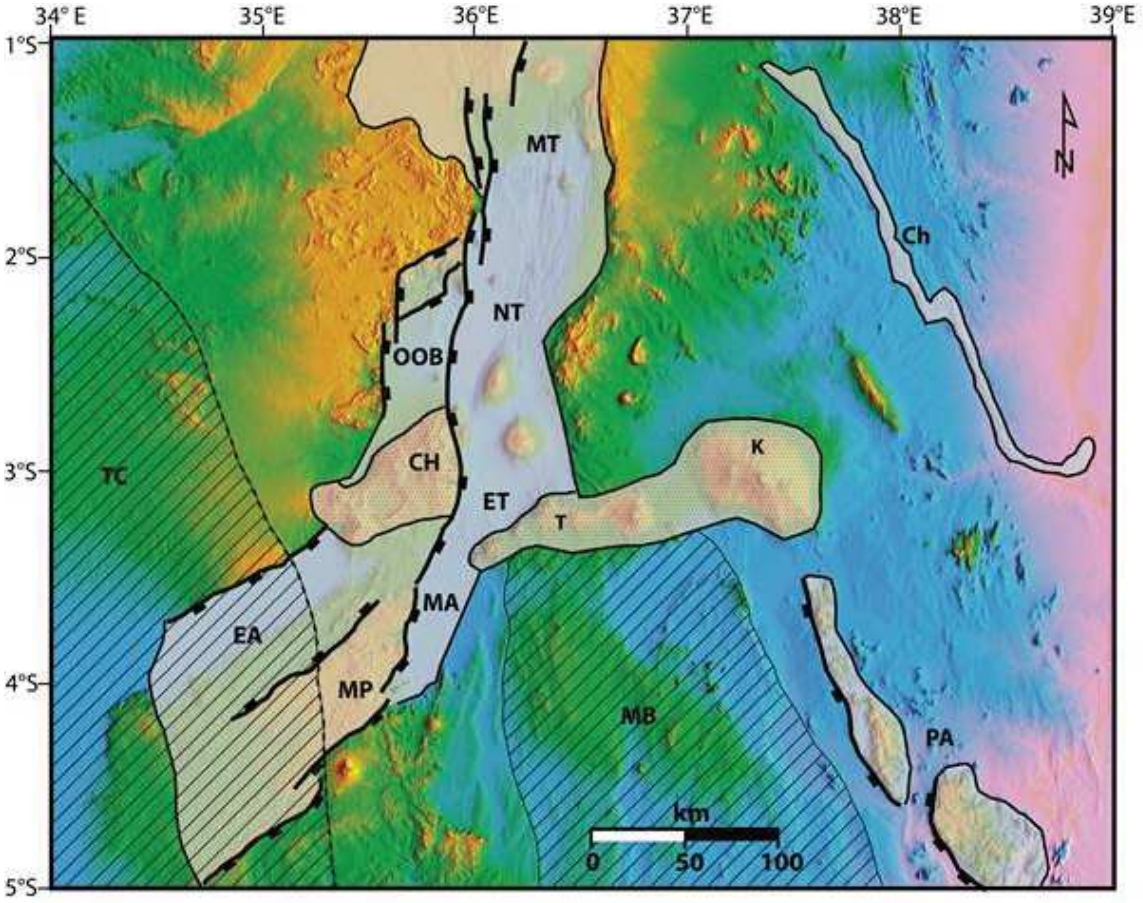

Fig. 1.7. Carte du RSK-DNT (Modèle numérique de terrain, GTopo30) montrant le rift Sud Kenya et la DNT avec ses trois branches ainsi que le craton. CH., Crater Highlands; EA., Eyasi rift arm; ET., Engaruka trough; K., Kilimanjaro volcano; MA., Manyara rift arm; MB., Masai block; MP., Mbulu plateau; MT. Magadi trough; NT., Natron trough; OOB., Ol Doinyo Ogol block; PA., Pangani rift arm; T., Tarosero volcano. En hachures, le craton tanzanien.

L'objectif de ce travail de thèse consiste donc à combler ce manque en nous focalisant sur les thèmatiques suivantes :

- préciser l'organisation morphostructurale du bloc ODO, ainsi que ses relations avec le fossé Magadi-Natron, puis comparer le style de la déformation dans chacun d'eux. L'organisation structurale de la DNT n'est que brièvement abordée à propos de ces deux branches occidentale et centrale (Eyasi et Manyara) qui ont déjà été précédemment étudiées (Le Gall et al., 2008). Celle de Pangani, isolée à l'est, n'est pas intégrée dans notre étude.

- quantifier l'extension accommodée à la fois par les failles bordières et les réseaux de failles intra-rift dans les deux compartiments (ODO et Magadi-Natron);

- élaborer un modèle cinématique rendant compte (1) du caractère polyphasé de l'ensemble du système RSK et (2) du rôle respectif des structures intra-socle protérozoïques *versus* archéennes dans la propagation anormale du rifting, non seulement au niveau du RSK, mais aussi de la DNT.

Les méthodes mises en œuvre pour atteindre ces objectifs reposent essentiellement sur l'analyse et l'interprétation d'imagerie satellitale SRTM, et les modèles numérique de terrain (MNT) correspondants. L'accent est mis sur l'expression morphostructurale des failles bordières, tandis que la dynamique des mouvements verticaux enregistrés par les compartiments de socle est déduite de l'étude des réseaux de drainage. Cette étude de réseaux de drainage a était faire en collaboration avec Nicolas Loget à ISTeP (Sorbonne Université de Paris) où j'avais faire une mission de deux semaines.

L'analyse quantitative de certains paramètres géométriques (longueur, déplacement, ..) des populations de failles, qu'elles soient bordières ou intra-rift, extraites du MNT permet notamment de préciser la distribution de l'extension dans le temps (7 Ma) et l'espace (compartiments ODO et Magadi-Natron).

L'analyse du dispositif morphostructural de surface est complétée par deux autres approches qui ne seront que succinctement présentées.

Des données de magnétotellurie enregistrées le long d'un transect EW de 150 km, recoupant le dispositif à la latitude du volcan Ketumbeine et de la province des Crater Highlands, ont été modélisées sur une épaisseur crustale de 20 km afin d'imager l'architecture de sub-surface du dispositif rifté.

Des données de terrain ont été recueillies au cours d'une courte mission réalisée du 2 au 10 mai 2017 au niveau du bloc « perché » ODO. L'objectif consistait principalement à préciser la nature, la structure et l'âge des séries de remplissage des différents 'sous-blocs' étagés dans le compartiment ODO. Un échantillonnage exhaustif des divers ensembles magmatiques (laves et intrusions) présents a été effectué en vue de les dater (âges disponibles controversés) et donc de contraindre l'âge des failles bordières. Une vingtaine d'échantillons sont en cours de datations par méthode ^{39}Ar-^{40}Ar au laboratoire de géochronologie de Curtin, Australie. Ces âges ne seront disponibles qu'à la fin 2018.

1.3 Contexte géologique

1.3.1 Le Rift Est Africain

Le Rift Est Africain (REA) s'étend sur 3500 km du Nord au Sud, depuis le triangle d'Afar jusqu'au golfe du Mozambique (Fig. 1.8). Il recoupe deux grands dômes topographiques, généralement interprétés comme l'expression de surface d'un ou deux panache(s) mantellique(s) en profondeur, ceux de l'Afar et Est-Africain (Pik et al., 2006). Le REA s'est développé au cours du Cénozoïque aux dépens d'un soubassement hétérogène constitué de blocs cratoniques archéens (Tanzanien et Masaï), présentant des âges compris entre 3,6 et 1,8 Ga, ceinturés par des chaînes orogéniques protérozoïques (Smith et Mosley, 1993).

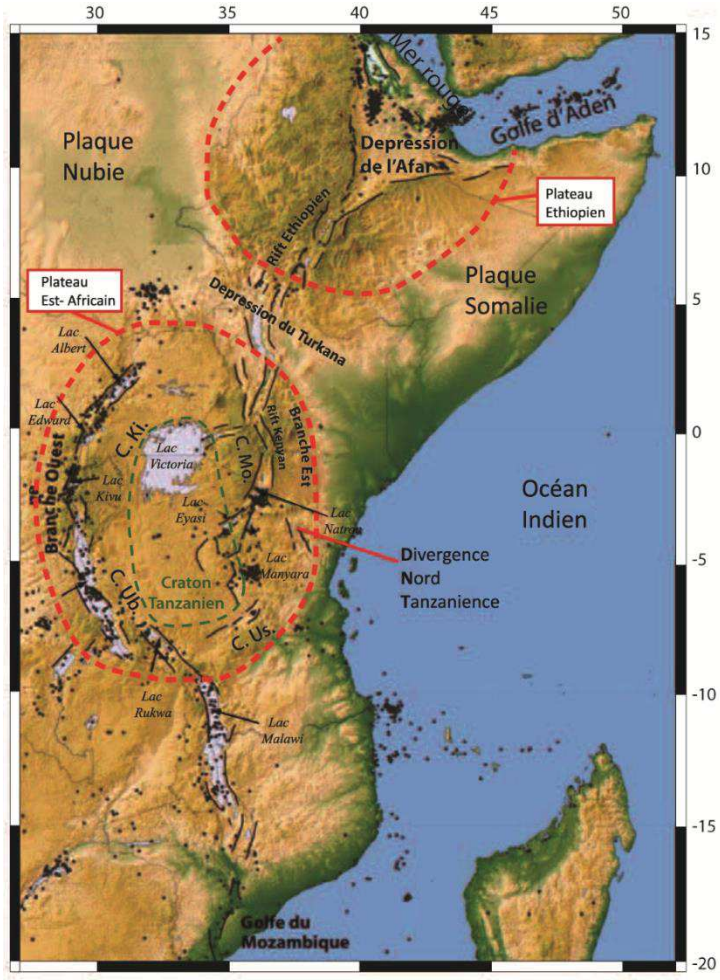

Fig.1.8. Carte structurale du Rift Est African (MNT, GTopo30, http://eros.usgs.gov) montrant le REA depuis la dépression Afar au nord jusqu'au golfe du Mozambique au sud. Les cercles rouges correspondent à la trace des dômes d'Ethiopie et du Kenya, d'après Albaric, 2009.

Ce socle a ensuite enregistré de multiples épisodes de rifting au cours du Permo-Trias (Karoo) et du Jurassique-Crétacé, antérieurement à l'extension cénozoïque (Fig.1.9). Le REA se divise en deux branches, à évolution très contrastée, de part et d'autre du craton Tanzanien : la branche Ouest, d'allure arquée depuis le linéament d'Assoua au nord jusqu' à celui du Zambèze au sud, est soulignée par de grands lacs qui coïncident avec des bassins effondrés de type graben, ou plus fréquemment de type hémi-graben (Tanganyika, Albert, Kivu, Malawi). Il s'agit d'un rift presque exclusivement tectonique le long duquel le magmatisme synrift, initié vers 16 Ma, n'est localisé que dans quelques provinces volcaniques de dimensions réduites (Sud Kivu, Rungwe, Virunga) (Kampunzu et al., 1998b; Pasteels et al., 1989; Ebinger et al., 1989; Smets et al., 2015 ; Pouclet et al., 2016 ; Wood et al., 2017). A l'inverse, la branche Est, qui se connecte vers le nord au système de dorsales de Mer Rouge et du golfe d'Aden, *via* le point triple Afar, et s'étend vers le sud à travers la Tanzanie continentale (Le Gall et al., 2004) et une partie de sa marge 'offshore' (Mulibo & Nyblade, 2016), correspond à un rift typiquement magmatique en relation avec la présence d'un ou de plusieurs panaches en profondeur. Le long de la branche orientale, référence pour les dispositifs de rifts continentaux en contexte magmatique, les premières preuves d'activité volcanique sont datées à 40-45 Ma dans la dépression du Turkana à la transition entre rifts éthiopien et kenyan (Ebinger et al., 1993 ; George et al., 1998). Celles-ci sont ensuite suivies, à l'Oligocène, par la mise en place vers le nord d'importantes quantités de laves basaltiques de type 'trapps' continentales au niveau du panache mantellique Afar (Mohr, 1983 ; Mohr et Zanettin, 1988 ; Furman, 2007). Les premières phases de rifting sont, quant à elles, datées à 35 Ma dans les rifts éthiopien et Nord kenyan (Morley *et al.*, 1992). Les déformations et le magmatisme vont ensuite migrer progressivement vers le Sud jusqu'à atteindre le Sud Kenya vers 8 Ma (Baker *et al.*, 1971 ; Cerling et Powers, 1977 ; Crossley et Knight, 1981, Macdonald, 1994). A un ordre inférieur, la propagation du rifting s'est faite de manière discontinue, par le biais de petites «cellules magmatiques» isolées, à l'origine de segments de rift qui vont ensuite se connecter les uns aux autres (Ebinger et Casey, 2001).

Depuis le Pliocène, les activités magmatique et tectonique de la branche Est ont tendance à se concentrer dans une zone étroite, d'environ 50 km de large, coïncidant avec la vallée axiale du REA (Baker *et al.*, 1971 ; Baker et Wohlenberg, 1971 ; Morley, 1999). Cette évolution spatio-temporelle, d'un rift largement distribué à un rift très focalisé le

long du futur axe de rupture lithosphérique, est parfaitement documentée au niveau du système Afar, à un stade plus mature (e.g., Agostini et al., 2011a ; Corti, 2009, ; Hayward and Ebinger, 1996 ; Keir et al., 2013). Il faut toutefois noter le développement, au cours du Quaternaire, d'un important magmatisme «hors-axe», décalé vers le flanc oriental du rift et responsable de l'édification de massifs volcaniques de très grande taille tels que le Marsabit (rift Turkana), le Mont Kenya (Kenya Central) et la chaîne transverse Kilimanjaro-Tarosero (Nord Tanzanie) ; la signification de ce volcanisme « hors axe » étant encore sujette à discussion (Bosworth, 1987).

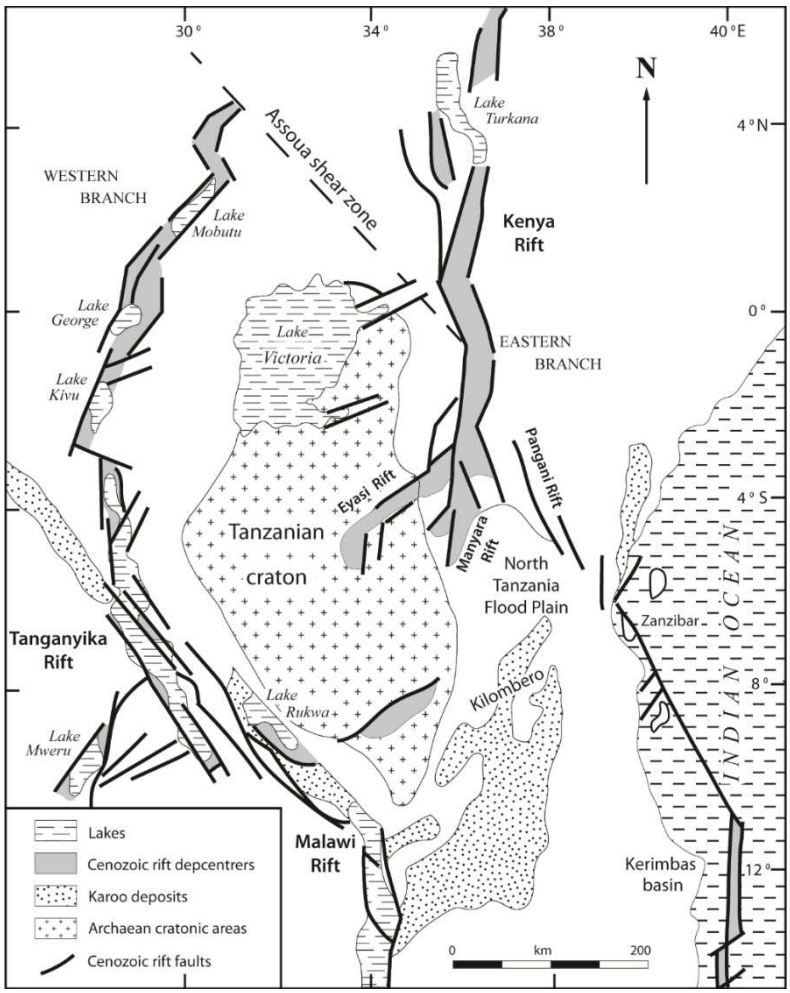

Fig. 1.9. Distribution spatiale des rifts cénozoïques et permo-triasiques dans le REA, modifié d'après Chorowicz and Sorlien (1992), Morley (1995) et Le Gall et al., 2004.

Les enregistrements géodésiques indiquent une direction d'extension actuelle globalement E-W (Saria et al., 2014), confirmée par l'analyse de la sismicité (Lambert et al., 2014) ou par inversion des tenseurs de contraintes (Delvaux & Barth, 2010). Les

reconstitutions cinématiques indiquent par ailleurs que la direction d'extension ne semble pas avoir varié au cours des derniers Ma (Calais et al., 2008). A l'échelle crustale, les données géophysiques de sismique réfraction révèlent un taux d'amincissement modéré à la verticale de la vallée axiale du Kenya, avec une épaisseur crustale diminuant d'environ 40 km au niveau des flancs à 35 km à l'axe (Fig. 1.10) (Maguire & Long, 1976; Henry et al., 1990 ; Mooney & Christensen, 1994; Birt et al., 1997 ; Prodehl et al., 1997). Un plus fort gradient longitudinal est observé depuis la croûte très amincie (25 km d'épaisseur) du segment Turkana, résultat d'un long processus de rifting initié il y a plus de 35 Ma, vers celles des segments plus jeunes Sud-éthiopien et Central-kenyan où l'épaisseur crustale est de l'ordre de 35 km (Mooney & Christensen, 1994; Mechie et al., 1994 ; Prodehl et al., 1997).

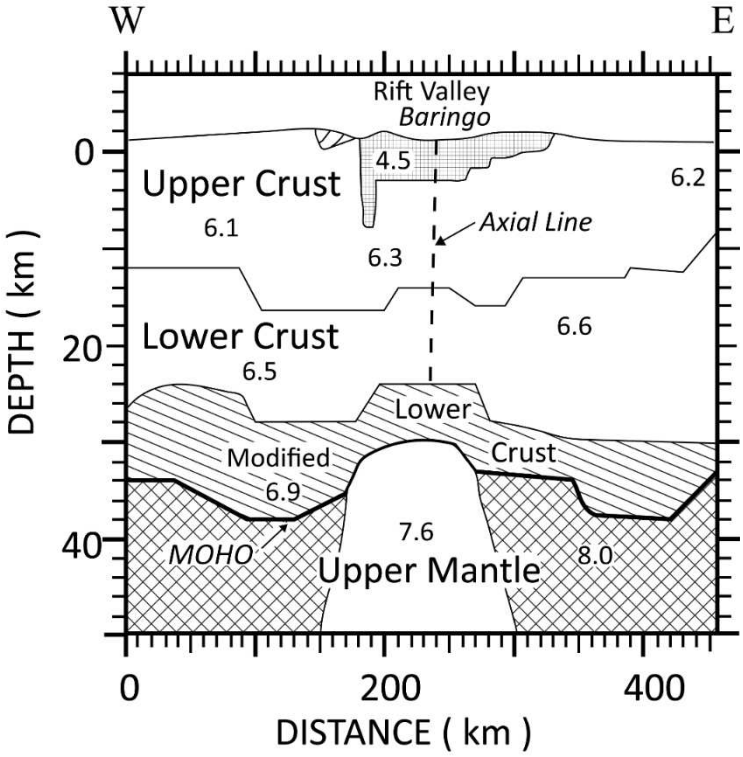

Fig. 1.10. Profil de la lithosphère du rift Kenya au niveau du Lac Baringo au nord du dôme Kenya montrant la variation d'épaisseur crustale entre les flancs et l'axe de la vallée (D'après Prodehl et al., 1997).

1.3.2 La Divergence Nord Tanzanienne

Située sur la retombée Sud du dôme kenyan, la DNT se marque par des changements importants dans l'expression de surface du rifting, qui passe d'une vallée

axiale unique, de type magmatique (Sud Kenya) à trois branches divergentes (Eyasi au N60°E, Manyara au N10-20°E et Pangani au N140°E) où la déformation, plus diffuse, est dominée par des systèmes de blocs basculés, fortement contrôlés par l'héritage structural du substratum hétérogène, et totalement dépourvus de magmatisme (Ebinger *et al.*, 1997 ; Le Gall *et al.*, 2004). Les bassins associés aux branches d'Eyasi et de Manyara sont des hémi-grabens à polarité SE, longs d'environ 100 km et larges de 50 km, dont la profondeur maximale déduite d'enregistrements aéromagnétiques est <3 km (Ebinger et al., 1997), indiquant une faible extension cumulée (Foster et al., 1997).

La transition brutale entre ces deux types de rifts, à savoir (1) localisé et magmatique au Nord, et (2) diffus et amagmatique au Sud, intervient au niveau de deux chaînes volcaniques transverses, situées de part et d'autre de la vallée axials du RSK, celle du Crater Highlands, orientée NE-SW sur le flanc ouest et celle de Kilimanjaro-Tarosero, orientée E-W sur le flanc oriental. Ces deux chaînes magmatiques 'hors-axe', d'âge Néogène, marquent la limite méridionale, en surface, de l'influence thermique du panache mantellique du Kenya ; celle-ci paraissant entravée par la présence de blocs cratoniques (Tanzanien et Masaï) (Ebinger et al., 1997 ; Le Gall et al., 2008).

La DNT connaît une activité sismique relativement intense (Nyblade et al., 1996) avec quelques événements de magnitude élevée pour un rift, les plus forts ayant eu lieu en 1964 au sud du lac Eyasi (mb=6.3) et en 2007 au sud du lac Natron (Mw=5.9), La sismicité se concentre essentiellement en deux essaims, à 4°S et 5.5°S, dans l'axe de sa branche centrale (Manyara). Leur distribution en profondeur est anormalement profonde >35 km (Nyblade and Langston, 1995; Brazier et al., 2005 ; Albaric et al., 2009), fournit des informations sur le comportement mécanique/rhéologique de sa lithosphère, en relation étroite avec, d'une part, sa nature initiale hétérogène, et d'autre part, sa structure thermo-mécanique, elle-même fonction pour partie du caractère magmatique *versus* amagmatique du contexte. La lithosphère 'froide' coïncide avec le rift amagmatique et la sismicité ; (Albaric et al., 2009).

A l'échelle lithosphérique, des zones à faible vitesse ont été mises en évidence dans le manteau supérieur, à la fois sous l'axe du rift et à la verticale des blocs cratoniques (Ritsema et al., 1998; Weeraratne et al., 2003; Park and Nyblade, 2006). D'après Huerta et al. (2009), elles sont la continuité de remontées thermiques étroites au sein de la zone

de transition, qui s'enracinent au niveau d'une très grande anomalie thermique proche de la discontinuité à 660 km, elle-même causée par le super-panache Africain.

1.4 Organisation du manuscrit

Les conditions particulières dans lesquelles s'est déroulée cette thèse, et notamment la durée très courte (3 fois 3 mois grâce à l'ambassade de France en Tanzanie et quelques mois en financement propres du laboratoire LGO) de mon séjour cumulé au Laboratoire « Géosciences Océan », impliquent que mon travail effectif sur la thématique de la thèse a été relativement limité dans le temps. Par soucis d'efficacité, les principaux résultats acquis lors de ce travail sont donc présentés sous la forme de trois articles (un soumis à Tectonics, un autre en cours de soumission et un troisième en préparation).

Mon manuscrit se décline en 6 chapitres et des annexes.

Chapitre I. Introduction et problèmatique

Chapitre II. Méthodologie.

Seule la méthodologie mise en œuvre pour l'analyse de l'imagerie SRTM, base ce travail, est décrite dans ce chapitre. Elle est également présentée dans le papier 'Anomalously-propagating rift pattern and structural inheritance. Insights from the south Kenya rift and the North Tanzanian Divergence, East Africa', Gama et al., Chapitre III.

Les méthodologies relatives à l'analyse quantitative des populations de failles et au réseau de drainage sont largement décrites dans les deux papiers correspondants (Chapitres III et IV, respectivement).

Chapitre III. Organisation morphostructurale du RSK et analyse quantitative de la déformation.

Sur la base des nouveaux résultats acquis, nous proposons un modèle cinématique du rifting qui privilégie le rôle d'une discontinuité transverse intra-socle lors de la propagation anormale du rift au niveau de l'ensemble RSK-DNT. Ces résultats sont présentés sous la forme d'un papier soumis à **Tectonics** 'Anomalously-propagating rift

pattern and structural inheritance. Insights from the south Kenya rift and the North Tanzanian Divergence, East Africa', Gama et al.

Chapitre IV. Réseau de drainage et tectonique verticale des compartiments de socle bordiers.

Les résultats de ce travail sont synthétisés dans le papier soumis à Basin Research 'Drainage pattern and multi-stage rift-flank uplift in the North Tanzanian Divergence, East Africa', Gama et al.

Chapitre V. Structure du segment de rift Ol Doinyo Ogol.

Ce chapitre concerne la structure du bloc d'Ol Doinyo Ogol, qui borde à l'ouest le fossé axial Magadi-Natron et dont l'évolution tectono-magmatique a enregistré les stades précoces du rifting. Seuls les résultats préliminaires de l'étude morphostructurale, complétée par les observations de terrain, sont présentés sous la forme d'une ébauche de papier qui sera soumis à **Tectonophysics** 'Tectono-magmatic development of an offset rift basin in the North Tanzanian Divergence framework, East Africa. The Ol Doinyo Ogol uplifted basin, South Kenya'. Le Gall et al.

Les résultats partiels de l'étude géochimique des laves sont brièvement décrits. Ce papier sera finalisé, avec l'élaboration d'un modèle cinématique du RSK, lorsque les résultats des datations de ces laves seront disponibles (fin 2018).

Chapitre VI. Discussion, Conclusion et Perspectives

Bibliographie

Annexes

Nous avons présenté dans les annexes A – C les travaux réalisés en parallèle des articles détaillés dans les chapitres précédents. Ces travaux donnent des informations complementaires à des résultats presenté dans les articles. L'annexe D est l'article publié par M. Plasman pour lequel nous avons contribué dans l'acquisition et pour la partie structurale.

Chapitre 2
Données et Méthodologie

Chapitre 2. Méthodologie et données

2. Présentation des données et méthodes.

Les résultats présentés dans ce travail sont principalement basés sur l'analyse et l'interprétation des modèles numériques de terrain (MNT) essentiellement SRTM (Shuttle Radar Topography Mission) couvrant les secteurs des rifts sud Kenya et nord Tanzanie dont la Divergence Nord Tanzanienne (DNT). L'utilisation de l'imagerie satellitaire dans le rift Est Africain a notamment permis l'étude des déformations récentes affectant la vallée axiale (e.g. Coussement, 1995; Le Turdu, 1998; Gloaguen, 2000; Vétel, 2005 and Molini & Corti, 2015). Dans cette thèse, ces MNT sont utilisées pour 1) une analyse géométrique et statistique des failles, et 2) l'étude des réseaux de drainage affectés par les soulèvements du rift. Les mêmes images sont utilisées pour les deux objectifs et nous avons appliqués les mêmes traitements préliminaires sur les MNT.

Ce chapitre présente les principales étapes des traitements généraux des données. Les applications spécifiques aux failles et aux réseaux de drainage sont détaillées dans les articles (chapitres 3 et 4). Nous décrivons ici les MNT utilisés, leurs avantages mais aussi leurs limitations. Nous décrivons l'ensemble des étapes et des critères utilisés, du téléchargement des données jusqu'à leur utilisation finale : la création d'une mosaïque, la correction des erreurs, l'extraction des populations de failles et l'extraction de réseaux de drainages.

2.1 Les Modèles Numériques des Terrain

J'ai utilisé 20 images MNT-SRTM 30 m (SRTM V3.1, 1 seconde d'arc projeté sur un système géodésique transverse Universal Mercator, WGS84), chacune de dimensions 1° x 1° couvrant la zone d'étude située entre 1.5° et 4.75° Sud et entre 34.5° et 37° Est (Fig. 2.1). Ce sont des données en libre accès depuis septembre 2014 (https://reverb.echo.nasa.gov/) qui présente une nette amélioration de la résolution par rapport aux précédentes données SRTM (90 m) disponible depuis 2003. La notice des MNT montre que ces images ont une résolution latérale de 30 m et une résolution verticale

de 16 m, mais plusieurs évaluations de la précision effectuées récemment ont montré que la résolution verticale pouvait être meilleure qu'indiqué, pouvant atteindre 6 m (Santillan and Santillan, 2016; Elkahrachy, 2017). Grâce à ces résolutions, les MNT sont devenus un outil majeur pour la visualisation 3D des structures, en particulier les systèmes de failles et des réseaux de drainage.

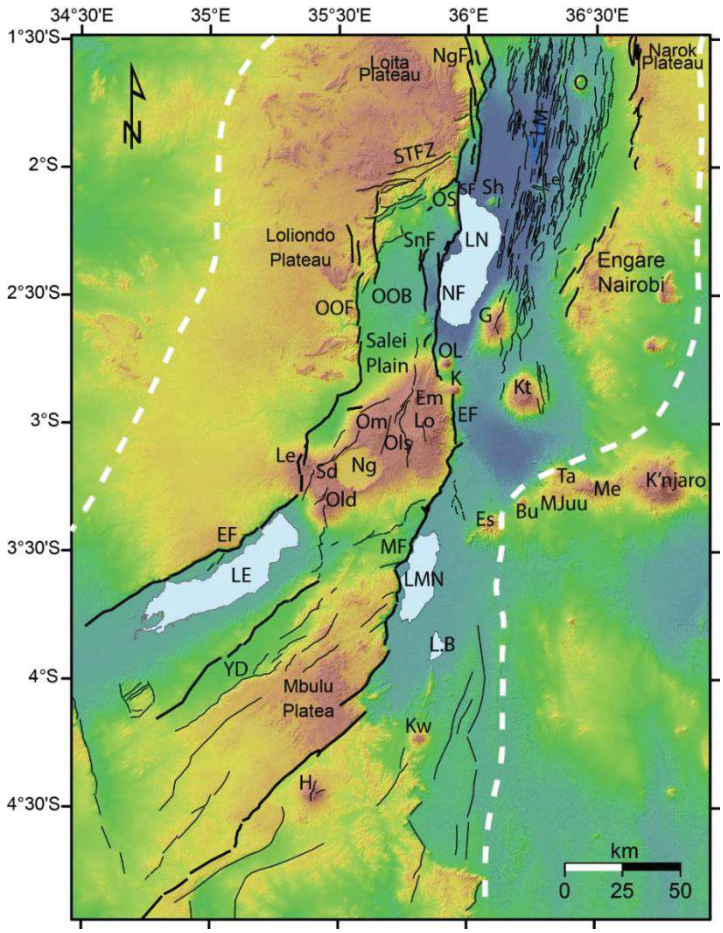

Fig. 2.1. Topographie (SRTM 30m) du rift Sud Kenya – Nord Tanzanie. En noir, l'ensemble des systèmes de failles, les lettres correspondent aux principales structures de la région. La zone d'étude est délimitée par des traits blancs. OOB., Oldoinyo Ogol block; STFZ., Sonjo transfer fault zone., NgF. Nguruman Fault, LM., Lake Magadi; LMN., Lake Manyara; NF., Natron fault; OOF., Ol Doinyo Ogol fault; SF., Sambu fault; SnF., Sanjan fault; Volcanoes: E., Embagai; G., Gelai; K., Ketumbeine; Ke., Kerimasi; L., Lenderut; Lo., Loolmalsin; M., Mosonik; O., Olorgesailie; OL., Ol Doinyo Lengai; Ols: Olsirwa; Om., Olmati; OS., Ol Doinyo Sambu; Sh., Shompole.

Dans notre cas, ils vont nous permettre de déterminer d'une part les déplacements de failles, leur espacement et leur longueur et d'autre part, l'organisation spatiale du drainage contrôlée par la tectonique. La plupart des travaux sur l'imagerie ont été effectués avec le logiciel ArcMap version 10.3.1.

2.2 Traitement préliminaire des images

Les 20 MNT, de dimensions 1°x1°, couvrant la zone d'étude ont été réunis en une mosaïque à l'aide de l'extension Data Management Tools du logiciel ArcMap 10.3.1 (Fig.2.2)

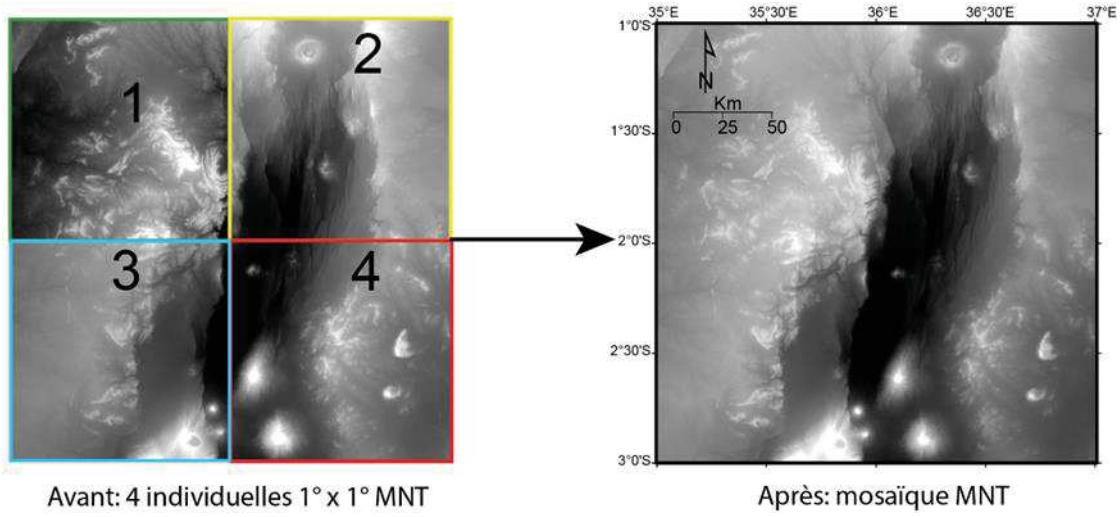

Fig. 2. 2. Création d'une mosaïque de MNT. A gauche: la compilation d'images individuelles et à droite : la mosaïque créée.

Les images MNT brutes peuvent comporter des erreurs caractérisées par l'absence de données dans le pixel pouvant être liées aux capteurs, au traitement ou à des effets de relief. Ces erreurs pouvant induire une mauvaise contrainte des structures étudiées, elles doivent donc être corrigées avant d'effectuer les analyses morpho-structurales et l'étude des réseaux de drainage. Pour ce faire, nous avons utilisé les outils d'analyse spatiale de ArcMap dans le cas d'erreurs de type 'Nodata' et notamment la méthode d'interpolation du plus proche voisin (Neighborhood focal statistic). Cette méthode va permettre de générer des données dans les cellules sans donnée, en prenant en compte les valeurs des

cellules environnantes (Burrough et McDonnel, 1998). Le produit final est un nouveau jeu de données complet pour la zone d'étude (fig. 2. 3)

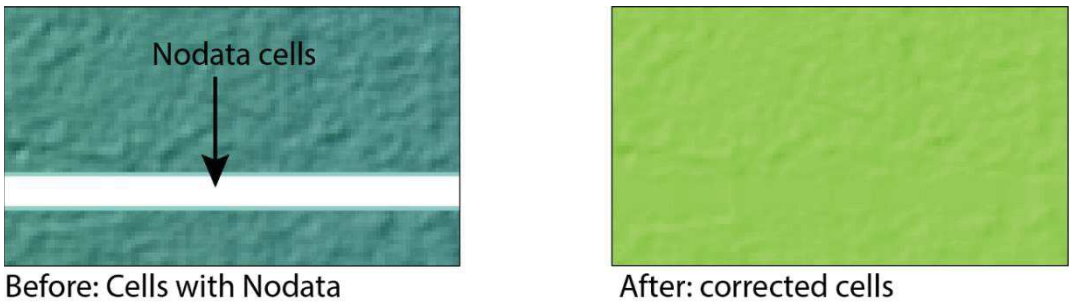

Fig. 2.3 : Correction d'erreurs du MNT. A gauche un MNT présentant des cellules avec des erreurs (No data) et à droite le même MNT après corrections.

2.3 Numérisation des populations des failles

Une fois les corrections effectuées, nous utilisons la mosaïque des MNT corrigés comme base pour la suite des traitements.

La visualisation des structures est généralement faite en ombrant le MNT afin d'éclairer le relief dans différentes directions. Cette image ombrée permet de visualiser des structures dans la gamme de la résolution spatiale des images (limitée ici à 30 m). Les structures de dimensions plus faibles sont donc de fait exclues, ce qui constitue une limite dans ce type d'étude. Après plusieurs tests d'angles d'éclairage pour mieux contraindre les structures, il s'avère que l'azimut et inclinaison optimaux sont 315° et 45° respectivement. Sur le MNT ombré les failles ont été identifiées comme étant les structures morphologiques linéaires ou segmentées majeures. Les critères similaires à ceux de Kinabo et al. 2008 ont été utilisés pour l'identification des structures : i) des changements abrupts dans les couleurs et les tonalités utilisées pour visualiser les MNT, ii) des escarpements topographiques abrupts, iii) un schéma de drainage linéaire, et iv) des unités décalées verticalement. Après avoir identifié toutes les structures linéaires, l'étape suivante a été de confirmer ou infirmer si ces structures linéaires étaient bien des failles. L'approche choisie pour cette vérification a été de réaliser des profils topographiques perpendiculaires à la direction de la faille supposée pour quantifier un éventuel déplacement. Pour décider si deux ou plusieurs segments constituent des éléments d'une même faille, les critères suivants ont été utilisés i) la présence d'une zone

de failles en relais peu séparés (Walsh et al., 2003, Vétel et al., 2005), ii) la direction équivalente d'un rejet vertical entre segments (Walsh et al., 2003, Vétel et al., 2005), et iii) la similitude de pendage de segments adjacents (e.g. Peacock & Sanderson, 1991; Cartwright et al., 1995; Cardon, 1999; Gloaguen, 2000; Walsh et al., 2003). Les failles vérifiant ces critères ont été numérisées manuellement à l'écran grâce à l'outil de dessin 'editor toolbar' dans l'ArcGis (fig. 2.4). La numérisation permet de produire des documents géoréférencés permettant ainsi de calculer directement les paramètres quantitatifs de la géométrie des failles. Un total de 206 failles a ainsi été numérisé dont 56 failles dans les zone d'Oldoinyo Ogol, Ngorongoro, Eyasi et Manyara, et 140 failles avec 307 segments dans l'ensemble du rift Magadi – Natron (fig. 2.1).

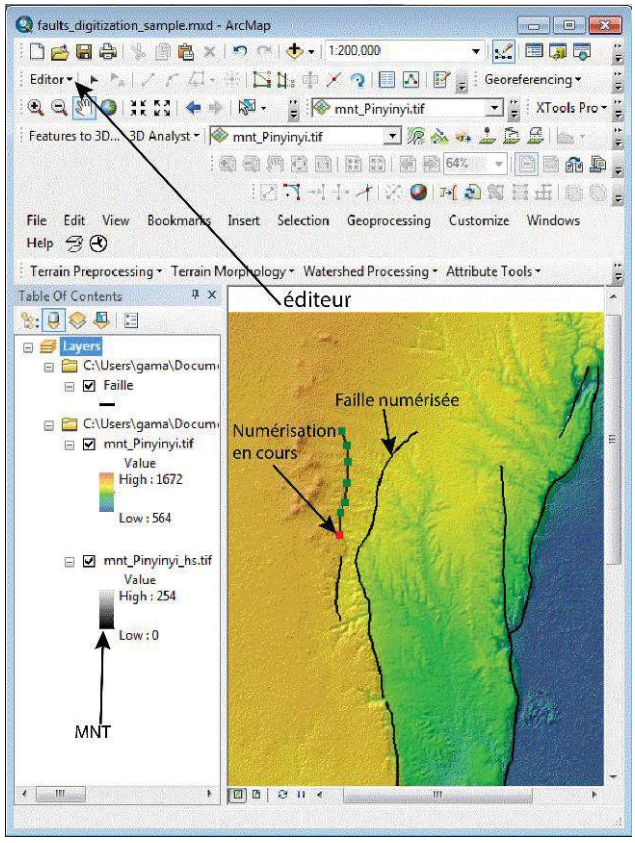

Fig. 2.4. Capture d'écran montrant la numérisation d'une faille à aide de l'outil « editor toolbar » du logiciel ArcGis.

- Longueurs de failles, nombre de segments de failles

Les longueurs des failles ont été déterminées grâce à l'extension X-Tool Pro d'ArcGis. Le détail de la méthodologie est décrit dans l'article présenté de chapitre 3. On

constate que la faille la plus longue dans le secteur Magadi-Natron fait 49 km (A117) et la plus courte 2.4 km (A110). La plupart des failles sont segmentés; la plus segmentée étant A71 avec 9 segments (fig. 2.5).

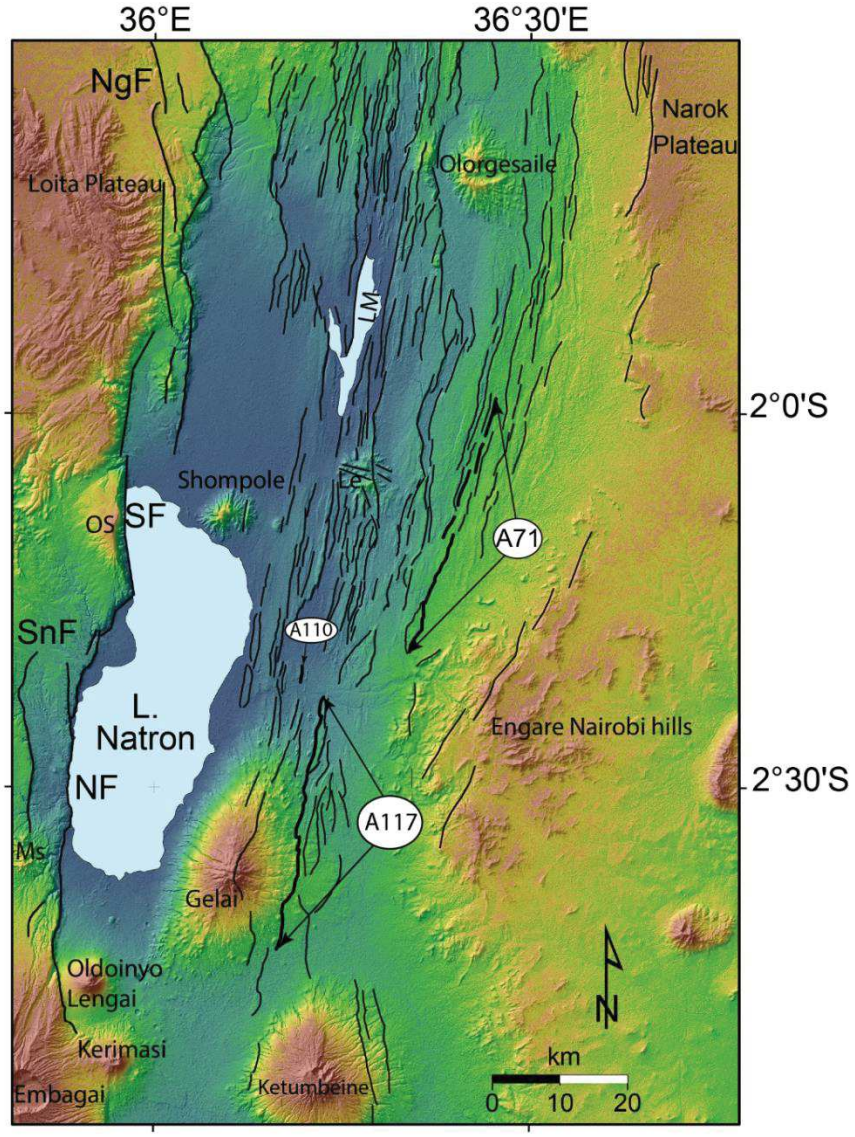

Fig. 2.5: Réseau de failles de la vallée axiale sud Kenya – nord Tanzanie extraite depuis le MNT SRTM-30m. Les failles les plus longues (A117), courtes (A110) et segmentées (A71) sont représentées en gras. L'ensemble des systèmes de réseaux de failles seront utilisés pour les études géométriques et statistiques dans les chapitres suivants.

- Calcul de déplacements et profils de failles

Les déplacements le long des failles ont été calculés à partir des valeurs du rejet vertical mesuré le long du profil orthogonal à la direction de la faille (l'approche est décrite en détail dans l'article présenté (chapitre 3). Ces déplacements permettent de

déterminer les profils de faille importants pour caractériser leur propagation. Ces profils sont représentés en reportant les déplacements normalisés D/Dmax en fonction des longueurs normalisées L/Lmax, (fig. 2.6). La normalisation permet d'éviter le biais lié aux différences de longueur de failles individuelles (Cowie & Scholz, 1992; Nicol et al., 1996 et références). La longueur de faille pour un déplacement donné est la distance à partir d'un point de référence sur la faille. Dans cette étude nous avons fait le choix de mesurer cette distance à partir de la terminaison nord de chaque faille ; la distance maximale étant alors la longueur de la faille.

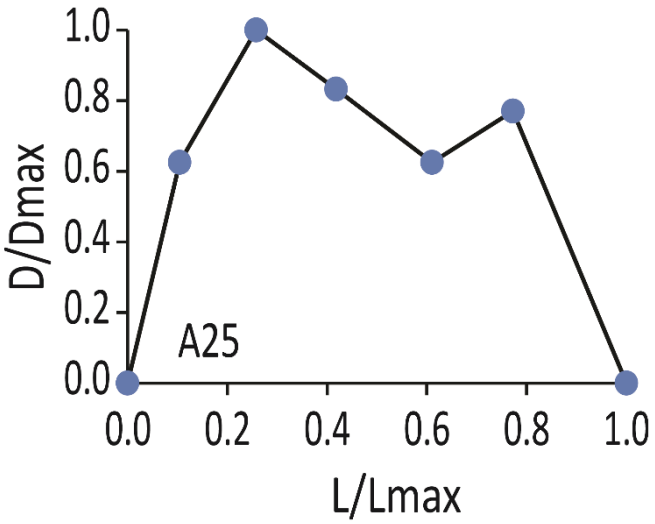

Fig.2.6 : Exemple d'un profil de faille montrant les déplacements normalisés D/Dmax en fonction des longueurs normalisées L/Lmax.

2.4 Réseaux de drainage

La seconde partie de cette étude est l'analyse des réseaux de drainage. Cette analyse a pour but de caractériser le soulèvement du 'rifting' dans le flanc ouest de la Divergence Nord Tanzanienne ainsi que la mise en œuvre de l'organisation des réseaux hydrographiques par rapport aux structures tectoniques et les effets liées aux activités volcaniques. Dans cette partie je présente les manipulations préliminaires des traitements des données MNT et les méthodologies détaillées sont présentée dans l'article du chapitre 4. Cette étude a été réalisée à partir des modèles numériques de terrain présentés dans la partie précédente.

Les images MNT sont régulièrement utilisées pour les études hydrographiques (e.g. Freeman, 1991 ; Vieux, 1993 ; Arun et al, 2005). En effet les systèmes hydrographiques peuvent être obtenus à partir des données altimétriques comprises dans le MNT et ainsi d'extraire diverses structures des réseaux de drainage permettant de caractériser par exemple les écoulements et transports de dépôts sédimentaires (Jana et al, 2007; Mandlaburger, 2009 ; Yang et al, 2010).

J'ai utilisé le logiciel ArcMap pour extraire de l'information hydrographique, contenue dans les images MNT, les réseaux de drainage. Dans cette étude j'ai utilisé l'extraction automatique des réseaux de drainage car elle permet de présenter un réseau en continu de largeur constante (Hentati et al., 2008) en suivant successivement les étapes suivantes : a) élimination des dépressions, b) calcul des directions d'écoulement, c) calcul des zones d'accumulation d'eau, d) extraction des réseaux hydrographiques, et e) détermination des bassins versants.

a) Élimination des dépressions

Les traitements de MNT (e.g. interpolation) peuvent induire des artefacts de l'altimétrie (O'Callaghan and Mark, 1984 ; Band, 1986, Hentati et al., 2008), ces artefacts pouvant résulter en points bas dans les MNT. L'existence de ces points bas perturbe l'écoulement de l'eau et peut conduire à des résultats erronés des réseaux de drainage (Schauble, 2003). Les dépressions piégeant l'eau, la continuité des réseaux de drainage est empêchée et on peut alors obtenir des réseaux ne représentant pas la réalité. Il faut donc corriger ces anomalies par la méthode du comblement des dépressions (Jenson et Domingue, 1998), dans toutes les dépressions existantes dans le MNT. Avec cette méthode de comblement, l'altitude de l'exutoire de la dépression est affectée à toutes les cellules de la dépression (Hentati et al., 2008).

b) Calcul de la direction d'écoulement

Sur ArcMap, la direction d'écoulement est la direction de la pente la plus forte. D'après la méthode des huit voisins (eight-neighbor method, Martz and Garbrecht, 1998 et les références à l'intérieur), chaque cellule reçoit une des 8 valeurs de ses plus proches voisines et celle avec la plus grande pente devient la direction d'écoulement.

c) Calcul de zones d'accumulation d'eau

À partir de la direction d'écoulement calculée précédemment, le calcul des surfaces drainées est réalisé. D'après mes directions d'écoulement, chaque pixel est affecté par un certain nombre d'autres pixels. Ce nombre de pixels est traduit comme l'accumulation d'eau. Plus ce nombre de pixels est important et plus la zone drainée est importante.

d) Extraction des réseaux hydrographiques

L'extraction des réseaux hydrographiques est faite automatiquement à partir des deux informations précédentes (direction d'écoulement et accumulation d'eau). Les réseaux hydrographiques sont présentés comme des pixels avec une quantité de surfaces suffisante (les valeurs cumulées). Pour présenter ce réseau dans un format raster, un seuil de 2500 pixels cumulés a était choisi pour constituer un réseau de drainage pour cette étude. Dans cette étape j'ai déterminé plusieurs types de réseaux de drainage dans la DNT, les plus courants sont i) les réseaux dendritiques, ii) les réseaux parallèles et iii) les réseaux treillis (fig. 2.7)

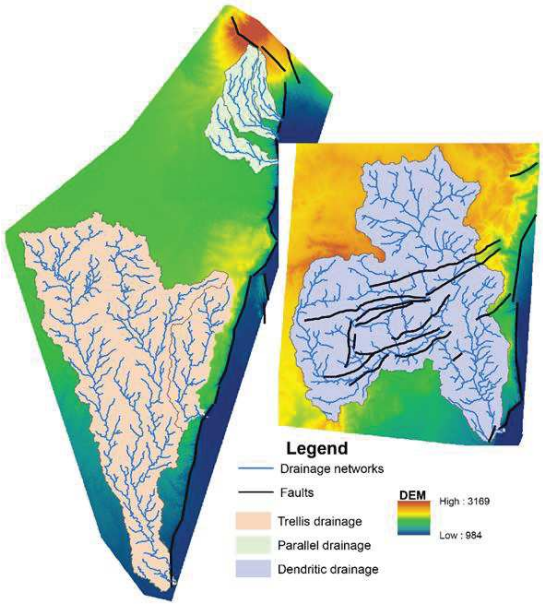

Fig. 2.7. Différent types de réseaux de drainage identifiés au niveau de la DNT. Pour plus de détails voir chapitre 4.

e) Détermination des bassins versants

Les bassins versants sont aussi calculés en utilisant les informations de direction d'écoulement. Sur ArcMap il faut choisir le point exutoire dans lequel on souhaite connaître sa zone amont. Une fois ce point exutoire choisi, les limites du bassin versant

qui appartiennent à ce point seront déterminées. Ces limites couvrent l'ensemble du réseau de drainage qui s'écoule vers cet exutoire (fig. 2.8A). Pour cette étude, j'ai calculé 25 bassins versants (fig. 2.8B) de différentes largeurs sur lesquelles les études des réseaux de drainage et géomorphologiques sont basées.

Des réseaux de drainage obtenus dans cette étape ont ensuite été utilisés dans le but d'établir une organisation de ces réseaux par rapport aux effets de soulèvement vertical et l'extension horizontale dans la DNT (voir détails dans le chapitre 4).

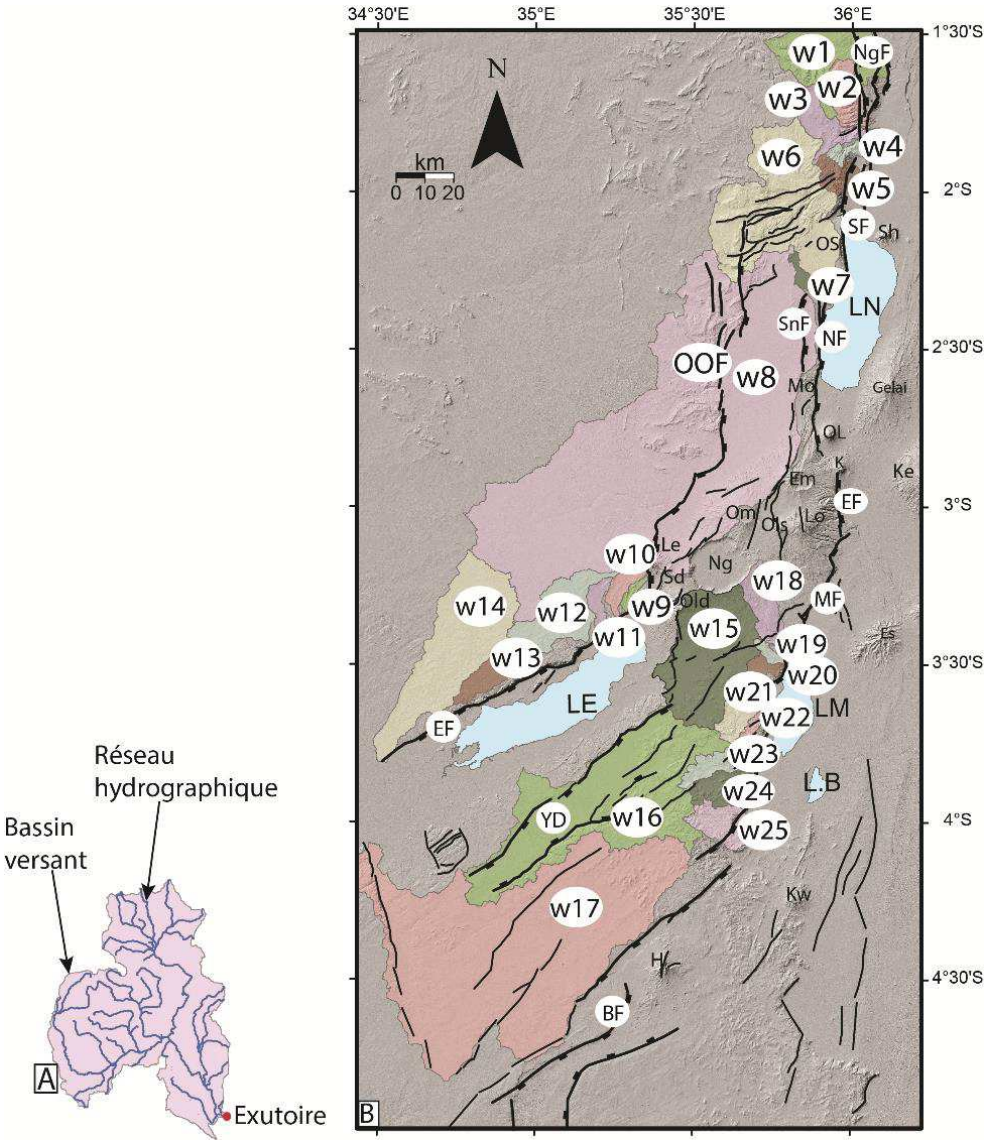

Fig. 2.8. A. Exemple de bassin versant et de réseaux de drainages associés délimités à partir du MNT. B. Distribution spatiale des 25 bassins versants (W1-W25) identifiés sur le flanc ouest de la DNT.

Chapitre 3

Organisation morphostructurale du Rift Sud Kenya et analyse quantitative de la déformation.

Ce chapitre présente un article soumis à la revue 'Tectonics' dans l'article nous étudions la propagation anormale du rift Est Africain entre le sud du Kenya et le nord de la Tanzanie (rift Magadi-Natron), qui en résulte en la formation d'une structure unique, la Divergence Nord Tanzanienne (DNT). Cette étude est la première intègrant en même temps le rift sud kenyan, le bloc Oldoinyo Ogol, la zone des failles de Sonjo (Sonjo Transfer Faults System-STFZ), le Crater Highland et la structure transverse Eyasi-Engare Nairobi Salient (ENS) pour expliquer la formation de la DNT.

Les données utilisées dans cette étude comprennent : les modèles numériques des terrains (MNT) type SRTM avec une résolution de 30 m, des observations géologiques lors des mission de terrains et enfin des données de magnétotelluriques (MT). L'interprétation des résultats est intégrée aux données chronologiques existantes. Nous extrayons manuellement des MNT les failles desquelles ses attributs physiques (longueurs, déplacements maximum et extension) sont mesurés ou calculés puis utilisés pour l'analyse de la déformation dans le rift sud Kenya-nord Tanzanie. Les donnée MT (Plasman et al., 2017) acquis le long d'un profil E-W de 150 km de long traversant la zone du Crater Highland et le volcan Ketumbeine sont utilisés pour l'interprétation de structures en profondeur.

Interprétation conjointe du SRTM-30 m, des observations de terrain et des données MT nous a conduit à décrire un modèle cinématique de propagation du rift sud Kenya en deux phases pour les 7 derniers Ma.

Chapitre 3

Submitted to "Tectonics"

Anomalously-propagating rift pattern and structural inheritance. Insights from the South Kenya rift and the North Tanzanian Divergence, East Africa.

Remigius Gama[1,2], Bernard Le Gall[1*], Nicolas Loget[3], Pascal Tarits[1], Ahmed Mohamed Daoud [4], Mathieu Plasman[5], Gilles Chazot[1], Alexander Koptev[6], Nelson Boniface[2], Sophie Hautot[7]

[1]UMR 6538 Géosciences Océan, IUEM, Brest university, France

[2] Department of Geology, University of Dar es Salaam, Tanzania

[3]UMR 7193, ISTeP, Sorbonne university, Paris, France

[4]Centre d'Etudes et de Recherche de Djibouti, Djibouti

[5] UMR 5243 Géosciences Montpellier, Montpellier university, France

[6]Department of Geosciences, University of Tübingen, Wilhelmstrasse 56 D-72074 Tübingen, Germany

[7]IMAGIR sarl, Brest, France

* corresponding author, blegall@univ-brest.fr

Abstract

One of the most atypical structure of the entire East African Rift occurs at the southern extremity of the Eastern branch, in South Kenya (SKR), where the axial rift trough splits southwards into three diverging arms in the 200 km-wide North Tanzanian Divergence (NTD). Causal mechanisms of the NTD are discussed in a new kinematic rift model that also incompasses, for the first time, structural disturbances exposed in the SKR, such as the generally neglected Ol Doinyo offset block, west of the Magadi-Natron axial trough. Interpretation of SRTM-30 satellite imagery, further completed by local field investigations and magnetotelluric data, leads us to depict the highly segmented arrangement of the ~7 Ma-lasted SKR system, and then to apply a two-stage kinematic model comprising an initially offset and segmented rift

configuration (7-1.3 Ma) that later evolved into a more linear half-graben pattern at around 1.3 Ma. New insights onto individual fault growth and the spatio-temporal distribution of strain in the SKR are supplied by the quantitative analysis of both border and intra-rift fault populations. The amount of total extension, estimated at ~ 7 km (10%), was mostly achieved by slip along the rift-bounding fault system (~ 80%) during nearly the 7 Ma-lasted rift basin development, but with a marked decrease through time. The intra-rift faulting that occurred during the last 1 Myrs over the Magadi-Natron volcanic axial floor, in response to inward focusing of strain, was not the prominent mode of strain accommodation during the late rift stage, in contradiction with kinematic models applied to more mature rift segments in Kenya and Ethiopia. Most of structural and magmatic disturbances in the SKR-NTD rift system, such as intra-rift basement salient, rift offset (Ol Doinyo Ogol basin), off-axis magmatic segment (Crater Highlands) and transverse fault-basin pattern (Eyasi rift arm), are attributed to the multistage rejuvenation of a newly-identified transverse discontinuity (ENS-Eyasi), Archaean in age, hence emphasizing the key role of cratonic fabrics on the structural arrangement of the SKR-NTD system during Neogene-Present rifting.

3.1 Introduction

Dynamics of continental rifting result from the interference of multiple parameters related to plate-scale kinematics (far-field stress field) and more specific physical attributes dealing with the thermal and mechanical structures of the rifted domains. The respective role of these controlling factors during rifting process has been extensively addressed through both analog/numerical modelling experiments (McClay et al., 2002; Michon & Sokoutis, 2005; Corti, 2009) and natural examples, with emphasis on the reference structure for continental rifting, i.e. the East African Rift System (EAR) (Fig. 3.1A). With regards to the structural inheritance issue, it is generally agreed that the large-scale structure of the EAR into the Western and Eastern rift branches results from the preferential locus of extension within mechanically

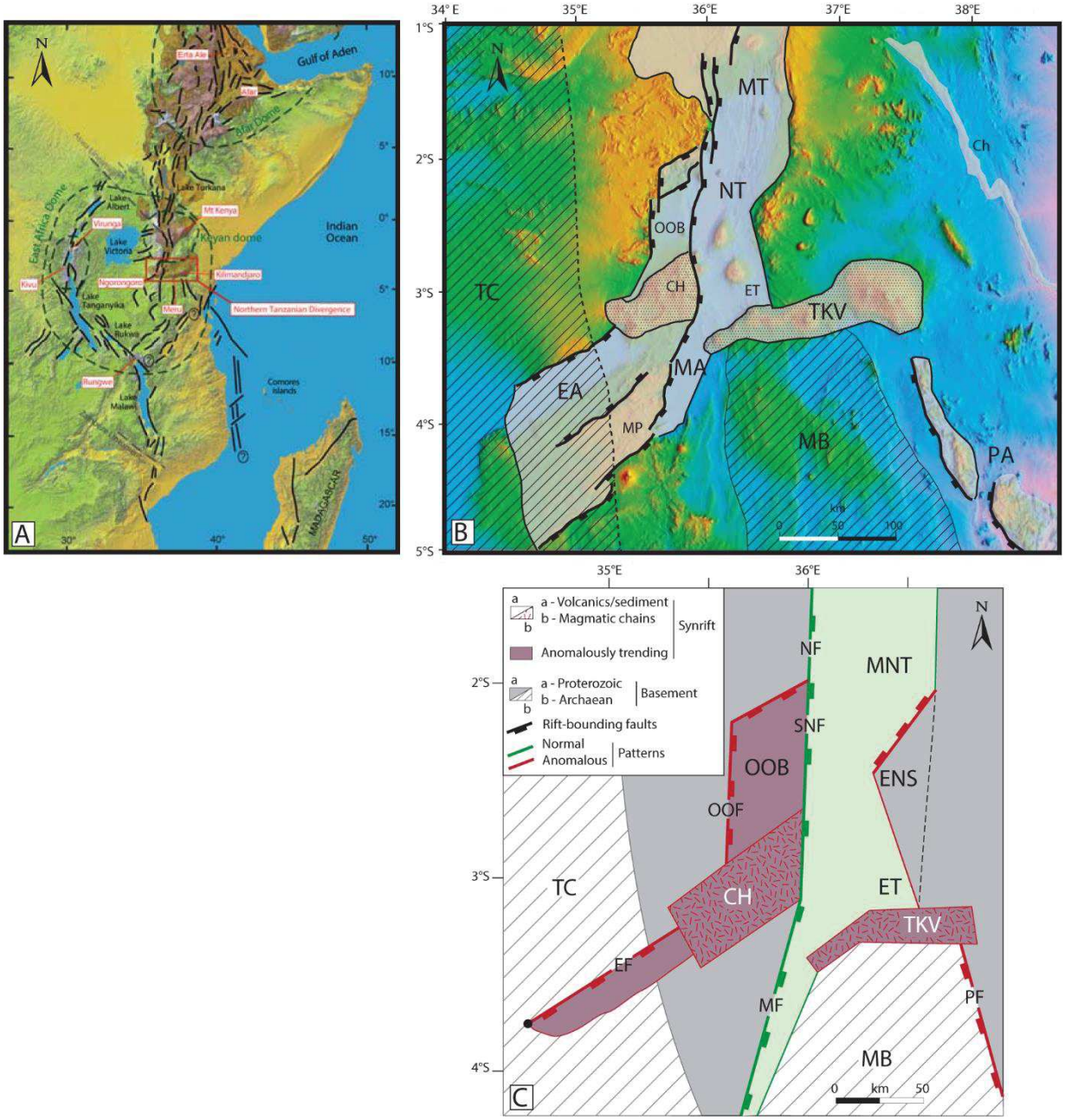

Fig. 3.1. Main structural and magmatic features in the South Kenya (SKR) and North Tanzania rift (NTD) system. A. Topo30 digital elevation model showing the distribution of topographic domes with relation to rift structures in East Africa. B. Sketch map of major rift structures in the SKR-NTD system on a Topo30 DEM. CH., Crater Highlands; EA., Eyasi rift arm; ET., Engaruka trough; K., Kilimanjaro volcano; MA., Manyara rift arm; MB., Masai block; MP., Mbulu plateau; MT. Magadi trough; NT., Natron trough; OOB., Ol Doinyo Ogol block; PA., Pangani rift arm; T., Tarosero volcano. The dashed line is the trace of the boundary between the Tanzanian craton and the Proterozoic belts. C. Sketch map showing regional-scale structural disturbances (in red) with respect to the archetypal, linear and submeridian arrangement of the SKR (in green), orthogonal the EW direction of extension. The synrift magmatic chains are the Crater Highlands (CH) and Tarosero-Kilimanjaro (TKV) structures. Same abbreviations as in Fig. 1B. ENS., Engare-Nairobi salient; Faults: EF., MF., NF., OOF., PF., SNF., Eyasi, Manyara, Nguruman, Ol Doinyo Ogol, Pangani, Sambu-Natron fault.

weaker Proterozoic Mobile belts surrounding the strong and rigid Tanzanian craton (McConnell, 1972). The impact of the latter on the magmatic/amagmatic nature of the Eastern and Western rifts, respectively, is further confirmed by results of 3D-thermo-mechanical modelling showing the deflection of mantle plume-related melts at the base of the thick cratonic root during their upward migration through the strained continental lithosphere (Koptev et al., 2016, 2018).

The internal architecture of the two rift branches is in turn strongly influenced by the inherited Proterozoic framework, as evidenced about: i) the oblique rift configuration of the Main Ethiopian rift (Eastern branch) (Bonini et al., 1997; Corti, 2008; Agostini et al., 2011), and ii) the zig-zag and segmented trajectory of the Kenya rift further south via a network of transverse faults rooting at depth along rejuvenated NW/SE Proterozoic ductile shear zones (Smith & Mosley, 1993; Chorowicz, 1989; Le Turdu et al., 1999). The impact of basement fabrics on rift geometry can be also inferred about the more intricate structural pattern displayed by the South Kenya rift (SKR in the text), as approaching the Tanzanian craton (Figs.3.1, 3.2). There, the SKR is dextrally offset in the so called Ol Doinyo Ogol block (OOB) on the western flank of the Natron axial trough, before spliting southwards into three diverging rift arms (Eyasi, Manyara and Pangani) over the >200 km-wide North Tanzanian Divergence zone (NTD) (Dawson, 1992).

A few explanations have been yet proposed, but only for individual rift structures such as: i) the Eyasi fault that might follow inherited Archaean weakness zones trending at NE/SW in the Mbulu plateau (Ebinger et al., 1997), or ii) the EW-oriented Tarosero-Kilimanjaro transverse volcanic chain, assumed by Le Gall et al. (2008) to result from the arrest of southerly-migrating mantle plume-derived melts against the northern edge of the Masai cratonic microblock (Figs. 3.1B, C). Alternatively, the impact of inherited structures on the SKR rift arrangement was minimized by some authors who instead favoured the role of magma-induced stress rotations on the oblique trend of transverse rift structures (Weinstein et al., 2017).

The lack of any comprehensive kinematic model about the causal mechanisms of the entire SKR-NTD disturbed rift pattern partly motivated the present work. The SKR-NTD rift pattern under study extends at 1°30’-3°30’S and encompasses generally neglected structures, such as the OOB offset block and additional features

described below (Figs. 3.1B, C). Our study is chiefly based on interpreted 30 m-resolution Shuttle Radar Topography Mission satellite (SRTM) imagery that provides new insights onto: i) the yet poorly-investigated Magadi-Natron-OOB rift-bounding fault scarp network, west of the SKR, ii) geometrical attributes of the intra-rift fault population in the Magadi-Natron volcanic floor, and iii) the key-role of inherited Archaean discontinuities on rift propagation. Our work also integrates local field observations and newly-acquired magnetotelluric records that both help constraining the surface/subsurface structure of the OOB offset block.

3.2 Rift setting

At ~2°S, the linear and archetypal half-graben architecture of the SKR (King, 1978; Chapman et al., 1978), gives way southwards to a more intricate rift configuration due to the presence of the 30 x 70 km losange-shaped OOB offset block, west of the Natron axial depression (Fig.3.2). The corresponding rift-bounding fault-scarp network comprises from N to S: the Nguruman, Sanjan, and Ol Doinyo Ogol (OOF) faults in an outer position to the west, and the innermost Sambu and Natron faults in the southern prolongation of the Nguruman fault. At the same latitude (2°S), the continuity of the eastern margin is disrupted by a 100 km-long and 30 km-wide triangle-shaped basement salient, the so-called Engare-Nairobi structure (ENS) that causes the narrowing of the Natron trough (<40 km-wide), accordingly. At ~2°45'S, the trend of the Natron rift axis swings southwards into the NW/SE Engaruka depression, before abutting against the Essimingor-Tarosero volcanic lineament (Figs. 1B, C). The latter is part of a series of transverse volcanic chains that also include the NE/SW Crater Highlands to the west and the EW-trending Tarosero-Kilimanjaro volcanic axis between the SKR magmatic rift and the mostly amagmatic NTD to the south (Figs. 3.1B, C) (Dawson, 1992; Le Gall et al., 2008; Isola et al., 2014). Rifting in the 200 km-wide NTD is achieved along three discrete diverging rift arms that are from W to E (Figs. 3.1B, C): i) the 150 km-long Eyasi arm that forms a NE/SW-oriented half-graben basin, facing to the SE, at high angle to the Archaean-Proterozoic boundary, and filled up with <3.5 km-thick sedimentary sequences (Ebinger et al., 1997). Its SW fault tip point occurs in Archaean metamorphic terranes,

70 km away from the craton/Proterozoic exposed boundary. ii) The submeridian Manyara arm is a <1.4 km-deep, easterly-facing half-graben, in the southern prolongation of the Natron axis (Ebinger et al., 1997). The dense array of NE/SW horst-grabens in the intervening Mbulu basement plateau likely resulted from flexural warping in the Eyasi hangingwall block (Foster et al., 1997). The Manyara rift arm continues southwards via a transverse network of seismically active faults (Macheyeki et al., 2008) into reactivated Karoo-age normal faults bounding the Kilombero valley (Le Gall et al., 2004) that then connects via the Rungwe volcanic province into the Malawi rift further south (Fig. 3.1A) (Grijalva et al., 2018). iii) The Pangani basement ridge, south of the Kilimanjaro volcano, is composed of three right-stepping en echelon uplifted segments possibly following an inherited NW/SE (ASWA-type) Proterozoic trend (Le Gall et al., 2008) that extends offshore into the Indian ocean along the Davie Ridge (Fig. 3.1A) (O'Donnell et al., 2013; Mulibo & Nyblade, 2016).

The SKR-NTD rift pattern developed in a highly heterogeneous lithosphere comprising two major cratonic blocks (Tanzanian and Masai) which were overlain to the E by westerly-displaced Proterozoic thrust-nappes during the collision-related East African orogeny at ~620 Ma (Figs. 3.1B, C) (Mosley, 1993; Moller et al., 2000). The basement frontal thrust pattern roots eastwards along a deep thrust-ramp following the deeply-buried edge of the craton, 100-200 km east of its exposed boundary in the Mbulu plateau (Shakleton, 1993; Fritz et al., 2009; Baudouin et al., 2016). According to the geophysical interpretations of Fletcher et al. (2018), the Tanzanian craton is in turn composed of smaller continental blocks amalgamated along NE/SW-oriented suture zones that parallel mafic dyke swarms dated at 1,775 Ma in the Singida area (Fig. 3.1B) (Mruma et al., 2014). Most of basement uplifted plateaus bounding the SKT-NTD rift are composed of metamorphic rocks that typically display shallowly6dipping foliations, further involved into later map-scale folds (Figs. 3.1B, C) (Baker, 1958; Thomas et al., 2016). Geophysical records indicate that the 40 km-thick crust beneath the basement uplifted flanks thins to 35 km beneath the rift axis, with a shallowest Moho depth in the Magadi trough to the north (Birt et al., 1997; Thybo et al., 2000; Sippel et al; 2017; Plasman et al., 2017). Recent receiver function modelling reveals that NE/SW-oriented oblique zones of lithospheric thinning occur at greater depths beneath the rift axis from the Crater Highlands to the

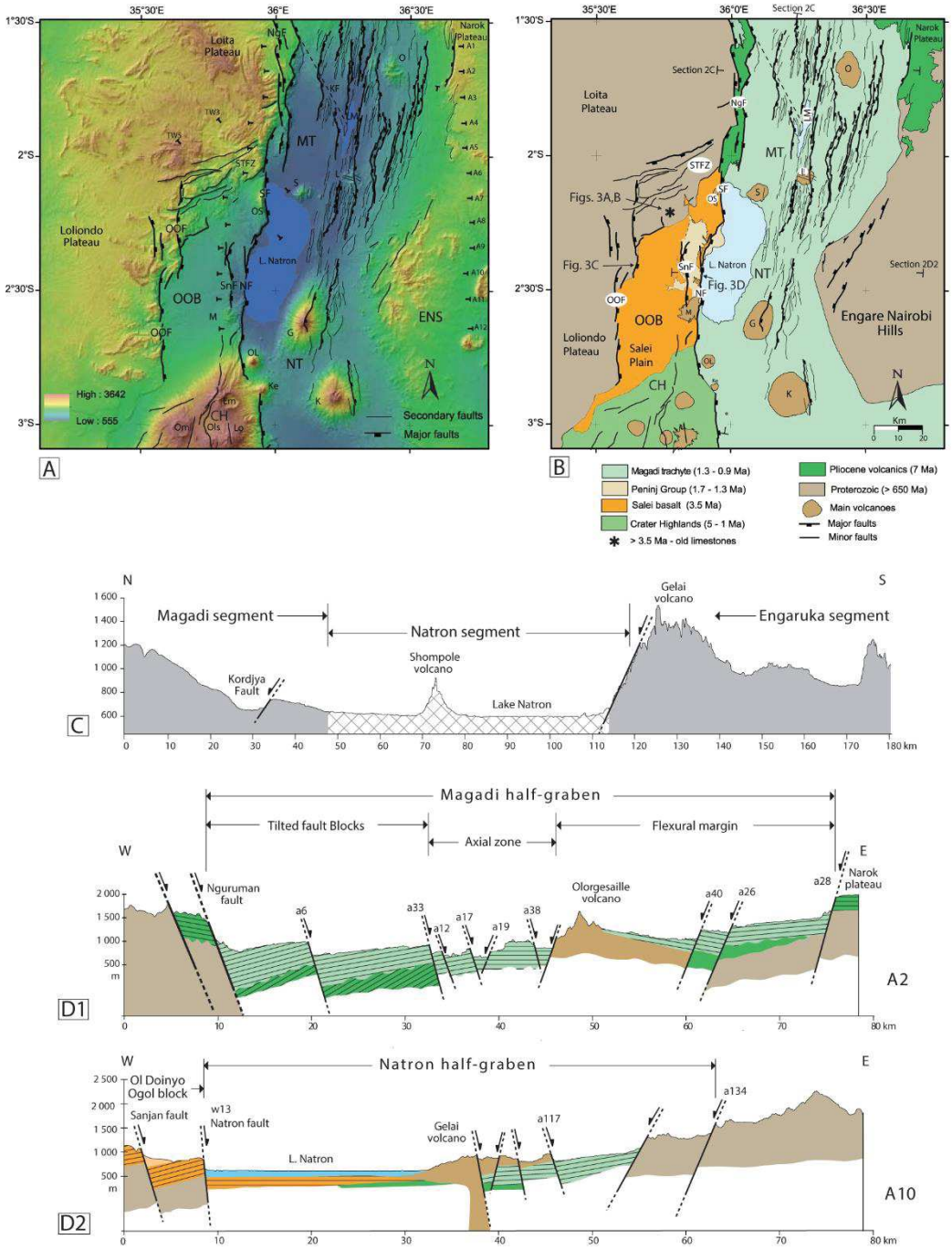

Fig.3. 2. Geology of the South Kenya rift. A. SRTM-30 DEM showing the SKR offset rift pattern with the Ol Doinyo Ogol block on the western flank of the Natron axial trough. LM., Lake Magadi; Faults : KF., NF., NgF., OOF., SF., SnF., Kordjya, Natron, Nguruman, Ol Doinyo Ogol, Sambu, Sanjan fault; Volcanoes: E., Embagai; G., Gelai; K., Ketumbeine; Ke., Kerimasi; L., Lenderut; Lo., Loolmalsin; M., Mosonik; O., Olorgesailie; OL., Ol Doinyo Lengai; Om., Olmati; OS., Ol Doinyo Sambu; S., Shombole. The trace of 12 cross-sections ($A_{1\text{-}12}$) and 2 oblique sections ($Tw_{3\text{-}5}$) discussed in the text is drawn. B. Corresponding simplified geological map of the SKR (Magadi-Natron trough and Ol Doinyo Ogol offset block). Same abbreviations as in Fig. 3.2A. The trace of sections 2C, D_1, D_2 is shown. C. Rift-parallel topographic profile showing the along-strike morphological segmentation of the axial floor. Vertical exaggeration = 14. $D_{1\text{-}2}$. Geological cross-sections in the Magadi (D_1) and Natron (D_2) segments. Vertical exaggeration = 5. Same colours as in Fig. 2B. Location in Fig. 3.2B.

Magadi trough (Plasman et al. (2017). A similarly-oriented, but shallower, network of seismically-active faults is evidenced in the Gelai upper crust, i.e. the Naibor Saito earthquake swarm of Weinstein et al. (2017), as well as in the Manyara area further south (Albaric et al., 2010). These transverse rift trends are oblique to the EW extension determined from inversion of stress tensors (Ibs-von Seht et al., 2001; Delvaux & Barth, 2010; Albaric et al., 2014), geodetic records (Saria et al., 2014), and earthquake focal mechanism analyses (Lambert et al., 2014). Their origin as either inherited features (Albaric et al., 2010), or due to local stress rotations (Weinstein et al., 2017) is still debatable. Earthquake focal depths in the range 20-40 km, i.e. partly below the brittle-ductile transition, reflect the relatively strong and mafic rheology of the lower crust (Albaric et al., 2009) and the importance of high fluid pressures related to magmatic chambers (Weinstein et al., 2017).

The general southerly younging of the ~7 Ma-lasted SKR rift framework (Le Gall et al., 2008; Mana et al., 2015) is disturbed southwards by anomalous age patterns in the transverse volcanic chains where magmatism migrated either to the NE (Lemagrut-Embagai and Essimingor-Tarosero lineaments) or to the E (Tarosero-Kilimanjaro chain) from discrete nucleation sites (Nonnotte et al., 2008; Mana et al., 2015).

The tectono-magmatic evolution of the SKR-NTD system can be subdivided into two successive main stages. The early stage (7-1.3 Ma) is dominated by two various styles of magmatism with specific spatial distribution (Fig. 3.2). Extensive flood-type lavas were emplaced over the nascent Magadi-OOB-Natron axial floor, with ages younging markedly southwards. Magmatism started with the ~7 Ma-old Lengitoto trachytes that initially occurred as far south as 2°S and were later punctuated by a series of shield volcanoes comprising the Olorgesalie (2.7-1.7 Ma), Lenderut and Shombole (2.0 Ma) edifices (Baker, 1958; Baker et al., 1971; Fairhead et al., 1972; Crossley, 1979; Birt et al., 1997). The Lengitoto trachytes are currently preserved as narrow faulted strips on top of uplifted basement relief bounding the Magadi trough to the west along the Nguruman fault system (Baker, 1958). The Narok basement bounding plateau to the east is capped by nearly coeval, but unfaulted lavas. Magmatism initiated later in the OOB offset block with the effusion of 3.5 Ma-old flood-type basalts (Fig. 3.3A) (Muirhead et al., 2016), referred here to as the Salei

series in order to avoid any confusion with the <3.5 Ma-old lavas from the Ol Doinyo Sambu shield volcano (Isaac & Curtis, 1974). Earlier development of the OOB basin, prior to the < 3.5 Ma Salei basaltic event, is hypothetized from the local occurrence of hydrothermally-brecciated (undated) lacustrine limestones resting directly over metamorphic basement rocks in the hangingwall of the OOF (Figs. 3.2B, 3.3A, B). In the time-range 1.7-1.3 Ma, the Sanjan faulted sub-basin, in the eastern part of the OOB, was the locus of the Peninj series composed of terrigeneous deposits and interlayered lavas (Isaac & Curtis, 1974; Manega, 1993; Forster et al., 1997).

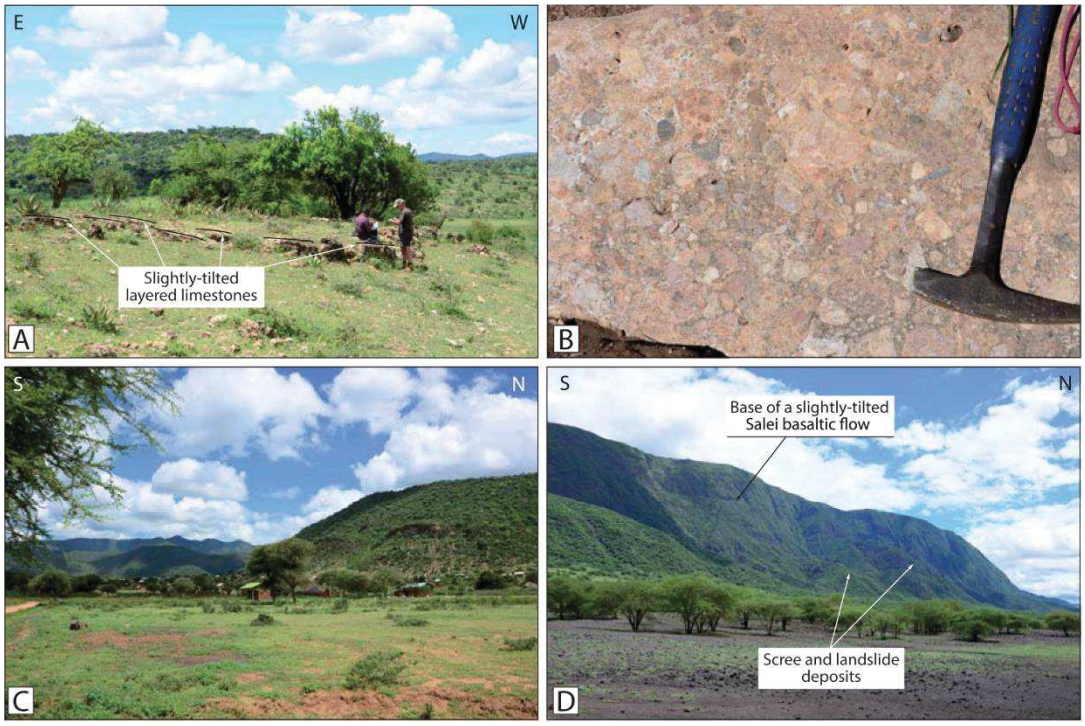

Fig.3.3. Field views of rift structures in the Ol Doinyo Ogol offset block. Location in Fig. 3.2B. A. Stratified lacustrine limestones (slightly tilted to the south) overlying Proterozoic metamorphic rocks in the immediate footwall of the OOF border fault, at the northern extremity of the OOB offset basin. B. Brecciated (hydrothermal?) facies. C. Incised topography of the OOF border fault in the background. Photo taken from the limestone site. D. Scree and landslide deposits at the foot of the Natron border fault. The Salei basaltic flows are slightly tilted to the SW in the fault scarp.

Further south, off-axis magmatic intrusions occurred as early as 5 Ma in the Crater Highlands range, in association with Si-undersaturated lavas (Paslik et al., 1995) younging gradually to the NE. During the later stage (1.3 Ma-Present), a second episode of flood lava expressed by the effusion of the 1.3-0.9 Ma-old Magadi

trachytes (ca 400 m-thick) over the Magadi-Natron axial floor (Isaac & Curtis, 1974; Muirhead et al., 2016), concomitantly to fault activity along the E/Nguruman-Sambu-Natron fault. Trace-elements and isotopic geochemistry reflect contributions from both crustal contamination and deep sources in the mantle at that stage (Mana et al., 2015; Nonnotte et al., 2008).

The general southerly propagation of rifting in the SKT-NTD system during Neogene-Recent times was accompanied by the inward migration of strain/magmatism towards the rift axis (Baker et al., 1988; Muirhead et al., 2016), in a similar way as in the Central-North Kenya and Ethiopian rifts (Baker & Wohlenberg, 1971; Cerling & Powers, 1977; Ebinger & Casey, 2001).

3.3 Methodology

The SKR-NTD rift system under study extends at 1°30'-3°30' and 35°30'-37°E (Figs. 3.1B, C). It does not include the discrete Pangani rift arm on the eastern side of the NTD (readers can refer to Le Gall et al. (2008) for details). Our main objectives are: i) to investigate a number of yet poorly-defined rift structures in the SKR, such as some border faults and the OOB block that are rarely (never) included in previous studies, ii) to get a complete 3D-view of the rift architecture in the SKR-NTD and ii) to provide a more accurate quantitative estimate of bulk strain recorded by the entire fault system during the last 7 Myrs.

Our study is based on SRTM-30 m imagery (SRTM V3.1,1 arcsec., Universal Transverse Mercator projection following Geodetic System WGS84) with lateral and vertical resolutions of 30 m and 8 m, respectively. The qualitative and quantitative analysis of the intra-rift fault population (n = 140) extracted from this dataset helps to define the structural style of extension in the Magadi-Natron trough, both in map-view and cross-sections. The main structural attributes of individual faults (length, maximum displacement,..) are estimated, owing to the above-mentioned resolutions of SRTM dataset. Since most of fault map traces are tortuous and highly segmented, fault lengths have been measured as tip-to-tip linear distances, including the cumulative lengths of overlapping segments (Fig. 4A) (Vétel et al., 2005). The height

of exposed individual fault scarps is considered as a proxi for vertical displacement (throw) along recent (inner) faults (Fig. 3.4B), being aware that: i) the top-most part of uplifted footwall blocks might have been partly removed by erosion (Fig. 3C, in this case, their envelop surface is used as a marker), ii) the foot of fault planes is usually covered by scree deposits, as observed in the field about the OOF and Natron-Sambu faults (Fig. 3.3D), and iii) the early history of faults might not have been recorded by their visible scarps. Therefore, height/throw values obtained here are minimum estimates. Throw estimates along master rift-bounding faults have been calculated from three complementary dataset supplied by: i) geophysically-recorded basement depths, ii) thicknesses of presumably syn-tectonic hangingwall sequences, and iii) fault scarp elevations. Throw values are used in two complementary ways. For individual faults (both inner and border structures), they have been regularly measured on a series of short topographic profiles, orthogonal to the fault trace, with a constant spacing depending on the total length of the fault. The maximum throw value (T_{max}) obtained for each fault has been converted to maximum displacement (D_{max}) and extension (e = heave) by assuming an optimal 60° dip for the fault plane (in agreement with previous works elsewhere in the EAR (e.g. Ebinger et al., 1989; Wheeler & Rosendahl, 1994), and by using the classical trigonometric equations:

$e = T.tg60°$, $D = T.sin60°$ (Fig. 3.4B).

The corresponding fault displacement profiles (x 140), commonly used to constrain mechanisms of fault propagation (Cowie & Scholz, 1992; Nicol et al., 1996, and references therein), are used here to test whether the ENS intra-rift salient may have acted as a mechanical barrier to rift/fault propagation.

Secondly, master fault-and inner fault-related extension have been summed along 12 regularly-spaced (10 km) cross-sections in order to document any lateral variations of extension along a 110 km-long, rift-parallel transect (Figs. 3.2A, 3.5A). The eventual strike-slip component of faults in the SKR is assumed to be minor, given the general submeridian orientation of the entire fault population, nearly orthogonal to the EW direction of extension. Since our quantitative fault analysis is

primarily focused on throw (extension) measurements, only 3D-dataset provided by SRTM-30 imagery and corresponding DEM's have been used in the present work.

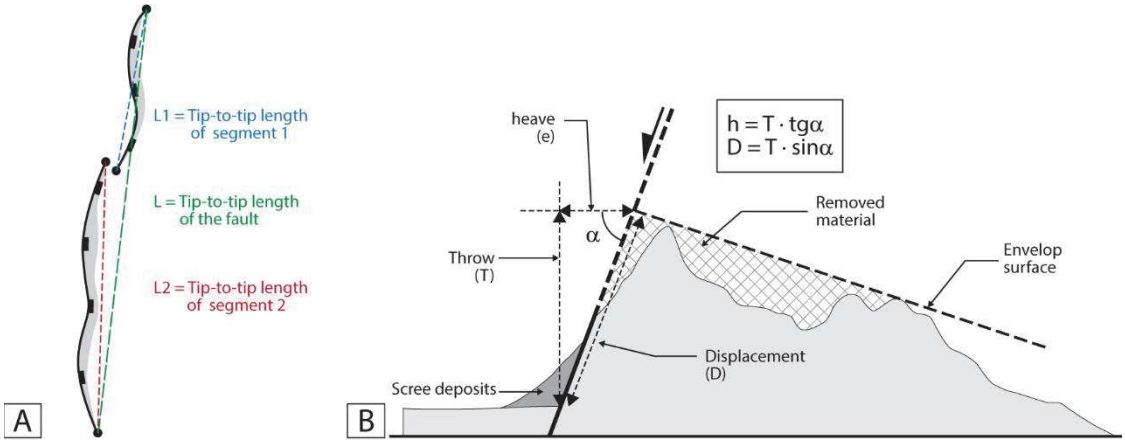

Fig.3.4. Conventional rules used in this work for estimating fault length and fault scarp elevations. A. Length measurement of a segmented fault. The length of the fault is significantly longer than its tip-to-tip length. Note that the tip-to-tip length and azimuth of segments do not equal that for the entire fault. B. Geometrical attributes of an eroded topographic fault profile. No scale.

For that reason, better resolution 2D-imagery data (aerial photos) that could have provided more accurate length values have not been used here, hence leading us to undersampling minor fault populations beyond the SRTM-30 resolution. But, since the latter are assumed not to contribute a significant amount to extension with respect to the km-scale basement depth estimates derived from geophysical modelling (see below), biases in throw and length measurements are minor and do not degrade our values that are thus considered as acceptable data for comparative purposes.

Lastly, new insights onto the subsurface structure of the OOB offset block are supplied by magnetotelluric (MT) data recorded on a 150 km-long, EW-oriented transect, at the latitude of the Ketumbeine volcano (Fig.3.2B) (see Plasman et al., 2017, for details about the MT method).

3.4 Results

The complete morphostructural arrangement of the SKR has been precised by focusing, not only on the prominent and relatively young Magadi-Natron rift valley,

but also on more eroded rift structures occurring on its western flank (OOB and W/Nguruman fault scarp), or identified on its eastern flank (ENS) (Fig. 3.2).These presumably older rift structures, which might have recorded early rift stages, are integrated here, for the first time, in a quantitative strain analysis in order not to underestimate the bulk extension experienced by the entire SKR rift system (Muirhead et al., 2016).

3.4.1 Morphostructural rift pattern in the SKR

3.4.1.1 The western rift-bounding fault network

The highly-segmented master fault network bounding the Magadi-Natron/OOB depressed area comprises the linear Nguruman-Natron fault-scarp, and the more topographically subdued OOF and Sonjo transverse fault zone (STFZ) to the west (Fig. 3.2).

To the north, the >60 km-long Nguruman fault network is composed of a >10 km-long spaced double-fault system, and associated uplifted footwall blocks (Fig. 3.5). The narrow and <1800 m-high inner block is capped by the 7 Ma-old Lengitoto trachytes that exceed 400 m in thickness to the south (Fig. 3.2D1) (Baker, 1958). They are cut to the east by the E/Nguruman fault-scarp that limits the Magadi trough with elevations in the range 1000-1800 m. At its southern tip line, it splits into two closely-spaced and steep faults (Fig. 3.5). The outer and higher footwall block is exclusively composed of highly-folded metamorphic (Proterozoic) rocks in the >2400 m-high Loita plateau. The sharp truncation of map-scale basement folds by the three right-stepping and overlapping fault segments forming the W/Nguruman fault-scarp indicates that Proterozoic basement ductile fabrics did not exert any structural control on the Magadi bounding fault network (Fig. 3.5A). The deep incision of the W/Nguruman basement footwall block, as well as the eroded profile of its fault-scarp, typically evoke early rift structures (Figs. 3.2D1, 3.5B) that likely developed synchronously to the effusion of the 7 Ma-old Lengitoto lavas in the proto-Magadi half-graben (Baker et al., 1978; Crossley, 1979). The less incised topography of these lavas in

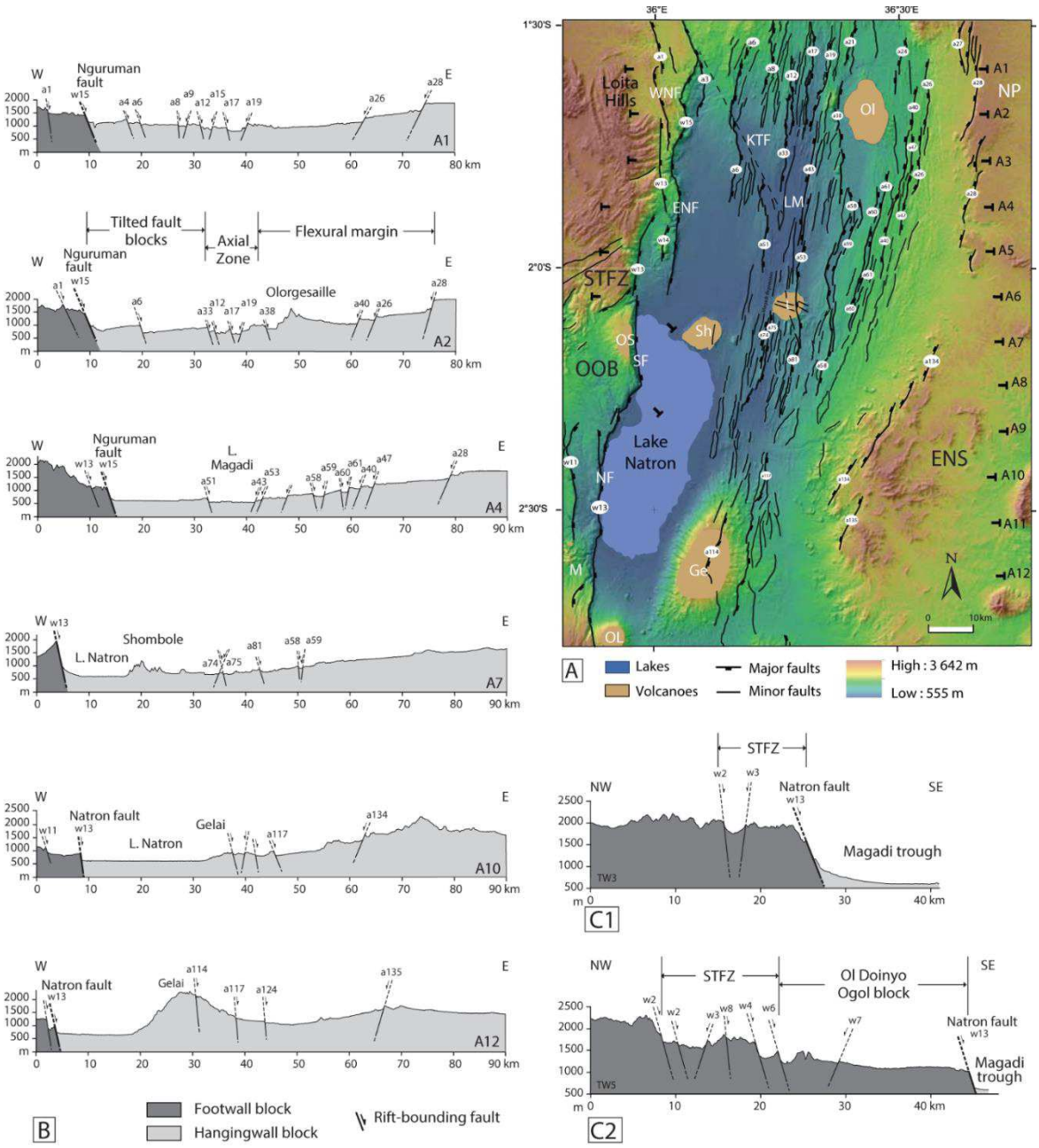

Fig.3.5. Map-distribution and cross-sectional geometry of the normal fault network in the South Kenya rift. A. Map traces of the extensional fault grid (and corresponding numbers) extracted from the SRTM-30 DEM. The position of 12 parallel and regularly-spaced (10 km) cross-sections ($A_{1\text{-}12}$), used for extension estimates, is shown. Same abbreviations as in Fig. 3.2A. B. 6 (over the 12) morphostructural cross-sections showing marked changes in structural style from the Magadi ($A_{1\text{-}2\text{-}4}$) to the Natron ($A_{7\text{-}10\text{-}12}$) segments. Vertical exaggeration = 5. Note the double-fault network forming the W/ and E/Nguruman bounding scarp (A_1-$W_{13\text{-}15}$). C. Two transverse morphostructural sections across the Sonjo transfer fault zone, showing a prominent (apparent) dip-slip extensional component along individual faults. Vertical exaggeration = 5. Location in Fig. 3.2A.

the footwall of the E/Nguruman fault suggests younger uplift in a more inner position, presumably during the emplacement of the1.3-0.9 Ma Magadi trachyte series in the Magadi hangingwall trough (Baker, 1958; Muirhead et al., 2016). In agreement with Baker (1958), we come to the conclusion that the twinned Nguruman master fault scarps (W/ and E/) initiated diachronously during a multistage faulting process, concomitantly to two successive flood lava episodes.

At 1°53'S, the Nguruman border fault system splits into two diverging faults (Figs. 2, 5): i) its overlapping zone with the colinear Sambu fault is a 20 x 10 km relay zone occupied by a 400 m-thick succession of Lengitoto trachytes. Further south, the 40 km-long and >1300 m-high Sambu fault-scarp cuts through the 3.5-1.9 Ma-old Sambu volcano (Isaac & Curtis, 1974; Muirhead et al., 2016) and underlying Proterozoic basement terrains. It connects southwards, via a 20 km-long transfer fault, into the > 60 km-long and 600-700 m-high seismically active Natron fault-scarp, the footwall of which is composed of the 3.5 Ma-old Salei basalts (Muirhead et al., 2016) flooring the OOB offset block (Fig. 3.3D). Its immediate hangingwall is occupied by Lake Natron and recent sediments overlying the Magadi trachytes series at depth.

At 1°53'S', the Nguruman fault system also connects laterally westwards into the N60°-oriented STFZ that forms a 40 x 25 km transfer fault zone extending through Proterozoic metamorphic terrains (Figs. 3.2, 3.5). It comprises a dense network of closely-spaced normal faults (x 5-6), facing dominantly to the SE, that bound narrow (2-3 km-wide) faulted-blocks (and locally horst-grabens) stepping down gradually towards the OOB volcanic floor (Fig. 3.5C). Individual fault scarps, >700 m-high, limit deeply incised basement blocks, probably uplifted during an early faulting event. The SFTZ in turn links to the SW with the submeridian and segmented OOF fault-scarp that sharply cuts through highly-folded Proterozoic footwall rocks in the Loliondo plateau. These eroded basement flanks, as high as 2300 m to the north (Fig. 3.3C), topographically decrease southwards down to 1700 m towards a tip point close to the Crater Highlands (Figs. 3.2A, B). The flat-lying hangingwall floor of the OOF corresponds to the upper surface of the Salei basalts that are exposed further east as a >200 m-thick volcanic pile in the Sanjan fault scarp (Figs. 3.2B, D2). Assuming that the 3.5 Ma-old Salei

basalts were erupted synchrounously to the OOF activity suggests that the entire offset bounding fault network propagated diachronously southwards in the time-range 7-3.5 Ma.

3.4.1.2 The intra-rift structural pattern

The OOB offset block

On the geological map in Fig. 3.2B, the OOB offset block is subdivided into two submeridian compartments on both sides of the 30 km-long Sanjan normal fault. The latter is capped and post-dated to the south by lavas of the 3.6-3.1 Ma-old Mosonik volcano (Sherrod et al., 2013). The largest compartment to the west is the 25 x 80 km Salei plain which is floored by the Salei basalts in the OOF hangingwall. Their flat-lying surface attests that they did not record any significant extension since 3.5 Ma, provided that any tilted-fault block has not been later erased by erosion. By contrast, younger extension occurred to the east and resulted in the 10 x 30 km Sanjan faulted basin and its 1.7-1.3 Ma-old Peninj lacustrine/volcanic series (Isaac, 1965; Manega, 1993; McHenry et al., 2011), on top of the Salei basaltic substratum (Fig. 3.2D2).

Structural style in the Magadi-Natron rift valley

The EW morphostructural asymmetry of the Magadi-Natron trough typically characterizes an easterly-facing half-graben (Baker, 1958) which narrows gradually southwards from 70 to 40 km at the latitude of the ENS salient (Figs. 3.2B, D). Its along-strike segmentation into the Magadi (N) and Natron (S) segments is variously expressed by: i) the decreasing elevation of the bounding footwall relief from ~2400 m (Nguruman) down to ~1300 m (Sambu-Natron) (Fig. 3.5), ii) the step-like topographic profile of the inner floor that dips southwards from 1200 m to 600 m over 50 km (Magadi), and then shallows over 40 km (Natron), before rising up abruptly, *via* a major fault-like step close to the Gelai volcano, into the 950 m-high Manyara floor (Fig. 3.2C), and iii) the southerly shallowing of basement depth from 3 km to 1.6 km along the Magadi-Natron basinal transect (Birt et al., 1997; Ebinger et al., 1997).

The most complete structural cross-section of the Magadi-Natron half-graben occurs north of the Kordjya transverse fault and exhibits three distinct domains that are from W to E (Figs. 3.2B, D1, 5B): i) two westerly-tilted fault blocks, 10 km-wide

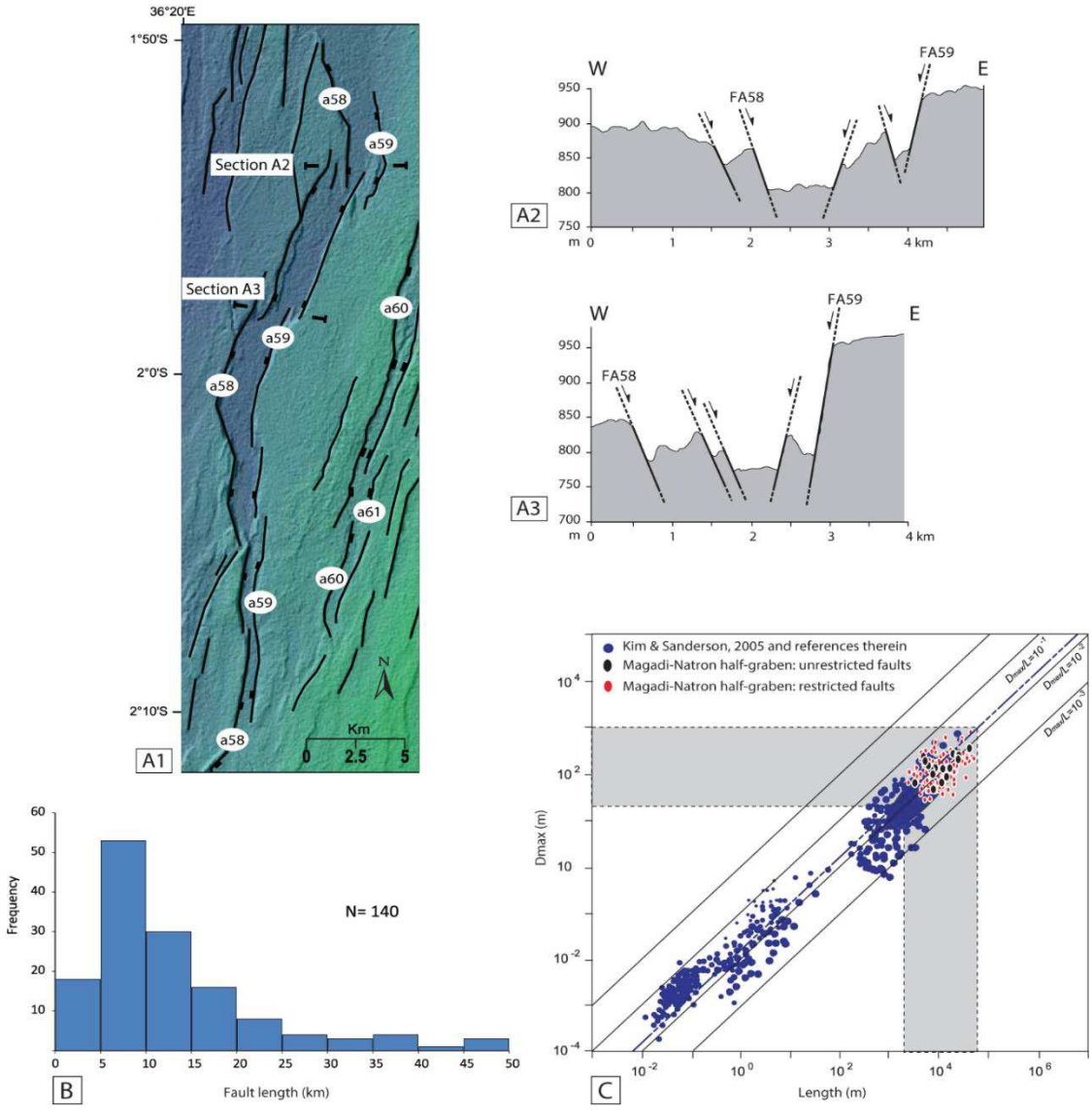

Fig.3.6. Geometrical attributes of the inner fault population in the Magadi-Natron trough. A. Focused view of a narrow and highly-segmented, asymmetric half-graben, south of the Olorgesaile volcano. Location in Fig. 5A. A1. Morphological expression on the SRTM-30 DEM. The trace of sections A_2 and A_3 is shown.$A_{2\text{-}3}$. Two topographic cross-profiles showing its asymmetrical morphology with increasing flank uplift to the east. Vertical exaggeration = 10. Location in Fig. A1. B. Histogram of inner fault azimuth (n = 140 data). B. Log-log plot of maximal displacement (D_{max}) *versus* fault length (L). Our data fit with published results about extensional systems elsewhere.

each, bounded by normal faults, synthetic to the master fault, and with maximum displacement of ~300 m. Their southern extent is masked in the topographically

subdued lake Natron area. ii) A 15 km-wide axial fault belt, dissected by a closely-spaced (<1 km) network of both synthetic/antithetic normal faults extending as far south as the Gelai volcano. The resulting horst/graben pattern is dominated by two >40 km-long asymmetrical grabens that both narrow southwards (Fig. 3.6A), one of each hosting the Magadi lake to the NW. Most of axial fault lengths are in the range 2-50 km (Fig. 3.6A). Their zig-zag map-traces involves numerous fault segments (<7-8 in average), identified following Vétel et al. (2005), with lengths ranging from <1 km to 30 km. Various types of segment linkages are identified as collinear synthetic, approaching and synthetic overlapping patterns (Fig. 3.5A), according to the classification of Morley (1999). iii) The >30 km-wide flexural margin to the east is a weakly faulted monocline, dipping regularly to the west from 1300 m up to 2000 m-high basement bounding relief that are locally overlain by the Narok lava plateau, as far south as 1°55'S (Fig. 3.2). This flexural margin surface is cut by a limited number of minor extensional faults displaying dips antithetic to the western master fault. Further south, at 2°S, the submeridian margin of the half-graben is disturbed by a transverse structure, never so far depicted, and evoked earlier as the ENS basement salient (Fig. 3.7). It forms a >2000 m-high, highly eroded transverse relief, arranged into asymmetric tilted fault-blocks. Their SE-dipping envelop surfaces are cut to the NW by a network N60°E normal faults, <5 km in length, facing consistently riftwards.

3.4.2 Intra-rift fault analysis

3.4.2.1 Fault distribution in the Magadi-Natron trough

In the SKR under study, intra-rift faults are restricted to the Magadi-Natron inner floor, as being totally absent in the OOB, except the abovementioned Sanjan fault. For simplicity, the volcanic inner floor is here considered to be uniformly composed of the Magadi trachyte series, since its subdivision into poorly-defined volcanic formations (Muirhead et al., 2016) does not appear to supply any further insights onto the spatio-temporal development of inner strain. In the same way, the thin sediments that locally overlie the volcanic floor (Baker, 1958) are assumed not to have recorded any significant fault-related strain history. The inner fault array is not homogeneously distributed over the volcanic axial floor. Fault density is maximum in the ~15 km-

wide axial belt extending continuously from the Magadi Lake (N) to the Gelai volcano (S). Unfaulted, lense-shaped regions are observed around a number of axial volcanoes (Olorgesaile and Gelai), indicating that the latter likely acted as resistant nuclei with respect to brittle strain. The flexural hinge zone to the east is much less faulted, with a 15 km-wide monoclinal volcanic surface, dipping regularly westwards (Figs. 3.2, 3.5). The relatively high density of inner faults is also expressed by a mode (maximum frequency) for spacing < 3 km along the 12 seriated cross-sections in Fig. 3.2A. One of the most striking structural features of the intra-rift fault population is the NE/SW alignment of the southern tip points of the easternmost structures (x 19 data), parallel to the NW edge of the ENS basement salient, while keeping a nearly constant submeridian orientation (Fig. 3.7A). The origin of this specific fault map-arrangement, as resulting from the barrier effect exerted by the ENS salient on fault propagation, is tested below from fault displacement/length profiles.

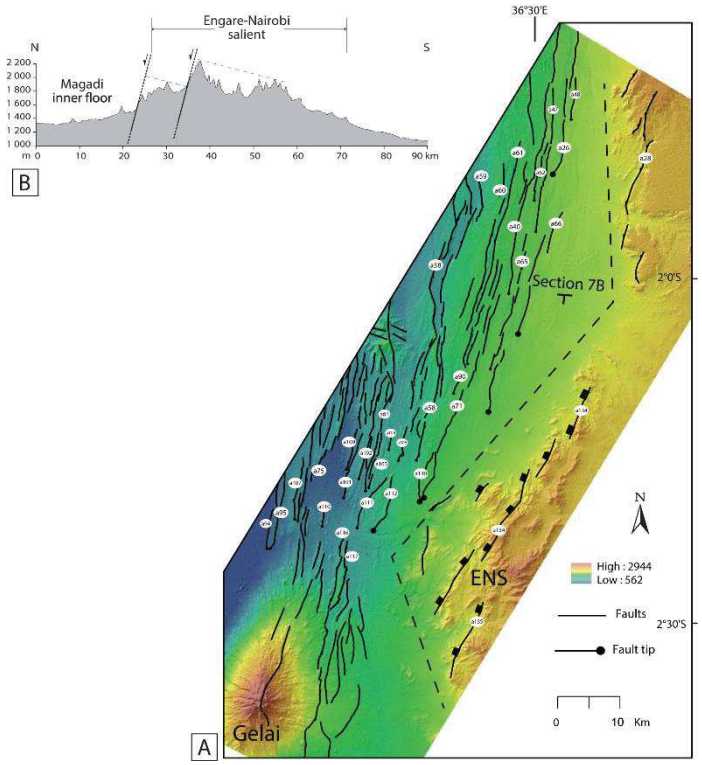

Fig.3.7. The Engare Nairobi transverse basement salient (ENS) on the eastern flank of the Natron trough. A. Map-trace of the inner fault array, immediately N of the ENS, on the SRTM-30 DEM. Note the NE/SW alignment of their southern tip points, parallel to the NW edge of the ENS. B. Topographic section showing the tilted-fault block structure of the ENS in relation to a transverse normal fault network, facing inwards to the NW. Vertical exaggeration = 20. Location in Fig. 7A.

3.4.2.1 Displacement/length profiles

Displacement and length values of 140 inner faults have been analyzed in an attempt to provide insights into the propagation and slip history of the intra-rift fault array in the Magadi-Natron axial trough. Fault lengths range over three orders of magnitude from 2 km up to >50 km, with a peak value in the class 5-10 km (Fig. 3.6B). When plotted on the log-log diagram in Fig. 3.6C, their D_{max}/L ratios define a field that fits within the linear distribution established from published data (Kim & Sanderson, 2005).

Most of displacement profiles display second-order corrugations that coincide with higher displacement gradients at overlapping segment tips, as examplified by faults A6 and A71 in Fig. 3.8A. Such fault patterns are classically attributed to the shift of the slip peak towards interacting segment tips in the stress shadow of adjacent faults (Walsh & Watterson, 1988; Peacock & Sanderson, 1991). More interestingly for our purpose is the asymmetrical *versus symmetrical* shape of fault displacement profiles, known to define specific fault histories. Three main slip profiles are usually distinguished (Pollard & Segall, 1987; Scholz & Cowie, 1990). Elliptical or bell-shaped profiles, with a linear decrease in displacement from the fault center to tip lines, characterize isolated, or unrestricted faults (Figs. 3.8B, C) (Dawers et al., 1993). In this ideal, but rare case, growth of a given fault is not disturbed by any adjacent structures. But, most of natural examples display higher displacement gradients adjacent to either one (half-restricted) or both (double-restricted) tip-lines (Figs. 3.8B, C), in response to impeded fault growth by interaction with confining features (Peacock, 1991; Burgmann et al., 1994; Nicol et al., 1996). Abrupt terminations of slip at fault ends are attributed to various mechanisms, including either interferences with adjacent faults (Dawers & Anders, 1995), or the mechanical effect of heterogeneities or stronger material acting as barriers to fault propagation (Aki, 1979).

In the present study, we are *a priori* concerned by the latter process, given the plausible barrier effect of the triangle-shaped ENS on fault propagation, south of 2°S. One way to test this hypothesis is first to verify the expected southerly-restricted profiles of these faults, with steep displacement gradients southwards, and then to compare these results to those obtained about the remaining inner fault population

which should not be necessarily restricted structures. Among the 19 analyzed fault profiles in the eastern zone, the majority of them (x 18, i.e. 94%) are restricted, hence in agreement with the working hypothesis above (Fig. 3 . 8B, Table 1). However, the weak number of expected southerly-restricted tips (x 1, i.e. 6%, Fault A47 in Fig. 3.8B), which furthermore does not occur specifically close to the ENS, does not give any support to the presumed model. Displacement profiles of the remaining inner fault population (x 121), which should have propagated more freely away from the ENS indenter (Table 3.1), still show a majority of restricted profiles (x 100, i.e. 82%), most of them are restricted on both tips (x 72, i.e. 59%), whereas the same amount of faults (x 14) are restricted on either northern or southern tips (Fig. 3.8C). Again, southerly-restricted faults are evenly distributed within the Magadi-Natron axial fault belt. Comparing the two analyzed fault populations (140 data) shows that: i) they both display a high ratio of restricted/unrestricted faults, as similarly documented about most fault systems elsewhere (Manighetti et al., 2004), ii) southerly-restricted faults are very few, and iii) not spatially confined north of the hypothetical ENS mechanical barrier. Our results contradict those of Muirhead et al. (2016) who inversely assessed that most of their analyzed inner faults (40 data) display symmetric (bell-shaped) displacement profiles, typical of unrestricted fault growth. Based on the exhaustive analysis of 140 inner fault displacement profiles, we come to the conclusion that the restricted nature of most intra-rift normal faults in the Magadi-Natron half-graben is not an unambiguous diagnostic criteria for inhibition of tip propagation against a mechanical barrier. Without any further detailed analysis of the inner fault population, its prominent restricted nature should be rather related to strong interactions of closely-spaced faults in a structurally mature rift, as documented elsewhere (Dawers & Anders, 1995). This is in agreement with the low average fault spacing (<3 km, see above) which does not seem to conform to the stress-reduction shadow commonly documented around normal faults (Ackermann & Schlische, 1997) and that likely indicates that the entire inner fault system in the SKR has attained saturation (Wu & Pollard, 1995).

The only conceivable structural impact of the ENS triangle-shaped basement salient on the SKR rift pattern is to have provoked the gradual narrowing of its axial trough southwards over a >30 km-long rift parallel section, and thus to have caused a deficit of extension, accordingly. Extension estimates are presented below, not only

about the Magadi-Natron half-graben as previously performed by Muirhead et al. (2016), but also about the OOB offset rift block to the west.

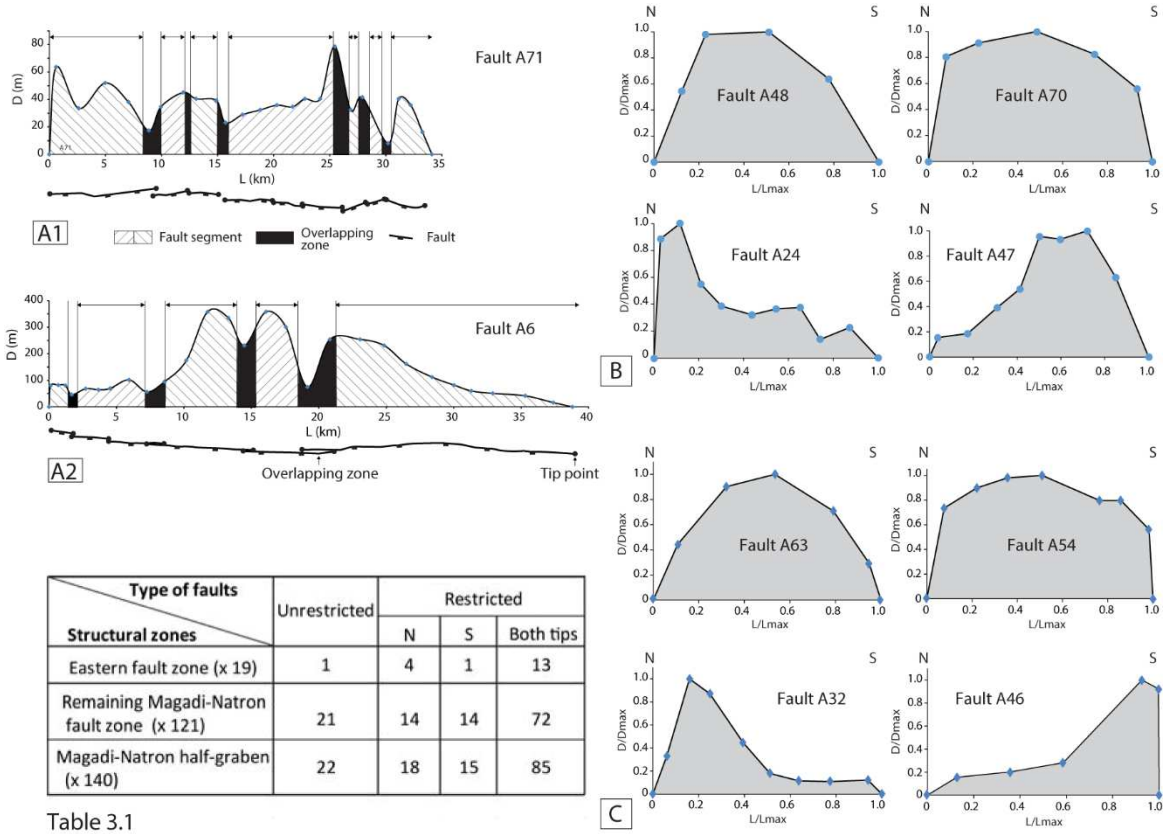

Type of faults / Structural zones	Unrestricted	Restricted		
		N	S	Both tips
Eastern fault zone (x 19)	1	4	1	13
Remaining Magadi-Natron fault zone (x 121)	21	14	14	72
Magadi-Natron half-graben (x 140)	22	18	15	85

Table 3.1

Fig.3.8. Map traces and displacement profiles for inner normal faults in the Magadi-Natron rift trough. A. Faults traces and corresponding slip distribution along two highly-segmented faults (A6, A71), facing eastwards. Location in Fig. 5A. Segment tip point (full circle). Overlapping segments in black. B. Examples of displacement profiles for unrestricted (A48), double-tip restricted (A70), half-restricted (to the north, A24, and to the south, A47) faults, north of the ENS basement salient. Location in Fig. 7A. C. Examples of displacement profiles for unrestricted (A63), double-tip restricted (A54), half-restricted (to the north, A32, and to the south, A46) faults in the axial part of the trough. Location in Fig. 5A.

Table 3.1. Restricted versus unrestricted fault populations in the Magadi-Natron half-graben.

4.3. Extension estimates

Extension estimates have been made in various ways in order: i) to discriminate rift-bounding fault- and intra-rift fault-related strain, ii) to precise the spatio-temporal distribution of strain in both the Magadi-Natron half-graben and the OOB offset block, and iii) to evaluate the respective contribution of these two rift structures in the total extension recorded by the entire SKR system.

The total throw/extension values have been calculated along 12 seriated EW cross-sections ($A_{1\text{-}12}$) that span the entire width of the SKR system with a constant spacing of 10 km (Figs. 3.2A, 3.5). Throw estimates along the Nguruman and Natron border faults benefit from basement depth values derived from geophysical records in the Magadi (3 km) and Natron (1.6 km) troughs, respectively (Birt et al., 1997; Ebinger et al., 1997). Cumulative extension values have then been calculated by adding topographic elevations of their exposed bounding fault scarps (Fig. 3.9). The step-like geometry (in terms of both vertical amplitude and tightness) of most extension profiles at the Magadi-Natron transition zone is probably exaggerated because of the prominent contribution of the two geophysically-derived (and constant) basement depths (3 and 1.6 km) in the cumulative throw estimates. Provided that hangingwall (volcanic) sequences are synchronous to fault activity, their respective thickness provides additional insights into the sequential development of the corresponding master faults. These syn-faulting volcanics are: i) the ca 400 m thick Magadi trachyte series (1.3-0.9 Ma-old) (Baker, 1958) in the hangingwall of the relatively young E/Nguruman fault, and ii) the 7 Ma-old and probably more localized Lengitoto trachytes exposed as a nearly 400 m-thick succession in the older W/Nguruman footwall block, and inferred to underlie the Magadi trachyte inner floor as far south as 2°S. Syn-faulting volcanics in the hangingwall of the OOF are represented by the >400 m-thick Salei basalts, 3.5 Ma in age.

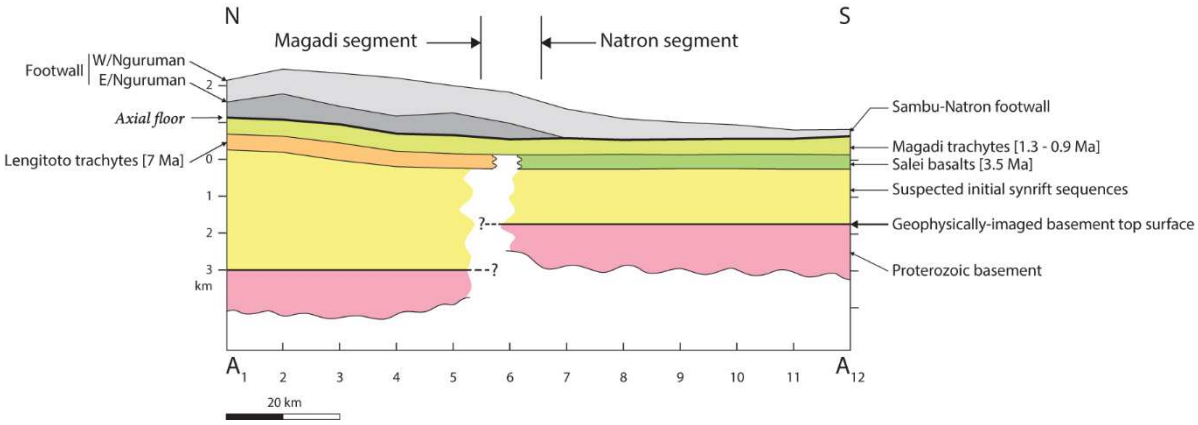

Fig. 3.9. Rift-parallel sketch section showing the composite dataset (geophysically-derived basement depths, topographic elevations and syntectonic volcanics thickness) used to calculate cumulative throw/extension on the 110 km-long Nguruman-Sambu-Natron border fault network. ($A_{1\text{-}12}$ transects are located in Fig. 5A). See text for explanations.

Inner fault-related extension has been obtained by summing individual fault extension along each cross-section ($A_{1\text{-}12}$) (Fig. 3.2A). As mentioned above, these are minimum estimates that might not have recorded earlier (not visible) slip history. Extension values in the 20 km-wide immediate hangingwall of the border fault system have been accurately measured (195 m) along only two continuously exposed cross-section to the north ($A_{1\text{-}12}$), and then extrapolated southwards to its masked extent in the Natron subdued area.

One additional extension bias might exist in cross-sections A_2, A_3, and A_6 because of the "shadow" effect of the Olorgesailie and Lenderut volcanoes that tend to minimize the amount of brittle strain. Being aware of these uncertainties, our extension measurements are regarded as accurate parameters for comparative purpose. Extension estimates are represented as either finite extension values in km (W_1-W_0), where W_0 and W_1 are the initial and final width of the rifted domain, respectively, or as the ratio (in %)

$e = W_1 – W_0 / W_0$ (Table 3.2).

The interpretation of extension diagrams in Fig. 3.10 first needs to define the temporal development of each fault pattern in the two-stage rift scenario envisaged above. Early extension was exclusively accommodated by slip along the W/Nguruman-SFTZ-OOF offset bounding fault network, whilst younger extension was achieved by the combined activity of the linear E/Nguruman-Sambu-Natron border fault system and axial rift faulting in the Magadi-Natron trough.

Extension profiles about each individual fault pattern in Fig. 3.10A supply interesting insights, as follows:

- The early (blue curve) and late (yellow curve) border fault-related extension profiles are both segmented at the Magadi-OOB/Natron basin transition zone (section A5 in Fig. 3.2A), hence indicating that the along-strike segmentation of the SKR initiated at an early rifting stage and then persisted through time, but with contrasted vertical amplitudes and opposite extension gradients.

- Early border fault-related extension decreases sharply southwards at A_5 from 3500-4500 m (W/Nguruman) down to <1000 m (STFZ-OOF), whereas younger extension

values inversely rise southwards from <1000 m (E/Nguruman) up to ca 2000 m (Sambu-Natron). The ~3000 m vertical amplitude of the break at the A_5 transition zone should be minimized since early displacement/throw along the poorly-constrained OOF border fault might be greater than those estimated from only surface geology (in the range 500-1000 m).

- In contrast, the inner fault-related extension values decrease gradually southwards from ~1100 m (A_2) to 450 m (A_{12}), without any break at the Magadi-Natron segment transition.

- The expected shadow effect of the Olorgesaile volcano is not observed along the transect A_1-A_3, neither any marked drop of extension at the latitude of the ENS basement salient (A_7-A_{10}).

- The contribution of the spatially-and temporally-restricted inner faults (black curve) relative to the synchronous border faults (yellow curve) can be only addressed about the late rifting stage recorded by the Magadi-Natron half-graben. The relative contribution of the bounding fault network increases markedly southwards from ~50% in the Magadi basin (E/Nguruman fault), where the two extension profiles nearly coincide (in the range 1000-500 m), up to ~75 % in the newly-formed Natron basin where border fault-(Sambu-Natron structure) and intra-rift fault-related extension values average 2000 m and 700-500 m, respectively.

The diagram in Fig. 3.10B, about the extension pattern experienced by the multistage Magadi-Natron half-graben during its 7 Ma-lasted rift development shows the following features:

- The border fault-related extension profile still shows a similar segmentation at the Magadi-Natron transition, with a vertical amplitude (from 6000-4500 m to ~2000 m) mainly caused by early displacement along the large-offset W/Nguruman fault.

- The relative contribution of border faults versus intra-rift faults decreases slightly southwards from ~84-82% in the Magadi segment down to 80-66% in the Natron segment.

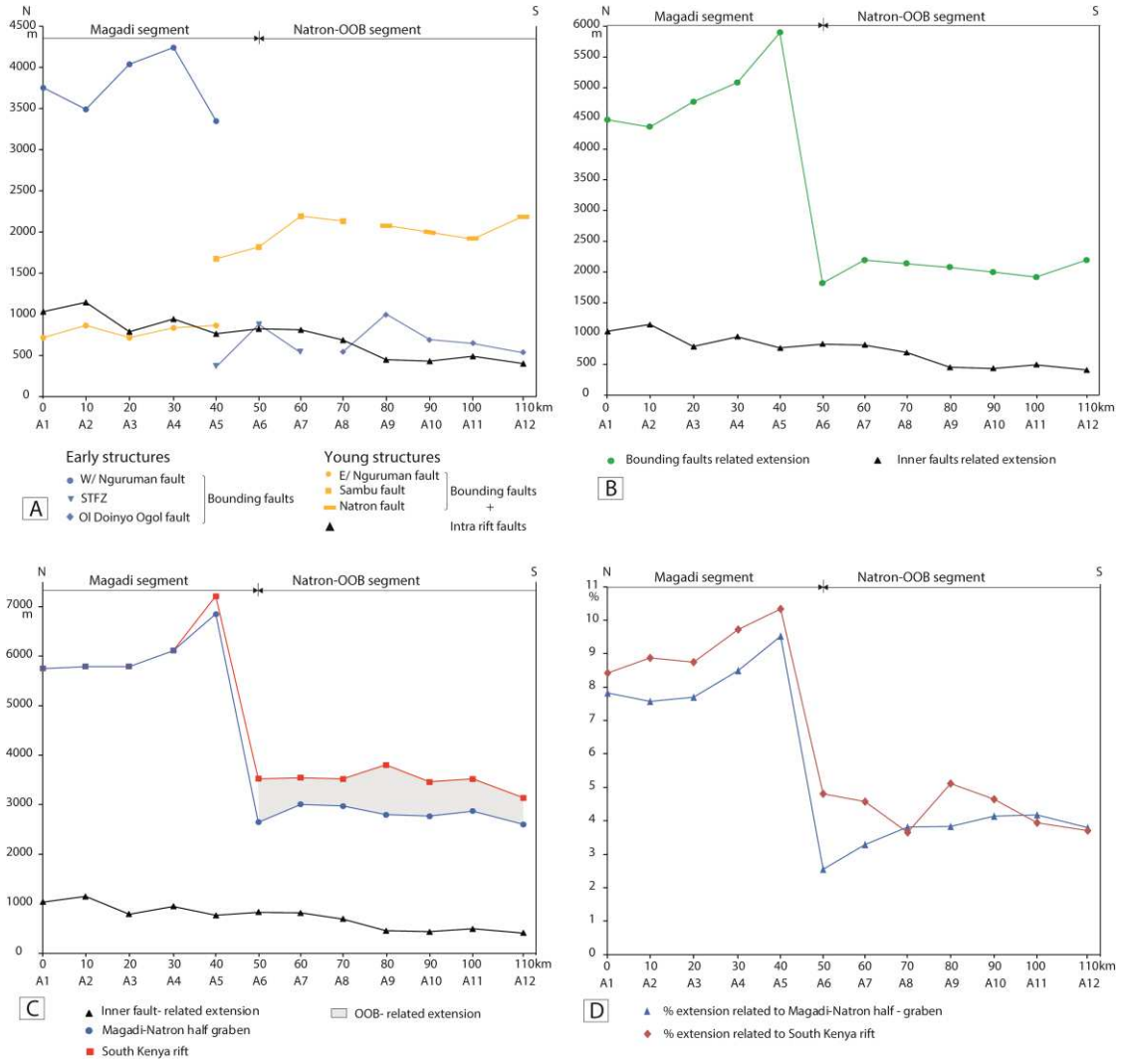

Fig.3.10. Diagrams showing the distribution of cumulative extension in the SKR along the 12 regularly-spaced (10 km) cross-sections $A_{1\text{-}12}$ in Fig. 5A. A. Extension estimates about: i) early rift-bounding faults (blue curve), ii) younger rift-bounding faults (yellow curve), and iii) inner faults (black curve). B. Cumulative extension estimates about inner faults (black curve) and bounding faults (green curve) in the Magadi-Natron half-graben. Note the drop in border fault-related extension from the Magadi to the Natron segment, whilst inner fault-related extension decreases smoothly southwards. Cumulative extension estimates about: i) inner faults (black curve), ii) the Magadi-Natron half-graben (inner and border faults, blue curve), and iii) the entire SKR (Magadi-Natron-OOB, red curve). Rate of extension in the Magadi-Natron half-graben (blue curve) and in the entire SKR (red curve). Except the inner fault curve, all extension profiles consistently show the prominent segmentation of the SKR system into the Magadi and Natron segments at $A_{6\text{-}7}$.

Lastly, the profiles in Figs. 3.10 C, D about cumulative extension and extension rates in both the Magadi-Natron half-graben and the entire SKR rift system show that:

- Extension drops abruptly southwards from the Magadi (6-7000 m, 8-9%) to the Natron (~3000 m, 4%) segment at the A_5-A_6 transition zone.

- The contribution of the OOB offset rift pattern relative to the total extension experienced by the OOB-Natron southern segment, though being modest (<1000 m in average, i.e ~20%), is not negligible, being aware that these values are probably largely underestimated for reasons mentioned above.

Parameters / Section	Width (km)		Extension (m)			
	Initial (L_o)	Final (L1)	%extension = (L_1-L_o) *100/L_o	Fault scarp	Inner faults	Total
A1	60	65	7.82	4717	1035	5752
A2	61	66	7.57	4642	1147	5789
A3	65	70	7.69	5000	788	5788
A4	61	66	8.49	5164	947	6111
A5	64	70	9.52	6085	765	6850
A6	71	73	2.56	1819	827	2646
A7	67	69	3.28	2194	814	3008
A8	60	62	3.82	2282	690	2972
A9	60	62	3.83	2287	451	2738
A10	53	55	4.13	2183	431	2614
A11	54	56	4.17	2240	493	2733
A12	58	60	3.80	2194	406	2600

Parameters / Section	Width (km)		Extension (m)			
	Initial (Lo)	Final (L_1)	%extension = (L_1-L_o) *100/L_o	Fault scarp	Inner faults	Total
A1	68	74	8.43	4717	1035	5752
A2	65	71	8.88	4642	1147	5789
A3	66	72	8.74	5000	788	5788
A4	63	69	9.72	5164	947	6111
A5	70	77	10.33	6446	765	7211
A6	73	77	4.80	2699	827	3526
A7	77	81	4.57	2728	814	3542
A8	96	100	3.65	2828	690	3818
A9	74	78	5.12	3349	451	3800
A10	75	78	4.65	3032	431	3463
A11	89	93	3.93	3026	493	3519
A12	85	88	3.70	2731	406	3137

Table 3.2. Extension estimates in terms of width ratio and rates (%) in: i) the Magadi-Natron half-graben (above) and ii) the entire South Kenya rift (Magadi-Natron-OOB, below).

4.4. Evidence for a first-order inherited transverse discontinuity

The structural sketch map of the SKR-NTD rift system in Fig. 3.11 is compiled from SRTM-30 DEM features, surface geology (Baker, 1958) and the seismicity pattern of Weinstein et al. (2017). It clearly shows, in addition to the western border fault-scarp network described above, a prominent transverse lineament extending over >200 km in a NE/SW direction from the ENS to the Eyasi fault tip.

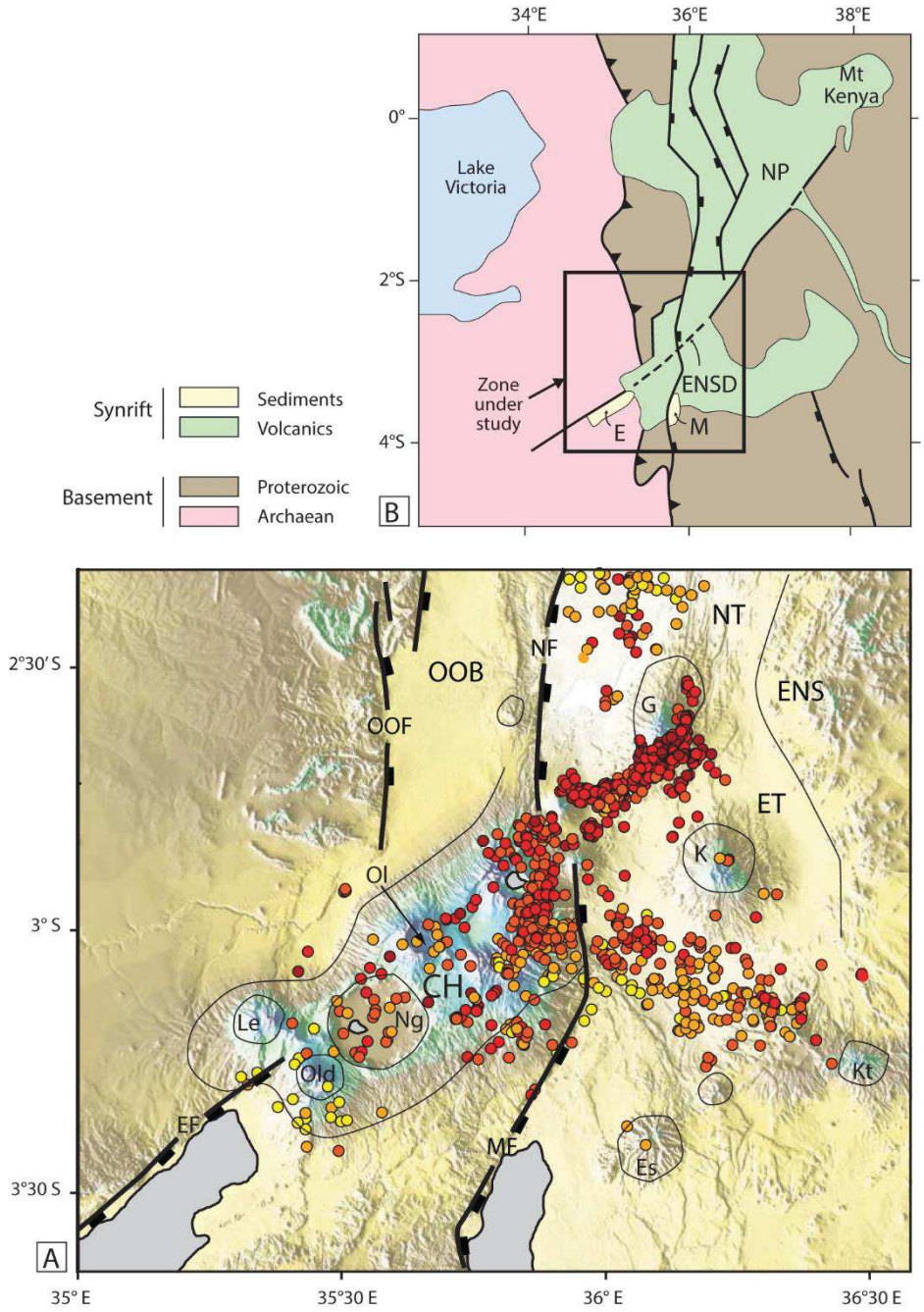

Fig.3.11. Structural evidence for a first-order transverse discontinuity (ENS-Eyasi) through the SKR-NDT rift system. A. Earthquake distribution (red and yellow circles, modified from Weinstein et al., 2017). B. Shows a pronounced morphological structure bounding the Narok-Nairobi-Mont Kenya Miocene lavas in the NE continuation of the ENS-Eyasi lineament (extracted from the Geological Map of Kenya, 1: 1,000,000, Ministry of Energy of Kenya, 1987). E., M., N., Eyasi, Manyara, and Natron lakes, respectively; ENSD., ENS-Eyasi discontinuity; NP., Nairobi volcanic plateau.

The map-trace of the so-called ENS-Eyasi lineament is outlined by the alignment, assumed here not to be fortuitous, of various rift structures that are from NE to SW as

follows: i) The early normal fault network associated to the ENS transverse tilted fault blocks on the eastern margin of the Natron trough. ii) The Gelai volcanoe, 1 Ma in age, and the surrounding Naibor Soito earthquake swarm (Weinstein et al., 2017) that includes events related to the 2007 Lengai-Gelai seismo-tectonic crisis with nodal fault planes typical of NNE-trending extensional structures (Calais et al., 2008; Baer et al., 2008; Albaric et al., 2010). iii) The fault-like morphological scarp that disrupts the inner floor at the Natron/Engaruka segment transition. iv) The prominent Crater Highlands magmatic range and its similarly-aligned NE/SW-oriented eruptive centres, parallel to seismically active faults (Lee et al., 2017). v) The 150 km-long Eyasi fault-basin system that dies out in Archaean terranes, 70 km SW of the craton-Proterozoic boundary. On the sketch inset map in Fig. 3.11, the ENS-Eyasi lineament appears to be prolonged to the NE, far beyond the study area, by a >200 km-long morphological feature that limits to the SE the Narok-Nairobi phonolite plateau (Upper Miocene lavas) and even Pleistocene lavas of Mount Kenya. In the study area, the linear map-trace of the ENS-Eyasi lineament sensu stricto, along with the variety and contrasting ages of associated rift features, typically characterize a steeply-dipping, inherited structure that recorded a multistage reactivation during Neogene-Present extension.

3.5 Discussion. Implications about rift propagation

3.5.1 Space-timing distribution of strain in the SKR

Combining morphostructural and quantitative data about fault populations in the SKR system supplies new insights onto the mechanisms of rifting during its 7 Ma-lasted development. Though uncertainties exist about the exact timing of the onset of displacement along rift-bounding faults, their contrasting erosional profiles suggest a two-stage faulting process, tentatively calibrated by available age dataset of synrift volcanics (Fig. 3.12). Initial rifting in the time-range 7-1.3 Ma was primarily achieved by displacement along the large-offset W/Nguruman/OOF boundary fault network and the associated STFZ transfer zone that all accommodated asymmetric subsidence in the nascent Magadi-Natron-OOB half-graben basin (Fig. 3.12B). Earlier

development of the Magadi basin, prior to 7 Ma, is hypothetized from geophysically-derived basement depths (Birt et al., 1997; Ebinger et al., 1997) that suggest the existence of a >2 km-thick synrift package beneath the Lengitoto lavas (Fig. 3.9). The sedimentary nature of these suspected initial synrift sequences is suggested by the discrete inliers of lacustrine limestones occurring in a quite similar pre-volcanic position in the OOB offset basin, at the foot of the OOF and on top of Proterozoic basement rocks, hence pre-dating the Salei basalts (Figs. 3.2B, 3.3A, B). The inferred proto-Magadi and-OOB sedimentary synrift basins should correspond to the basement-derived sedimentary deposits known to pre-date magmatic activity in Central (Kerio) and North Kenya (Turkana) rift segments (Chapman et al., 1978; Morley et al., 1992; Mugisha et al., 1997; Hautot et al., 2000).

At one stage of initial rifting, it cannot be excluded that the W/Nguruman fault propagated as far south as the ENS-Eyasi transverse lineament, as envisaged below about one possible mechanism of rift offset. Transfer of strain from the W/Nguruman to the OOF border fault was achieved via the STFZ that displays quite distinct structural features with respect to most transfer faults in the EAR. Its atypical map-dimensions (25 x 40 km) evoke a large-scale breached relay ramp (Gawthorpe & Hurst, 1993) with internal transverse fault lengths that strictly equal the 40 km-wide overstep of the W/Nguruman-OOF fault system. The inherited origin of these faults is suggested by their parallelism with Proterozoic fabrics in the Mbulu plateau further south, though no direct structural evidence is supplied by the DEM imagery (Fig. 3.2A). The dominantly dip-slip tectonics experienced by the STFZ transverse faults is also at odds with the strike-slip nature of most transfer faults in the Kenya-Ethiopia rift (Keir et al., 2015). It further indicates that the juvenile SKR system recorded a complex 3D-extensional pattern with local clockwise stress rotation (from EW to NNW/SSE in the STFZ), as commonly reported about transfer fault zones elsewhere (Kattenhorn, 2004).

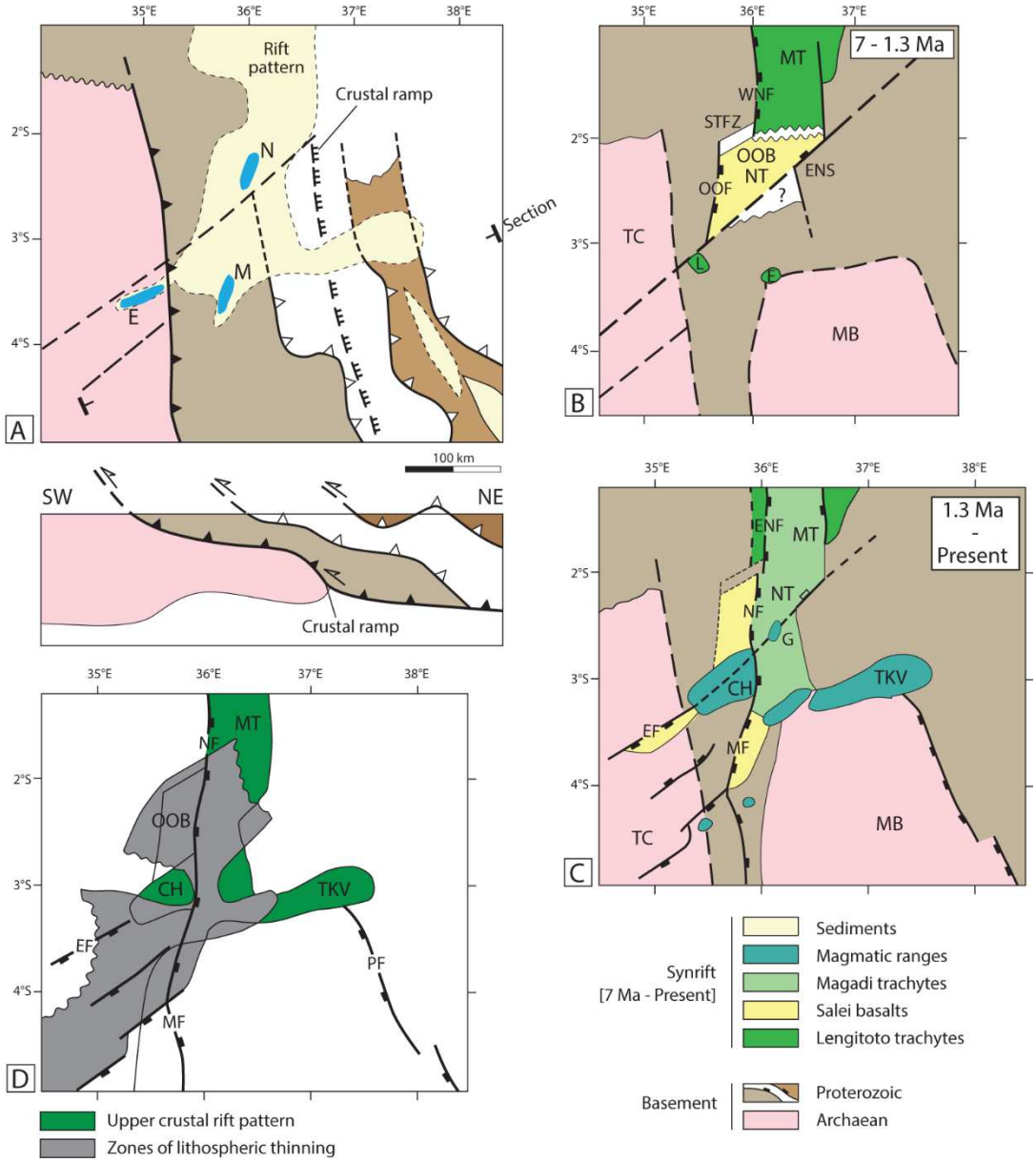

Fig. 3.12. Two-stage kinematic rift model of the SKR-NTD system during the last 7 Myrs. A. Pre-rift basement framework in map and cross-section. The traces of Archaean suture zones and Proterozoic thrusts are from Fletcher et al. (2018) and Fritz et al. (2009), respectively. The Masai craton is not drawn on the map (buried beneath the shallow thrust-nappe pattern). E., M., and N. are the location of the Eyasi, Manyara and Natron lakes, shown as geographical coordinates. The sketch cross-section runs north of the Masai craton (not drawn). The rift pattern is not drawn on the section. B. Early rift stage (7-1.3 Ma) dominated by the dextrally-offset SKR system and the off-axis emplacement of incipient magmatism in the Lenderut (nascent Crater Highlands) and Essimingor areas to the south. C. Late rift stage (<1.3 Ma) showing the southerly split of rifting *via* the multistage reactivation of the ENS-Eyasi inherited discontinuity. D. Intricate architecture of the SKR-NTD rift system at depth with transverse zones of thinned lithosphere disconnected from the upper crustal rift, compiled from Plasman et al. (2017) and Fletcher et al. (2018). Same abbreviations as in Figs. 1B, 2B.

Concomitantly, the Magadi and Natron/OOB segmented hangingwall basins were the locus of diachronous flood-type magmatism younging southwards from 7 Ma (Lengitoto trachytes) to 3.5 Ma (Salei basalts), respectively. The flat-lying and apparently unfaulted structure of the latter attests that the OOB basin, and by extrapolation the proto-Magadi/Natron basin, did not experience any significant intra-rift strain at this early stage, thus arguing that the bounding fault system was the chief contributor to bulk brittle strain during initial rifting in the SKR.

The general southerly propagation of both tectonic and magmatic early rift structures in the time-period 7-1.3 Ma was disturbed as early as 5 Ma by the off-axis emplacement of magma in the discrete Crater Highlands range to the SW (Lenderut, Sadiman edifices).

Major changes in the mechanisms of rifting occurred in the time-range 1.7-0.9 Ma with the easterly shift of strain. That resulted in the inward migration of border fault activity: i) from the W/ to the E/Nguruman fault to the north, and ii) to the south, from the abandoned OOF towards the Sanjan intra-basin fault and then to the Sambu-Natron fault, in the southern prolongation of the E/Nguruman fault. The resulting linear and narrower Magadi-Natron half-graben basin was floored by more evolved flood-type lavas (the Magadi trachyte series), in turn disrupted by a dense swarm of minor intra-rift faults accommodating, for the first time, part of the regional extension. Such inward focussing of strain is commonly reported in most of Kenya (Morley, 1999; Hautot et al., 2000; Vétel & Le Gall, 2006) and Afar/Ethiopia rift segments (Ebinger & Casey, 2001; Keranen et al., 2004; Keir et al., 2006), and is generally attributed to thermal weakening of the axial crust via magmatic intrusions (Ebinger & Casey, 2001; Wright et al., 2006) and release of fluids (Muirhead et al., 2016).

However, our quantitative analysis of fault-related strain in the SKR leads to opposite conclusions about the contribution of inner fault population (moderate) relative to rift-bounding faults (prominent), the latter decreasing slightly southwards from ~84-82% (6000-4500 m) in the Magadi segment down to 80-66% (2000 m) in the Natron segment. We therefore come to the conclusion, in contradiction with Muirhead et al. (2016), that there is no sharp transition from border fault-to intra-rift fault-dominated strain accommodation through time, in agreement with results

obtained by these authors about the 10 Ma-lasted Tanganyika rift on the Western branch that instead show no fundamental differences in the processes driving continental rifting along either the magma-rich (Eastern) and magma-poor (Western) branches in the EAR (Muirhead et al., 2019).

It is also demonstrated that the OOB offset rift pattern (exclusively the OOF) accounts for ~1000 m (25%) of the total extensional strain in the OOB-Natron southern segment, being aware that these moderate values are minimized because missing data about cumulative displacement along the OOF bounding fault. Nonetheless, our work demonstrates the need to integrate the early rift history recorded by the OOB offset domain in any quantitative structural study of the SKR rift system.

From only considering brittle strain achieved along both border and intra-rift faults, we obtain an upper crustal extension >7 km (>10%) for the 7 Ma-lasted SKR rift system. This is a minimum value which does not include the probable magma-assisted extension that occurred through dyking at depth, more specifically during the intra-rift faulting, as documented elsewhere in the EAR (Beutel et al., 2010; Bialas et al., 2010). The upper crustal extension value applied here to the SKR rift (7 km) fits with the magnitude of crustal stretching (35-29 = 6 km, ß-factor of 1.2) deduced from geophysical data in the Magadi half-graben segment (Birt et al., 1997; Ebinger et al., 1997).

3.5.2 Rift-bounding faults and crustal pattern

The concept of Baker (1958) about the Nguruman rift-bounding fault as being one fundamental structure in the SKR was later confirmed by geophysical records showing: i) crustal thickness variations (from 35 to 29 km) beneath its exposed scarp (Birt et al., 1995; Plasman et al., 2017), and ii) ca 3km of downthrow of the Magadi hangingwall basin (Ebinger et al., 1997). Because appropriate geophysical data are missing in the OOB, basement depth and correlative cumulative displacement along the OOF border fault are still unknown. Therefore, the modest throw value estimated above from surface geology is probably underestimated, and does not fit with newly-

acquired magnetotelluric data that rather argue for the crustal nature of the OOF. These data have been recorded on a 150 km-long MT profile extending at 3°S close to the OOB/Crater Highlands boundary, orthogonal to the NS rift axis (Fig. 3.13A).

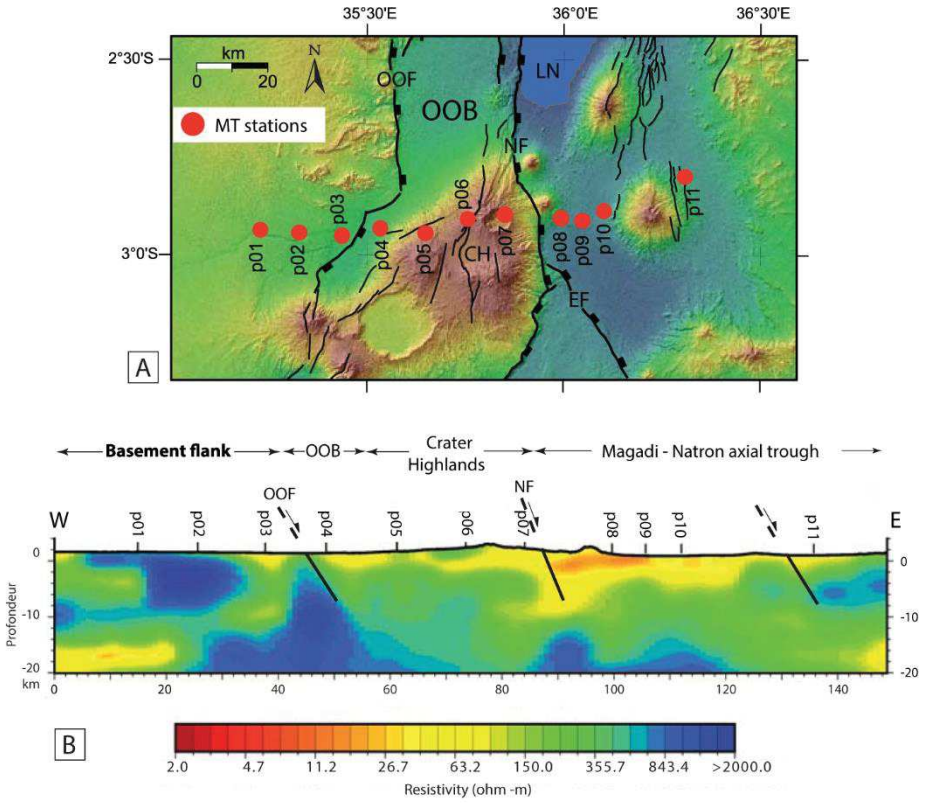

Fig. 3.13. Upper crustal structure of the Ol Doinyo Ogol offset block from magnetotelluric (MT) records. A. Trace of the 150 km-long MT profile on the SRTM-30 DEM. B. Interpreted upper crustal cross-section (20 km-deep) from the western bounding basement edge to the Ketumbeine axial volcano. Note the marked variations in the resistivity record on both sides of the Ol Doinyo Ogol (OOF) and Natron (NF) faults.

On the interpreted section in Fig. 3.13B, two contrasted upper crustal domains are juxtaposed at shot points P03-P04, on both sides of the extrapolated trace of the OOF. The more resistive domain to the west corresponds to the cold and upper crust of the unrifted basement domain, close to the western craton edge. The more conductive upper crust to the east correlates with the OOB-Crater Highlands-Natron magmatic rifted domain. A highly conductive body is evidenced at shallow depth (<2 km) on the 20 km-long Kerimasi-Ketumbeine axial volcanic chain, immediately east of the Natron master fault (Fig. 3.13B). The crustal nature of the OOF master fault is further confirmed by receiver function modelling that reveals the step-like geometry

of the Moho, not beneath the Natron rift trough as should be expected, but instead beneath the OOB hangingwall block where it shallows westwards from 40 km beneath the basement uplift block up to 30 km beneath the Salei plain, with a steepest gradient towards the OOF master fault (Plasman et al., 2017). If excluding any significant magmatic underplating beneath the present-day Natron rift axis, the shallowing of the Moho further west would indicate marked crustal thinning and increasing extension in the OOB offset block. This result contradicts previous geophysical models suggesting axial crustal thinning along the entire Kenya rift trough (KRISP, 1991; Green et al., 1991). As emphasizing the prominent role of the OOF, our unexpected result has major implications about the hierarchy of rift-bounding faults in the SKR system.

3.5.3 Structural inheritance and synrift strain/magmatism

It has long been established that the NW/SE transverse fault pattern in the highly segmented North-Central Kenya rift nucleated along reactivated Proterozoic shear zones during Tertiary extension (Chorowicz, 1989; Smith and Mosley, 1993; Ring, 1994; Le Turdu et al., 1999; Le Gall et al., 2000; Hautot et al., 2000; Le Gall et al., 2005; Vétel and Le Gall, 2006). Similarly-trending transverse faults are very few in the SKR under study, i.e. the Kordjya fault in Fig. 2B (Muirhead & Kattenhorn, 2018). Instead, transverse rift structures in the SKR are oriented NE/SW (STFZ, ENS/Eyasi and Crater Highlands). Their origin, structural significance and causal mechanisms are discussed below in a coherent tectonic model about rift propagation at the Tanzanian craton margin.

3.5.3.1 Inherited origin of the ENS-Eyasi lineament

The variety and contrasting ages of rift structures aligned along the linear map-trace of the ENS-Eyasi lineament undoubtedly indicate that the latter resulted from the multistage and segmented reactivation of a >200 km-long inherited discontinuity during Neogene-Recent times. Basement surface geology supplies no clear evidence

about the initial nature of this inferred discontinuity. The folded and generally shallowly-dipping attitude of the foliation plane in the Proterozoic basement host-rocks (i.e. the granulite belts of Fritz et al., 2009) indicates that Proterozoic ductile strain exerted no control on the trajectory of the ENS-Eyasi lineament. The latter more likely roots at a greater depth along a steeply-dipping discontinuity, presumably Archaean in age, that likely correlates with similarly-oriented structures identified as suture-related features on gravimetry modelling in the Eyasi-Mbulu area, further SW (Fig. 3.12A) (Fletcher et al., 2018). This assertion implies that the Tanzanian craton should extend at depth, beneath the westerly-translated Proterozoic thrust-nappe pattern, as far east as the ENS lineament. Our interpretation is in agreement with the structural sections of Fritz et al. (2009) that show the Proterozoic thrust terranes rooting eastwards into a steep crustal ramp, ca 200 km east of the exposed frontal thrust (Fig. 3.12A).

The various types of rift structures along the ENS-Eyasi discontinuity suggest that its rejuvenation under the regional EW extension might have not operated by simple extensional reactivation, and was instead achieved by a combination of processes, possibly controlled by the thermal state of the crust. This is supported by the specific distribution of brittle strain at the two extremities of the lineament (ENS and Eyasi faults), i.e. on the rift flanks where the crust is colder, whereas tectono-magmatic structures took place, as either minor dyking along the Gelai-Naibor Soito axis or prominent intrusions in the Central Highlands, in the hotter, axial rift crust (Fig. 3.11). The importance of the ENS-Eyasi inherited transverse discontinuity is further argued by its NE prolongation, away from the rift axis, by the >200 km-long morphological structure bounding the Narok-Nairobi-Mount Kenya volcanic plateaus and which likely formed as a pre-rift topography, in response to plume-induced uplift of the East African plateau in Miocene times (> 13 Ma) (Winchura et al., 2010).

3.5.3.2 Causal mechanisms of the OOB offset rift block

The structural development of the OOB offset block, on the western flank of the SKR axial trough, can be satisfactorily explained in two different ways, not exclusive, that are both related to transverse faulting. The first hypothesis is based on the temporal and spatial correlations displayed by the STFZ and ENS structures that both initiated early, probably in the time-range 7-1.3 Ma, and at the same latitude (Figs. 3.2, 3.3). It can be thus envisaged that, in response to the narrowing of the Natron basin (up to 20 km) caused by the ENS basement salient, the rifted domain shifted westwards, via the STFZ transfer zone, into the 40 km-wide OOB offset block, in order to maintain a nearly constant border fault aspect ratio along-strike (ratio between fault throw and hangingwall width dimension). The second scenario implies that the W/Nguruman border fault propagated as far south as 2°45', until it encountered the ENS-Eyasi transverse discontinuity (Fig. 3.14). In this case, kinematics of the resulting triangle-shaped hangingwall block primarily depend on two parameters that are: i) the opposite versus similar dip directions of the two intersecting faults and ii) their acute versus obtuse angle (Fig. 3.14A) (Lezzar et al., 2002; Vétel & Le Gall, 2006).

In the present case, the opposite dip directions and acute angle of the two structures are unfavourable conditions for any downthrow of the hangingwall block. Consequently, the southerly propagation of the W/Nguruman fault was inhibited, and that in turn induced the shift of strain backwards to the NW along the STFZ/OOF network. According to this second scenario, the Sambu-Natron fault should represent a multistage structure, initially formed as an early inner fault in the OOB-paleo Natron basin.

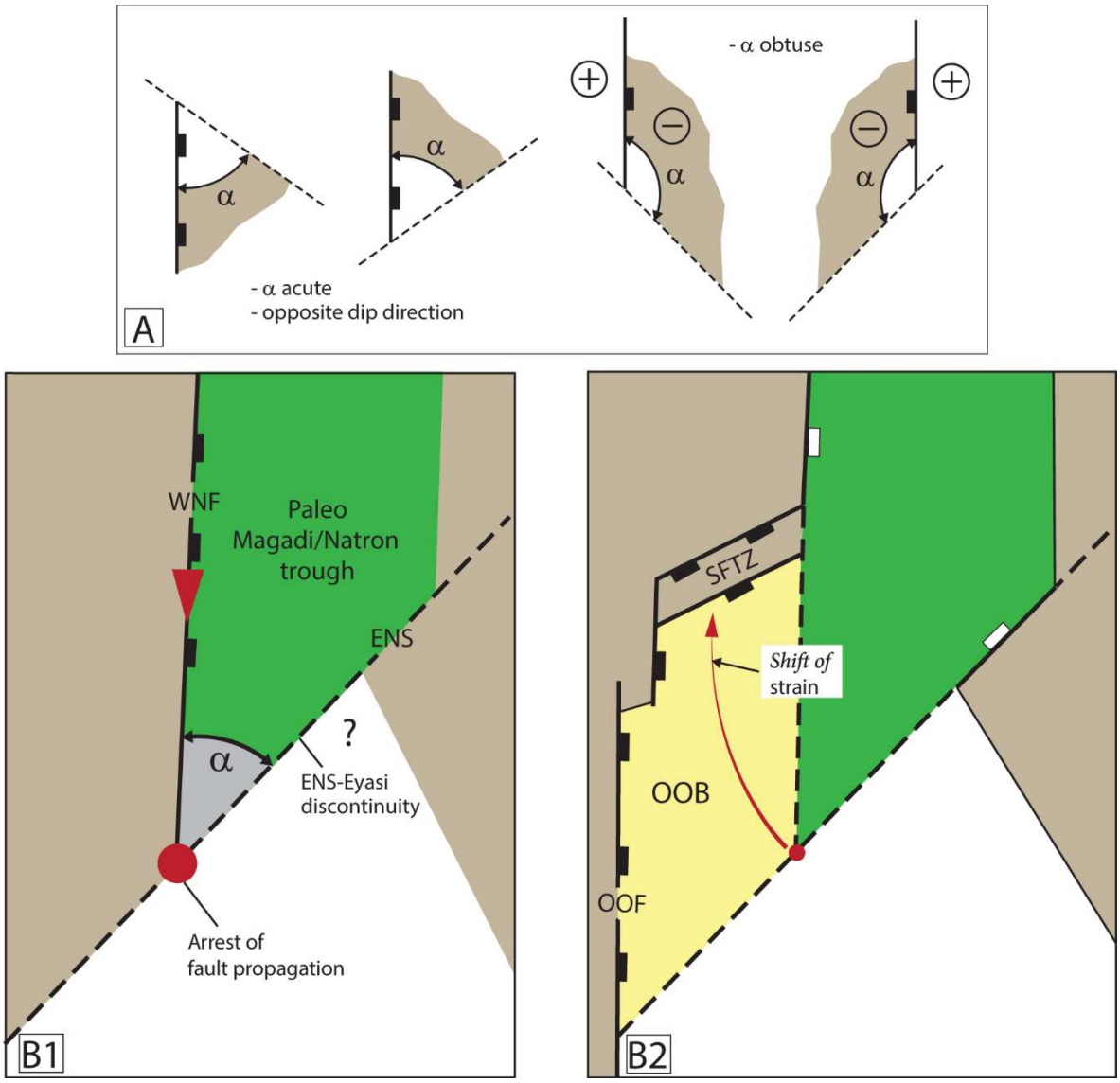

Fig. 3.14. Mechanisms of a dextrally-offset rift in South Kenya. A. Geometrical parameters related to an intersecting fault pattern, modified from Vétel & Le Gall (2006). B. Kinematic model implying: i) fault arrest (proto-Natron) against the ENS-Eyasi transverse discontinuity, and ii) shift of strain northwestwards via the STFZ transfer fault zone. According to this interpretation, the Lengitoto trachytes should extend as far south as the ENS-Eyasi discontinuity.

3.5.3.3 Off-axis magmatism and strain initiation in the Crater Highlands

With respect to the general southerly-propagating SKR-NTD rift framework, the Crater Highlands magmatic range is unusual in that: i) it occurs in an off-axis position, ii) its NE/SW trend is oblique to the submeridian rift axis, and iii) its magmatism is younging northeastwards from the Lemagrut (5 Ma), Sadiman (4 Ma)

and Ngorongoro (3.7 Ma) volcanoes to the Olmoti (1.6 Ma), Loolmalasin (1.2 Ma) and Embagai (0.5 Ma) edifices (Figs. 3.15A, B) (Bagdasaryan et al., 1973; McIntyre et al., 1974; Manega, 1993; Foster et al., 1997). Initiation of the off-axis magmatism in an outermost position, close to the exposed eastern edge of the Tanzanian craton, and its later migration towards the Natron rift axis to the NE (Le Gall et al., 2008; Mana et al., 2015), are here attributed to four interacting processes that involved (Figs. 3.15C, D): i) the deflection of ascending plume-related mantle melts beneath the thick lithospheric root of the craton, in agreement with the 3D-thermo-mechanical numerical models of Koptev et al. (2016, 2018) and the scenario applied to the Rungwe volcanic province further south, in relation with the Bangweulu craton (Grijalva et al., 2018), ii) their uprising along one topographic step at the base of the cratonic lithosphere, iii) the NE/SW channelling of lateral mantle flow by transverse zones of thinned lithosphere (Fletcher et al., 2018), and finally, iv) the migration of associated magmas through the upper crust along similarly-oriented weakness zones that guided the NE/SW alignment of eruptive centres at the surface in the Crater Highlands. The intricate infra-lithospheric pattern, with a number of transverse NE/SW thinned zones branching eastwards along a NS one (Fletcher et al., 2018), might continue beneath the Natron axial trough and connect with the ~50 km-wide infra-lithospheric antiform-like structure identified on receiver function modelling, parallel to the ENS-Eyasi linament (Fig. 3.12D) (Plasman et al., 2017). Lateral channelling of asthenospheric upwelling, at high angle (about 40°) to the submeridian SKR rift axis, implies a major decoupling between the two structural levels, with an increased control of the regional tectonic stress in the upper crust. A quite similar heterogeneous crust/lithosphere pattern is documented about off-axis magmatic ranges in the Ethiopian rift (Bastow et al., 2008; Corti, 2012; Rooney et al., 2014; Chiasera et al., 2018).

In terms of strain/magmatism relationships, magmatic segments are known to constitute potential strain nucleation sites in response to lithospheric thermal weakening (Benes & Davy, 1996; Callot et al., 2002). The location of the Eyasi fault, immediately SW of the Sadiman-Lemagrut-Ngorongoro zone of initial volcanism in

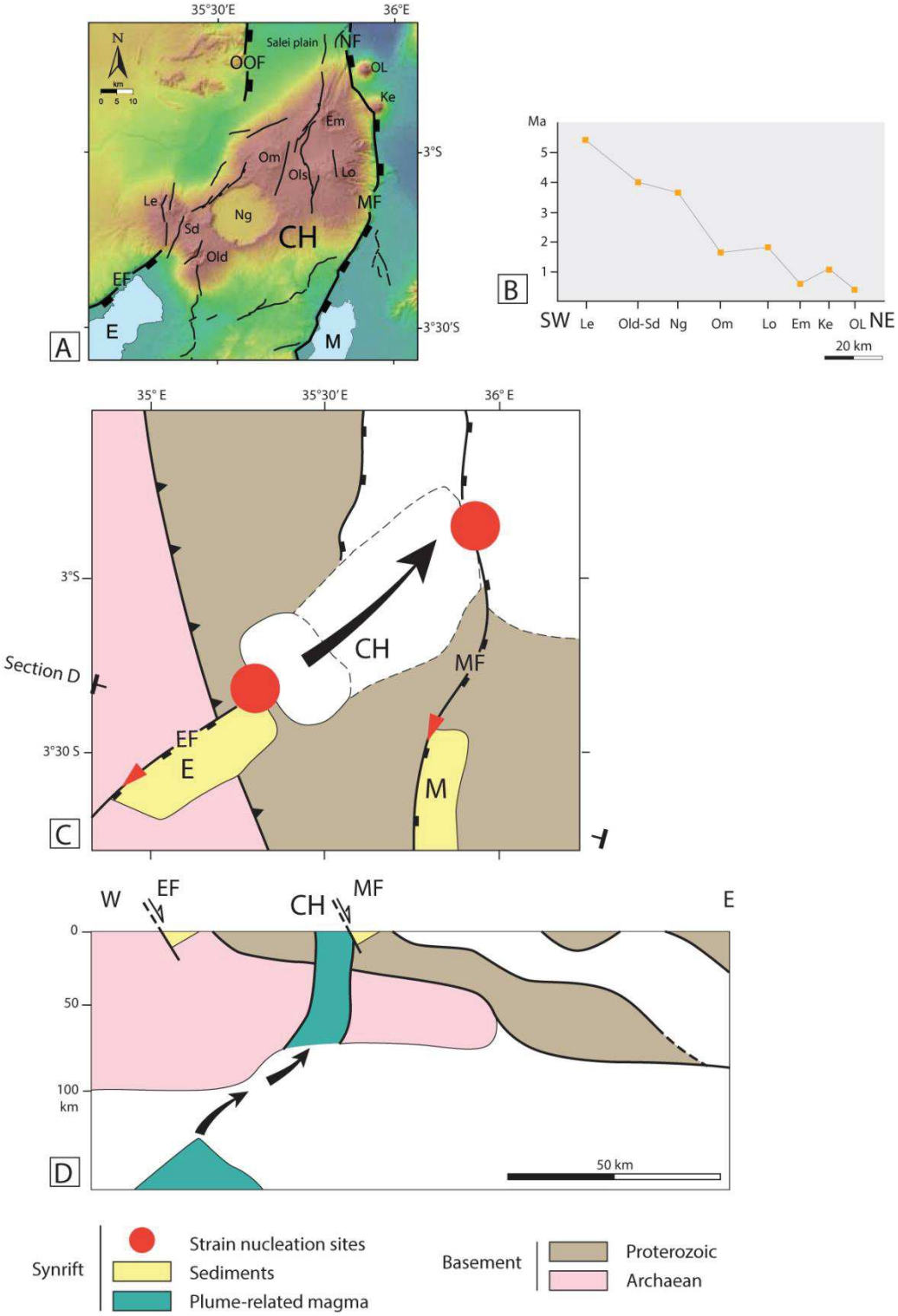

Fig. 3.15. Strain/magmatism relationships in the structurally-disturbed western part of the NTD. A. Major tectono-magmatic structures in the Eyasi and Crater Highlands areas, extracted from the SRTM-30 DEM in Fig. 2A. Same abbreviations as in Fig. 2A. B. Diagram showing the northeasterly younging of lavas in the Crater Highlands off-axis magmatic segment. C. Sketch map showing the location of strain nucleation sites (Eyasi and Manyara faults) with respect to northeasterly-migrating magmas in the Crater Highlands range. D. Vertical pathway of plume-related melt/magma at the base of the cratonic lithosphere (composite section).

the Crater Highlands, suggests that its nucleation <3.1 Ma ago (Foster et al., 1997) was triggered by thermal softening of the lithosphere during early magmatism (5-3 Ma) at the SW edge of the Crater Highlands (Fig. 3.15D). A similar process likely occurred later (<1.2 Ma) at the NE end of the volcanic range (Foster et al., 1997), and promoted the southerly propagation of the Natron bounding fault through the initially stiff ENS-Eyasi discontinuity (as suggested above), and then its linkage with the Manyara fault. Lastly, the density of monogenetic volcanic vents, further aligned at N70°E, in the Crater Highlands reflects a high degree of dyking at depth, and a relatively high amount of magma-assisted crustal extension, accordingly. That might account for the lack of tectonic extension along the NW flank of the Crater Highlands, in the low-relief Olbalbal depression, where morphological evidence for hard-linkage between the Eyasi and OOF rift-bounding faults are missing (Figs. 3.2A, B) (Ebinger et al.,1997).

3.6 Conclusions

New insights onto mechanisms of rifting at the South Kenya/North Tanzania boundary are here supplied by integrating, for the first time, in a coherent structural model: i) the relatively well-known Magadi-Natron axial trough, ii) the much more neglected Ol Doinyo Ogol offset block (both forming the SKR), and iii) the western part of the NTD, i.e. the Crater Highlands, Eyasi and Manyara rift arms. The main contributions of our work consist as follow:

- A two-stage rift model is applied to the 7 Ma-lasted development of the SKR by combining relative timing constraints deduced from the contrasting topography of the highly-segmented bounding fault network on SRTM-30 satellite imagery, and available age dataset of synrift volcanics.

- The early rift stage (7-1.3 Ma) is dominated by the formation of the highly-segmented proto-Magadi-OOB-Natron half-graben basins along the W/Nguruman-OOF dextrally offset bounding fault system and the STFZ transfer fault zone. 2D-magnetotelluric records demonstrate the crustal-scale nature of the OOF, whereas the atypical structure of the STFZ is argued from both its dimensions (40 x 25 km) and the kinematics of its

internal faults that all display prominent dip-slip displacement (without any evidence of a strike-slip component) in response to an intricate 3D-extensional context in the SKR at this early rift stage.

- The southerly propagation of early rifting is expressed by the diachronous emplacement of flood-type lavas from the Magadi (7 Ma-old Lengitoto trachytes) to the OOB (3.5 Ma-old Salei basalts) basins. However, earlier initiation of rifting (>7 Ma) is suggested by synrift packages, suspected to occur at depth beneath the Lengitoto axial lavas from geophysically-derived basement depths, and assumed to form pre-volcanic sedimentary basins by correlations with lacustrine limestone deposits that overlie crystalline basement rocks in the OOB, prior to the 3.5 Ma-old Salei basalts.

- Pronounced changes in the style of rifting occurred during the younger rift stage (1.3 Ma-Present) in response to the inward focussing of strain, and resulted in the easterly shift of border fault activity from the OOF to the Sambu-Natron fault, and from the W/ to E/Nguruman fault. Concomitantly, the resulting, linear and narrower Magadi-Natron half-graben was the locus of extensive flood-type volcanism (Magadi trachytes), in turn subsequently involved into a dense array of minor extensional inner faults.

-The quantitative analysis of both border and intra-rift fault populations indicates that >7 km (>10%) of upper crustal extension was recorded by the 7 Ma-lasted SKR rift. Most of it (>80%) was primarily accommodated by large displacement along the rift bounding fault network during a long-lived process that nearly spanned the lifetime of the evolving rift basins, with a marked decrease of activity through time. From the modest amount (<20%) of intra-rift fault-related extension experienced by the Magadi-Natron volcanic axial floor during recent rift stage (<1.3 Ma), it is thus argued that: i) inner faulting was not the dominant mode of strain accommodation in the SKR rift during inward focusing of strain, and ii) no sharp transition exists from border fault-to intra-rift fault-dominated strain accommodation over time. These results do not fit with kinematic models usually applied to more mature segments in the Kenya and Ethiopia magmatic rifts.

- With respect to the Neogene-Recent rift history of the SKR system as a whole, our work emphasizes the need to integrate the early rifting stage recorded by the OOB offset block in order not to bias any quantitative estimates of bulk strain (~25%).

- Displacement profiles of 140 analyzed inner faults show that most of them (85%) are asymmetric and typically characterize restricted faults. Their origin is rather attributed to strong interactions of closely-spaced faults in a mature rift system, than to any barrier effect exerted by the ENS basement salient on fault propagation, as initially envisaged.

- The rift model applied here further emphasizes the critical role of a first-order transverse basement discontinuity, i.e. the Archaean ENS-Eyasi structure, in influencing major structural and magmatic disturbances in the SKR-NDT system, as approaching the Tanzanian craton edge.

- Its possible influence on the early dextral offset of the SKR rift pattern is envisaged in two various ways, but, more importantly, its multistage rejuvenation under the EW extension resulted in a variety of diachronous tectono-magmatic events, possibly controlled by the thermal state of the crust/lithosphere. Indeed, brittle tectonics were strictly confined to its extremities (ENS and Eyasi fault networks), i.e. beyond the rift axis where the crust was colder, whereas both off-axis and axial dominantly magmatic processes took place along its central part through the rifted and hotter lithosphere. The extent of the Eyasi fault throughout the Archaean craton, in apparent contradiction with the structural inheritance concept evoked earlier, was possibly triggered by the thermal weakening of the lithosphere during the Crater Highlands magmatic event. The off-axis emplacement of the latter, as early as 5 Ma, is attributed to the combined effects of: i) the deflection of plume-related melts beneath the thick Tanzanian craton, ii) their ascending along a topographic step at the base of the lithosphere, and iii) the lateral pathway of the resulting magma through the crust, along ENS-Eyasi-type inherited transverse structures.

- Asthenospheric upwelling along transverse lithospheric thinned zones, at high angle (about 40°) to the submeridian SKR rift axis, implies a major decoupling level at depth, with an increasing control of the regional tectonic stress in the upper crust, as similarly

envisaged about off-axis magmatic ranges in the Ethiopian rift (Bastow et al., 2008; Corti, 2012; Rooney et al., 2014; Chiasera et al., 2018). In all cases, a first-order connection between crust and mantle magmatic processes did not exist.

Acknowledgments

This work is part of a PhD thesis program (Remigius Gama), partially funded by the French Ambassy in Dar Es Salaam. The help and assistance of the ambassadors and administrative staffs (both previous and current), Louise Crayssac, Philippe Boncour, Emelie Drillet, Pascale Camy, Frederique Reynes and Veronika Lengyel, are greatly appreciated. Field investigations (may 2017) in the Natron-OOB area have been funded by 'Geosciences Océan' UMR/CNRS 6538 Brest, IUEM Brest, Pr. Pascal Tarits (GO Brest) and Christel Tiberi (CNRS Montpellier, France) who are all warmly thanked.

3.7 References

Ackermann, R., Schlische, R., 1997. Anticlustering of small normal faults around larger faults, Geology, 25, 12, 1127-1130.

Agostini, A., Bonini, M., Corti, G., Sani, F., Manetti, P., 2011. Distribution of Quaternary deformation in the central Main Ethiopian Rift, East Africa: Deformation in the Main Ethiopian Rift. Tectonics, 30, doi.org/10.1029/2010TC002833.

Aki, K., 1979. Characterization of barriers on an earthquake fault. J. Geophys. Res., 84, B11, 6140-6148.

Albaric, J., Deverchère, J., Petit, C., Perrot, J., Le Gall, B., 2009. Crustal rheology and depth distribution of earthquakes: insights from the central and southern East African Rift System. Tectonophysics, 468, 1-4, 28-41.

Albaric, J., Perrot, J., Deverchère, J., Deschamps, A., Le Gall, B., Wambura, R., Petit, C., Tiberi, C., Sue, C., Songo, M., 2010. Contrasted seismogenic and rheological behaviours from shallow and deep earthquake sequences in the North Tanzanian Divergence, East Africa. J. Afr. Earth Sci., 58, 5, 799-811.

Albaric, J., Deverchère, J., Perrot, J., Jakovlev, A., Deschamps, A., 2014. Deep crustal earthquakes in North Tanzania, East Africa: Interplay between tectonic and magmatic processes in an incipient rift. Geochem. Geophys. Geosyst., 15, 374-394.

Baer, G., Hamiel, Y., Shamir, G., Nof, R., 2008. Evolution of a magma-driven earthquake swarm and triggering of the nearby Ol Doinyo Lengai eruption, as resolved by InSAR, ground observations and elastic modelling, East African Rift. Earth Planet. Sci. Lett., 272, 1-2, 339-352.

Bagdasaryan, G., Gerasimovskiy, V., Polykov, A., Gukasyan, R., 1973. Age of volcanic rocks in the rift zones of East Africa. Geokhimiya, 1, 84-90.

Baker, B., 1958. Geology of the Magadi area. Geol. Surv. Kenya Report, 42, 81 pp.

Baker, B., Williams, L., Miller, J., Fitch, F., 1971. Sequence and geochronology of the Kenya rift volcanics. Tectonophysics, 11, 191-215.

Baker, B., Wohlenberg, J., 1971. Structure and Evolution of the Kenya Rift Valley. Nature, 229, 538.

Baker, B., Mitchell, J., Williams, L., 1988, Stratigraphy, geochronology and volcanotectonic evolution of the Kedong-Naivasha-Kinangop region, Gregory Rift Valley, Kenya. J. Geol. Soc., London, 145, 107-116.

Bastow, I., Nyblade, A., Stuart, G., Rooney, T., Benoit, M., 2008. Upper mantle seismic structure beneath the Ethiopian hot spot: Rifting at the edge of the African low-velocity anomaly: Geochem. Geophys. Geosystems, 9, 12, doi.org/10.1029/2008GC002107.

Baudouin, C., Parat, F., Denis, C., Mangasini, F., 2016. Nephelinite lavas at early stage of rift initiation (Hanang volcano, North Tanzanian Divergence). Contrib. Mineral. Petrol., 171, 7, doi 10.1007/s00410-016-1273-5.

Benes, V., Davy, P., 1996. Modes of continental lithospheric extension: experimental verification of strain localization processes. Tectonophysics, 254, 69-87.

Beutel, E., van Wijk, J., Ebinger, C., Keir, D., Agostini, A., 2010. Formation and stability of magmatic segments in the Main Ethiopian and Afar rifts. Earth Planet. Sci. Lett. 293, 225-235.

Bialas, R., Buck, W., Qin, R., 2010. How much magma is required to rift a continent? Earth Planet. Sci. Lett. 292, 68-78.

Birt, C., Maguire, P., Khan, M., Thybo, H., Keller, G., Patel, J., 1997. The influence of pre-existing structures on the evolution of the southern Kenya Rift Valley. Evidence from seismic and gravity studies. Tectonophysics, 278, 211-242.

Bonini, M., Souriot, T., Boccaletti, M., Brun, J.P., 1997. Successive orthogonal and oblique extension episodes in a rift zone: Laboratory experiments with application to the Ethiopian Rift. Tectonics, 16, 347-362.

Burgmann, R., Pollard, D., Martel, S., 1994. Slip distributions on faults: effects of stress gradients, inelastic deformation, heterogeneous host-rock stiffness, and fault interaction. J. Struct. Geol., 16, 1675-1690.

Calais, E., d'Oreye, N., Albaric, J., Deschamps, A., Delvaux, D., Deverchère, J., Ebinger, C., Ferdinand, R., Kervyn, F., Macheyeki, A., Oyen, A., Perrot, J., Saria, E., Smets, B., Stamps, D., Wauthier, C., 2008. Strain accommodation by slow slip and dyking in a youthful continental rift, East Africa. Nature, 456, 783-787.

Callot, J.P., Geoffroy, L., Brun, J.P., 2002. Development of volcanic margins: three dimensional laboratory models. Tectonics, 21, doi: 10.1029/2001TC901019.

Cerling, T., Powers, D., 1977. Paleorifting between the Gregory and Ethiopian Rifts. Geology, 5, 441-444.

Chapman, G., Lippard, S., Martyn, J., 1978. The stratigraphy and structure of the Kamasia Range, Kenya Rift Valley. J. Geol. Soc., London, 135, 265-281.

Chiasera, B., Rooney, T., Girard, G., Yirgu, G., Grosfils, E., Ayalew, D., Mohr, P., Zimbelman, J., Ramsey, M., 2018. Magmatically-assisted off-rift extension-the case for broadly distributed strain accommodation. Geosphere, 14, 4, 1544-1563.

Chorowicz, J., 1989. Transfer and transform fault zones in continental rifts: examples in the Afro-Arabian rift system. Implications of crust breaking. J. Af. Earth Sci., 8, 203-214.

Corti, G., 2008. Control of rift obliquity on the evolution and segmentation of the main Ethiopian rift. Nature Geosci., 1, 258-262.

Corti, G., 2009. Continental rift evolution: From rift initiation to incipient break-up in the Main Ethiopian Rift, East Africa. Earth-Sci. Rev. 96, 1-53.

Corti, G., 2012, Evolution and characteristics of continental rifting: Analog modelling-inspired view and comparison with examples from the East African Rift System. Tectonophysics, 522-523, 1-33.

Cowie, P., Scholz, C., 1992. Displacement-length scaling relationship for faults: data synthesis and discussion. J. Struct. Geol., 14, 10, 1149-1156.

Crossley, R., 1979. The Cenozoic stratigraphy and structure of the western part of the Rift Valley in southern Kenya. J. Geol. Soc., London, 136, 4, 393-405.

Dawers, N., Anders, M., Scholz, C., 1993. Growth of normal faults: displacement-length scaling. Geology, 21, 1107-1110.

Dawers, N., Anders, M., 1995. Displacement-length scaling and fault linkage. J. Struct. Geol., 17, 607-614.

Dawson, J., 1992. Neogene tectonics and volcanicity in the North Tanzania sector of the Gregory Rift Valley: contrasts with the Kenya sector. Tectonophysics, 204, 1/2, 81-83.

Delvaux, D, Barth, A., 2010. African stress from formal inversion of focal mechanism data.Tectonophysics, 482, 105-128.

Ebinger, C., Deino, A., Drake, R., Tesha, A., 1989. Chronology of volcanism and rift propagation: Rungwe volcanic province, East Africa. J. Geoph. Res., 94, 15,785-15,803.

Ebinger, C., Casey, M., 2001. Continental breakup in magmatic provinces: an Ethiopian example. Geology, 29, 527-530.

Ebinger, C., Poudjom Djomani, Y., Mbede, E., Foster, A., Dawson, J., 1997. Rifting Archaean lithosphere: Eyasi-Manyara-Natron rifts, East Africa. J. Geol. Soc., London, 154, 947-960.

Fairhead, J., Mitchell, J., Williams, L., 1972. New K/Ar determinations on rift volcanics of S. Kenya and their bearing on age of rift faulting. Nature Physic. Scien., 238, 66-69.

Fletcher, A., Abdelsalam, M., Emishaw, L., 2018. Lithospheric controls on the rifting of the Tanzanian craton at the Eyasi basin, Eastern branch of the East African rift system. Tectonics, 37, 9, 2818-2832.

Foster, A., Ebinger, C., Mbede, E., Rex, D., 1997. Tectonic development of the northern Tanzanian sector of the East African Rift System. J. Geol. Soc., London, 154, 689-700.

Fritz, H., Tenczer, V., Hauzenberger, C., Wallbrecher, E., Muhongo, S., 2009. Hot granulite Nappes-Tectonic styles and thermal evolution of the Proterozoic granulite belts in East Africa. Tectonophysics, 477, 3-4, 160-173.

Gawthorpe, R., Hurst, J., 1993. Transfer zones in extensional basins: their structural style and influence on drainage development and stratigraphy. J. Geol. Soc., London, 150, 1137-52.

Green, W., Achauer, U., Meyer, R., 1991. A three-dimensional seimic image of the crust and upper mantle beneath the Kenya rift. Nature, 354, 199-203.

Grijalva, A., Nyblade, A., Homman, K., Accardo, N., Gaherty, J.B., Ebinger, C., et al., 2018. Seismic evidence for plume-and craton-influenced upper mantle structure beneath the Northern Malawi rift and the Rungwe volcanic province, East Africa. Geochem. Geophys. Geosyst., 19, 10, 3980-3994.

Hautot, S., Tarits, P., Wheeler, K., Le Gall, B., Tiercelin, J.J., Le Turdu, C., 2000. Deep structure of the Baringo Rift Basin (central Kenya) from three-dimensional magnetotelluric imaging: implications for rift evolution. J. Geophys. Res., 105, 23,493-23,518.

Ibs-von Seht, M., Blumenstein, S., Wagner, R., Hollnack, D., Wohlenberg, J., 2001. Seismicity, seismotectonics and crustal structure of the southern Kenya Rift-new data from the Lake Magadi area. Geophys. J. Intern., 146, 2, 439-453.

Isaac, G., 1965. The stratigraphy of the Peninj Beds and the provenance of the Natron Australopithecine mandible. Quaternaria 7, 101-130.

Isaac, G., Curtis, G., 1974. Age of early Acheulian industries from the Peninj Group, Tanzania. Nature, 249, 624-627.

Isola, I., Mazzarini, F., Bonini, M., Corti, G., 2014. Spatial variability of volcanic features in Early-stage rift settings: the case of the Tanzania Divergence, East African rift system. Terra Nova, 26, 6, 461-468.

Kattenhorn, S., 2004. Strike-slip evolution of Europa from tailcrack geometries. Icarus, 172, 582-602.

Keir, D., Bastow, I., Corti, G., Mazzarini, F., Rooney, T., 2015. The origin of along-rift variations in faulting and magmatism in the Ethiopian Rift. Tectonics, 34, 3, 464-477.

Keir, D., Ebinger, C., Stuart, G., Daly, E., Ayele, A., 2006. Strain accommodation by magmatism and faulting as rifting proceeds to breakup: Seismicity of the Northern Ethiopian Rift. J. Geophys. Res., 111, B05314, doi: 10.1029/2005JB003748.

Keranen, K., Klemperer, S., Gloaguen, R., and the EAGLE Working Group. 2004. Three-dimensional seismic imaging of a protoridge axis in the Main Ethiopian Rift. Geology, 32, 949-952.

Kim, Y., Sanderson, D., 2005. The relationship between displacement and length of faults: a review. Earth-Sci. Rev., 68, 317-34.

King, B., 1978. Structural evolution of the Gregory rift valley. In: Bishop, W. (Ed.), Geological Background to Fossil Man, 6, Geol. Soc., London, 29-45.

Koptev, A., Burov, E., Calais, E., Leroy, S., Gerya, T., Guillou, L. Cloetingh, S., 2016. Contrasted continental rifting via plume-craton interaction: Applications to Central East African rift. Geoscience Frontiers, 7, 2, 221-236.

Koptev, A., Cloetingh, S., Gerya, T., Calais, E., Leroy, S., 2018. Non-uniform splitting of a single mantle plume by double cratonic keels: Insights into the origin of central and southern East African Rift System. Terra Nova, 30, 2, 125-134.

KRISP Working Group, 1991. The Kenya rift: pure shear extension above a mantle plume. Nature, 345, 223-227.

Lambert, C., Muirhead, J., Ebinger, C., Tiberi, C., Roecker, S., Ferdinand-Wambura, R., Kianji, G., Mulibo, G., 2014. Lower crustal seismicity, volatiles, and evolving strain fields during the initial stages of cratonic rifting. AGU, Fall Meeting, abs. T53B-4678.

Lee, H., Fischer, T., Muirhead, J., Ebinger, C., Kattenhorn, S., Sharp, Z., Kianji, G., Sano, Y., Takahata, N., 2017. Incipient rifting accompanied by the release of subcontinental lithospheric mantle volatiles in the Magadi and Natron basin, East Africa. J. Volcanol. Geotherm. Res., doi:10.1016/j.jvolgeores.2017.03.017.

Le Gall, B., Tiercelin, J.J., Richert, J.P., Gente, P., Sturchio, N., Stead, D., Le Turdu, C., 2000. A morphotectonic study of an extensional fault zone in a magma-rich rift: The Baringo Trachyte fault system, central Kenya Rift. Tectonophysics, 320, 87-106.

Le Gall, B., Gernigon, L., Rolet, J., Ebinger, C., Gloaguen, R., Nilsen, O., Dypvik, H.,

Deffontaines, B., Mruma, A., 2004. Neogene-Holocene rift propagation in central Tanzania: morphostructural and aeromagnetic evidence from the Kilombero area. Bull. Geol. Soc. Am., 116, 490-510.

Le Gall, B., Vétel, W., Morley, C., 2005. Inversion tectonics during continental rifting: The Turkana Cenozoic rifted zone, northern Kenya. Tectonics, 24, TC2002, doi: 10.1029/2004TC001637.

Le Gall, B., Nonnotte, P., Rolet, J., Benoit, M., Guillou, H., Mousseau-Nonnotte, M., Albaric, J., Deverchère, J., 2008. Rift propagation at craton margin: distribution of faulting and volcanism in the North Tanzanian Divergence (East Africa) during Neogene times. Tectonophysics, 448, 1-19.

Le Turdu, C., Richert, J.P., Xavier, J.P., Renaut, R., Tiercelin, J.J., Rolet, J., Lezzar, K., Coussement, C., 1999. Influence of preexisting oblique discontinuities on the geometry and evolution of extensional fault patterns: Evidence from the Kenya Rift using SPOT imagery. In Morley, C., (ed.), Geoscience of Rift Systems. Evolution of East Africa. AAPG. Studies in Geology, 44, 173-191.

Lezzar, K., Tiercelin, J.J., Cohen, A., Reynolds, D., Le Gall, B., Scholz, C., 2002. Control of normal fault interaction on the distribution of major Neogene sedimentary depocenters, Lake Tanganyika, East African rift. AAPG. Bull., 86, 1027-1059.

Macheyeki, A., Delvaux, D., De Batist, M., Mruma, A., 2008. Fault kinematics and tectonic stress in the seismically active Manyara-Dodoma Rift segment in Central Tanzania- Implications for the East African Rift. J. Af. Earth Sc., 51, 4, 163-188.

Mana, S., Furman, T., Turrin, B., Feigenson, M., Swisher, C., 2015. Magmatic activity across the East African North Tanzanian Divergence Zone. J. Geol. Soc., London, 172, 368-389.

Manega, P. 1993. Geochronology, geochemistry and isotopic study of the Plio-Pleistocene hominid sites and the Ngorongoro Volcanic Highland in northern Tanzania. PhD. thesis, Univ. Colorado.

Manighetti, I., King, G., Sammis, C., 2004. The role of off-fault damage in the evolution of normal faults. Earth Planet. Sci. Lett., 217, 399-408.

McClay, K., Dooley, T., Whitehouse, P., Mills, M., 2002. 4-D evolution of rift systems: insights from scaled physical models. AAPG. Bull., 86, 935-959.

McConnell, R., 1972. Geological development of the rift system of eastern Africa. Geol., Soc. Am., Bull., 83, 2549-2572.

McHenry, L., Luque, L., Gomez, J., Diez-Martın, F., 2011. Promise and pitfalls for characterizing and correlating the zeolitically altered tephra of the Pleistocene Peninj Group, Tanzania. Quat. Res., 75, 3, 708-720.

McIntyre, R., Mitchell, J., Dawson, J., 1974. Age of fault movements in the Tanzanian sector of the East African Rift system. Nature, 247, 354-356.

Michon, L., Sokoutis, D., 2005. Interaction between structural inheritance and extension direction during graben and depocentre formation: an experimental approach. Tectonophysics, 409, 125-146.

Ministry of Energy and Regional development of Kenya, 1987. Geological map of Kenya, 1:1, 000 000. (Eds) BEICIP, Rueil-Malmaison, France.

Möller, A., Mezger, K., Schenk, V., 2000. U-Pb dating of metamorphic minerals: Pan-African metamorphism and prolonged slow cooling of high pressure granulites in Tanzania, East Africa. Precambrian Res., 104, 123-146.

Morley, C., Wescott, W., Stone, D., Harper, R., Wigget, S., Karanja, F., 1992. Tectonic evolution of northern Kenya Rift. J. Geol. Soc., 149, 333-348.

Morley, C., 1999. Patterns of displacement along large normal faults: Implications for basin evolution and fault propagation, based on examples from east Africa. AAPG. Bull., 83, 613-634.

Mosley, P., 1993, Geological evolution of the late Proterozoic Mozambique Belt of Kenya.Tectonophysics, 221, 223-250.

Mruma, A., Ernst, R., Soderland, U., 2014. Evidence for ca. 1.775 Ma large igneous province (LIP) in the Tanzanian Craton. Abst., 25th Coll. Af. Geol., Dar es Salaam, Tanzania, p. 9.

Mugisha, F., Ebinger, C., Strecker, M., Pope, D., 1997. Two-stage rifting in the Kenya Rift: Implications for half-graben models. Tectonophysics, 278, 61-81.

Muirhead, J., Kattenhorn, S., Lee, H., Fischer, T., Mana, S., Turrin, B., Kianji, G., Dindi, E., Stamps, D., 2016. Evolution of upper crustal faulting assisted by magmatic volatile release during early-stage continental rift development in the East African Rift. Geosphere, 12, 1670, doi:10.1130/GES01375.1.

Muirhead, J., Kattenhorn, S., 2018. Activation of preexisting transverse structures in an evolving magmatic rift in East Africa. J. Struct. Geol., 106, 1-18.

Muirhead, J.,Lachlan, J., Wright, C., Sholz, C., 2019. Rift evolution in regions of low magma input in East Africa. Earth Planet. Sc., Lett., 506, 332-346.

Mulibo, G., Nyblade, A., 2016. The seismotectonics in Southeastern Tanzania: Implications for propagation of the eastern branch of the East African Rift. Tectonophysics, 676, 20-30.

Nicol, A., Walsh, J., Watterson, J., Gillespie, P., 1996. Fault size distributions-are they really Power-law? J. Struct. Geol., 18, 2-3, 191-197.

Nonnotte, P., Guillou, H., Le Gall, B., Benoit, M., Cotten, J., Scaillet, S., 2008. New K-Ar age determinations of Kilimanjaro volcano in the North Tanzanian diverging rift, East Africa. J. Volcan. Geoth. Res., 173, 1-2, 99-112.

O'Donnell, J., Adams, A., Nyblade, A., Mulibo, G., Tugume, F., 2013. The uppermost mantle shear wave velocity structure of eastern Africa from rayleigh wave tomography: constraints on rift evolution. Geophys. J. Int., 194, 2, 961-978.

Paslick, C., Halliday, A., James, D., Dawson, J., 1995. Enrichment of the continental lithosphere by OIB melts: Isotopic evidence from the volcanic province of northern Tanzania. Earth Planet., Sci., Lett., 130, 109-126.

Peacock, D., 1991. Displacements and segment linkage in strike-slip fault zones. J. Struct. Geol., 13, 1025-1035.

Peacock, D., Sanderson, D., 1991. Displacements, segment linkage and relay ramps in normal fault zones. J. Struct. Geol., 13, 721-733.

Plasman, M., Tiberi, C., Ebinger, C., Gautier, S., Albaric, J., Peyrat, S., Deverchère J., Le

Gall, B. et al., 2017. Lithospheric low-velocity zones associated with a magmatic segment of the Tanzanian Rift, East Africa. Geophys. J. Int., 210, 1, 465-481.

Pollard, D., Segall, P., 1987. Theoretical displacements and stresses near fractures in rock: with applications to faults, joints, veins, dikes, and solution surfaces. In: Atkinson, B. (ed.), Fracture Mechanics of Rock. Acad. Press, London, 277-349.

Ring, U., 1994. The influence of preexisting structure on the evolution of the Cenozoic Malawi rift (East African rift system). Tectonics, 13, 313-326.

Rooney, T., Bastow, I., Keir; D., Mazzarini, F., Movsesian, E. et al., 2014. The protracted development of focused magmatic intrusion during continental rifting. Tectonics, 33, 6, 875-897.

Saria, E., Calais, E., Stamps, D., Delvaux, D., Hartnady, C., 2014. Present-day kinematics of the East African Rift. J. Geophys. Res., 119, 3584-3600.

Scholz, C., Cowie, P., 1990. Determination of total strain from faulting using slip-measurements. Nature, 346, 837-839.

Shackleton, R., 1993. Tectonics of the lower crust: a view from the Usambara Mountains, NE Tanzania. J. Struct. Geol., 15, 663-671.

Sherrod, D., Magigita, M., Kwelwa, S., 2013. Geologic map of Oldonyo Lengai and surroundings, Arusha region, United Republic of Tanzania. U.S. Geol. Surv. Open-File Report 2013-1306, 1:50,000, 50 p.

Sippel, J., Meessen, C., Cacace, M., Mechie, J., Fishwick, S., Heine, C., Scheck, M., Strecker, M., 2017. The Kenya rift revisited: insights into lithospheric strength through data-driven 3D gravity and thermal modelling. J. Geophys. Res., Solid Earth, 8, 1, 45-81.

Smith, M., Mosley, P., 1993. Crustal heterogeneity and basement influence on the development of the Kenya Rift, East Africa. Tectonics, 12, 591-606.

Thomas, R., Spencer, C., Bushi, A., Baglow, N., Boniface, N., de Kock, G., et al., 2016. Geochronology of the central Tanzania craton and its southern and eastern orogenic margins. Precambrian Res., 277, 47-67.

Thybo, H., Maguire, P., Birt, C., Perchuc, E., 2000. Seismic reflectivity and magmatic underplating beneath the Kenya Rift. Geophys. Res. Lett., 27, 2745-2748.

Vétel, W., Le Gall, B., Walsh, J., 2005, Geometry and growth of an inner rift fault pattern: The Kino Sogo Fault Belt, Turkana Rift (North Kenya). J. Struct. Geol., 27, 2204-2222.

Vétel, W., Le Gall, B., 2006. Dynamics of prolonged continental extension in magmatic rifts: the Turkana Rift case study (North Kenya). In: Yirgu, G., Ebinger, C., Maguire, P. (eds.), The Structure and Evolution of the East African Rift System in the Afar Volcanic Province. Geol. Soc. London, Sp. Pub., 259, 211-235.

Walsh, J., Watterson, J., 1988. Analysis of the relationship between displacements and dimensions of faults. J. Struct. Geol., 10, 239-247.

Wheeler, W., Rosendahl, B., 1994. Geometry of the Livingstone mountains border fault, Nyasa (Malawi) rift, East Africa. Tectonics 13, 303-312.

Wichura, A., Bousquet, R., Oberhänsli, R., Strecker, M., Trauth, M., 2010. Evidence for Middle Miocene uplift of the East African Plateau. Geology, 38, 6, 543-546.

Weinstein, A., Oliva, S., Ebinger, C., Roecker, S., Tiberi, C., Aman, M., Lambert, C., Witkin, E., Albaric, J., Gautier, S., Peyrat, S., 2017. Fault-magma interactions during early continental rifting: seismicity of the Magadi-Natron-Manyara basins, Africa. Geochem. Geophys. Geosyst., doi.org/10.1002/2017GC007027.

Wright, T., Ebinger, C., Biggs, J., Ayele, A., Yirgu, G., Keir, D., Stork, A., 2006. Magma-maintained rift segmentation at continental rupture in the 2005 Afar dyking episode. Nature, 442, 7100, 291-294.

Wu, H., Pollard, D., 1995. An experimental study of the relationship between joint spacing and l ayer thickness. J. Struct. Geol., 17; 887-905.

Chapitre 4

Réseau de drainage et tectonique verticale des compartiments de socle bordiers.

Ce chapitre présente un article en cours d'écriture sur l'étude des réseaux de drainage de la DNT. Ce travail se concentre sur le flanc ouest du rift sud Kenya-nord Tanzanie, comprenant les blocs : Nguruman, Sonjo, Oldoinyo Ogol, Eyasi et Manyara-Mbulu. Chaque bloc présent des caractéristiques uniques notamment sur la propagation du rift et spécialement sur la formation de la divergence nord Tanzanienne (DNT).

A partir des modèles numériques de terrain SRTM 30 m nous avons extrait 25 bassins versants pour lesquels les réseaux de drainage ont étudiés. L'analyse porte à la fois sur l'étude des bassins versants et des réseaux de drainage. Pour les bassins versants, nous avons calculé des indices morpho-métriques et réalisé des profils le long des différentes rivières pour évaluer notamment les ruptures de pente. Notre interprétation tectonique intègre à la fois de l'information géologique et structurelle existante ainsi que des données géochronologiques afin de faire une interprétation tectonique.

Chapitre 4

To be submitted

Drainage pattern and multi-stage rift-flank uplift in the North Tanzanian Divergence, East Africa.

Remigius Gama[1, 3*], Nicolas Loget[2], Bernard Le Gall[1], Nelson Boniface[3]

[1]UMR 6538 Géosciences Océan, IUEM, Brest University, France

[2]UMR 7193, ISTeP, Sorbonne university, Paris, France

[3] Department of Geology, University of Dar es Salaam, Tanzania

* Corresponding author, Remigius Gama (remmygama@yahoo.com)

Abstract

The south Kenya rift (SKR) is well known as presenting a major segment of the eastern branch of the East African rift (EAR) in which the rift propagates southward and so in the process it is younging southwards. As the half-graben SKR (Magadi trough) passes 1.5°S it starts to diverge and thus enlarging from a classical ~ 60 km wide south Kenya rift to a wider north Tanzanian rift. This southward propagation results into several faulted, elevated blocks in the western flank and so resulting into the major diverging arm with a remarkable topography. This resulting topography provided us with an opportunity to study the organization of drainage networks and their relationship to tectonic uplift. We used Digital Elevation Models (SRTM-30 m) to first extract 25 water catchments that cover five blocks namely Nguruman-Loita (NL), Sonjo transfer fault zone (STFZ), Oldoinyo Ogol Block (OOB), Eyasi and Manyara-Mbulu block each with different topographical characteristics and then drainage networks were also extracted and analysed. Our analysis of drainage is mainly based on the characteristisc of drainage networks in relation to structures mainly faults, lithological contrasts (foliations) and magmatic centers. Our results are complemented with existing chronological data to propose a two stage-flank uplift which is i) the first uplift-stage dated between 7 and 3.5 Ma, in which rifting was focused in the northern 3 blocks (i.e. NL, STFZ and OOB) and

ii) the second stage which is presented by the time less than 3.5 Ma in which uplift was focused in the southern end and the eastern flanks of the Natron and Manyara scarps.

4.1 Introduction

On the earth's surface, there is a competition between internal tectonic and external forces whereby fluvial system mainly dictates landscape evolution by shaping the topographic relief and mountain ranges (Howard, 1994; Whipple and Tucker, 1999a). Any tectonic process or climatic forcing lead into the shift of equilibrium from steady state to disequilibrium state corresponding to a transient state (Giletycz et al., 2015; Mathew et al., 2016; Montgomery and Foufoula-Georgiou, 1993; Willgoose, 1994). In active continental rifts like the East African Rift System, active continental extension zones lead into formation of characteristic landscapes (Flores-Prieto et al., 2015). In such regions, extension is associated with fault formations whose growth, interaction and linkage has an effect on the uplift and subsidence and therefore affect the development of rift topography and configuration of drainage networks and depositional systems (e.g., Cowie et al., 2006; Duffy et al., 2015; Gawthorpe and Leeder, 2008; Leeder and Jackson, 1993). In regions of active deformation, the geometry and evolution of drainage systems are sensitive to uplift and climatic patterns and therefore can record tectonic and structural evolution (e.g., Clark et al., 2004; Cox, 1994; Howard, A.D., 1967; Jackson and Leeder, 1994; Kirby and Whipple, 2012; Kirby and X. Whipple, 2001; Seeber and Gornitz, 1983).

Tectonic processes such as folding and faulting control the drainage patterns and accelerate river incision, basin asymmetries, drainage geometry and river diversions (Cox, 1994; Mahmood and Gloaguen, 2012). Due to this, in tectonically active regions, the impact of tectonic activities on landscapes and geomorphic processes can quantitatively and qualitatively be analysed through the study of drainage systems (Bahrami, 2013; Delcaillau et al., 2006; Jackson et al., 1998; Joseph Mathew, 2016; Ramsey et al., 2008; Sung and Chen, 2004). Such analyses are done by interpreting drainage anomalies that are the product of active tectonic deformation and bedrock resistance (Clark et al., 2004; Howard, A.D., 1967; Zernitz, 1932). The aforementioned drainage anomalies are the result of deviation of course of present-day river network from their common regional patterns (Joseph Mathew, 2016).

Geomorphological features such as linear valleys, ridgelines, steep slopes and tilting of terrain result from tectonic motions (Jordan, 2003). Tectonic deformation can geomorphically be described with the aid of geomorphic markers, i.e. identifiable displaced features (Burbank and Anderson, 2012), such description can either be qualitative or quantitative. In such studies, fluvial parameters known as geomorphic indices are used to analyse spatially distributed landscapes in order to compare the level of tectonic activities in different landscapes (Joseph Mathew, 2016; Keller and Pinter, 2002).

In half-graben rift systems it has been shown that the response of topography and drainage networks is mainly constrained in particular: i) the spatial configuration of catchments and depositional systems (e.g., Leeder and Jackson, 1993; Jackson and Leeder, 1994; Eliet and Gawthorpe, 1995; Gawthorpe and Leeder, 2000; Archer, 2006, Cowie et al., 2006; Duffy et al., 2014); ii) how individual fault segments control the size, spacing and morphology of catchments along them (Ellis et al., 1999; Allen and Densmore, 2000; Densmore et al., 2004; Duffy et al., 2014;); iii) how sediment dispersal patterns are influenced by relays and transfer zones between fault and rift segments (e.g., Gawthorpe and Hurst, 1993; Peacock et al., 2000; Trudgill, 2002; Densmore et al., 2003); iv) how distributed normal faulting control the evolution of topography and drainage in regions of multiple active and closely spaced fault segments such as Corith rift in Greece (Duffy et al., 2014) or v) how the drainage systems evolve along the rift shoulders (tilted blocks) such as in Red Sea and Gulf of Aden (Frostick and Reid, 1989) or in the Southwestern Barents Sea (Marin et al., 2018).

In the East African Rift (EAR), an analysis of morphology and hydrography of the rift margin was recently conducted by Molin & Corti, 2015. They studied the reorganization of drainage networks as influenced by extensional tectonic setting in the Central Main Ethiopian Rift mainly by using DEMs in which they established how drainage types and anomalies are affected by recent tectonic activities. Further south of the EAR in the Turkana rift in northern Kenya, Vétel et al., (2004) detected drainage network anomalies that were then used to characterize the geometry of inferred fault structures in a region where the rift morphology is not well-marked.

Cases where a narrow linearly propagating rift diverges into a wider double fault rift system in few million years time are rare.

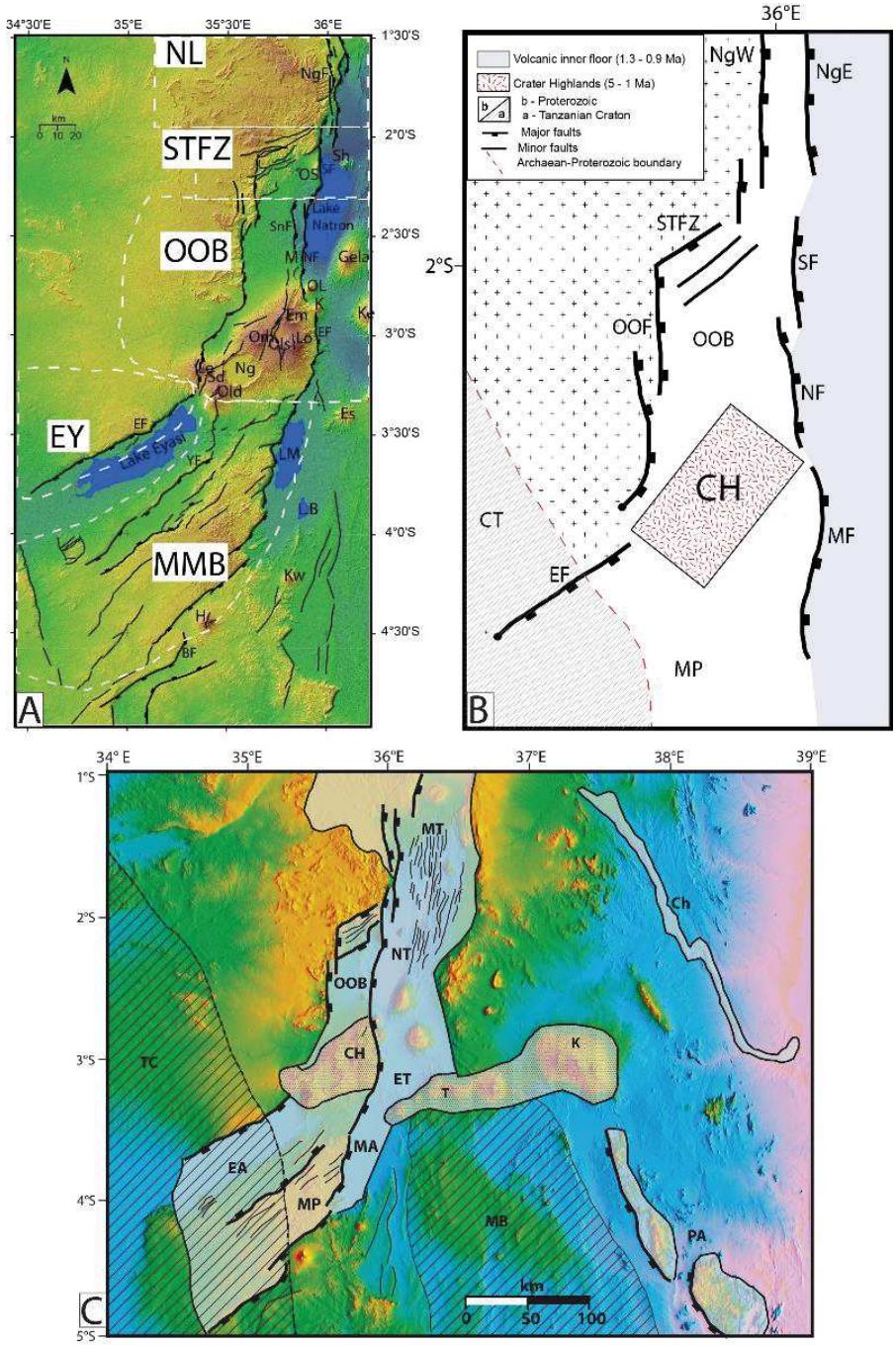

Fig. 4.1. Main structures of the South Kenya rift (SKR) and the western flank of the North Tanzania Divergence (NTD). A. SRTM-30 m showing the five main topographical domains used to analyse the drainage network systems. B. Simplified structural sketch illustrating the main structural domains of the NTD and C. Traces of both SKR and NTD rift trough patterns (modified from Gama et al., submitted). Abbreviations: CH., Crater Highlands; EA., Eyasi rift arm; ET., Engaruka trough; K., Kilimanjaro volcano; MA., Manyara rift arm; MB., Masai block; MP., Mbulu plateau; MT. Magadi trough; NT., Natron trough; OOB., Ol Doinyo Ogol block; PA., Pangani rift arm; T., Tarosero volcano. The dashed lines is the trace of the Tanzanian craton margin (W) with Proterozoic belts (E); SnF., Sanjan Fault; EF., Engaruka fault; BF., Balangida fault; OS., Oldoinyo Sambu; Sh., Shompole; Mo., Monsonik; OL., Oldoinyo Lengai; K., Kerimasi; Ke., Ketumbeine; Em., Embagai; Om., Olmoti; Ols., Olsirwa; Lo., Lolmalasin; Le., Lemagrut; Sd., Sadiman; Old., Oldeani; Ng., Ngorongoro Crater; Es., Essimingor; Kw., Kwaraha; H., Hanang; LB., Lake Burungi.

The transition from N-S propagating Magadi-Natron rift to a wider double faulted rift is marked by a series of transfer NE-SW striking faults here referred to as Sonjo fault transfer zone (SFTZ) which are superimposed on basement rocks (fig.4.1a and 4.1b). In a polyphased rift system where the topography is supposed to have resulted from both, the interaction between fault processes and magmatic processes as evidenced by the presence of both faulted blocks and volcanic cones. Such interaction may induce anomalies into the drainage networks as they adjust to both, fault propagation and magmatic actions. The western arm of the North Tanzanian Divergence (NTD) which include Nguruman-Loitta hills (NL) located in NW-Magadi rift, Sonjo transfer fault zone (STFZ) Oldoinyo Ogol block (OOB) which includes the Ngorongoro volcanic highlands, Eyasi block (EY) and Manyara-Mbulu block (MMB) are good representatives of such an interaction in a polyphased rift system of segmented fault systems which can be used as a case study for the study of interaction of topography and drainage organization as a response to multi-phase fault propagation.

This approach is applied here to atypical rift zone at the southern extremity of the eastern branch of the East African rift, in Northern Tanzania where the rift splits from a classical 50-60 km wide N-S rift valley to an approximately 200 km wide diverging rift pattern comprised of three rift arms, Magadi-Natron, Eyasi, and Pangani (fig.4.1c). This wider zone forms the core of the North Tanzanian Divergence (NTD), Dawson, 1992; Le Gall et al., 2008. The western sector of the NTD is comprised of the Oldoinyo Ogol sector, Ngorongoro Volcanic Highlands, Eyasi-Mbulu sector and Manyara. Major escarpments in the western sector of the NTD are the southern Nguruman, Natron, Oldoinyo Ogol, Manyara and Eyasi fault (fig. 4.1a).

The present-day morphostructural pattern of the NTD is dominated by (1) the submeridian, fault-bounded, Magadi-Natron axial half-graben and its bounding fault-scarp system to the west in South Kenya and (2) the Eyasi (NE-SW) and Manyara (NS) diverging rift arms in the NTD. In first approximation, relatively well preserved topographic profiles suggest relatively young rift structures (fig. 4.2). Ages of the onset of faulting are in the range between 7 and 1.0 Ma, < 3.0 Ma (Eyasi), 1.0 Ma (Natron), Manyara (1.5 Ma) Foster et al., 1997; MacIntyre et al.,1974). Earlier fault-activity is inferred to have occurred along more eroded fault-scarps, such as the West Nguruman master fault that bounds the Magadi segment or the Ol Doinyo Ogol fault (OOF) on the

western edge of the Ol Doinyo Ogol offset and uplifted block. Ages of the onset of displacement along these master faults are indirectly constrained by the dating of their hanging-wall volcanic sequences (6.9 Ma Kirikiti/Langitoto (Baker, 1958; Crosley, 1979; Birt et al., 1997) and OOB basalts (3.1 Ma) (Foster 1997) that only provide upper limits for the age of faulting.

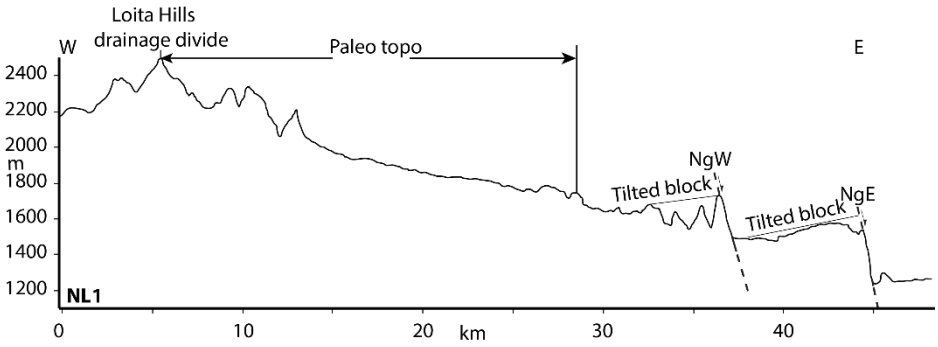

Fig. 4.2. E-W topographic profile showing along the Nguruman-Loita hills a remarkable morphology of the Nguruman faults (NgW and NgE), tilted block which are a result of vertical uplift movement and envelop of the paleo-topo. Vertical exaggeration X10. Location in Fig. 4.5.

Therefore, uncertainties exist about the exact temporal pattern of strain in the South Kenya Rift (SKR) and NTD system. Each of these inferred faulting event likely resulted in significant rift-flank uplift, in turn possibly associated to an intricate pattern of basement tilted surfaces along both rift-parallel (NS) and transverse (NE-SW) normal faults. The aim of this study is (1) to define the spatial distribution and the geometrical attributes of the river drainage network extracted from the basement bounding relief and (2) to elaborate a multistage kinematic rift model further completed by tectonic data from the adjoining and inferred younger axial trough. We address above objective through geomorphological analysis of the eastern flank of the NTD thanks to Digital Elevation Models (SRTM-DEM). We focus our approach especially on how fluvial networks evolve and reorganize due to tectonic constrains in this sector of the rift.

4.2 Geological and geomorphological setting

The eastern branch of the East African Rift System (EARS) formed preferentially to the Archaean Tanzanian craton and its initiation was controlled by the Pan-African lithosphere which imparted strong N-S fabrics to crustal rocks (Le Gall et al., 2008;

Plasman et al., 2017; Smith, M, and Mosley, P, 1993). The Nguruman - Loita hill, Sonjo transfer fault zone, Oldoinyo Ogol block (OOB), Eyasi block (Ey) and Manyara – Mbulu block (fig.4.3) are part of the NTD in which faulting and magmatism are less than 7 Ma (Baker, 1986; Mana et al., 2012).

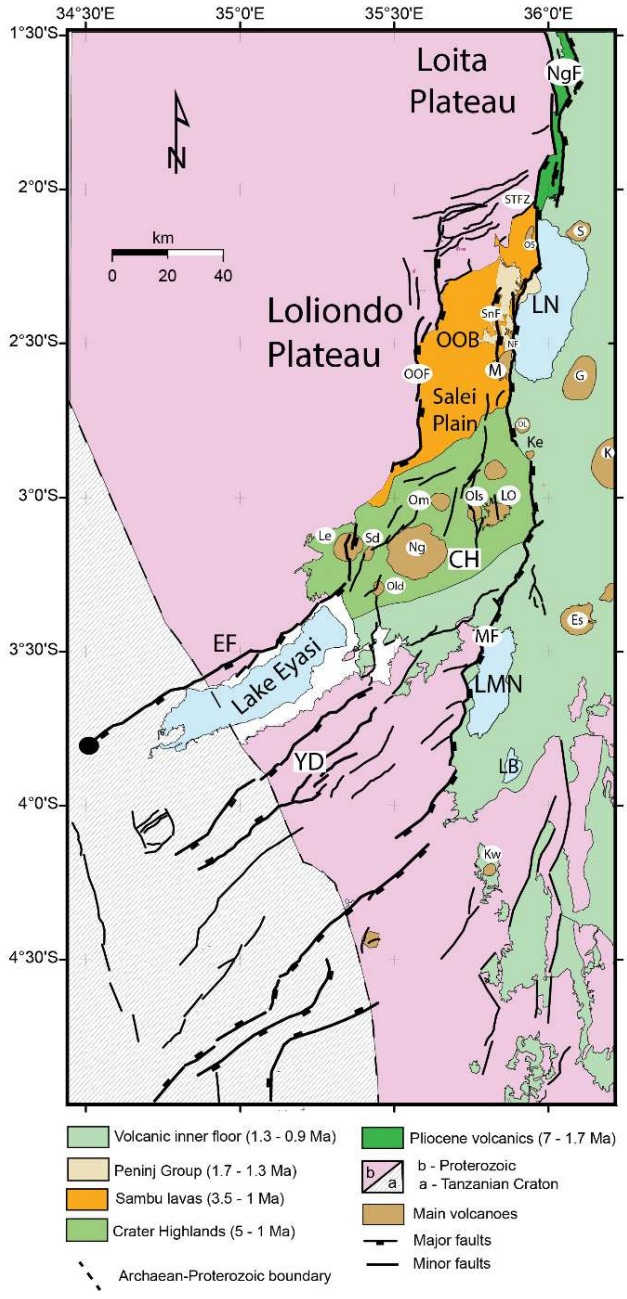

Fig. 4.3. Simplified geological map of the western flank of the North Tanzania divergence. Abbreviations as in Fig. 4.1.

In the NTD, magmatism, and volcanism started with the eruption of pre-rift phonolitic magma at Essimingor about 8.1 Ma (Bagdasaryan et al., 1973; Dawson, 1992; Le Gall et al., 2008; Mana et al., 2015). The main magmatic events followed in Lemagrut at about 5.5 Ma and Sadiman at about 4.6 Ma (Dawson, 1992; Le Gall et al., 2008). The eruption

of Lemagrut is considered to be the initiation of multiple eruptions that led to the formation of a volcanic chain known as the Crater Highland (CH) that is comprised of more than ten volcanic edifices, to mention a few: Lemagrut, Sadiman, Oldeani, Ngorongoro Crater, Loolmalasin, Olsirwa, Olmot, Embagai, Kerimasi, Oldoinyo Lengai and Kerimasi (fig.4.3). From the eruption of Lemagrut, magmatism migrated in a NE direction between 5.5 Ma and 0.5 Ma with the main activities concentrated at about 2.3 Ma (Mana et al., 2015). Existing chronological data show that there are two main linear trends of volcanism i.e., the west to east younging trend Essimingor to Kilimanjaro (Kilimanjaro is not included in this study) and the SW-NE trend, i.e., from Sadiman to Gelai (Le Gall et al., 2008b; Mana et al., 2015). The transverse magmatism trend (SW-NE) coincides with the N80°E lineaments observed by Le Gall et al., 2008. Other linear volcanic axes include N-S, N80°E and NW-SE (Le Gall et al., 2008). The only still active volcano is the carbonatitic Oldoinyo Lengai and is situated just at the northern tip of the Manyara border fault (Plasman et al., 2017).

The current landscape of the NTD lies above the Proterozoic Belt and the Archaean Tanzanian Craton. This morphology is a result of uplifting of the Victoria and Masai blocks that caused tectonic depression that is bounded by faults (Dawson, 1992) during the Mid-Tertiary. After uplifting, the major faulting episode followed at about 2 - 1.2 Ma (Macintyre et al., 1974). The orientation of border faults bounding basins and the topography in the NTD are thought to have been influenced by the presence of pre-existing heterogeneities in the Archaean crust (Ebinger et al., 1997; Mana et al., 2015).

During the Pliocene-Pleistocene, the areas surrounding the study area such as Olduvai gorge and Laetoli in the west of Ngorongoro Volcanic Highland experienced rainfall in the ranges of 500-900 mm/yr and 733-944 mm/yr, these were interpreted as representing arid to semi-arid climates (Sikes and Ashley, 2007; Driese and Ashley, 2015; Kasanzu et al., 2016). This arid to semi-arid climate is the reason that in some places of the study area, there are little vegetation cover leading into bare landforms which facilitate water flow during rain seasons and so shaping the morphology (Molini and Corti,.2015) and hence making tectonic interpretation of drainage network anomalies less difficulty.

Based on spatial variations in the topographic, tectonic configuration and drainage patterns, we sub-divide the study area into five domains as i) Nguruman escarpment and Loita hills domain, ii) Sonjo transfer fault zone (STFZ), iii) Oldoinyo Ogol Block, iv) Eyasi escarpment domain and v) Manyara – Mbulu domain. In each case we avaluated at

least the following; longitudinal river profiles for KPf and KPd, AF, HI and normalized steepness index (K_{sn}) and where necessary we made topographic profiles for topographic analysis.

4.3 Methodology

4.3.1 Drainage extraction and longitudinal river profiles

The morphological features, landscapes topography, drainage basins and drainage networks were extracted from the SRTM 1 arc second DEM (~ 30 m resolution) by using the Geographic Information Systems software ArcGIS version 10.3. A total of 25 catchments and associated drainage systems were extracted, they cover all five domains mentioned above.

Longitudinal profiles are commonly used to deduce information regarding competition between tectonic uplift and incision processes. From each studied catchment, the main trunk river was selected (named Rw1 to Rw25) with in some cases some additional river tributaries. For each long river profile, we also determined the presence or absence of knickpoints (corresponding to local convexities in the long profile) and their origin (i.e. associated with local change in lithology, base-level change or active faulting). Their extent and spatial distribution is useful in determining the extent to which active tectonic processes have influenced the landscape (e.g., Snyder et al., 2000; Wobus et al., 2006; Boulton & Whittaker, 2009; Kirby & Whipple, 2012; Duffy et al., 2014).

4.3.2 Normalized stream channel steepness index (Ksn)

Channel steepness (k_s) and concavity indices (θ) can be used to deduce recent tectonic uplift across the landscape (Snyder et al., 2000; Wobus et al., 2006 and references therein). At equilibrium state, such as when the incision is equal to tectonic uplift, the channel slope can be expressed by Flint's power-law (Flint, 1974):

$$S = k_s A^{-\theta}$$

Where S represents equilibrium channel slope, A is the upstream contributing drainage area, θ is the concavity index and k_s the channel steepness index (Snyder et al., 2000). Starting from a stream power incision law (e.g., Lague, 2014), channel concavity

reflect hydrology processes while channel steepness is a function of rock uplift and erodibility of rocks.

The values of θ range classically between 0.4 and 0.6 allowing to normalize steepness index thanks to a reference concavity index (θ_{ref}). Many studies used a value of 0.45 for θ_{ref} in order to compare normalized steepness index (named k_{sn}) (Kirby and Whipple, 2012; Lague, 2014). Considering a roughly uniform climate and substrate, K_{sn} values can be used as a proxy of tectonic uplift (Kirby and Whipple, 2012). In the case of transient profiles and if we assume that the response time of channels is longer than tectonic forcing, knickpoints separate equilibrium states (upstream part from downstream part, corresponding to paleo-equilibrium and new-equilibrium stage respectively) (Whipple and Tucker, 1999).

We calculated K_{sn} values for the study area using the script TopoToolbox-2.2 developed by Schwanghart and Scherler (2014) in a MATLAB environment.

4.3.3 Morphometric analysis

In this study, the following morphometric indices of the morphological features of drainage basins were analyzed: hypsometric integral (HI) and asymmetric factor (AF) similar to El Hamdouni et al., 2008.

4.3.3.1 Hypsometric Integral (HI)

HI is defined as the area below the hypsometric curve, (Alipoor et al., 2011; Cheng et al., 2018; Keller and Pinter, 2002; Mayer, 1990; Pike and Wilson, 1971; Schumm, 1956; Strahler, 1957). It provides a 3D information on river morphology in 2D approach (Bhattacharjee et al., 2016; Hurtrez et al., 1999). It is dependent on river erosion and uplift rate in the basin area (Bhattacharjee et al., 2016). HI is calculated by the following formula (Keller and Pinter, 2002) and indicated in fig. 4.4a.

$$HI = (H_{mean} - H_{minimum})/ (H_{maximum} - H_{minimum})$$

For tectonic interpretation, we adopt the HI classification as in El Hamdouni et al., 2008. We therefore classified HI values into three classes as: Class 1 (HI > 0.5;

strongly incised); Class 2 (0.4 ≤ HI ≤ 0.5; moderately incised); and Class 3 (HI < 0.4; weakly incised).

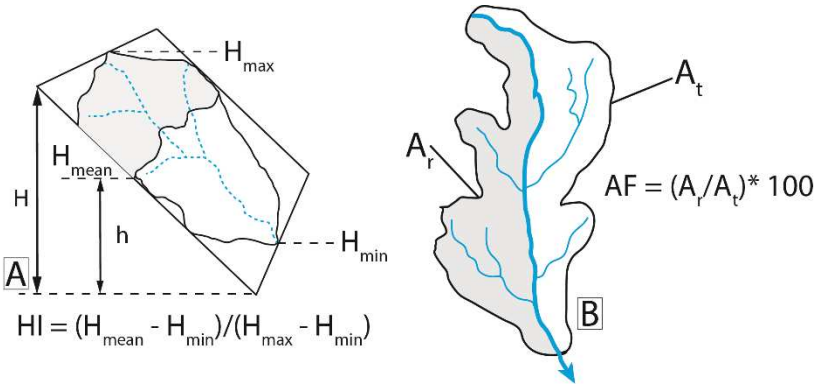

Fig. 4.4. Calculations of morphometric indices. A. Calculation of the hypsometric integral and B. Calculation of Asymmetric Factor (modified after Bull and McFadden, 1977; Keller and Pinter, 2002; Özsayın, 2016 and references therein).

4.3.3.2 Asymmetric Factor (AF)

The asymmetric factor is defined as AF = $(A_r/A_t)*100$, where A_t is the total area of the basin, A_r is the area to the right of the main channel (view from upstream). AF is an index that can be used to evaluate the existence or absence of tectonic tilting at the scale of a drainage basin (Cheng et al., 2018; El Hamdouni et al., 2008; Keller and Pinter, 2002; Paul W Hare and Thomas W Gardner, 1985) fig.4.4b. In this study, A_t was determined as a total area represented by drainage shape file of a respective water catchment, and A_r was calculated by using an open source QGIS software by first splitting A_t into two by using the major drainage channel as a splitter.

Asymmetric factor, AF is an index that describes the tilting state of the basin. 50 is the neutral value when the value of AF is close to 50, there is no tilt or the basin has undergone very little tilting (Cheng et al., 2018; El Hamdouni et al., 2008). Tectonic interpretation of AF is done by using the absolute value |AF-50| as in (El Hamdouni et al., 2008) and then adopt the classification of (Cheng et al., 2018). Class 1 (|AF-50| ≥ 15; strongly tilted basin); class 2 (7 ≤ |AF-50| < 15; moderately tilted); and class 3 (|AF-50| < 7; weakly tilted).

4.4 Results and discussions

4.4.1 Drainage networks along the double fault system in the Nguruman-Loita Hill sector.

This sector is located in the north of the study area, it is marked by an interesting topography that includes Loita Hills that are located west of Nguruman border faults (fig.4.2). Its topography is as high as ~ 2500 m a.s.l (fig. 4.5a). It lies on top of two major geological formations, the Proterozoic metamorphic basements and the syn-rift trachytes of the Lengitoto (Kirikiti) origin (7 - 1.7 Ma) (Baker, 1958; Crosley, 1979; Birt et al., 1997) (fig. 4.5b).The eastern end of this area is bordered by east facing, N-S striking Nguruman fault system which is composed of two parallel faults that have been active at different times. The oldest is the west Nguruman fault (NgW) whose age is estimated to be 7 Ma while the east Nguruman (NgE) which is dated at 1.7 Ma. Spacing between these faults decreases southward from 8 km in the north to 3 km in their southern tips. They are both segmented making relay zones whose length vary between 1.5 and 8 km (fig. 4.5a).

Drainage networks in this sector correspond to W1-3 catchments and Rw1-3 river systems (figs. 4.5a and 4.5b). Values of surface area, HI and AF in W1 are 721 km^2, 0.51, and 21, respectively. This indicates that this landscape is relatively incised and tilted (fig 4.5c and 4.5d respectively). Rw1 river system (Ewaso Ngiro) is a dendritic drainage pattern flowing from the uplifted metamorphic basements in the Loita hills, then becomes parallel crossing NgW, before turning eastward and cutting through NgE at right angle into the hanging-wall.

W2 is located to the south of W1, its high (0.65) HI values indicates that incision is high. It is a weakly tilted water catchment due to its low AF value (6). The main river network Rw2, is a trellis drainage pattern whereby its low order streams follow the shape of metamorphic foliation (circular flowing river networks) joining the high order stream at right angles which flow parallel to one of segments of NgW then passes in the southern tip of NgW segment and then flow South eastward for about 6 km before incising the hanging wall of NgE at 50° (fig.4.5).

W3 is located south of this sector and has HI 0.69 which can be interpreted as representing a water catchment with high incision rate its AF (4) shows that is weakly tilted.

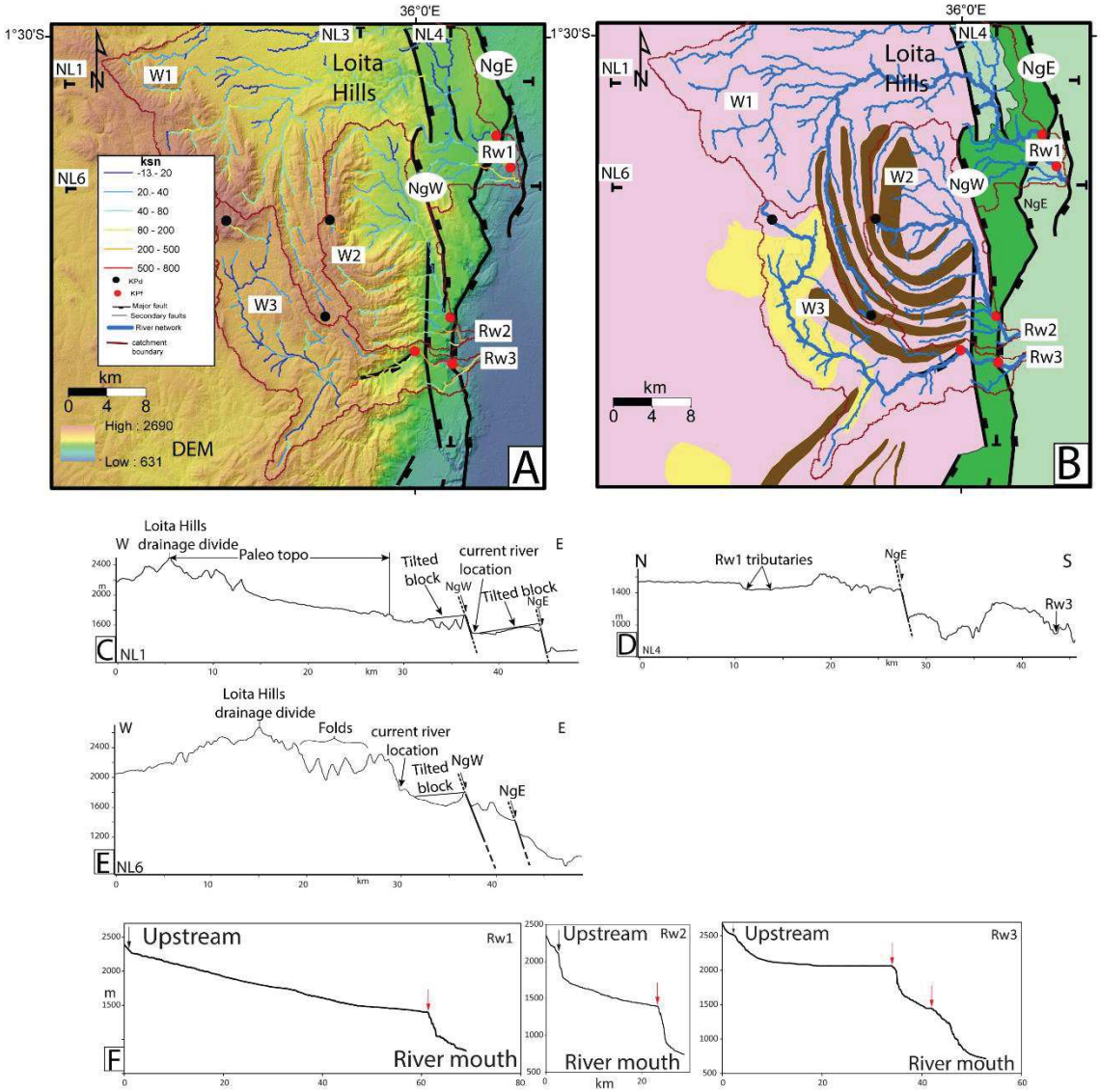

Fig. 4.5. Main topographical and geological units of the Nguruman-Loita domain. A. DEM showing main topographical variation and river steepness indices for main drainage networks. B. Simplified geological map incorporated with drainage networks (legend as in Fig.s 4.1 and 4.3). Main river streams are shown in thick lines. C, D and E. Main topographical and structural blocks. Vertical exaggeration X10. F. Along river profiles showing drainage shapes and main drainage anomalies marked as knickpoint (KPf in red and KPd in black arrows).

The main stream Rw3 is a dendritic drainage pattern that flows southward from Loita hills, depositing recent sediments into depression within Proterozoic terrain (fig. 4.5b) and then it is diverted to follow the morphology of metamorphic foliation before crossing both NgE and NgW at right angles and into the hanging wall of the NgE. The shape and the direction which this stream takes indicates the role of both lithology and structure on the control of the stream flow.

Long-river profiles of Rw1-3 system present some clear knickpoints either pinned to major faults (named KPf) or diffused in the drainage system (named KPd) (Figs. 4.5f). K_{sn} values obtained in this area range between 13 and more than 800. We observe a high correlation between high K_{sn} values and the presence of KPf pinned to NgW and NgE faults in the eastern part of this domain.

EW topographic profiles (fig. 4.5c and 4.5e) shows three major topographic observations i) paleo-topography dipping E, surface dipping N and S (these changes of tip direction are observed from the most elevated surface of the area); ii) first (older) tilted block due to NgW escarpment; iii) second (young) tilted block due to NgE. Topographic profiles above and fig. 4.5d show that i) Loita hills act as drainage divide due to its highest elevation leading into changes of water course direction either eastward, or southward; ii) there is a contrast of competence between rocks marked by the presence of folds and iii) in the eastern side of the study area, slope decreases southward making rivers run parallel to faults.

We also note that the deflection of Rw1 and Rw2 rivers (flowing E-W in the upstream part, from N-S in the middle part) crossing NgW escarpment seems to be controlled by the hanging wall motion of this normal fault. This pattern is classically described in the evolution of rift topography (e.g., Cowie et al., 2006).

General remarks on fault pattern and drainage organization is that, there are two main faults in which NgW is the oldest followed by NgE. Drainage network in the northern (Rw1) flows and cuts both faults changing its direction along, because to the far W of the NgW the main direction of the river is towards E, but once it cuts NgW it changes its direction and flow southward before changing its course in the tip of one of synthetic fault segments where it turns its direction toward E cutting through NgE. Other two drainages in this sector show strong control of both, lithology and tectonic where by rivers flow by following the shape of metamorphic foliation and also the effect of faults whereby rivers follow the fault direction e.g., Rw3 or Rw2 which flows passing through relay zones NgW segments. Also the flow direction of courses of rivers are controlled by differences of slopes of block, in the northern Rw1 starts as a N-S river then it is directed towards E by the influence of topography, while Rw2 and Rw3 start as N-S drainages before being diverted as discussed above.

4.4.2 Sonjo transfer fault zone (STFZ).

Sonjo transfer fault zone marks the transition zone from narrow N-S rift to a wide double border fault rift system which lies in a heterogeneous formations mainly composed of Proterozoic metamorphic basements and syn-rift volcanic rocks of the Lengitoto (7 Ma) and Oldoinyo Sambu (3.5 Ma) (Foster 1997) (fig 4.6a). Its topography is as high as ~ 2500 m a.s.l (fig. 4.6b). This sector is marked by two major fault systems: i) the N-S striking faults composed of the southern and northern tips of Nguruman and Oldoinyo Sambu faults respectively, and ii) a cluster of NE striking Sonjo transfer faults (STFZ). The STFZ is a transverse NE-SW fault system (striking between 40°-70°) juxtaposed between two major N-S faults namely the Nguruman-Sambu fault system in the East and the Oldoinyo Ogol fault in the West (fig. 4.6a). The STFZ is a major transitional area connecting the classical N-S South Kenya rift trough to a more diffuse wide rift. In this system faults are closely spaced between 0.5 to 4 km, forming horst and graben systems (e.g., fig. 4.6c).

Three water catchments W4-6 (rivers Rw4-6 respectively) are found in this in this part of the study area. W4 has, surface area 78 km^2, HI and AF, 0.62 and 11, respectively. Both HI and AF values correspond to a highly incised and relatively asymmetric catchment. Rw4 originates from the elevated block which is comprised of metamorphic foliations (fig.4.6a), flowing eastward through the southern tip of NgW and into the hanging wall of NgE.

W5 has an HI of 0.5 indicating that this drainage network is moderately incised. AF analysis indicates that this water catchment is weakly tilted with AF value of 4. The main river channel Rw5 originates from the uplifted block like Rw4, it flows south eastward passing through the north eastern end of the SFTZ then crossing the Oldoinyo Sambu fault at 50°, later it crosses the southern tip of NgE, so this river passes through both systems marking the beginning of the transfer systems from N-S to NE-SW faults.

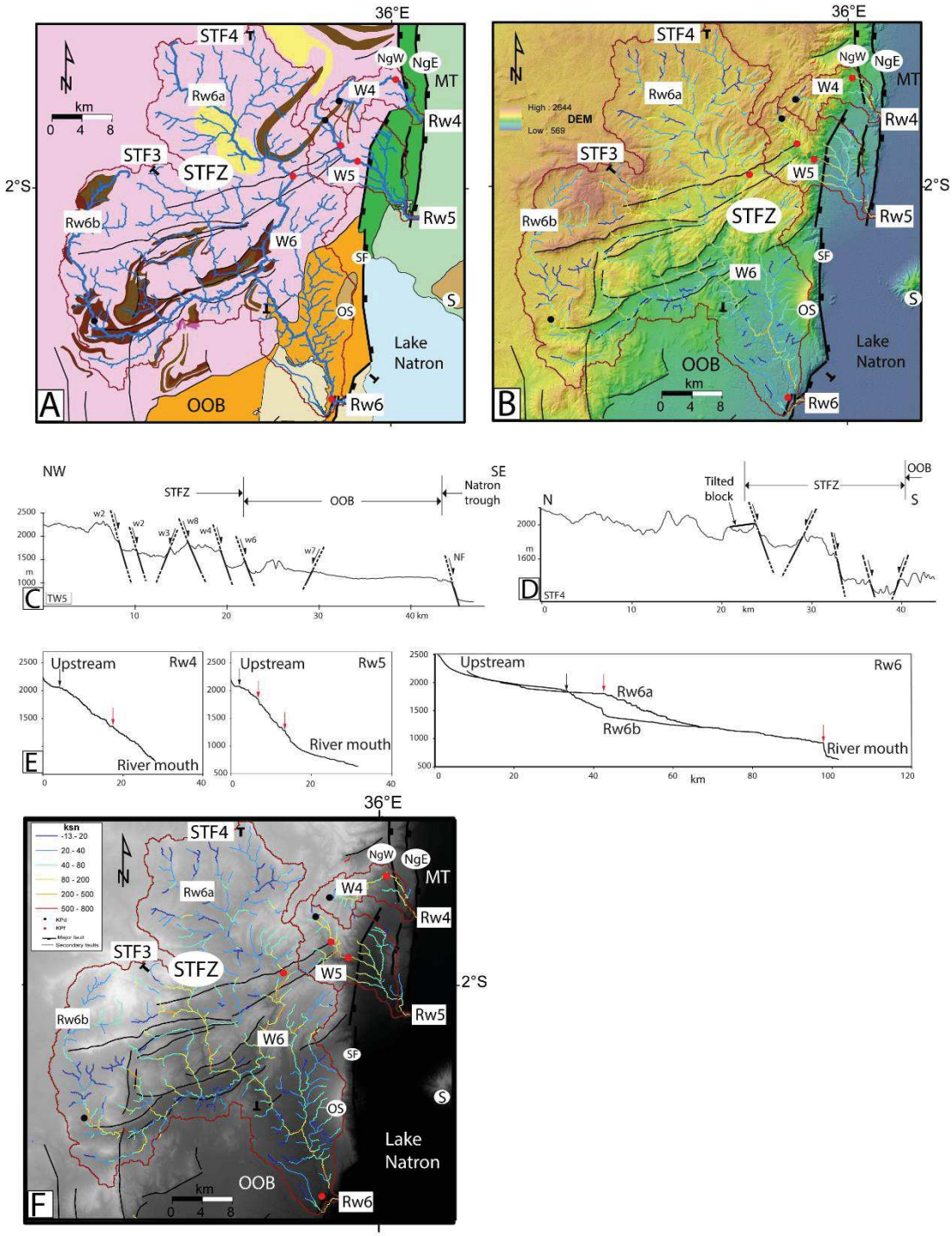

Fig. 4.6. Main topographical and geological units of the STFZ. A. Simplified geological map integrated with river networks (main rivers are shown as thick lines). B. DEM showing main topographical variation and river steepness indices for main drainage networks (Ksn legend as in Fig. 4.5a). C. NW-SE Topographical profile showing main STFZ faults. Vertical exaggeration X10. D. N-S topographical profile showing N-S structural trends. E. Along river profiles showing drainage shapes and main drainage anomalies marked as knickpoint (KPf in red and KPd in black arrows). F. DEM showing variations of KPf and KPd along river networks.

The largest water catchment in this domain is W6 covering the area with all transfer faults. This catchment has HI 0.58 meaning that it is a highly incised drainage network. AF value is 32 indicating that this drainage is strongly tilted. Drainage network is dendritic drainage pattern whose main river Rw6 has two main streams each representing different surficial characteristic and response to the SFTZ. The first main tributary (Rw6a) originates from northern uplifted block (fig. 4.6a and b) of the sector in which high order tributaries from all sides join each other into the low order main stream then flow southward at the crest of metamorphic foliations and bent into hemi-graben and join the other main tributary at the southern tip of the SFTZ. The second main tributary (Rw6b) flows southward from the western tip of the SFTZ bending eastward through the foliation and then flow parallel to one of NE-SW fault joining the other major tributary. At the confluence, the two main tributaries are joined by tributary that passes through the centre of the SFTZ and then flow at 30° towards the Natron hanging wall where they deposit sediments into the Lake Natron basin.

Along river profiles show that Rw4 and Rw5 are short rivers with less than 40 km of length and both profiles have steep slopes. For both rivers have KPf and KPd where their KPf are located few meters away from NgW and one of them is located at the north eastern tip of SFTZ while KPd are located in the metamorphic foliation. The location of KPf is in correlation with the elevated Ksn values for both river networks (Rw4 and Rw5) (fig.4.6e and f). The migration of KPf away from NgW is here interpreted as the old elevated fault system in which there was enough time for its readjustment to uplift that was caused by the formation of NgW. The main river stream in this sector is the Pinyinyi (Peninj) river here denoted as Rw6. Stream Rw6a passes through the transfer faults while Rw6b avoids crossing main faults, it rather runs parallel and bends at the fault tips (fig. 4.6a). Longitudinal profile of this river is ~100 km long with gentle slope except at ~ 35-40 km and 98 km downstream where both 2 knickpoint families are observed (fig. 4.6e). These knickpoints are associated with Sonjo-transfer faults (NE-NW) and the Natron fault (N-S fault) from upstream to downstream respectively. High values of Ksn (> 500) correspond to KPf which are pinned to main scarps due to Natron and STFZ uplift. A KPd is also observed in the foliated Proterozoic metamorphic basements. High Ksn values also correspond to slopes above 28°.

General remarks on drainage organization with respect to faults and uplifted block such as Oldoinyo Sambu volcano is that, in the northern part faults behave in a similar pattern to that of the Nguruman sector, that means faults have control on the direction of rivers in such way that Rw4 and Rw5 cross NgE at its tips. Rw4 is controlled by either lithology, faults or the uplifted block, that is in the western part, tributary Rw6b passes through metamorphic foliation before cutting across the northern tip of OOF and run parallel to one of transverse faults, and later flow approximately N-S through the control of Oldoinyo Sambu topography (fig.4.6a). These configurations of faults, drainage and faults indicate that the current drainage network is younger than both faults and Oldoinyo Sambu volcano.

4.4.3 Oldoinyo Ogol block (OOB).

Geologically this block is located between three major lithological formations as follows i) in the west of the uplifted Oldoinyo Ogol escarpment, the area is bordered by metamorphic Proterozoic basements, ii) at the centre and east there are syn-rift sedimentary and volcanic rocks marked by Oldoinyo Sambu volcanic rocks (3.5 Ma: Foster 1997), Peninj group and iii) syn-rift volcanic rocks of the Ngorongoro crater highland (5-1 Ma: Foster 1997, Le Gall, 2008) located in the south of the sector (Fig.4.7a). The Oldoinyo Ogol escarpment is as high as ~ 2300 m a.s.l while the most elevated sector is the Ngorongoro volcanic highland whose elevation is more than 2800 m a.s.l (fig.4.7b).

This sector is composed of three parallel N-S faults from east to west Natron, Sanjan and Oldoinyo Ogol fault (OOF), they are placed between 8 and 30 km where by Natron (NF) and Sanjan (SF) are relatively close to each other. The Natron fault (~ 60 km long) is the southern continuation of the Sambu fault, its hanging-wall borders Lake Natron which receives most of sediments that are eroded from the up-streams. The Sanjan fault (~ 30 km long) is located west of Natron fault, together with the Natron fault they mark the eastern border of the 30 x 60 km perched basin (Oldoinyo Ogol) that was probably uplifted during the uplift of Natron, Sanjan and Oldoinyo Ogol blocks. The more complex and oldest fault scarp is the Oldoinyo Ogol fault (~ 80 km long) that is dated synchronously with the Oldoinyo Sambu basalts at ~3.5 Ma (Foster 1997).

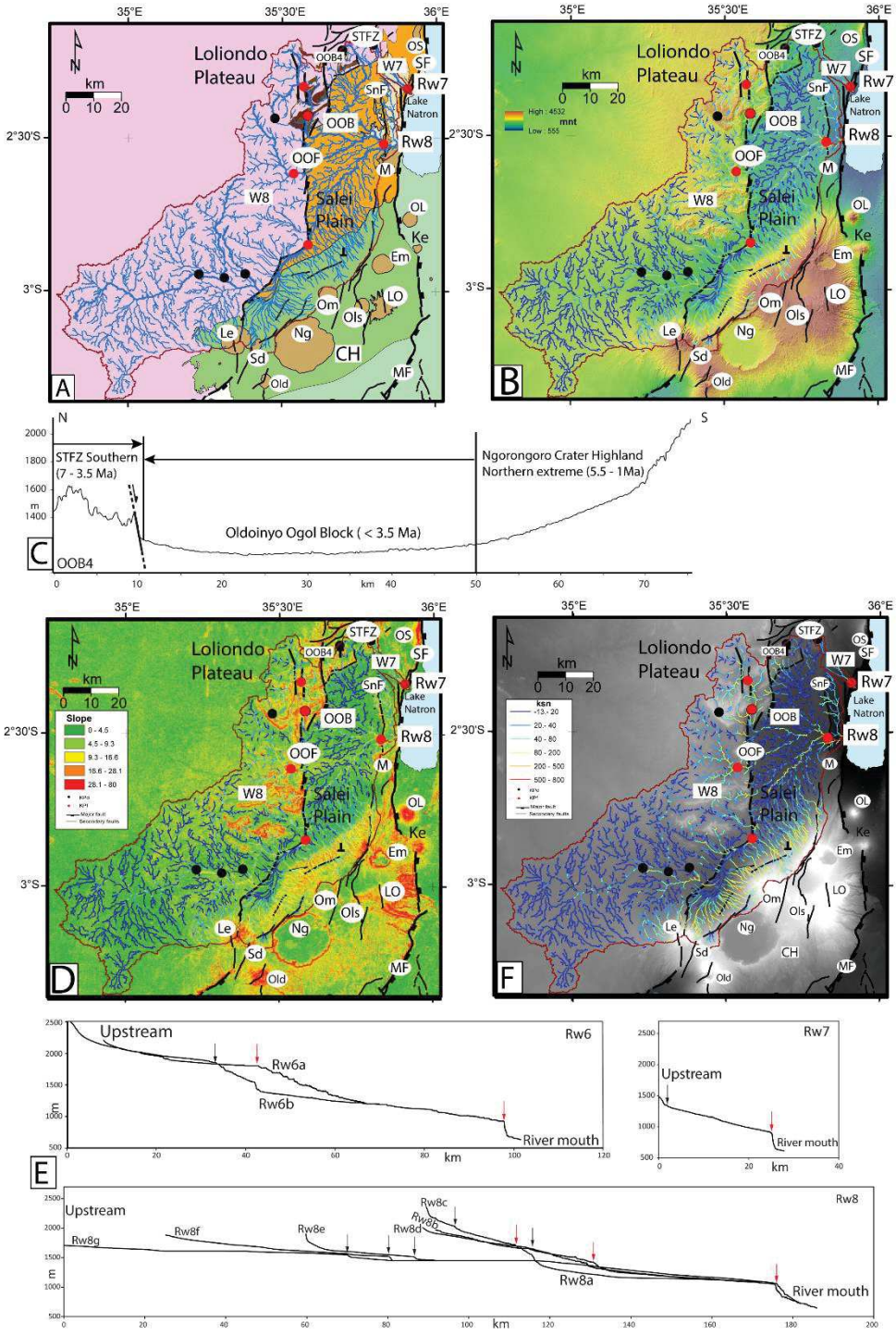

Fig. 4.7. Main topographical and geological units of the OOB. A. Simplified geological map integrated with river networks (main rivers are shown as thick lines). B. DEM showing main topographical variation and river steepness indices for main drainage networks (Ksn legend as in Fig. 4.5a). C. N-S Topographical profile showing main N-S topographical variation. The influence of Crater highland on the topography is well noted in the southern end and the lowest topography represents both the Salei plain and OOB plain. Vertical exaggeration X20. D. DEM showing slope variation, it is marked that high slopes are either represents fault scarps or crater highland. E. Along river profiles showing drainage shapes and main drainage anomalies marked as knickpoint (KPf in red and KPd in black arrows). F. DEM showing variations of KPf and KPd along river networks.

The north OOF is marked by closely spaced N-S segments (fig.4.7c) which die out in the Proterozoic metamorphic basement foliations. The OOF is the most uplifted scarp of the sector where the estimated elevation is 2300 m (a.s.l), it is sloping southwards attaining the minimum elevation of ~ 1300 m (a.s.l) (fig.4.7d).

The OOB is comprised of two water catchment, W7 and W8. i) W7 has an HI 0.57 indicating that its incision is high, moreover and its drainage network is highly tilted with AF value of 20. Its river (Rw7) a parallel drainage network whose main channel runs from the metamorphic basements, it flows south eastward incising the Natron fault at 80° depositing sediments (Peninj sediments) at the hanging wall of Lake Natron. ii) W8 with HI 0.38 and an AF values 28 which is a strongly tilted water catchment. Owing to its morphological complexity, W8 is comprised of a complex drainage system made up of six individual river tributaries that cover the entire OOB joining one another before incising the Natron escarpment at 90°. From south of the SFTZ, the geometry and flow direction of each main tributary is as follows a) the first tributary (Rw8a) originates from the southern extreme of SFTZ flowing southward before diverging into SE direction incising the Sanjan fault (fig.4.7a). b) The source of the second river (Rw8b) is from the NW of the OOB, it flows from the Proterozoic metamorphic basement foliations following the shapes of the folds and then bend eastward in the OOB plain. Both low and high order streams avoid passing through the basement, they rather find their way between structures, thus adapting their shape to the geometry of older structures. c) The tributary (Rw8c) flows through the centre of the OOB and OOF where the N-S topographic configuration is relatively low by ~ 500 m as compared to its northern and southern reliefs. High order stream of this river flows first SE and bends eastward due to influence of hard Proterozoic metamorphic foliation. d) and e) both (Rw8d and Rw8e) flow south eastward starting from the western terminal of the uplifted OOB flowing southward and parallel to the foot wall of OOF then they both bend to link up with another river stream. f) Rw7f is the longest river network of the OOB originating about 50 km off the OOB, it passes at the southern tip of the scarp and into the OOB plain, joining up with other rivers from the Ngorongoro volcanic highlands incising both Sanjan (at the northern tip of Monsonik volcano) and Natron faults to pour sediments into Lake Natron. The OOB plain is filled with Proterozoic basement sediments eroded by drainage networks flowing in this sector, the plain has high density due to the fact that it is composed of loose materials which are easily eroded and allow passage of water.

In the OOB, along river profiles for Rw7 and Rw8 are characterized by both KPf and KPd whereby KPf are localized along the two main scarps. In the Natron, Sanjan and along the Oldoinyo Ogol main scarp (fig.4.7e), all KDfs correspond to high Ksn values (above 500) (fig.4.7f). The Sanjan river (Rw8) is a complex drainage system that flows through out the Oldoinyo Ogol domain pouring its water into Lake Natron. In this domain Ksn values can be sub-divided into three categories. i) High localized Ksn values that correspond to most elevated areas with high values of slopes (fig. 4.7d), these are associated to recent fault activities. ii) high to medium Ksn values that are diffused away from the main scarps, corresponding to older faults especially the Oldoinyo Ogol fault and Ngorongoro volcanic highlands (> 3.5 Ma) and iii) low Ksn values in the Oldoinyo Ogol plateau, this is probably due to absence of active tectonic activities taking place during the quiety period (after tectonic activities that led to the placements of current system).

Topographical configuration of faults, crater highland and directions of drainage networks in OOB lead into the following interpretation of tectonic events, i) drainage networks pass through OOF perpendiculary in E-W direction, ii) same river networks pass through the Sambu fault perpendiculary, iii) there are three main drainage directions, i.e., N-S in the northern OOB, E-W in the OOB basin and NW in the crater highland. The presence of KPd in northern OOB and in the west of OOB and its absence in the crater highland when interpreted together with the presence of high Ksn along main escarpment of OOF, and in the elevated crater highland block and the low values of Ksn in the Salei plain and OOB block indicate that drainage in the OOB is older than that which flow from the crater highland. This brings about two tectonic scenarios which are i) in the first place drainage in the OOB evolved in which E-W direction was dominant (3.5 Ma ago) then ii) drainage NW drainage from crater highland evolved (fig.4.8). This is also supported by the fact that all drainage from the crater highland act as tributaries to main sub E-W main drainages which eventually pours its water into Lake Natron.

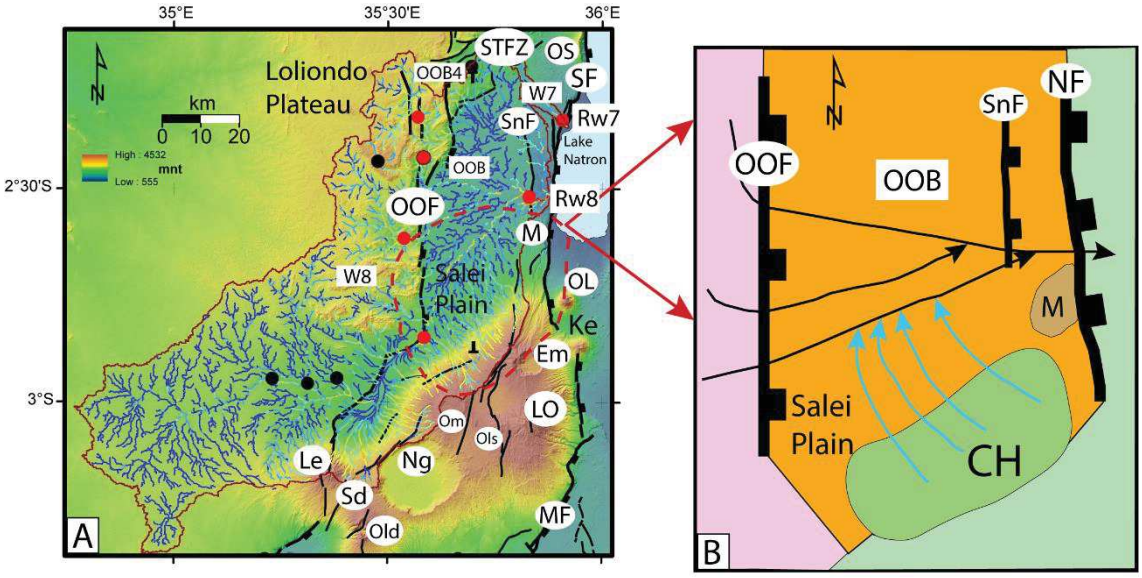

Fig. 4.8. Chronological arrangement of events taking place during uplift of both OOF and CH and their control on the direction of drainage networks. A. The SRTM-DEM with drainage networks and B is the proposed model. The first phase is the uplift of OOB and OOF which results into formation of main E-W drainage networks and the second phase is the uplift of CH which results into NW-networks which later join E-W drainages.

4.4.4 The NE-SW transverse structure of the Eyasi Escarpment.

The centre of Eyasi escarpment marks the limit between the Tanzanian craton and the Mozambique Proterozoic mobile belt (fig.4.9a). In NE the Eyasi scarp is bordered by the Ngorongoro crater highland which is highly marked in topographic profile of Fig. (fig. 4.9d). The most remarkable structure in this sector is a highly segmented Eyasi fault which makes an elevated block of approximately 1950 m (a.s.l). The scarp produced by the uplift of this fault can be divided into three segments of different altitudes, the north eastern tip has a maximum altitude of 1600 m (a.s.l), the central part is 1950 m high and the south western tip is approximately 1100 m high. These three segments make an asymmetric fault profile which is differentiated by different up-lifts which are also clearly observed in the DEM (fig. 4.9b and c).

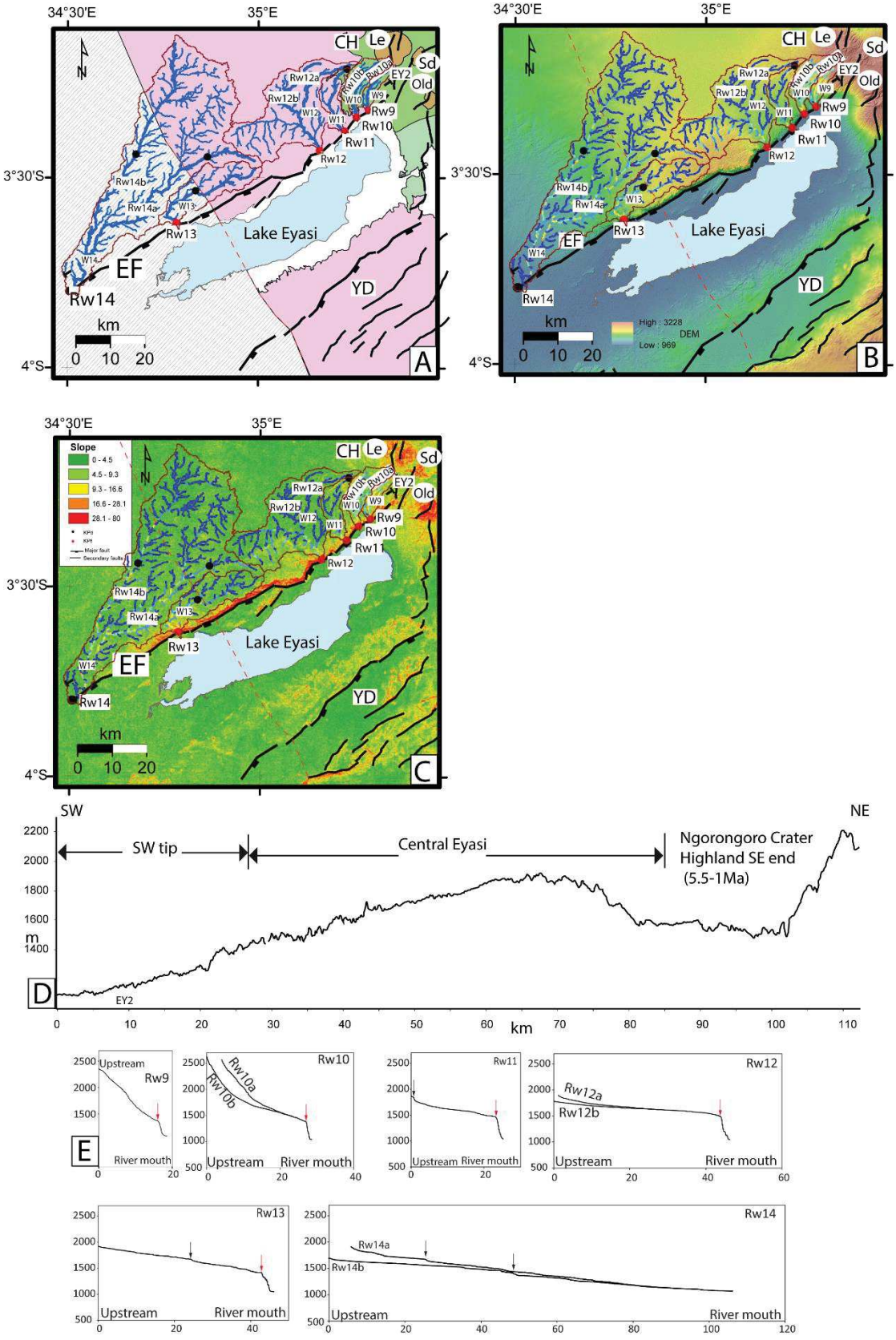

Fig. 4.9. Main topographical and geological units of the Eyasi scarp. Legend for A, B, C and E as in Fig. 4.7 above. D. Topographical profile along the Eyasi footwall. Three sections of the fault profile are shown. Vertical exaggeration X20.

This domain has 5 water catchments (W9-14) which are described below. i) W9-11 are small catchments whose surface areas are 42 (W9) with HI 0.49 and AF value of 3, 106 (W10) with HI 0.44 and AF value of 2 and 88 (W11) km^2 with HI 0.66 and AF value of 12.

River networks located in the north east are perpendicular to fault escarpment, Rw9 to Rw11 are all parallel drainage networks, they all flow from the Lemagrut volcano which probably indicates the effect of crater highland on the direction of drainage networks. W12 has HI value of 0.72 which is interpreted to represent a highly incised drainage pattern, its AF value of 12 means that this W12 is moderately tilted. Its river channel, Rw12 is a dendritic drainage network located in the transition zone, between the north eastern and the most elevated centre of the scarp. Its tributaries are diverted in two directions NE and SW, the NE tributary originate from the tip of the Ngorongoro crater highland (Lemagrut) while the south western tributary is diverted by the elevated basement which marks the boundary between Proterozoic Mozambique basement and the Tanzanian Craton. ii) W13 with HI value 0.71 and AF value of 15 which means the water catchment is strongly tilted and W14 with an HI value 0.54 and AF value of 30 have surface areas 228 and 1414 km^2 respectively. Drainage network Rw13 is located in the Tanzanian craton flowing south westward parallel to the fault's footwall from the elevated central Eyasi. Drainage network Rw14 flows ~40° away from the fault scarp. It has two main tributaries that originate from the basements and deposits its sediments at the SW fault tip of Eyasi fault.

Longitudinal river profiles for rivers in this domain are between 20 and 50 km long except Rw14 which is ~ 100 km long. Profiles in the NE tip of the Eyasi fault are steep with KPfs localized along the main scarp where the slope is also high (fig. 4.9d). Ksn values along the scarp are moderate in area with high slopes (fig.4.9e). Other longitudinal profiles are characterized by relatively flat profiles (fig. 4.9b) with low to moderate Ksn values. KPds have migrated away from the main scarp.

4.4.5 Manyara–Mbulu rifted block

This domain is located between two major geological formations, the Tanzanian craton and the metamorphic Proterozoic basements (fig. 4.10a). In its northern part the Manyara-Mbulu block is bordered by the Ngorongoro volcanic highlands. The Manyara escarpment is ~ 1800 m a.s.l while the Mbulu plateau is ~ 2300 m a.s.l as can be seen in DEM (fig. 4.10b). There are two main faults in this sector i.e. Manyara border fault and the Mbulu plateau faults, they all strike NE-SW. The major fault of the sector is the Manyara fault (MF) representing the main uplift of the Manyara scarp. Relatively few faults are found in the uplifted Proterozoic Mbulu plateau especially in the most elevated block. To the west of Manyara scarp is the sedimentary domain known as the Yaida depression wich is bordered by two segmented faults whose age is less than 3.5 Ma (Foster et al., 1997).

In this sector, there are 10 water catchments (W15-25) whose morphometric indices are as follow i) W15 has HI value 0.22 and AF value 4 has a surface area 1172 km^2. Streams of W15 (Rw15) are located south east of Ngorongoro crater highlands, they are parallel and they flow south eastward they bend to the east into the NE of lake Eyasi (fig.4.10b). ii) W16 with HI value 0.37 and AF value of 26 has a surface area 2519 km^2. In Rw16, tributaries run from Proterozoic basements into the Yaida depression, most of these tributaries are confined to the Yaida fault. Tributaries in the north NE and SE of the Yaida depression bend towards right while those in the SW of the depression are bent towards the left. Drainage network in this sector is responsible for the deposition of sediments in the Yaida depression and the Eyasi basin. iii) Water catchment W17 has HI value 0.41, AF value of 17 (strongly tilted) and a surface area 5353 km^2, its main river channel Rw17 run parallel to NE faults, they all tend to bend in SW where they join the main river which run towards Lake Eyasi basin. High order tributaries join main tributaries at right angle. iv) Water catchments located in the Proterozoic basement rocks along the Manyara escarpment (W18-25), have the following HI and AF values; W18 (HI:0.45, AF: 11), W19 (HI:0.53; AF:13), W20 (HI:0.68, AF:9), W21 (HI:0.58, AF: 1), W22 (HI:0.77, AF: 19), W23 (HI:0.65, AF:19), W24 (HI:0.67, AF: 26) and W25 (HI: 0.51, AF: 22) . Their drainage patterns are either dendritic or parallel (fig. 4.10a).

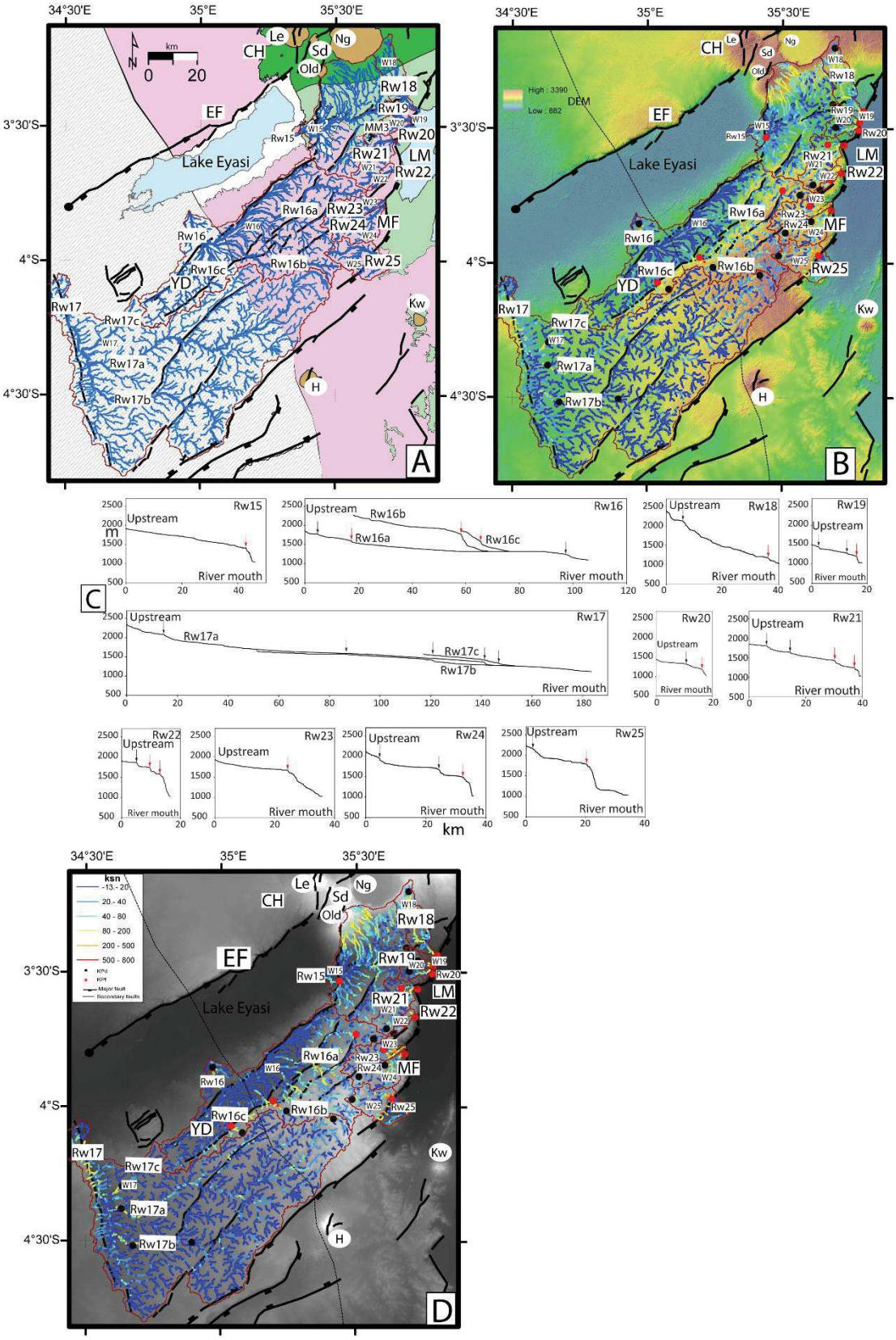

Fig. 4.10. Manyara-Mbulu plateau block. Legend as in Fig. 4.7.

Drainage networks in the uplifted Manyara escarpment have few tributaries. Main rivers in this area run either from Ngorongoro volcanic highland (Rw18) or from the Manyara footwall (Rw19-25) cutting through the Manyara fault at right angles.

Along river longitudinal profile analysis of main river channels shows that: Rw15 has a gentle slope (nearly flat), draining its water in the Lake Eyasi with KPf localized at the scarp (fig 4.10d). Rw16 has gentle slope except where it crosses the fault, KDf are observed. Some of Rw16 tributaries cut through the Yaida depression and the Mbulu plateau. In water catchment W17, Rw17 is in the south-west of the Mbulu plateau, its main channel has three gentle sloping tributaries in which the longest is ~180 km (fig.4.10c).

Eight water cachtments (W18-W25) were extracted in Manyara escarpment. River channels (Rw18-Rw25) flow towards the foot of the escarpment and into Lake Manyara. Most of these water channels are short (between 20 and 40 km long). River channel Rw18 shows an abrupt slope variation (fig. 4.10c), more than 1500 m of height difference for a 40 km long profile with one KPd near the Ngorongoro and one KPf along the Manyara escarpment. Channels Rw19 and Rw20 (fig. 4.10d) both are less than 20 km long and have a gentle slope with KPf along the Manyara escarpment and one KPd away from the escarpment. Rw21 is 40 km long with a gentle slope with two KPd and two KPf. Rw22 is approximately 18 km long, with a steep slope and two KPd and two KPf closely spaced. Rw3 has a gentle slope and only one KPf localized along the Manyara escarpment while Rw24 and Rw25 have similar lengths KPd located away from the escarpment and KPf located along the Manyara escarpment.

Ksn and slope values are categorized into three classes i) high Ksn values (200-500), these are found in elevated areas with high slopes (> 60°) such as the south east of Ngorongoro crater highland and along the Manyara scarp (fig.4.10c and 4.10d). ii) Moderate Ksn values < 200 found in the Yaida depression and SW result from the fault activities along the Yaida and Kitangili faults. iii) Low values > 20 in the Yaida depression.

4.5 Tectonic implications

This study was conducted in NTD in order to study the interaction between topography and drainage organization in response to multi-phase rift propagation which resulted into both, faults and several volcanic cones which are marked by the presence of Volcanic Highlands. Values of AF, HI, topographical analysis and Ksn analysis shown in the discussion of the main blocks above and their tectonic implication to the formation of the NTD have lead into consideration of a two stage up-rift model of the eastern flank of the NTD below.

4.5.1 First rifting phase (7-3.2 Ma)

Observations made on along river profiles have led into identification and location of knickpoints that are linked to recent faulting events (KPf) and those which are not directly linked to recent faulting (KPd) in NTD. In the first uplift phase when Nguruman fault is developing E-W drainage network is put in place with KPf pinned along the main fault scarp. These KPfs are marked as future KPd (fig.4.11). KPd are observable at the large scale and mainly in the northern part of the study area, i.e., Nguruman-Loita hill area (fig.4.5a), Sonjo transfer fault zone (fig.4.6d) and Oldoinyo Ogol block (fig. 4.7d).

Most of observed KPds in the study area are not pinned to faults, they have rather migrated upstream (fig.4.12). Since the migration of knickpoints upstream and away from main faults take long time we interpret these diffused KPds as corresponding to a first stage of rifting in the NTD, taking place between 7- 3.2 Ma synchroniously to the formation of NgW, STFZ, OOF and Sambu. The observed drainage pattern is not fully trellis drainage but rather a transverse drainage pattern and is already localized though not fully distributed. This can be argued as representing an early rifting stage in the NTD similar to Cowie et al., 2006. At this stage the fault interaction is not completed or achieved allowing to hinterland rivers (on footwall position) to be connected on downstream system (on hanging wall position) by gaps between early faults, this result is in correlation with numerical modelling results of Cowie et al., 2006 in which they showed that drainage network can be developed on the hinterland footwall during early rifting process. This pattern is also coherent with high values of HI which show that

erosion is developed in watersheds and does not fully correspond to a pure youth stage. We suspect that this drainage pattern could have been mainly formed during this rifting process and not really re-incised antecedent drainage because we have not identified opposite drainage systems or capture processes.

Upstream migrated KPd and diffused ksn are also observed in the southern domain in the Manyara-Mbulu block corresponding also to an early rifting stage that propagates on the southern part of the NTD.

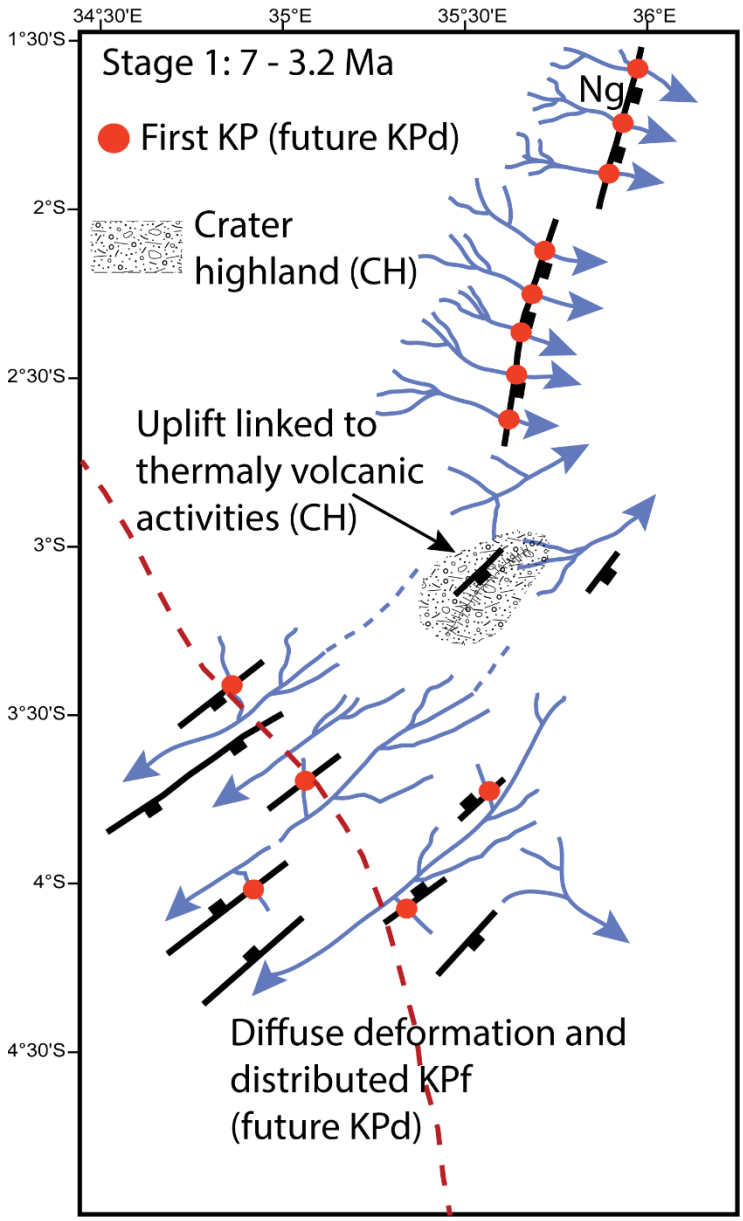

Fig. 4.11. First uplift stage in the NTD between 7 and 3.2 Ma. Formation of main escarpments and drainage network whose main anomalies (KPf: future KPd) are located along the main scarps

We propose that during the first phase of rifting (7-3.2 Ma) deformation is diffused and distributed where NE-SW flowing drainage system was initiated by the early doming in the crater highland (CH). Resulting drainage system is trellis probably due to NE-SW early faulting system often described in early rifting stages where diffused deformation have been observed (Cowie et al., 2006). The uplift of crater highland (< 5.5 Ma) is also suggested as being responsible to the change of direction of drainage networks located in the southern end of W8 where by drainage network in the northern end of CH are directed NW before joining the main Rw8 tributary that eventually flow towards the Natron fault (fig. 4.7a).

4.5.2 Second rifting stage (3.2 - 0 Ma)

This stage corresponds to the current situation at NTD where both KPf and KPd are observed. They are located at different locations of streams such that make us interpret them as representing different staged of rifting activities. KPf and localised ksn correspond to a second stage or late stage of rifting because knickpoints are pinned to recent faults due to the fact that there has been no enough time for them to migrate upstream.

Values of ksn away from the escarpments are either low (< 80) or moderate (80-500) especially in the Nguruman-Loita hills, in the upstream and middle parts respectively (Fig. 4.5a). Ksn variation is correlated to fluvial processes under the influence of tectonic activities. This observation is clear on NgE, Sambu and Natron faults for the northern part and a similar observation is made on Eyasi and Manyara faults in the southern part. These patterns correspond to a late stage (second stage) rifting evolution where fault interaction is achieved and footwall uplift/hangingwall subsidence is stronger. We propose that this stage correspond to 3.2-0 Ma where rifting moved to the east in the northern part and localised on the Eyasi and Manyara in the southern part. This late stage of faulting triggered a strong incision in the footwall linked to the uplift of this area e.g., Rw1, Rw2, Rw3 (Fig. 4.5a) or Rw7, Rw8 (Fig. 4.7a). This event could have also rejuvenated the drainage system linked to the first stage. This late rifting stage has also triggered capture effects in which Rw14 has been captured and runs parallel to EF rather than crossing it, this implies that the pace of tectonic activity was higher than incision rate at this southern tip of Eyasi fault. Moreover, this capture pattern is also responsible

to the increase of the drainage area of watersheds that are quite small on the footwall of Eyasi or Manyara faults.

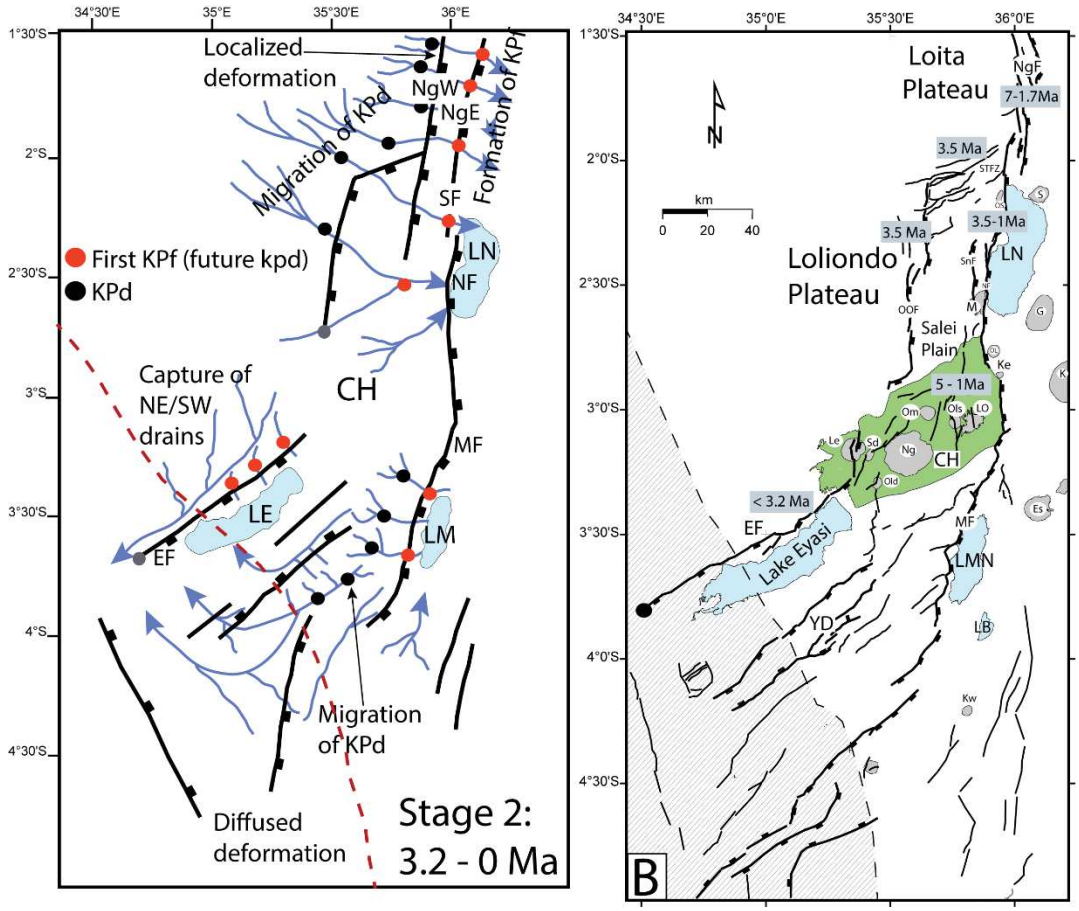

Fig. 4.12. Second uplift stage in the NTD from 3.2 Ma to present. A. Migration of former KPd (former KPf) upstream and formation of new KPf due to recent uplift manifested by recent faults in the NgE, NF and MF. (NgE., East Nguruman fault, NF., Natron fault and MF., Manyara fault). B. Map showing current situation in the NTD.

Shapes of along river profiles in which KPf and KPd were analysed in both uplifting stages above are convex up (Fig.s 4.5f, 4.6e, 4.7e, 4.9e and 4.10c), though in some cases straight river profiles are observed, these convex up shapes of river profiles are an indication of a system in transient state, contrary to the concave river profiles which are traditionally attributed to rivers in equilibrium (Mackin, 1948). These river shapes are typical of tectonically active environments (Cowie et al., 2006).

4.6 Conclusions

The NTD as the south-ward propagation of the South Kenya rift (SKR) presents a zone of both localized and diffused deformation. These deformation styles are recorded on surface by the presence of southward propagating faults, isolated volcanic cones (e.g., Oldoinyo Sambu, Mosonik, Shombole and Gelai) and the presence of the most prominent magmatic center known as crater highland (CH). It is believed that rifting in this zone is less than 8 Ma (Le Gall et al., 2008, Mana et al., 2015 and references therein). This zone represents a rift zone with different rifting style, it differs from Kenyan rift in the sense that regardless of the presence of volcanic highlands, it is still a rift with little magma in surface and therefore its propagation style is of particular interest. Since the SKR starts to record the westward divergence at around 1.5°S, the western rift flank of the NTD has become an important ingredient to unpuzzle the timing of tectonic events in this the study area. The study of drainage networks was applied in the zone which covers the whole western flank of the NTD by sub-dividing them into i) Nguruman-Loita, ii) STFZ, iii) OOB, iv) Eyasi and v) Manyara-Mbulu each with particular faults, magmatic and drainage network configuration. Our drainage network analysis supported by existing chronological data is in support of the following conclusion about the timing of events in the western flank of the NTD:

i) The northern part of the western flank of the NTD which includes a) Nguruman-Loita scarp (NL), b) Sonjo transfer fault zone (STFZ), Oldoinyo Ogol block (OOB) is the first to record the southward propagation of SKR and divergence between 7-3.5 Ma. This is strongly supported by the presence of upstream migrated knickpoints (KPds) that are not currently associated with recent faulting activities.

ii) The southern NTD which includes i) Eyasi and Manyara-Mbulu block recorded uplift events which are less than 3.2 Ma. This is supported by the presence of few upstream migrated knickpoints (KPds) especially marked in the Mbulu block and few in the Eyasi scarp (figs. 4.9 and 4.10).

iii) The drainage networks in this sector are controlled by a) recent tectonics where by rivers deviate when they encounter faults mostly in the northern sector in the Nguruman scarps, Sonjo transfer fault zone, OOB and Eyasi scarp for the southern sector. This control of drainage pattern is an indication that

drainage and uplift are still in competition and therefore equilibrium is not yet attained, this type of control is typical of young rift. b) Drainage network is also controlled by lithology, this is evident in Nguruman-Loita hills, STFZ and OOB while there is no clear evidence of lithological control in the southern sector.

iv) The placement of crater highland (CH) has played an important role in the control of direction of drainage networks. Most rivers flowing from the CH have a prominent NW-SE direction which in most part is contrary to the main drainage directions, which are E-W for older rivers in the north and recent rivers in the Sambu, Natron and Manyara scarps.

4.7 References

Alipoor, R., Poorkermani, M., Zare, M., El Hamdouni, R., 2011. Active tectonic assessment around Rudbar Lorestan dam site, High Zagros Belt (SW of Iran). Geomorphology 128, 1–14. https://doi.org/10.1016/j.geomorph.2010.10.014

Allen, P.A., Densmore, A.L., 2008. Sediment flux from an uplifting fault block. Basin Res. 12, 367–380. https://doi.org/10.1111/j.1365-2117.2000.00135.x

Bagdasaryan, G.P., Gerasimovskiy, V.I., Polyakov, A.I., Gukasyan, R.K., 1973. Age of volcanic rocks in the rift zones of East Africa. Geochemistry International 10, 66-71.

Bahrami, S., 2013. Analyzing the drainage system anomaly of Zagros basins: Implications for active tectonics. Tectonophysics 608, 914–928. https://doi.org/10.1016/j.tecto.2013.07.026

Baker, B.H., 1958. Geology of the Magadi area. Geological Survey of Kenya Report, 42. 81 pp.

Baker, B.H., 1986. Tectonics and volcanism of the southern Kenya Rift Valley and its influence on rift sedimentation. Geol. Soc. Lond. Spec. Publ. 25, 45–57. https://doi.org/10.1144/GSL.SP.1986.025.01.05

Bhattacharjee, D., Jain, V., Chattopadhyay, A., Biswas, R.H., Singhvi, A.K., 2016. Geomorphic evidences and chronology of multiple neotectonic events in a cratonic area: Results from the Gavilgarh Fault Zone, central India. Tectonophysics 677–678, 199–217. https://doi.org/10.1016/j.tecto.2016.04.022

Birt, C.S., Maguire, P.K.H., Khan, M.A., Thybo, H., Keller, G.R., Patel, J., 1997. The influence of pre-existing structures on the evolution of the southern Kenya Rift Valley — evidence from seismic and gravity studies. Tectonophysics 278, 211–242. https://doi.org/10.1016/S0040-1951 (97)00105-4

Boulton, S.J., Whittaker, A.C., 2009. Quantifying the slip rates, spatial distribution and evolution of active normal faults from geomorphic analysis: Field examples from an oblique-extensional graben, southern Turkey. Geomorphology 104, 299–316. https://doi.org/10.1016/j.geomorph.2008.09.007

Bull, W.B., McFadden, L.D., 1977. Tectonic geomorphology north and south of the Garlock Fault, California.

Burbank, D.W., Anderson, R.S., 2012. Tectonic geomorphology, 2nd ed. ed. J. Wiley & Sons, Chichester, West Sussex ; Hoboken, N.J.

Burrough, P.A., McDonnell, R.A., 1998. Creating continuous surfaces from point data. In: Burrough, P.A., Goodchild, M.F., McDonnell, R.A., Switzer, P., Worboys, M. (Eds.), Principles of Geographic Information Systems. Oxford University Press, Oxford, UK.

Cheng, K.-Y., Hung, J.-H., Chang, H.-C., Tsai, H., Sung, Q.-C., 2012. Scale independence of basin hypsometry and steady state topography. Geomorphology 171–172, 1–11. https://doi.org/10.1016/j.geomorph.2012.04.022

Cheng, Y., He, C., Rao, G., Yan, B., Lin, A., Hu, J., Yu, Y., Yao, Q., 2018. Geomorphological and structural characterization of the southern Weihe Graben, central China: Implications for fault segmentation. Tectonophysics 722, 11–24. https://doi.org/10.1016/j.tecto.2017.10.024

Clark, M.K., Schoenbohm, L.M., Royden, L.H., Whipple, K.X., Burchfiel, B.C., Zhang, X., Tang, W., Wang, E., Chen, L., 2004. Surface uplift, tectonics, and erosion of

eastern Tibet from large-scale drainage patterns: Surface uplift, Tectonics, and Erosion of Eastern Tibet. Tectonics 23, https://doi.org/10.1029/2002TC001402

Cowie, P.A., Attal, M., Tucker, G.E., Whittaker, A.C., Naylor, M., Ganas, A., Roberts, G.P., 2006. Investigating the surface process response to fault interaction and linkage using a numerical modelling approach: Surface process response to fault interaction and linkage. Basin Res. 18, 231–266. https://doi.org/10.1111/j.1365-2117.2006.00298.x

Cox, R.T., 1994. Analysis of drainage-basin symmetry as a rapid technique to identify areas of possible Quaternary tilt-block tectonics: An example from the Mississippi Embayment. Geol. Soc. Am. Bull. 106, 571. https://doi.org/10.1130/0016-7606(1994)106<0571:AODBSA>2.3.CO;2

Crossley, R., Knight, R.M., 1981. Volcanism in the western part of the Rift valley in Southern Kenya. Bulletin of Volcanology 44, 117–128.

Dawson, J.., 1992. Neogene tectonics and volcanicity in the North Tanzania sector of the Gregory Rift Valley: contrasts with the Kenya sector. Tectonics 81–92.

Delcaillau, B., Carozza, J.-M., Laville, E., 2006. Recent fold growth and drainage development: The Janauri and Chandigarh anticlines in the Siwalik foothills, northwest India. Geomorphology 76, 241–256. https://doi.org/10.1016/j.geomorph.2005.11.005

Densmore, A.L., 2004. Footwall topographic development during continental extension. J. Geophys. Res. 109. https://doi.org/10.1029/2003JF000115

Densmore, A.L., Dawers, N.H., Gupta, S., Allen, P.A., Gilpin, R., 2003. Landscape evolution at extensional relay zones: Landscape evolution at relay zones. J. Geophys. Res. Solid Earth 108. https://doi.org/10.1029/2001JB001741

Driese, S.G., Ashley, G.M., 2016. Paleoenvironmental reconstruction of a paleosol catena, the Zinj archeological level, Olduvai Gorge, Tanzania. Quat. Res. 85, 133–146. https://doi.org/10.1016/j.yqres.2015.10.007

Duffy, O.B., Bell, R.E., Jackson, C.A.-L., Gawthorpe, R.L., Whipp, P.S., 2015. Fault growth and interactions in a multiphase rift fault network: Horda Platform, Norwegian North Sea. J. Struct. Geol. 80, 99–119. https://doi.org/10.1016/j.jsg.2015.08.015

Ebinger, C., Djomani, Y.P., Mbede, E., Foster, A., Dawson, J.B., 1997. Rifting archaean lithosphere: the eyasi-manyara-natron rifts, east africa. J. Geol. Soc. 154, 947–960.

El Hamdouni, R., Irigaray, C., Fernández, T., Chacón, J., Keller, E.A., 2008. Assessment of relative active tectonics, southwest border of the Sierra Nevada (southern Spain). Geomorphology 96, 150–173. https://doi.org/10.1016/j.geomorph.2007.08.004

Eliet, P.P., Gawthorpe, R.L., 1995. Drainage development and sediment supply within rifts, examples from the Sperchios basin, central Greece. J. Geol. Soc. 152, 883–893. https://doi.org/10.1144/gsjgs.152.5.0883

Ellis, M.A., Densmore, A.L. & Anderson, R.S. (1999) Development of mountainous Topography in the basin ranges, USA. Basin Res., 11, 21

Flint, J.J., 1974. Stream gradient as a function of order, magnitude, and discharge. Water Resour. Res. 10, 969–973. https://doi.org/10.1029/WR010i005p00969

Flores-Prieto, E., Quénéhervé, G., Bachofer, F., Shahzad, F., Maerker, M., 2015. Morphotectonic interpretation of the Makuyuni catchment in Northern Tanzania using DEM and SAR data. Geomorphology 248, 427–439. https://doi.org/10.1016/j.geomorph.2015.07.049

Foster, A., Ebinger, C., Mbede, E., Rex, D., 1997. Tectonic development of the northern Tanzaian sector of the East African Rift System. J. Geol. Soc. 154, 689–700.

Frostick, L.E., Reid, I.A.N., 1989. Climatic versus tectonic controls of fan sequences: lessons from the Dead Sea, Israel. J. Geol. Soc. 146, 527–538. https://doi.org/10.1144/gsjgs.146.3.0527

Gawthorpe, R.L., Hurst, J.M., 1993. Transfer zones in extensional basins: their structural style and influence on drainage development and stratigraphy. J. Geol. Soc. 150, 1137–1152. https://doi.org/10.1144/gsjgs.150.6.1137

Gawthorpe, R.L., Leeder, M.R., 2008. Tectono-sedimentary evolution of active extensional basins. Basin Res. 12, 195–218. https://doi.org/10.1111/j.1365-2117.2000.00121.x

Giletycz, S., Loget, N., Chang, C.-P., Mouthereau, F., 2015. Transient fluvial landscape and preservation of low-relief terrains in an emerging orogen: Example from Hengchun Peninsula, Taiwan. Geomorphology 231, 169–181. https://doi.org/10.1016/j.geomorph.2014.11.026

Gloaguen, R. 2000. Analyse quantitative de l'extension continentale par imagerie Satellitale optique et radar. Application au rift sud-kenyan. Unpublished PhD Thesis, University of Brest, 200 p.

Howard, A.D., 1994. A detachment-limited model of drainage basin evolution. Water Resour. Res. 30, 2261–2285. https://doi.org/10.1029/94WR00757

Howard, A.D., 1967. Drainage analysis in geologic interpretation: a summation. Am. Assoc. Pet. Geol. Bull. 2246–2259.

Hurtrez, J.-E., Lucazeau, F., Lavé, J., Avouac, J.-P., 1999. Investigation of the relationships between basin morphology, tectonic uplift, and denudation from the study of an active fold belt in the Siwalik Hills, central Nepal. J. Geophys. Res. Solid Earth 104, 12779–12796. https://doi.org/10.1029/1998JB900098

Jackson, J., Leeder, M., 1994. Drainage systems and the development of normal faults: an example from Pleasant Valley, Nevada. J. Struct. Geol. 16, 1041–1059.

Jackson, J.A., White, N.J., Garfunkel, Z., Anderson, H., 1988. Relations between normal-fault geometry, tilting and vertical motions in extensional terrains: an example from the southern Gulf of Suez. J. Struct. Geol. 10, 155–170.

Jenson, S. K. and Domingue, J. O.: Extracting topographic structures from digital elevation data from geographic information system analysis, Photogramm. Eng. Rem. S., 54, 1593–1600, 1988.

Jordan, G., 2003. Morphometric analysis and tectonic interpretation of digital terrain data: a case study. Earth Surf. Process. Landf. 28, 807–822. https://doi.org/10.1002/esp.469

Joseph Mathew, M., 2016. Geomorphology and Morphotectonic Analysis of north Borneo. Lorient.

Keller, E.A., Pinter, N., 2002. Active tectonics: earthquakes, uplift, and landscape, 2nd ed. Ed, Books in the Prentice Hall earth science series. Prentice Hall, Upper Saddle River, N.J.

Kirby, E., Whipple, K.X., 2012. Expression of active tectonics in erosional landscapes. J. Struct. Geol. 44, 54–75. https://doi.org/10.1016/j.jsg.2012.07.009

Kirby, E., X. Whipple, K., 2001. Quantifying differential rock uplift rates via stream profi le analysis: Geology. Geology 29.

Lague, D., 2014. The stream power river incision model: evidence, theory and beyond: Stream power incision model. Earth Surf. Process. Landf. 39, 38–61. https://doi.org/10.1002/esp.3462

Le Gall, B., Nonnotte, P., Rolet, J., Benoit, M., Guillou, H., Mousseau-Nonnotte, M., Albaric, J., Deverchère, J., 2008. Rift propagation at craton margin. Tectonophysics 448, 1–19. https://doi.org/10.1016/j.tecto.2007.11.005

Leeder, M.R., Jackson, J.A., 1993. The interaction between normal faulting and drainage in active extensional basins, with examples from the western United States and central Greece. Basin Res. 5, 79–102.

Macintyre, R.M., Mitchell, J.G., Dawson, J.B., 1974. Age of Fault Movements in Tanzanian Sector of East African Rift System. Nature 247, 354–356. https://doi.org/10.1038/247354a0

Mackin, J. H. (1948), Concept of the graded river, Geol. Soc. Am. Bull., 59 (5), 463 (512), doi:10.1130/0016-7606(1948)59.

Mahmood, S.A., Gloaguen, R., 2012. Appraisal of active tectonics in Hindu Kush: Insights from DEM derived geomorphic indices and drainage analysis. Geosci. Front. 3, 407–428. https://doi.org/10.1016/j.gsf.2011.12.002

Mana, S., Furman, T., Carr, M.J., Mollel, G.F., Mortlock, R.A., Feigenson, M.D., Turrin, B.D., Swisher, C.C., 2012. Geochronology and geochemistry of the Essimingor volcano: Melting of metasomatized lithospheric mantle beneath the North Tanzanian Divergence zone (East African Rift). Lithos 155, 310–325. https://doi.org/10.1016/j.lithos.2012.09.009

Mana, S., Furman, T., Turrin, B.D., Feigenson, M.D., Swisher, C.C., 2015. Magmatic activity across the East African North Tanzanian Divergence Zone. J. Geol. Soc. 2014–072.

Mandlburger, G., Hauer, C., Höfle, B., Habersack, H., and Pfeifer, N.: Optimisation of LiDAR derived terrain models for river flow modelling, Hydrol. Earth Syst. Sci., 13, 1453–1466, 2009,http://www.hydrol-earth-syst-sci.net/13/1453/2009/.

Marín, D., Escalona, A., Grundvåg, S.-A., Nøhr-Hansen, H., Kairanov, B., 2018. Effects of adjacent fault systems on drainage patterns and evolution of uplifted rift shoulders: The Lower Cretaceous in the Loppa High, southwestern Barents Sea. Mar. Pet. Geol. 94, 212–229. https://doi.org/10.1016/j.marpetgeo.2018.04.009

Mayer, L., 1990. Introduction to quantitative geomorphology: an exercise manual. Prentice Hall, Englewood Cliffs, N.J.

Molin, P., Corti, G., 2015a. Topography, river network and recent fault activity at the margins of the Central Main Ethiopian Rift (East Africa). Tectonophysics 664, 67–82. https://doi.org/10.1016/j.tecto.2015.08.045

Molin, P., Corti, G., 2015b. Topography, river network and recent fault activity at the margins of the Central Main Ethiopian Rift (East Africa). Tectonophysics 664, 67–82. https://doi.org/10.1016/j.tecto.2015.08.045

Montgomery, D.R., Foufoula-Georgiou, E., 1993. Channel network source representation using digital elevation models. Water Resour. Res. 29, 3925–3934. https://doi.org/10.1029/93WR02463

Özsayın, E., 2016. Relative tectonic activity assessment of the Çameli Basin, Western Anatolia, using geomorphic indices. Geodin. Acta 28, 241–253. https://doi.org/10.1080/09853111.2015.1128180

Paul W Hare, Thomas W Gardner, 1985. Geomorphic indicators of vertical neotectonism along converging plate margins, Nicoya Peninsula, Costa Rica. Tecton. Geomorphol. 75–104.

Peacock, D.C.P., Price, S.P., Whitham, A.G., Pickles, C.S., 2000. The World's biggest relay ramp: Hold with Hope, NE Greenland. J. Struct. Geol. 22, 843–850. https://doi.org/10.1016/S0191-8141 (00)00012-2

Pike, R.J., Wilson, S.E., 1971. Elevation-relief ratio, hypsometric integral, and geomorphic area-altitude analysis. Geol. Soc. Am. Bull. 82, 1079–1084.

Plasman, M., Tiberi, C., Ebinger, C., Gautier, S., Albaric, J., Peyrat, S., Déverchère, J., Le Gall, B., Tarits, P., Roecker, S., Wambura, F., Muzuka, A., Mulibo, G., Mtelela, K., Msabi, M., Kianji, G., Hautot, S., Perrot, J., Gama, R., 2017. Lithospheric low-velocity zones associated with a magmatic segment of the Tanzanian Rift, East Africa. Geophys. J. Int. 210, 465–481. https://doi.org/10.1093/gji/ggx177

Ramsey, L.A., Walker, R.T., Jackson, J., 2008. Fold evolution and drainage development in the Zagros Mountains of Fars province, SE Iran. Basin Res. 20, 23–48. https://doi.org/10.1111/j.1365-2117.2007.00342.x

Schäuble H. (2003). HydroTools 1.0 for Arcview 3.x: hydrological analysis of small and large watersheds. Institute of Applied Geosciences Technical University of Darmstadt. 13 p.

Schumm, S.A., 1956. Evolution of drainage systems and slopes in Badlands at Perth Amboy, New Jersey. Geol. Soc. Am. Bull. 67, 597. https://doi.org/10.1130/0016-7606 (1956)67[597: EODSAS] 2.0.CO; 2

Schwanghart, W., Scherler, D., 2014. Short Communication: TopoToolbox 2 – MATLAB-based software for topographic analysis and modeling in Earth surface sciences. Earth Surf. Dyn. 2, 1–7. https://doi.org/10.5194/esurf-2-1-2014

Seeber, L., Gornitz, V., 1983. River profiles along the Himalayan arc as indicators of active tectonics. Tectonophysics 92, 335–367.

Sikes, N.E., Ashley, G.M., 2007. Stable isotopes of pedogenic carbonates as indicators of paleoecology in the Plio-Pleistocene (upper Bed I), western margin of the Olduvai Basin, Tanzania. J. Hum. Evol. 53, 574–594. https://doi.org/10.1016/j.jhevol.2006.12.008

Smith, M, Mosley, P, 1993. Crustal heterogeneity and basement influence on the development of the Kenya Rift, East Africa. Tectonics 591–606.

Snyder, N.P., 2000. Landscape response to tectonic forcing: Digital elevation model analysis of stream profiles in the Mendocino triple junction region, northern California. Geol. Soc. Am. Bull. 14.

Strahler, A.N., 1957. Quantitative analysis of watershed geomorphology. Trans. Am. Geophys. Union 38, 913. https://doi.org/10.1029/TR038i006p00913

Sung, Q.-C., Chen, Y.-C., 2004. Self-affinity dimensions of topography and its implications in morphotectonics: an example from Taiwan. Geomorphology 62, 181–198. https://doi.org/10.1016/j.geomorph.2004.02.012

Trudgill, B., Underhill, J.R., 2002. Introduction to the structure and stratigraphy of rift systems. AAPG Bull. 86, 931–934.

Vétel, W., Le Gall, B., Walsh, J.J., 2005. Geometry and growth of an inner rift fault pattern: the Kino Sogo Fault Belt, Turkana Rift (North Kenya). J. Struct. Geol. 27, 2204–2222. https://doi.org/10.1016/j.jsg.2005.07.003

Whipple, K.X., Tucker, G.E., 1999. Dynamics of the stream-power river incision model: Implications for height limits of mountain ranges, landscape response timescales, and research needs. J. Geophys. Res. Solid Earth 104, 17661–17674. https://doi.org/10.1029/1999JB900120

Willgoose, G., 1994. A statistic for testing the elevation characteristics of landscape simulation models. J. Geophys. Res. Solid Earth 99, 13987–13996. https://doi.org/10.1029/94JB00123

Wobus, C., Whipple, K.X., Kirby, E., Snyder, N., Johnson, J., Spyropolou, K., Crosby, B., Sheehan, D., 2006. Tectonics from topography: Procedures, promise, and pitfalls, in: Special Paper 398: Tectonics, Climate, and Landscape Evolution. Geological Society of America, pp. 55–74. https://doi.org/10.1130/2006.2398 (04)

Zernitz, E.R., 1932. Drainage patterns and their significance. J. Geol. 40, 498–521.

Chapitre 5

Structure du segment de rift Ol Doinyo Ogol

Ce chapitre concerne la structure du bloc d'Ol Doinyo Ogol, qui borde à l'ouest le fossé axial Magadi-Natron et dont l'évolution tectono-magmatique a enregistré les stades précoces du rifting. Seuls les résultats préliminaires de l'étude morphostructurale, complétée par les observations de terrain, sont présentés sous la forme d'une ébauche de papier qui sera soumis à **Tectonophysics** 'Tectono-magmatic development of an offset rift basin in the North Tanzanian Divergence framework, East Africa. The Ol Doinyo Ogol uplifted basin', Le Gall et al.

Ce papier sera finalisé, avec l'élaboration d'un modèle cinématique du RSK, lorsque les résultats des datations de ces laves seront disponibles.

Chapitre 5

Tectono-magmatic development of an offset rift basin in the North Tanzanian Divergence framework, East Africa. The Ol Doinyo Ogol uplifted basin.

Bernard Le Gall[1]*, Remigius Gama[1, 3], Gilles Chazot[1], Fred Jourdan[2], Nelson Boniface[3], Christel Tiberi[4], Nicolas Loget[5], Alain Le Hérissé[1], Pascal Tarits[1], Mathieu Plasman[4]

[1]UMR 6538 Géosciences Océan, IUEM, Brest University, France

[2] Western Australian Argon Isotope Facility, Centre and Department of Applied Geology, Curtin University, GPO Box U1987, Perth WA6845, Australia.

[3]Department of Geology, University of Dar es Salaam, Tanzania

[4]UMR 5243 Géosciences Montpellier, Montpellier University, France

[5]ISTeP, UMR 7193, Sorbonne University, Paris, France

*corresponding author, blegall@univ-brest.fr

5.1. Introduction

With regards to the archetypal half-graben architecture of the eastern magmatic branch of the East African rift (EAR), a number of anomalously-wide regional-scale patterns locally occur along the Kenya rift (Fig. 5.1). They all display an unusual breath (> 100 km) caused by an additional rift faulted block flanking consistently the axial depression to the west. In Central Kenya, the 100 km-wide Kerio-Baringo system comprises a pair of synthetic, easterly-facing half-grabens, filled with Miocene-Present volcanic and sedimentary sequences (Fig. 5.1) (Mugisha et al., 1997). Their similar rhomb-shaped geometry is the result of two intersecting bounding fault networks oriented NS (newly-formed) and NW-SE (inherited), such as the prominent Ol Kokwe fault (Dunkley et al., 1993; Le Turdu et al., 1999). According to the kinematic rift model of Hautot et al. (2000), the two adjoining half-grabens initially formed in Mio-Pliocene

times a wide rift domain which later experienced during Pleistocene times a focussing of strain/magmatism in the central part of the eastern basin.

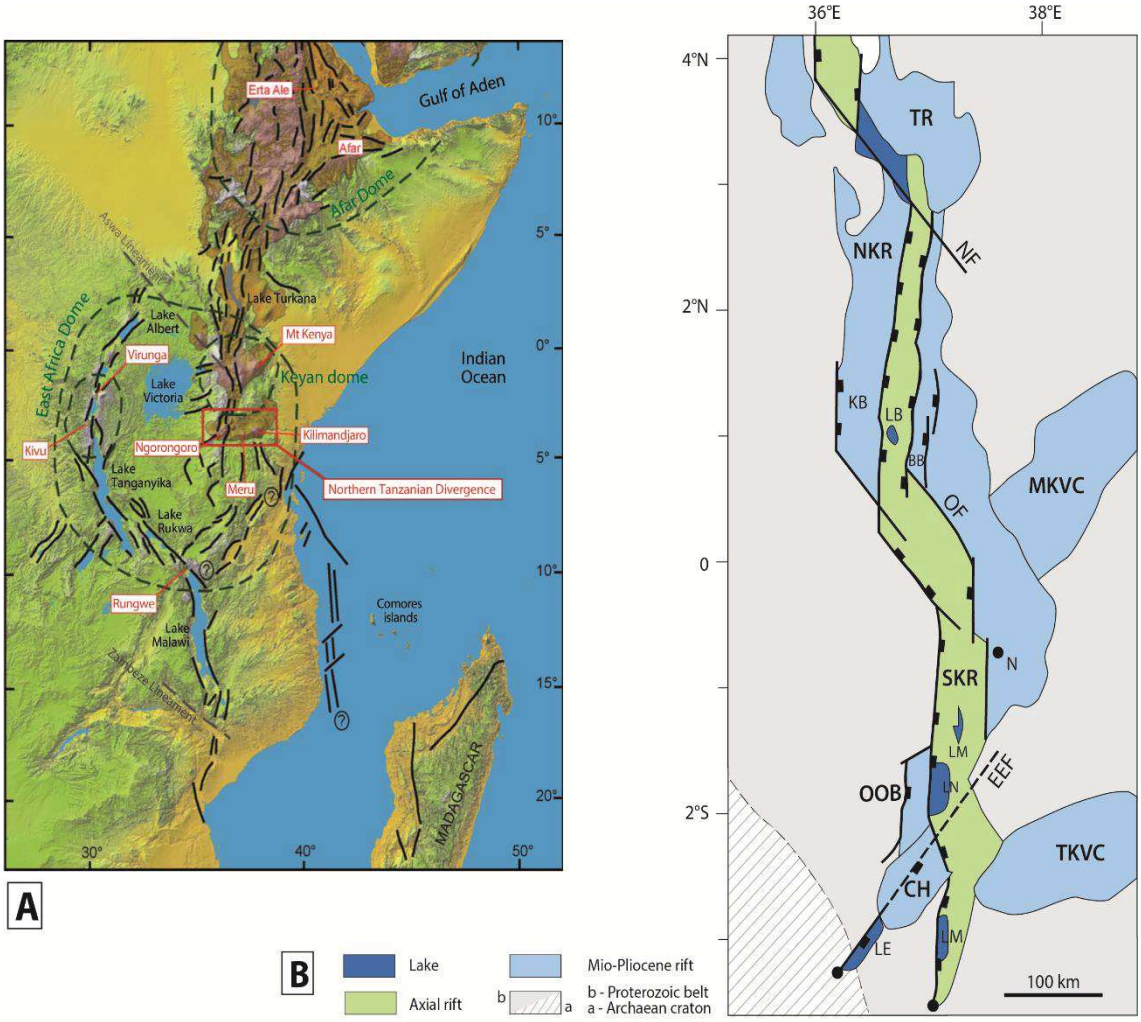

Fig. 5.1. Structural sketch map of the Kenya rift showing its segmented and zig-zag geometry in relation with inherited transverse faults oriented either (1) NW-SE in Northern and Central Kenya, or NE-SW in South Kenya. BB., Baringo-Bogoria basin; CH., Crater Highlands; EEF., ENS-Eyasi discontinuity; LE., lake Eyasi; Lm., lake Magadi; LM., lake Manyara; LN., lake Natron; MKVC., Mount Kenya volcanic chain; N., Nairobi; NF., N'Doto fault; NKR., North Kenya rift; OF., Ol Kowke fault; SKR., South Kenya rift; TKVC., Tarosero-Kilimanjaro volcanic chain; TR., Turkana rift. Inset shows the main morphostructural elements of the rift system in East Africa.

A quite similar scenario concerned the three synthetic half-graben basins extending further north in the >200 km-wide Turkana rift (Morley et al., 1992). In both cases, the submeridian (easterly-dipping) and transverse master fault networks define an obtuse angle, quite favorable to extensional downthrow and associated sedimentary depocenters (Hautot et al., 2000; Vétel & Le Gall, 2006), in agreement with natural or

experimental extensional patterns (Lezzar et al., 2002; Michon & Sokoutis, 2005), and which might have further triggered the lateral shift of strain in a number of adjoining faulted basins. Further south, a second anomalous rift pattern occurs between 2°-3°S in the South Kenya rift (SKR), but with significant structural changes (Figs. 5.1, 5.2).

There, the 70 km-wide Magadi-Natron axial trough is flanked to the west, along the bounding Natron fault, by a 40 km-wide rhomb-shaped uplift block composed of volcanic and sedimentary synrift series resting on top of Proterozoic basement rocks (Baker, 1958; Isaac & Curtis, 1974). The so-called Ol Doinyo Ogol block (OOB in the text) is limited to the west by a composite master fault-scarp system involving the submeridian Ol Doinyo Ogol fault (OOF) and a 25 km-wide zone of N70°-trending faults to the north, the so-called Sonjo transfer fault zone (STFZ). The latter connects northwards into the dextrally offset Nguruman master fault bounding the Magadi axial trough (Fig. 5.2A). NE-SW transverse rift trends are more extensively distributed further south in the North Tanzanian Divergence (NTD) where the rift is anomalously distributed over a >200 km-wide zone encompassing the Eyasi (W), Manyara (Central) and Pangani (E) diverging rift arms (Fig. 5.2A) (Dawson et al, 1992). The NE-SW Eyasi arm parallels Archaean and Proterozoic tectono-magmatic fabrics in the Mbulu plateau (Ebinger et al., 1997; Le Gall et al., 2008).

The spatial proximity of these atypical SKR and NTD rift patterns suggests common driving mechanisms, as recently proposed by Gama et al. (submitted), in relation with a crustal-scale basement-rooted discontinuity (ENS-Eyasi), oblique to the rift axis (Fig. 5.2C). However, timing of the onset of fault activity along the OOB-SFTZ bounding fault is still badly constrained because of missing age data about its volcanic hangingwall block, hence leading to uncertainties about the temporal development of the OOB offset block within the SKR-NTD framework. These limitations are further emphasized by the fact that the OOB has never so far benefitted from thorough structural studies.

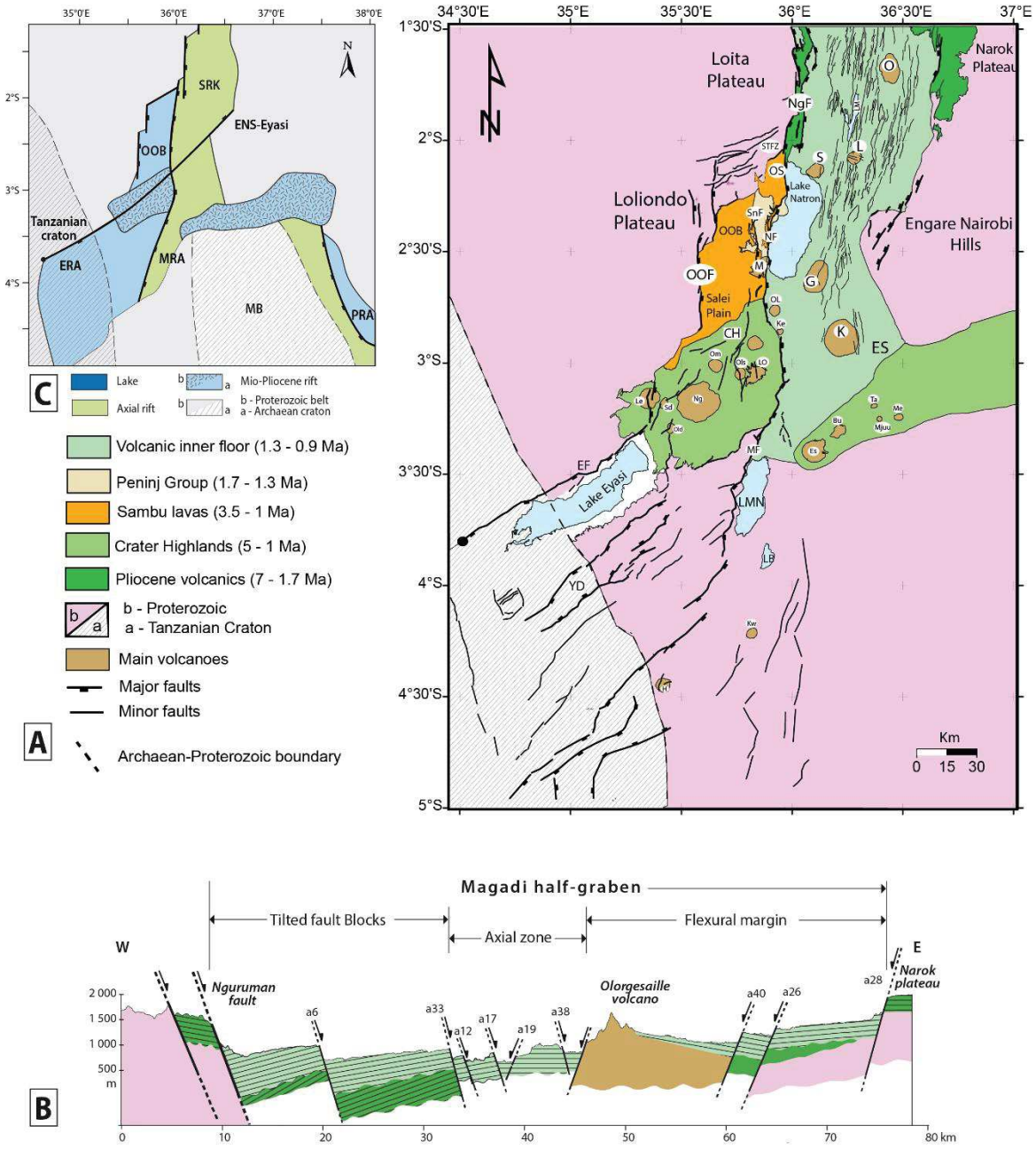

Fig. 5.2. Main rift structures in the South Kenya-North Tanzanian Divergence. A. Geological sketch map. CH., Crater Highlands; EA.,YD., Yaide depression; Eyasi rift arm; ET., Engaruka trough; K., Kilimanjaro volcano; MA., Manyara rift arm; MB., Masai block; MP., Mbulu plateau; MT. Magadi trough; NT., Natron trough; OOB., Ol Doinyo Ogol block; PA., Pangani rift arm; T., Tarosero volcano. B. Geological cross-section in the Magadi half-graben at the latitude of the Olorgesailie volcano. Vertical exaggeration = 5. Location in Fig. 5.2A. C. Structural sketch illustrating the role of a major inherited transverse discontinuity (ENS-Eyasi) on the rift architecture, modified from Gama et al. (submitted).

Most of previous works devoted to the OOB were rather focussed on (1) its volcano-sedimentary stratigraphic content (Isaac et al., 1974; McHenry et al., 2011), and (2) on the geochemistry/geochronology of its synrift volcanics (Manega, 1993; Foster et al., 1997). Consequently, the role of the OOB offset block during SKR rifting is neglected in most of published kinematic models, hence leading to underestimated bulk extension values (Muirhead et al., 2016).

It is the aim of the present work to propose a comprehensive structural history of the OOB offset rift domain by: (1) precising its morphostructural pattern, (2) constraining the timing of displacement along its bounding fault network, and (3) elaborating a multistage kinematic rift model that accounts for the origin and role of rift-parallel and transverse faults in the OOB-Magadi-Natron-Eyasi anomalously-propagating rift pattern. Our work is chiefly based on interpreted SRTM-30 m satellite imagery, combined to structural field observations, and further completed by new geochemical data and ^{40}Ar-^{39}Ar age dating of synrift volcanics.

5.2. Rift setting

The present-day rift configuration of the SKR with two adjoining rifted domains, i.e. the submeridian and linear Magadi-Natron axial trough to the east, and the OOB dextrally offset block to the west, is the result of a long-lived and polyphase rift history that initiated ca 7 Ma ago (Crossley, 1979), ahead of the grossly southerly-propagating EAR (Fig. 5.2A). Because of its prominent rift morphology, the Magadi-Natron trough is commonly regarded as representative of the entire SKR system. It forms a 70 km-wide, easterly-facing half-graben, bounded to the west by a highly-segmented master fault network that comprises from north to south the Nguruman double-fault system, the Sambu and Natron faults. Its inner floor is extensively covered by the 0.9-1.3 Ma-old Magadi Trachyte series (Isaac & Curtis, 1974; Muirhead et al., 2016) that dip gently westwards over the flexural margin of the basin (Fig. 5.2B). It is punctuated by a few axial volcanoes ranging in age from 2.0 Ma (Lenderut, Shombole) to 1.0 Ma (Gelai) (Evans et al., 1971; Foster et al., 1997; Mana et al., 2015). Oldest synrift volcanics are currently exposed over Proterozoic basement bounding relief either forming narrow faulted blocks along the Nguruman system to the west (ca 7 Ma-old Longitoto lavas), or capping the Narok plateau to the east (Baker, 1958). The 7 Ma-lasted rift history of the

SKR can be subdivided into two major successive rifting events. An early rift stage started at ca 7 Ma, and resulted in the development of the dextrally-offset proto-SKR half-graben, coeval to initial volcanism (Crossley et al., 1979). This early event is clearly documented to the North in the Nguruman fault-scarp framework, but it is much less accurately evidenced further south in the OOB under study. A younger rift event expressed by the emplacement of the 0.9-1.3 Ma Magadi Trachyte series over most of the entire Magadi-Natron half-graben. It was accompanied by extensional fault activity along the rejuvenated Nguruman fault-scarp and its southern prolongation along the newly-formed Sambu-Natron bounding fault. The intense intra-rift strain that occurred at that stage was accommodated by a dense normal fault grid dissecting the Magadi Trachyte inner floor (Fig. 5.2B). The spatial and temporal distribution of extension has been recently discussed in terms of inner fault- *versus* rift-bounding fault-related extension (Gama et al., submitted). These authors also emphasized the role of two specific structural features in the SKR, i.e. : (1) the Engare-Nairobi transverse basement salient on the eastern flank of the Natron trough and (2) the OOB offset block (Fig. 5.2B).

The OOB is a 30 x 70 km rhomb-shaped, faulted domain averaging 1200 m in altitude in the uplifted footwall block of the Natron fault (Fig. 5.3A). It is limited to the north and west by the OOF-STFZ composite fault-scarp system and to the south by volcanic transverse relief of the ca 5-1 Ma-old Crater Highlands (Bagdasaryan et al., 1973; Mollel, 2007). The bounding uplifted relief culminating at >2000 m in the Loliondo uplands, in the footwall of the OOF-STFZ fault network, are Proterozoic metamorphic terrains of the Usagaran belt (ca 600 Ma) (McConnell, 1972). Their deeply-incised topography is locally guided by km-scale folds in gneiss/micaschist rocks between more resistant quartzitic ridges (Fig. 5.3A). These folds are sharply cut by the OOF-STFZ master fault, hence demonstrating that basement ductile fabrics did not exert any control on rift fault trajectory in the OOB.

The OOB is composed of 2 juxtaposed rift domains displaying contrasted stratigraphic and structural contents, on both sides of the Sanjan submeridian fault (Figs. 5.3B, C). The resulting step-like cross-structure of the OOB*, via* its bounding (OOF and Natron) and intra-rift (Sanjan) fault networks, helps deciphering its synrift stratigraphic pattern. The oldest series form the unexposed and flat-lying floor of the 30 km-wide Salei plain to the west, in the hangingwall of the OOF.

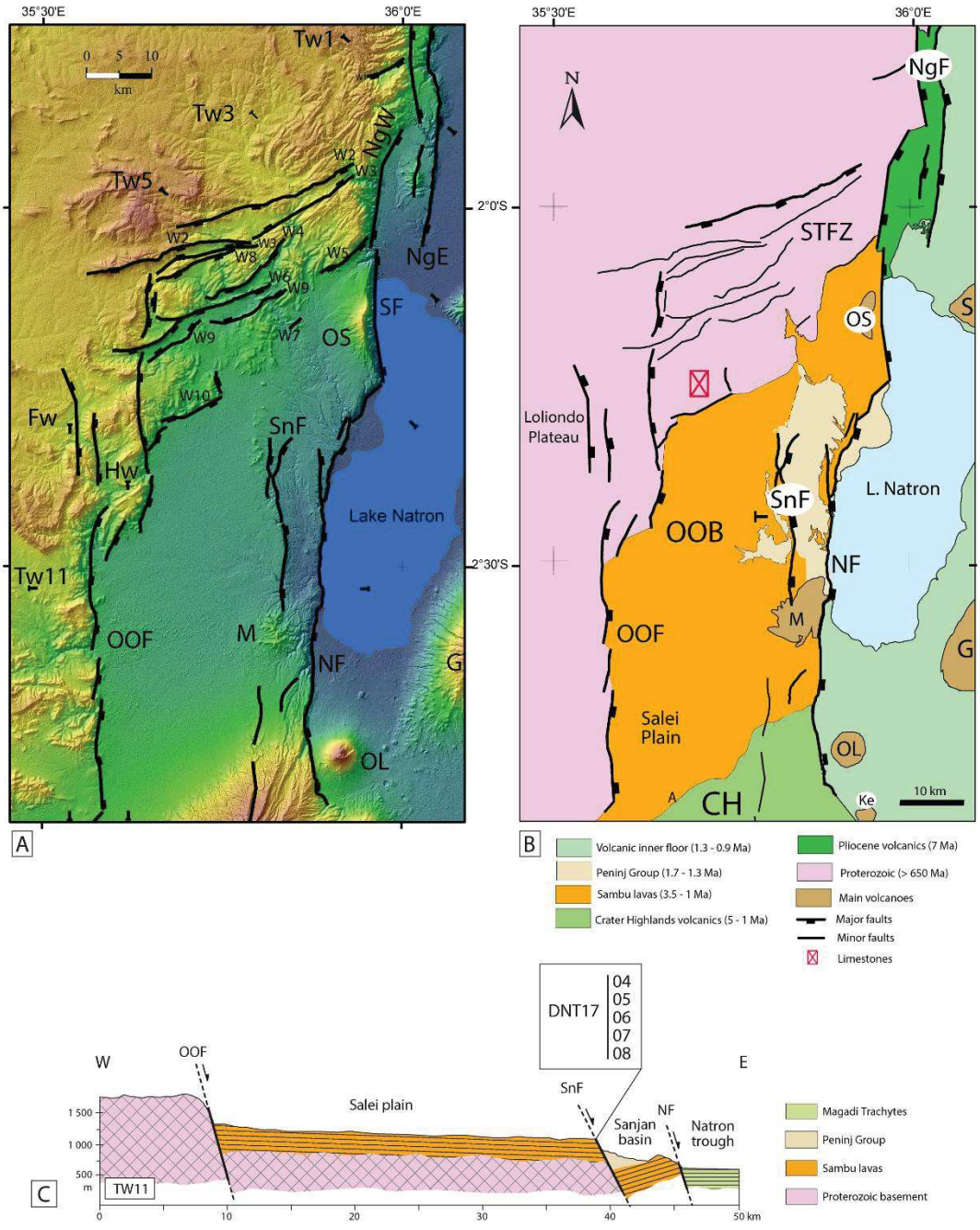

Fig. 5.3. Morphostructural and geological patterns in the Ol Doinyo Ogol offset rift domain. A. Topo30 digital elevation model. Location of (1) transverse (T1-3-5, Fig. 5.5), (2) cross-sections (TW11, Fig. 5.3C), and along-strike sections (Fw and Hw, Figs. 5.6). B. Corresponding (simplified) geological map, modified from Dundas & Adwalla (1999). Surficial sediments are not drawn. C. Geological cross-section showing the unfaulted volcanic floor of the Salei plain. The extrapolated position of volcanic samples in the Sanjan fault scarp is shown. Vertical exaggeration = 5.

These terrains are exposed to the east along the Sanjan fault scarp, as a succession of (undated) lava flows, averaging 5-6 m-thick each (Fig. 5.4D). These lavas might extend

continuously to the NE, beyond the northern tip point of the Sanjan fault, and connect with the 3.5-1.9 Ma volcanics of the Ol Doinyo Sambu magmatic complex. The Sambu lavas are also exposed further south along the Natron fault scarp (Figs. 5.4A, B) where they form the substratum of the Pleistocene Peninj Group filling the 30 km-long Sanjan faulted depression to the west (Figs. 5.3B, C) (Isaac & Curtis, 1974; Dundas & Adwalla, 1999).

Fig. 5.4. Field view of morphostructural and volcanic structures in the Ol Doinyo Ogol offset rift block. A. The Natron fault scarp cutting the Ol Doinyo Sambu volcano in the background. B. Focused view of the nearly flat-lying lava pile involved in the Natron footwall scarp (ca 80 m-high). C. Lavas of the Mosonik volcano covering, and post-dating the southern course of the Sanjan fault-scarp. D. Sampling of Sambu lavas from the Sanjan fault-scarp. E. Volcanic series forming topographic mesas on top of the Salei plain, NW of the Sanjan fault tip. Location in Fig. 5.3B.

It thus appears that the Sambu lavas lying in the immediate hangingwall of the OOF are only dated by lateral correlations with the (3.5-1.9 Ma) Ol Doinyo Sambu volcanics occurring >70 km further NE, hence leading to uncertainties about the temporal development of the OOF. More reliable ages should be supplied by the lavas exposed along the Sanjan fault scarp, in direct topographic connection with the OOF hangingwall volcanics. 6 lavas flows have been sampled for this purpose (see below).

5.3. Methodology

5. 3.1. Satelitte imagery analysis

Our work is principally based on the structural interpretation of SRTM-30 m imagery (SRTM V3.1,1 arcsec, Universal Transverse Mercator projection following Geodetic System WGS84), covering the SKR at 1°-3° and 35°30'-36°10'E,with lateral and vertical resolutions of respectively, 30 m and 8 m (Fig. 5.3A).

5.3.2. $^{40}Ar/^{39}Ar$ geochronology

Groundmass chips from 16 samples were separated from either the 150-215 μm or the 215-315 μm fractions using a Frantz isodynamic magnetic separator and were hand-picked grain-by-grain under the binocular stereomicroscope. The chips were further leached using diluted HF (2N) for 5 minutes and thoroughly rinsed in distilled water and loaded in an aluminium disc, along with unrelated samples and standards. The disc containing the groundmass samples was irradiated for 3 hours and included a series of fully intercalibrated FCs standards for which ages of 99.74 Ma (±0.10%; Renne et al., 2011) were used. The discs were Cd-shielded (to minimize undesirable nuclear interference reactions) and irradiated in the Oregon State university nuclear reactor (USA) in central position. The mean J-values computed from standard grains within the small pits yielded a value of 0.0008284 (± 0.11%).

Mass discrimination was monitored regularly through the analysis using an automated air pipette and provided mean values ranging from 0.992634 (± 0.03%) to 0.993714 (± 0.04%) per dalton (atomic mass unit) relative to an air ratio of 298.56 ± 0.31. The correction factors for interfering isotopes were ($^{39}Ar/^{37}Ar$) Ca = 6.95×10^{-4} (± 1.3 %), ($^{36}Ar/^{37}Ar$) Ca = 2.65×10^{-4} (± 0.84 %) and ($^{40}Ar/^{39}Ar$) K = 7.30×10^{-4} (± 12.4 % ; Renne et al., 2013). The $^{40}Ar/^{39}Ar$ analyses were performed at the Western Australian Argon Isotope Facility at Curtin University. Groundmass populations (5mg per sample) were step-heated using a continuous 100 W PhotonMachine© CO_2 (IR, 10.4 μm) laser fired on the chips during 60 seconds. Each of the standard crystals was fused in a single step. The gas was purified in an extra low-volume stainless steel extraction line of 240cc and using one SAES AP10 and two GP50 getter. Ar isotopes were measured in static mode using a low volume (600 cc) ARGUS VI mass spectrometer from Thermofisher© (Phillips & Matchan, 2013) set with a permanent resolution of ~200. Measurements were carried out in multi-collection mode using 4 faradays to measure mass 40 to 37 and a low-noise compact discrete dynode ion counter to measure mass 36. We measured the relative abundance of each mass simultaneously using 10 cycles of peak-hopping and 16 seconds of integration time for each mass. Detectors were calibrated to each other electronically and using Air shot beam signals. The raw data were processed using the ArArCALC software (Koppers, 2002) and the ages have been calculated using the decay constants recommended by Renne et al. (2011). Blanks were monitored every 2 to 3 steps. All parameters and relative abundance values are provided in Annex 1 and have been corrected for blank, mass discrimination and radioactive decay. Individual errors in Annex 2 are given at the 1σ level.

Following Oostingh et al. (2017), we provide both the inverse isochron ages and we use the $^{40}Ar/^{36}Ar$ value and its uncertainty as measured by the inverse isochron, to correct for the true value of the trapped ratio. Only inverse isochron $^{40}Ar/^{36}Ar$ values derived from an isochron fit with probability of fit (p) > 0.05 were used for the correction. We did not calculate any plateau ages using insignificant inverse isochrons. Our criteria for the determination of plateau and isochrons are as follows: they must include at least 70% of ^{39}Ar and should be distributed over a minimum of 3 consecutive steps agreeing at 95% confidence level and satisfying a probability of fit (p) of at least 0.05. Plateau ages are given at the 2σ level and are calculated using the mean of all the plateau steps, each

weighted by the inverse variance of their individual analytical error. Mini-plateaus are defined as plateaus except that they include only between 50 and 70% of ^{39}Ar released, and are deemed less reliable than plateaus. Uncertainties include analytical and J-value errors. Errors with all sources of uncertainties are indicated by a square bracket (e.g., ±0.16 Ma).

5.4 Results

5.4.1. The morphostructural pattern

- The Sonjo transverse fault zone

At ca 1°53'S', the Nguruman master fault system bounding the Magadi trough to the west connects laterally westwards into a quite atypical N60°-oriented fault zone (SFTZ), exclusively developed in Proterozoic metamorphic terrains (Figs. 5.3A, 5). The STFZ radically differs from others transverse fault structures in the Kenya rift with (1) its map-dimensions (40 x 25 km), and (2) the geometry and displacement patterns of its internal fault structures. The 5-6 individual closely-spaced normal faults involved in the STFZ, face dominantly to the SE, and limit narrow (2-3 km-wide) faulted-blocks (and locally horst-grabens) that step down gradually to the SE towards the OOB volcanic floor. The >700 m-high individual fault scarps are deeply incised and thus typically evoke early rift structures. It is striking to note that the length of the internal fault array strictly equals the 40 km-wide overstep of the W/Nguruman-OOF fault system, in a similar way as a breached relay ramp (Gawthorpe & Hurst, 1993) connecting two collinear rift-bounding faults. Though being oriented obliquely to the direction of the regional extension (nearly EW), the transverse fault pattern shows dominantly dip-slip displacement on the cross-profiles (Fig. 5.5), without any evidence for strike-slip component on the DEM in Fig. 5.3A. This appears to be a common structural feature of transfer faults in the EAR (Bosworth, 1985; Ebinger et al., 1989). It is thus suggested that the entire SKR system experienced a relatively intricate 3-dimensional extensional pattern at an early rifting stage, possibly in relation with local stress rotation, as commonly reported about transfer fault zones in the EAR (Morley, 1988), or elsewhere (Kattenhorn, 2004). Lastly, the origin of transverse faults in the STFZ, in relation with either structural inheritance and/or paleostress orientations, is not directly constrained, but their parallelism with Proterozoic

fabrics further south in the Mbulu plateau (Fig. 5.2B) suggests their possible control by basement brittle discontinuites.

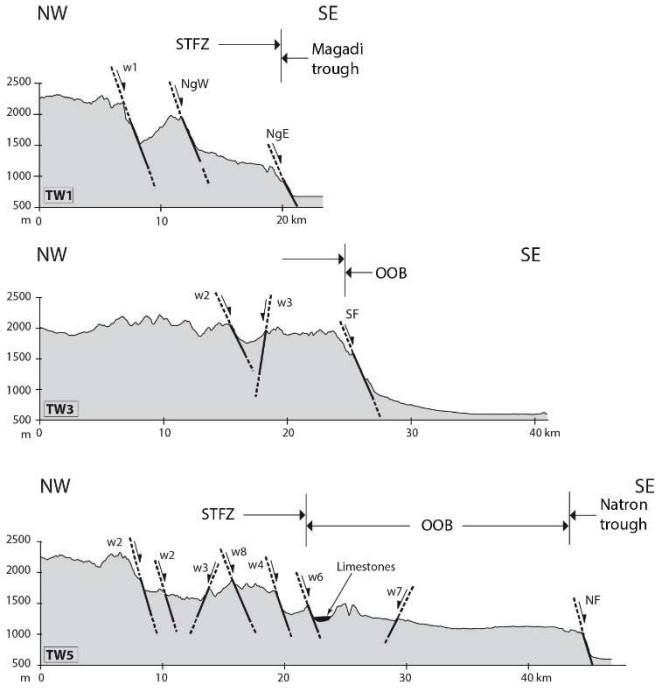

Fig. 5.5. Topographic profiles in the Sonjo transverse fault zone showing (1) the incised topography of the basement faulted blocks and (2) the apparently prominent extensional component of the STFZ inner fault network. The position of lacustrine limestones discussed in the text is drawn in section TW5. Vertical exaggeration = 10. Location in Fig. 5.3A.

- The Ol Doinyo Ogol segmented fault

The OOF is a >80 km long, submeridian, easterly-facing segmented fault composed of two major dextrally offset segments that connect *via* a ca 5 km-long, sigmoid-shape overlapping zone at around 2°25'. The along-strike topographic profile in Fig. 5.6 shows the highly-dissected morphology of its basement footwall uplift block, with altitudes decreasing progressively southwards from 2300 to 1500 m, in contrast with the regular and shallowly-dipping (to the N) geometry of its hangingwall surface.

The throw profile of the OOF, obtained by compiling the two topographic transcts, typically characterizes a half bell-shaped profile ending at a southern tip point located at ca 50 km south of the maximum fault height (T_{max} = 1000 m) in Fig. 5.6. Assuming that fault activity along the OOF initiated synchronously to the eruption of the OOB lavas, inferred to be > 400 m-thick in the OOB (Baker, 1958; Dundas & Adwalla, 1999), would

indicate a maximum extension (e_{max}) value of ca 2400 m, provided that the average dip of the OOF equals the classical value of 60°, and applying the equation (1) $e_{max} = T.tg60°$.

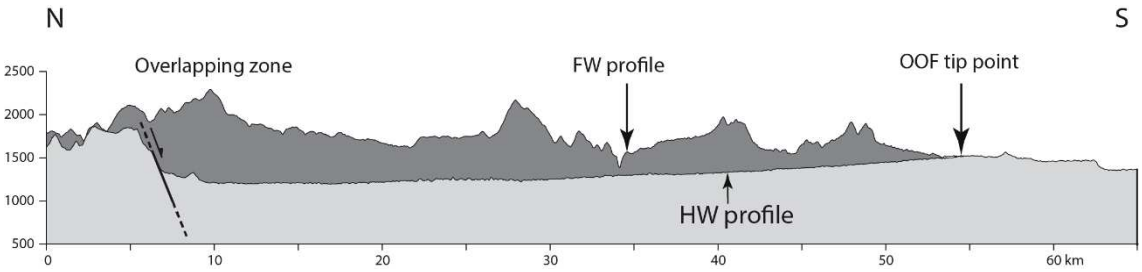

Fig. 5.6. Superposed along-strike topographic sections in the immediate footwall (Fw) and hangingwall (Hw) blocks of the OOF showing the throw profile of the fault. Note (1) the incised topography of the Proterozoic basement footwall block, (2) the regular and slightly-dipping (to the N) attitude of the volcanic (Sambu lavas) hangingwall surface, and (3) the southerly decrease of throw towards a tip point located 50 km south of the overlapping zone. Vertical exaggeration = 6. Location in Fig. 5.3A.

The similarly-eroded topography of both the Nguruman and OOF footwall blocks indicates their early development during initial rifting in the SKR. Initiation of the Nguruman fault-scarp as early as 7 Ma, synchronously to the Lengitoto synrift lavas, has long been assessed (Baker, 1958). Applying the same reasoning to the OOF fault/lavas offset pattern to the SW, should imply that it initiated later, according to the oldest available ages (< 4 Ma) about synrift volcanics in the OOB. Confirming and precising this hypothesis is one of the main target of the present work.

About the timing of fault activity along the STFZ, one interesting information is supplied by the published geological map of Dundas & Adwalla (1999) that shows discrete inliers of sedimentary limestones resting directly on top of Proterozoic metamorphic rocks in the lowest faulted blocks of the STFZ, but systematically higher than the volcanic inner floor in the OOB (Fig. 5.3B). According to these authors, these porcelaneous limestones are lacustrine sediments enclosing specific, but undated, faunas (ostracods). The thin section in Fig. 5.8A also reveals no-diagnostical stromatolith-like organisms. Intra-formational brecciated facies observed in the field likely resulted from syn- to post-hydrothermal events (Fig. 5.8B). If excluding the complete removing of volcanic material by erosion in these uplifted fault blocks, it can be suggested that these limestones were deposited above basement terrains flooring the paleo-Magadi-Natron lake, with fresh lacustrine water, at an initial fault stage, but prior to synrift magmatism.

- The Sanjan fault-basin system.

The sketch structural map of the 8 x 30 km Sanjan faulted basin in Fig. 5.7B is compiled from SRTM DEM data (Fig. 5.7A), field data, and the published map of Sherrod et al. (2013) for its southernmost part (south of 2°30').

Its infilling synrift series correspond to the Pleistocene Peninj Group that comprises two superposed volcano-sedimentary formations (Isaac & Curtis, 1974; Dundas & Adwalla, 1999). The lowest Humbu Fm. is extensively exposed over most of the length of the Sanjan faulted basin. Its deep incision supplies relatively-high vertical sections suitable for structural issues (Fig. 5.8C). It is mainly composed of poorly-sorted deltaic sandstones and interstitial clays (Fig. 5.8D), in addition to layers and lenses of trachytic tuffs (Fig. 5.8F) that yielded 1.7 Ma ages (Isaac & Curtis, 1972). The overlying Moinik Fm. is restricted to the southernmost part of the Sanjan basin. It mainly comprises clay facies, typical of more stable lacustrine conditions (Dundas & Adwalla (1999). It also contains interstratified nephelinitic lavas that have been dated at 1.5-1.1 Ma (McIntyre et al., 1974; Manega, 1993; Foster et al., 1997).

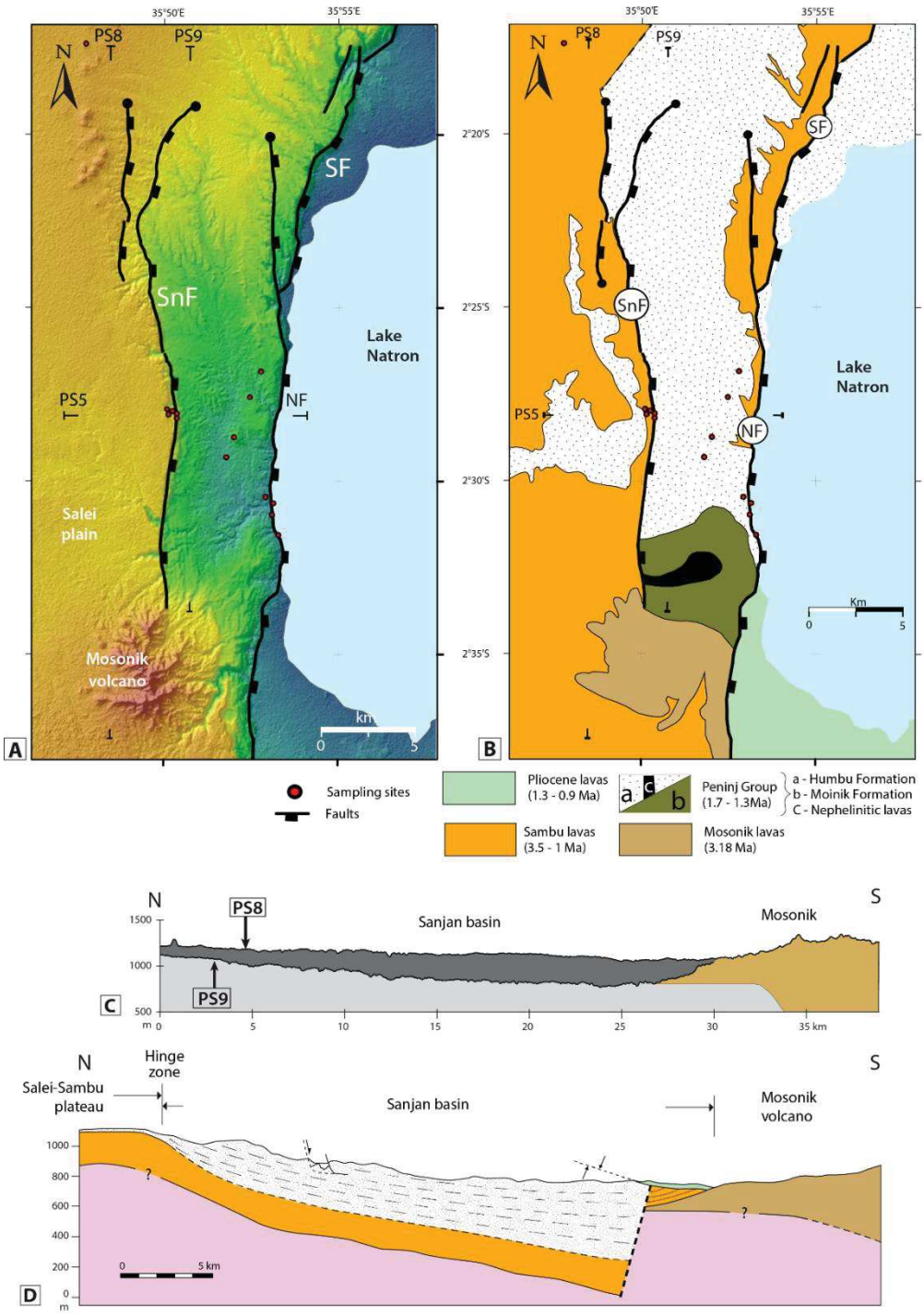

Fig. 5.7. Structure of the Sanjan Pleistocene faulted basin. A. Focused view of the SRTM30 DEM showing the map-trace of its two bounding faults. Note the Mosonik lavas overlying the Sanjan fault to the south. Full circles are fault tip points. Location of topographic PS8-9 in Fig. 5.7C is shown. B. Corresponding geological map. Surficial sediments not shown. The location of sampled volcanic rocks and field photographs in Figs. 5.4 and 5.8 is shown. C. Superposed along-strike topographic sections in the immediate footwall (PS8) and hangingwall (PS9) blocks of the Sajan fault showing the throw profile of the fault. Vertical exaggeration = 5. Location in Fig. 5.7A. D. Along-strike geological section (PS9) showing the NS flexural geometry of the basin, in relation with increasing displacement along the Sanjan fault.

The along-strike architecture of the Peninj filling series on the submeridian, 30 km-long geological section in Fig. 5.7D provides fruitful insights into the structural development of the Sanjan basin. The topographic profile first shows the abrupt southerly change from (1) the <1200 m-high tabular surface of the Ol Doinyo Sambu bounding plateau to (2) the incised and shallowing topography, down to 6-700 m, of the Peninj basin infilling that (3) rises abruptly along the northern flank of the Mosonik volcano. The Peninj thickness pattern strictly fits with the topography, as evolving southwards from a thin sedimentary layer over the plateau to a wedge-shaped package, inferred to be as thick as 600 m in the most complete stratigraphic section (Fig. 5.7D) (Isaac & Curtis, 1974; Dundas & Adwalla, 1999).

The Peninj stratigraphy also youngs progressively southwards, up to the Moinik Fm, in agreement with regional strata dips <10° in average. Interestingly, direct correlations exist between the varying topography/thickness pattern above and the submeridian throw profile of the Sanjan fault in Fig. 5.7C. Inded, the flexural hinge line of the basin at around 2°20’ nearly coincides with the northern tip point of the fault, hence arguing for the syntectonic development of the Sanjan basin in Pleistocene times, as the hangingwall block of the Sanjan normal fault. This fault/basin event was likely accompanied by intra-basinal deformation, evidenced in the Humbu layered sequences by the structures in Fig. 5.8E. They express by an intricate network of fold/fault structures within an extensional sliding wedge, bounded by a SE-facing normal fault that connects downwards into a flat-lying decollement level. The N70°E orientation of the bounding normal fault is nearly parallel to the northern basin flexure. The presence of a regional-scale transverse fault structure at the southern extremity of the Sanjan basin is also inferred from the following stratigraphic evidences. Assuming that the basaltic lavas occurring in the topographically lowest part of the basin to the south, close to the Moinik Fm, are parts of the Sambu volcanic substratum, implies that the Humbu Fm is absent, or very reduced in this area. The more likely explanation for this stratigraphic pattern is a transverse synsedimentary normal fault, facing globally to the north, coeval to Humbu deposits, and the substratum (volcanic) footwall of which is only overlain by the younger Moinik lavas (Fig. 5.7D).

The initial extent of the ancestral lake Natron to the east, in the hangingwall block of the younger Natron fault, is unknown.

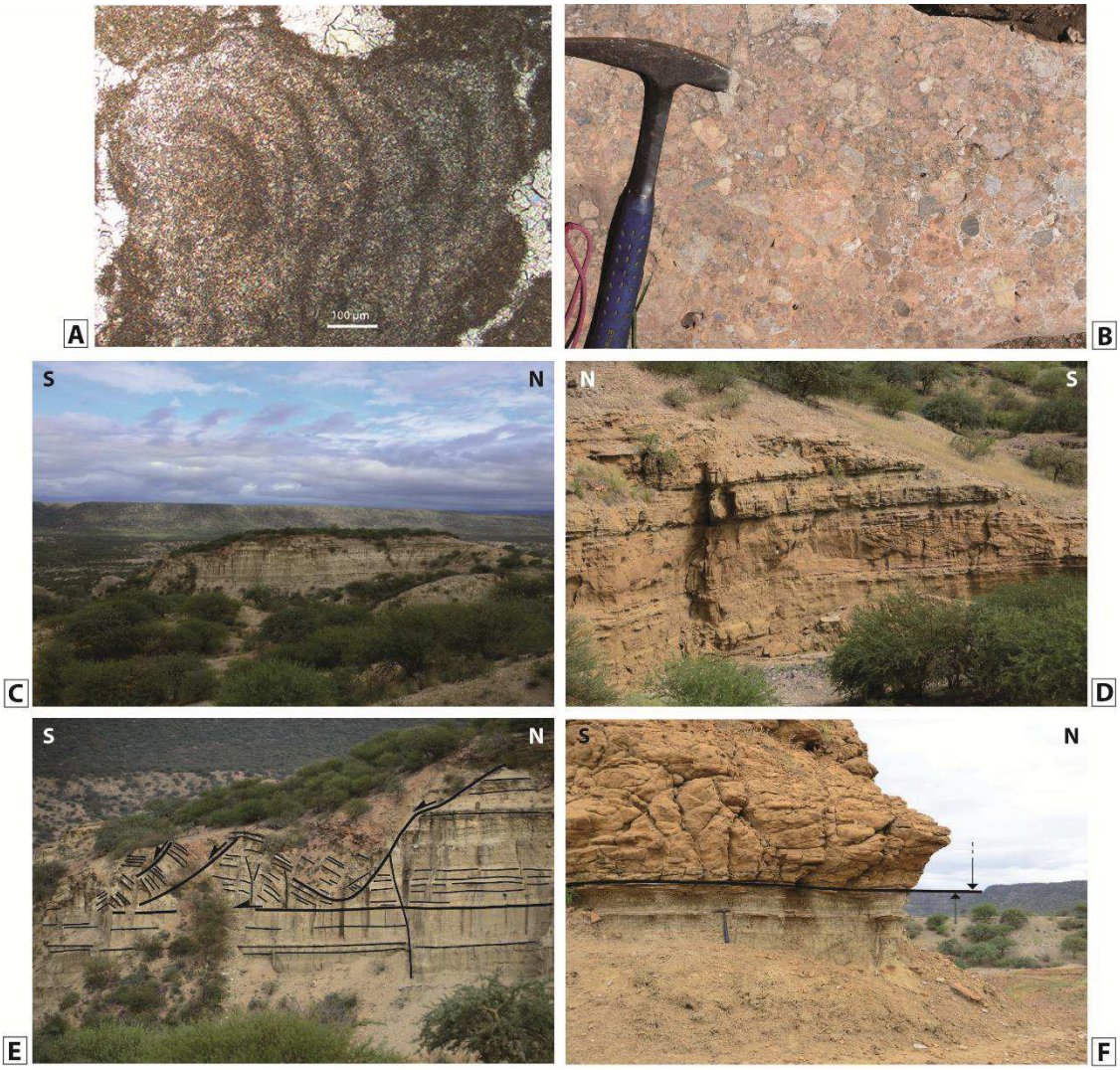

Fig. 5.8. Field view of sedimentary and tectonic structures in the synrift series in the OOB. A. Thin section of fossileferous (stromatolith-like organisms) limestones overlying basement terrains in the STFZ. Location in Fig. 5.3B. B. Brecciated (hydrothermal ?) facies in the STFZ limestones. C. Incised topography of the Humbu deltaic Fm. Note (1) the shallow southerly dip (a few °) of the strata and (2) the Sanjan fault scarp in the background. D. Flat-lying grit sequences in the Humbu Fm. with a medium level displaying oblique stratifications. The cliff is ca 20 m-high. E. A large-scale collapse-related sliding package (SE-directed) in the Humbu Fm. F. Upper tuff sequence overlying conformably terrigeneous facies in the Humbu Fm. Location in Fig. 5.7B.

5.4.2. Synrift volcanics

Synrift volcanic rocks in the OOB occur in various stratigraphic and structural patterns. Our sampling strategy was performed in order to get the most comprehensive overview of the geochemical and geochronological patterns of its entire volcanic content,

including Peninj and pre-Peninj substratum series. 16 rock sampling have been collected as follows: 5 samples in the thick lava succession exposed along the >200 m-high Sanjan fault scarp at 2°27''S (DNT17-O4, 05, 06, 07, 08); 3 rock samples in the neck-like hills emerging from the footwall surface to the NE, in the Nakuta area (NTD17-09, 10, 11); 1 rock sample from the Ol Doinyo Sambu volcano (NTD17-12); 6 rock samples from volcanics either interstratified in or underlying the OOB sedimentary infill (NTD17-13, 14, 15, 16, 17, 18), and 1 rock sample from the inferred youngest volcanics capping the Upper Peninj volcanics to the south (NTD17-20).

- Petrogaphy and geochemistry

The volcanic succession exposed along the 200 m-high Sanjan fault scarp is composed of relatively thick lava flows, 5-6 m in average, with no clear internal magmatic structures. Their respective contacts have not been observed. The 5 collected lava samples come from the highest part (DNT17-04), middle part (DNT17-05, -06, -O7), and lowest part (DNT17-08) of the fault scarp (Fig. 5.3B). They correspond to relatively porphyritic and crystallized basaltic lavas. The porphyritic facies contain olivine, clinopyroxenes and plagioclase phenocrysts.

5.5 Conclusion actuelle

Dans l'état actuel de ce travail, les analyses chimiques ont été réalisées et doivent être inclues dans l'article avec les datations attendues dans les mois qui viennent. Ce chapitre finit donc avec les derniers points présentés au dessus.

5.6 References

Baker, B.H., 1958. Geology of the Magadi area. Geological Survey of Kenya Report, 42. 81 pp.

Bosworth, W., 1985. Geometry of propagating rifts. Nature 316, 625–627.

Crossley, R., 1979. The Cenozoic stratigraphy and structure of the western part of the Rift Valley in southern Kenya. J. Geol. Soc. 136, 393–405. https://doi.org/10.1144/gsjgs.136.4.0393

Dawson, J.., 1992. Neogene tectonics and volcanicity in the North Tanzania sector of the Gregory Rift Valley: contrasts with the Kenya sector. Tectonics 81–92.

Dundas, D. L., and G.W. Awadalla. 1999. "Quarter Degree Sheet 16 & 27 Loliondo." Geological Survey of Tanzania. Dodoma.

Dunkley, P.N.; Smith, M.; Allen, D.J.; Darling, W.G.. 1993 The geothermal activity and geology of the northern sector of the Kenya Rift Valley. Nottingham, UK, British Geological Survey, 202pp. (SC/93/001).

Ebinger, C., Djomani, Y.P., Mbede, E., Foster, A., Dawson, J.B., 1997. Rifting archaean lithosphere: the eyasi-manyara-natron rifts, east africa. J. Geol. Soc. 154, 947–960.

Ebinger, C.J., Deino, A.L., Drake, R.E., Tesha, A.L., 1989. Chronology of volcanism and rift basin propagation: Rungwe Volcanic Province, East Africa. J. Geophys. Res. Solid Earth 94, 15785–15803. https://doi.org/10.1029/JB094iB11p15785

Evans, A.L., Fairhead, J.D., Mitchell, J.G., 1971. Potassium—Argon Ages from the Volcanic Province of Northern Tanzania. Nat. Phys. Sci. 229, 19.

Foster, A., Ebinger, C., Mbede, E., Rex, D., 1997. Tectonic development of the northern Tanzaian sector of the East African Rift System. J. Geol. Soc. 154, 689–700.

Gawthorpe, R.L., Hurst, J.M., 1993. Transfer zones in extensional basins: their structural style and influence on drainage development and stratigraphy. J. Geol. Soc. 150, 1137–1152. https://doi.org/10.1144/gsjgs.150.6.1137

Hautot, S., Tarits, P., Whaler, K., Le Gall, B., Tiercelin, J.-J., Le Turdu, C., 2000. Deep structure of the Baringo Rift Basin (central Kenya) from three-dimensional magnetotelluric imaging: Implications for rift evolution. J. Geophys. Res. Solid Earth 105, 23493–23518. https://doi.org/10.1029/2000JB900213

Isaacs, G.L., Curtis, G.H., 1974. Age of early Acheulian industries from the Peninj Group, Tanzania. Nature 249, 624.

Kattenhorn, S.A., 2004. Strike-slip fault evolution on Europa: evidence from tailcrack geometries. Icarus 172, 582–602. https://doi.org/10.1016/j.icarus.2004.07.005

Kiram E. Lezzar, 1 Jean-Jacques Tier, 2002. Control of normal fault interaction on the distribution of major Neogene sedimentary depocenters, Lake Tanganyika, East African rift. AAPG Bull. 86. https://doi.org/10.1306/61EEDC1A-173E-11D7-8645000102C1865D

Le Gall, B., Nonnotte, P., Rolet, J., Benoit, M., Guillou, H., Mousseau-Nonnotte, M., Albaric, J., Deverchère, J., 2008. Rift propagation at craton margin. Tectonophysics 448, 1–19. https://doi.org/10.1016/j.tecto.2007.11.005

Le Turdu, C., Tiercelin, J.J., Richert, J.P., Rolet, J., Xavier, J.P., Renaut, R.W., Lezzar, K.E., Coussement, C., 1999. Influence of preexisting oblique discontinuities on the geometry and evolution of extensional fault patterns: evidence from the Kenya Rift using SPOT imagery. Geosci. Rift Syst. East Afr. 44, 173–91.

Macintyre, R.M., Mitchell, J.G., Dawson, J.B., 1974. Age of Fault Movements in Tanzanian Sector of East African Rift System. Nature 247, 354–356. https://doi.org/10.1038/247354a0

Mana, S., Furman, T., Turrin, B.D., Feigenson, M.D., Swisher, C.C., 2015. Magmatic activity across the East African North Tanzanian Divergence Zone. J. Geol. Soc. 2014–072.

Manega, P.C. 1993. Geochronology, geochemistry and isotopic study of the Plio-Pleistocene hominid sites and the Ngorongoro Volcanic Highland in northern Tanzania. PhD thesis, Univ. Colorado.

McHenry, L.J., Luque, L., Gómez, J.Á., Diez-Martín, F., 2011. Promise and pitfalls for Characterizing and correlating the zeolitically altered tephra of the Pleistocene Peninj Group, Tanzania. Quat. Res. 75, 708–720. https://doi.org/10.1016/j.yqres.2010.11.008

Michon, L., Sokoutis, D., 2005. Interaction between structural inheritance and extension direction during graben and depocentre formation: An experimental approach. Tectonophysics 409, 125–146. https://doi.org/10.1016/j.tecto.2005.08.020

Morley, C.K., 1988. Variable extension in lake Tanganyika. Tectonics 7, 785–801.

Morley, C.K., Wescott, W.A., Stone, D.M., Harper, R.M., Wigger, S.T., Karanja, F.M., 1992. Tectonic evolution of the northern Kenyan Rift. J. Geol. Soc. 149, 333–348. https://doi.org/10.1144/gsjgs.149.3.0333

Mugisha, F., Ebinger, C.J., Strecker, M., Pope, D., 1997. Two-stage rifting in the Kenya rift: implications for half-graben models. Tectonophysics 278, 63–81. https://doi.org/10.1016/S0040-1951 (97)00095-4

Muirhead, J.D., Kattenhorn, S.A., Lee, H., Mana, S., Turrin, B.D., Fischer, T.P., Kianji, G., Dindi, E., Stamps, D.S., 2016. Evolution of upper crustal faulting assisted by magmatic volatile release during early-stage continental rift development in the East African Rift. Geosphere 12, 1670–1700. https://doi.org/10.1130/GES01375.1

Phillips, D., Matchan, E.L., 2013. Ultra-high precision 40Ar/39Ar ages for Fish Canyon Tuff and Alder Creek Rhyolite sanidine: New dating standards required? Geochim. Cosmochim. Acta 121, 229–239. https://doi.org/10.1016/j.gca.2013.07.003

Renne, P.R., Balco, G., Ludwig, K.R., Mundil, R., Min, K., 2011. Response to the comment by W.H. Schwarz et al. on "Joint determination of 40K decay constants and 40Ar∗/40K for the Fish Canyon sanidine standard, and improved accuracy for 40Ar/39Ar geochronology" by P.R. Renne et al. (2010). Geochim. Cosmochim. Acta 75, 5097–5100. https://doi.org/10.1016/j.gca.2011.06.021

Renne, P.R., Deino, A.L., Hilgen, F.J., Kuiper, K.F., Mark, D.F., Mitchell, W.S., Morgan, L.E., Mundil, R., Smit, J., 2013. Time Scales of Critical Events Around the Cretaceous-Paleogene Boundary. Science 339, 684–687. https://doi.org/10.1126/science.1230492

Vetel, W., Le Gall, B., 2006. Dynamics of prolonged continental extension in magmatic rifts: the Turkana Rift case study (North Kenya). Geol. Soc. Lond. Spec. Publ. 259, 209–233. https://doi.org/10.1144/GSL.SP.2006.259.01.17

Chapitre 6.
Discussion, Conclusions et Perspectives

6.1 Discussion

Notre disccusion est basée sur les résultat majeurs présentés dans cette thèse qui inègre nos données et les données existantes qui nous ont permis de réaliser des analyses morphostrucrale et des analyses de réseaux des drainages.

6.1.1 La structure et propagation du rift sud Kenya-nord Tanzanie

Nous discuterons ici nos résultats sur la structure et la propagation du rift sud Kenya-nord Tanzanie basés sur l'étude morpho-structurale et quantitative des populations de failles au cours des derniers 7 Ma. Notre étude morpho-structurale, associée aux âges radiométriques existant nous ont permis de subdiviser l'histoire l'extension du rift en deux périodes.

La première, qui s'étend de 7 à 1.3 Ma est principalement associé à une extension le long des failles bordières occidentales, Nguruman ouest et Oldoinyo Ogol, ainsi qu'au niveau de la zone de transfert associée Sonjo (Sonjo Transfer Fault Zone, ou STFZ). Le système d'Oldoinyo Ogol peut être expliqué en prenant l'hypothèse que la faille Nguruman ouest se prolongeait initialement vers le sud jusqu'à la structure transverse (NE-SO) ENS-Eyasi et que son blocage frontal a provoqué le transfert de l'extension vers le NO, au niveau du système de failles transverses STFZ, puis de celui d'Ol Doinyo Ogol (OOF). La géométrie de la STFZ est particulière, par rapport à celle des zones de transfert dans le REA ; elle évoque une structure de type rampe de transfert (relay ramp) (Gawthorpe et Hurst, 1993), possiblement héritée de discontinuités protérozoïques, parallèles à celles bien documentées au sud, dans le bloc Mbulu. En parallèle avec la migration du rift sud Kenya vers l'ouest au niveau d'OOB, on peut remarquer que le magmatisme se propage également vers le sud, à partir de Lengitoto (7 Ma) et jusqu'à Salei (3.5 Ma). Entre 7 Ma et 1.3 Ma la propagation du rift vers le sud a été perturbée par la mise en place d'un grand dispositif magmatique hors-axe, au niveau de l'extrémité sud du Crater Highlands.

Pendant la période 1.7-0.9 Ma l'évolution du rifting se marque par la migration axiale de l'extension vers l'est. Ceci s'exprime d'abord par la migration des failles bordières depuis celle de Nguruman ouest vers celle de Nguruman est, puis par un

processus similaire au niveau du « bloc » Ol Doinyo Ogol, où la déformation migre latéralement depuis celle d'OOF jusqu'à celles de Sanjan, puis de Sambu-Natron. Un autre processus majeur se marque par l'abandon des failles bordières au profit d'un réseau de failles axiales, longitudinales, découpant le plancher trachytique de l'hémi-graben Magadi-Natron. Cette situation où les contraintes d'extension se focalisent au centre du bassin est aussi observée ailleurs dans le REA, notamment le long de segments du rift Kenyan (Morley, 1999; Hautot et al., 2000; Vétel & Le Gall, 2006), ainsi qu'en Afar et en Ethiopie (Ebinger & Casey, 2001; Keranen et al., 2004; Keir et al., 2006). Ce processus tectonique est probablement associé à l'affaiblissement thermique de la croûte par des intrusions magmatiques (Ebinger & Casey, 2001; Wright et al., 2006), ainsi que par l'émission de fluides (Muirhead et al., 2016).

Notre analyse quantitative des failles bordières ainsi que des failles intra-rift montre que l'accommodation de l'extension par des failles bordières est importante et que cette extension décroît du nord au sud de environ 84 à 82% au niveau de Magadi (soit 6000 à 4500 m d'extension accommodée) au niveau Magadi et environ80 à 60% au niveau de Natron (soit 2000 m). Contrairement à nos résultats, Muirhead et al. (2016) proposent qu'il existe une transition brutale entre l'extension accommodée par des failles bordières et celle liée aux failles intra-rift au cours de temps. Ces résultats sont en accord avec les résultats obtenus par ces auteurs sur le rift-Tanganyika dans la branche ouest du REA qui montre que il n'y a pas des différences fondamentales dans les processus conduisant au rifting continentale le long des rift magmatiques (branche est) et amagmatiques (branche ouest) (Muirhead et al., 2019). Nos résultats montrent aussi que, au niveau du bloc Oldoinyo Ogol, la faille d'Ogol (OOF) a accommodé environ 1000 m, soit 25% de l'extension totale dans le système Oldoinyo Ogol-Natron (OOB-Natron).

Par cette étude quantitative des failles sur l'ensemble du rift sud Kenya, tantsur les failles bordières que des failles intra-rift, nous obtenons une extension crustale supérieure minimum d'environ 7 km (>10%) pendant les dernières 7 Ma. Ce résultat est similaire aux résultats (6 km) déduits des données géophysiques au niveau du rift Magadi-Natron par Birt et al. (1997) et Ebinger et al.(1997).

6.1.2 Les failles bordières et la nature de la croûte

La notion de Baker (1958) selon laquelle la faille bordière de Nguruman soit une structure fondamentale du rift sud Kenya a été confirmée par des mesures géophysiques montrant que : i) l'épaisseur de la croûte varie entre 35 et 29 km sous l'escarpement (Birt et al., 1995 ; Plasman et al., 2017), et ii) environ 3 km d'affaissement du 'hanging-wall' du bassin de Magadi (Ebinger et al., 1997). La profondeur du socle et le déplacement cumulatif le long la faille bordière OOF sont toujours inconnus, à cause d'un manque des données géophysique au niveau du bloc OOB. Par conséquent, les valeurs moyennes estimées en surface sont probablement sous-estimées. D'ailleurs, ellesne correspondent pas aux données magnétotelluriques récemment acquises, qui montrent plutôt la nature crustale de la faille d'Ol Doinyo Ogol (Fig. 3.13A).

L'interprétation de profil MT (Fig. 3.13B) montre qu'il existe une croûte supérieure avec deux domaines contrastés juxtaposés de chaque côté de l'OOF, sous les stations P03-P04. La croûte supérieure froide est représentée par un domaine plus résistant à l'ouest d'OOF, domaine qui correspond à la bordure du socle non-rifté, tandis que l'est domine par un domaine plus conducteur, magmatique, rifté, celui du secteur OOB-Crater Highlands et Natron. À l'est de la faille de Natron, au niveau de la chaîne volcanique Kerimasi-Ketumbeine, un corps conducteur est observé à faible profondeur (<2 km) est observée (Fig. 3.13B). La même nature crustale de la faille d'OOF a été confirmée par des analyses de la fonction de récepteur montrant unegéométrie du Moho en forme de marche d'escalier dans le bloc OOB, à la verticale de l'OOF comme prévu. Les résultats montrent que l'épaisseur crustale diminue depuis le bloc soulèvé d'OOB (40 km) en allant vers l'est, au niveau de la plaine du Salei (30 km), vers la vallée axiale (Plasman et al. 2017). Si on ne prend pas en compte les sous-placages éventuels de magmas à l'axe actuel de la faille de Natron, la diminution de la profondeur du Moho à l'ouest indiquerait un amincissement crustal très marqué et une extension plus élevée dans le bloc hors axe OOB. Ce résultat est en contradiction avec les modèles géophysiques précédents qui suggèrent un amincissement axial de la croûte le long du rift Kenyan (KRISP, 1991 ; Green et al., 1991). Notre résultat, inattendu, souligne le rôle majeur de la faille de Natron par rapport aux autres failles bordières du rift sud Kenya.

6.1.3 L'héritage structural et le magmatisme syn-rift

Depuis longtemps il a été établi que, au niveau du rift nord et centre Kenya, les failles transverses de direction NW-SE sont influencées par la réactivation du socle protérozoïque durant l'extension tertiaire (Chorowicz, 1989; Smith and Mosley, 1993; Ring, 1994; Le Turdu et al., 1999; Le Gall et al., 2000; Hautot et al., 2000; Le Gall et al., 2005; Vétel and Le Gall, 2006). Au niveau du rift sud Kenya, les failles transverses NW-SE sont très peu nombreuses (e.g., la faille de Kordjya ; Fig. 3.2B (Muirhead & Kattenhorn, 2018)). Par contre on retrouve des structures transverses d'orientation NE-SW (STFZ, ENS/Eyasi et Crater Highlands). Leurs origines, importances structurales et mécanismes de mise en place sont discutés ci-dessous dans un modèle tectonique de propagation du rift en bordure du craton Tanzanien.

6.1.3.1 Le linéament ENS-Eyasi

L'âge et la nature contrastés des structures syn-rift alignées le long la structure linéaire ENS-Eyasi indiquent que celle-ci est le résultat de plusieurs phases de réactivation des segments d'une discontinuité héritée, de plus de 200 km, au cours du Néogène-Récent. La structure plissée et généralement peu inclinée du plan de foliation dans le socle protérozoïque (les chaînes granulitique de Fritz et al., 2009) indique que la déformation ductile du Protérozoïque n'a pas contrôlé la trajectoire du linéament ENS-Eyasi. Il est donc possible que ce dernier s'enracine plus profondément, le long d'une discontinuité à pendage fort, probablement d'âge archéen, en corrélation avec des structures de même orientation, montrées par la modélisation gravimétrique réalisée dans le domaine Eyasi-Mbulu au SW (Fig. 3.12A) (Fletcher et al., 2018). Cette affirmation implique que le craton tanzanien devrait s'étendre en profondeur, de l'ouest sous la nappe protérozoïque, à l'est du linéament ENS. Notre interprétation est en accord avec les profils structuraux de Fritz et al. (2009) qui montrent que les nappes protérozoïque s'enracinent vers l'est selon une rampe crustale raide, située environ 200 km à l'est du front de nappe actuellement exposé (Fig. 3.12A).

Les différents types de structures de rift le long de la discontinuité ENS-Eyasi suggèrent que sa réactivation dans le cadre de l'extension régionale EW n' a pas fonctionné par un processus unique d'extension simple, mais a plutôt été obtenu par une combinaison de différents processus, éventuellement contrôlés par l'état thermique de la croûte. Ceci est confirmé par la distribution spécifique des déformations fragiles aux deux extrémités du linéament (failles d'ENS et Eyasi), c'est-à-dire sur les flancs de rift, où la croûte est plus froide, alors que des structures tectono-magmatiques ont été mises en place comme des dykes mineurs le long de l'axe Gelai-Naibor Soito ou des intrusions dans le Crater Highlands, dans la partie crustale de l'axe du rift plus chaude (Fig. 3.11). L'importance de la discontinuité héritée ENS-Eyasi est également argumentée par son prolongement vers le NE, éloigné de l'axe du rift, via la structure morphologique longue de plus de 200 km délimitant les plateaux volcaniques Narok-Nairobi-Mont Kenya et qui s'est probablement formée en réponse au soulèvement induit par le panache de l'Afrique de l'Est au Miocène (> 13 Ma) (Winchura et al., 2010).

6.1.3.2 Offset du bloc Ol Doinyo Ogol (OOB)

Le développement structural du bloc Ol Doinyo Ogol sur le flanc oriental de la vallée axiale sud Kenyan peut être expliqué de manière satisfaisante de deux façons non exclusives, toutes deux liées aux failles transverses (SFTZ).

La première hypothèse est basée sur les corrélations spatio-temporelles montrées par deux structures majeures, la STFZ et ENS, toutes deux initiées tôt, probablement entre 7 et 1.3 Ma, et à la même latitude (Figs. 3.2, 3.3). On peut donc envisager qu'en réponse au rétrécissement du bassin du Natron (jusqu'à 20 km), rétrécissement causé par la structure du socle ENS (ENS basement salient), le domaine rifté se soit déplacé vers l'ouest via la zone de transfert STFZ, dans le bloc offset OOB, sur une largeur d'environ 40 km, afin de maintenir un rapport de forme presque constant avec certains paramètres des failles bordières (longueur, déplacement, ..).

Le deuxième scénario implique que la faille bordière W/Nguruman se soit propagée jusqu'à 2°45' vers le sud et ait rencontré la discontinuité transverse ENS-

Eyasi (Fig. 3.14). Dans ce cas, la cinématique du bloc triangulaire résultant dépend principalement de deux paramètres importants, à savoir: i) le sens opposé des pendages versus le sens de pendage similaires des deux failles interagissant et ii) leur angle aigu versus obtus (Fig. 3.14A) (Lezzar et al., 2002 ; Vétel et Le Gall, 2006).

Dans le cas présent, les sens opposés de pendages des failles interagissant et l'angle aigu des deux structures constituent des conditions défavorables au mouvement subsidant du compartiment supérieur (hanging-wall). En conséquent, la propagation vers le sud de la faille W/Nguruman a été inhibée par la discontinuité ENS-Eyasi, ce qui en retour provoque le saut latéral de la déformation vers le NW le long du domaine STFZ/OOF. Selon ce deuxième scénario, la faille Sambu-Natron devrait représenter une structure complexe multi-stades, initialement formée comme une faille interne précoce dans le bassin OOB-paléo Natron.

6.1.3.3 Le Segment magmatique 'hors-axe' et l'initiation du Crater Highlands

En ce qui concerne le cadre général de la propagation vers le sud du rift sud Kenya-DNT, la position de Crater Highland est anormale par rapport à : i) sa position hors-axe, ii) son orientation NE-SW, oblique par rapport à l'axe de la vallée axiale et iii) la migration du magmatisme vers le NE depuis les volcans Lemagrut (5 Ma), Sadiman (4 Ma), Ngorongoro (3.7 Ma), Olmoti (1.6 Ma), Loolmalasin (1.2 Ma) et Embagai (0.5 Ma) (Fig. 3.15A) (Bagdasaryan et al., 1973; McIntyre et al., 1974; Manega, 1993; Foster et al., 1997). L'initiation du magmatisme hors axe, près de la limite orientale exposée du craton tanzanien, et sa migration ultérieure vers l'axe de rift Natron vers le NE (Le Gall et al., 2008 ; Mana et al., 2015) sont ici attribuées à quatre processus en interaction qui impliquent (Fig. 3.15C, D) : i) la déflexion des produits de fusion de la tête de panache sous la lithosphère rigide du craton, en accord avec les modèles 3D thermomécaniques (Koptev et al., 2017, 2018) et le scénario appliqué à la province volcanique de Rungwe plus au sud, en relation avec le craton de Bangweulu (Grijalva et al., 2018), ii) leur remontée le long de la topographie à la base de la lithosphère cratonique, iii) la canalisation NE/SW de l'écoulement latéral des produits de fusion par les zones transversales de la lithosphère amincie (Fletcher et al.,

2018) et iv) la migration de magmas à travers la croûte supérieure, le long de zones des discontinuités NE-SW conduisant à un alignement des centres éruptifs à la surface du Crater Highlands. La configuration complexe infra-lithosphérique, avec un certain nombre de zones amincies transverses NE/SW se ramifiant vers l'est (Fletcher et al., 2018), pourrait se prolonger sous la vallée axiale Natron et se connecter avec la structure de type lithosphérique de type antiforme d'environ 50 km de large et parallèle au linéament ENS-Eyasi, identifiée par modélisation des fonctions de récepteur (Fig. 3.12D) (Plasman et al., 2017). La canalisation latérale de la remontée asthénosphérique est fortement oblique (environ 40°) par rapport à l'axe du rift subméridien sud Kenya et implique un découplage majeur entre les deux structures, avec un contrôle accru de la contrainte tectonique régionale dans la croûte supérieure. Un modèle assez similaire de croûte/lithosphère hétérogène est documenté à propos du magmatisme hors axe au niveau du rift éthiopien (Bastow et al., 2008 ; Rooney et al., 2014 ; Chiasera et al., 2018).

En matière de relations entre magmatisme et contrainte, on sait que les segments magmatiques constituent des sites potentiels de nucléation, en réponse à l'affaiblissement thermique de la lithosphère (Benes & Davy, 1996 ; Callot et al., 2002. L'emplacement de la faille d'Eyasi immédiatement au sud-ouest de la zone de mise en place des volcans du Crater Highland (Sadiman-Lemagrut-Ngorongoro), suggère que sa nucléation il y a moins de 3.1 Ma (Foster et al., 1997) a été provoquée par un réchauffement thermique de la lithosphère lors d'un magmatisme précoce (5-3 Ma) au SW de la bordure du Crater Highland (Fig. 3.15D). Un processus similaire a dû se produire plus tard (<1.2 Ma) à l'extrémité NE de la chaîne volcanique (Foster et al., 1997) et a ainsi favorisé la propagation vers le sud de la faille bordière de Natron qui recoupe ainsi la discontinuité ENS-Eyasi pour venir se connecter ensuite avec la faille de Manyara. Enfin, la densité d'édifices volcaniques monogénétiques et leur alignement N70°E dans le Crater Highlands doit refléter la présence de dykes en profondeur, ces derniers ayant pu accommoder une part significative de l'extension. Cela devrait expliquer l'absence d'extension tectonique le long du flanc NW du Crater Highlands dans la dépression Olbalbal, où les évidences de liaison entre les failles bordières OOF et Eyasi sont manquantes (Fig. 3.2A, B) (Ebinger et al., 1997).

6.1.4a) L'organisation des réseaux de drainage et leurs contrôle structural

Au nord-ouest de la zone d'étude, les réseaux de drainage sont de direction E avant e passer sur le système de failles Nguruman, où la faille de Nguruman W est la plus ancienne. En rencontrant les failles bordières de Nguruman (NgW et NgE), leur direction d'écoulement bascule d'abord vers la vallée axiale (Magadi-Natron). Le secteur Nguruman est dominé par le socle métamorphique et les laves trachytiques de Lengitoto (7 - 1.7 Ma) (Baker, 1958 ; Crossley, 1979 ; Birt et al., 1997) (fig. 4.5b). On remarque que les directions des rivières sont contrôlées par la lithologie, la topographie et des structures. La majorité des bassins versants dans les Nguruman sont basculés et moyennement incisés. Les profils des rivières au niveau du Nguruman montrent que les ruptures de pentes (knickpoints) sont fixes le long des failles majeures (KPf) et que celles non associées aux failles (KPd) se décalent vers l'ouest. Les profils topographiques EW (Fig. 4.5c et 4.5e) nous permettent de faire trois interprétations : i) la paléo-topographie est pentée soit vers l'E et vers le N, soit vers l'W ; la variation de direction des pentes est importante pour la direction de drainage (ligne de partage des eaux, ou water divide). Le vieux basculement de premier ordre est lié à la faille de Nguruman W et donc contrôle l'écoulement des rivières, iii) un second basculement lié à la faille de Nguruman E est plus jeune. Les changement de direction des rivières, et notamment Rw1 et Rw2 au niveau de l'escarpement du Nguruman, sont contrôlés par les mouvements du compartiment supérieur (hanging-wall) de la faille normale, en corrélation avec le modèle classique décrit dans l'évolution de la topographie de rift (e.g. Cowie et al., 2006).

L'organisation du drainage en ce qui concerne les failles et les blocs soulevés au niveau du volcan Oldoinyo Sambu montre que des rivières coulent vers l'est puis suivent les failles (fig. 4.6a). Plus à l'ouest de cette zone, les réseaux de drainage sont contrôlés par une foliation métamorphique et elles coulent parallèlement aux failles. Dans ce secteur les KPd ont migré vers l'intérieur (ouest), montrant qu'il y avait assez de temps pour un réajustement et que les KPf sont collés au niveau des failles. La configuration des failles et des réseaux de drainage indique que le réseau de drainage actuel est plus jeune que les failles de Nguruman et le volcan Oldoinyo Sambu.

Dans le domaine soulevé du bloc Oldoinyo Ogol (OOB), on retrouve un certain nombre des structures majeures, notamment les failles Oldoinyo Ogol, Sanjan et Natron ;

Crater Highland et plaine Salei. Les analyses morpho-métriques nous montrent que les bassins versants sont incisés et basculés, que les réseaux de drainage ne sont pas très jeunes et que le rôle des failles dans l'organisation des drainages est important. L'organisation des failles du Crater Highlands et les caractéristiques des réseaux de drainage montrent que les directions de ces derniers sont contrôlées à la fois par des failles et par la topographie du Crater Highlands, dans lesquels les réseaux sont divisés en trois directions différent selon leur position : i) On retrouve des directions N-S au nord du bloc OOB, ii) EW dans le bassin Salei et iii) NW au niveau du cratère. La présence de KPd au nord d'OOB et à l'ouest de l'OOB, ainsi que son absence dans la zone élevée sur le cratère, peut être interprétée conjointement avec la présence de Ksn élevée le long de l'escarpement principal d'OOF et dans le bloc élevé du cratère : ainsi, la plaine de Salei et le bloc OOB indiquent que le drainage dans l'OOB est plus ancien que celui qui provient du cratère. Cela entraîne deux scénarios tectoniques successifs, à savoir: i) premièrement, un drainage dans l'OOB évolué dans lequel la direction E-W a été dominante (il y a 3.5 Ma), puis ii) un drainage au NW du cratère (Fig. 4.8). Cela est également corroboré par le fait que tout le drainage des hauts plateaux du cratère agit comme un affluent du principal drainage de l'E-W qui finit par déverser son eau dans le lac Natron.

Le centre de la faille d'Eyasi est près de la limite entre le socle tanzanienne et les formations du Protérozoïque. Les réseaux de drainages au NE d'Eyasi sont affectés par la topographie liée aux volcans du Crater Highland (Lemagrut) et ainsi que par l'escarpement qui contrôle les directions des rivières vers le lac Eyasi. Les analyses morpho-métriques montrent que les bassins versants dans ce secteur sont incisés et basculés. Les profils longitudinaux des rivières montrent des pendages forts au niveau de la faille et que les anomalies KPf sont localisées au niveau de failles quant aux drainages localisés au NE d'Eyasi. Le profil au SW de la faille présente une pente faible avec des KPds plus loin de la faille indiquant que cette rivière est localisée à la terminaison de la faille d'Eyasi, ce qui peut être interprété comme une indication de la direction de la propagation de la faille d'Eyasi (NE vers SW).

Dans les plateaux Mbulu et Manyara, les KPf sont localisés dans des failles (Manyara et Yaïda) tandis que des KPd migrent vers l'intérieur. Ksn et des valeurs de

pentes sont classées en trois catégories: i) les valeurs hautes de Ksn (200 – 500), qui se trouvent dans les zones élevées, avec des pentes élevées (> 60°), telles que le SE du Crater Highland (Fig. 4.10c et 4.10d). ii) Les valeurs moyennes de Ksn, intérieures à 200, sont localisées dans le bassin de Yaïda et au SW et montrent des activités des failles Yaïda et Kitangili. iii) les faibles valeurs, supérieures à 20 dans la dépression de Yaïda.

6.1.4b) Implications tectoniques

Les valeurs de l'AF, l'HI, de l'analyse topographique et de Ksn discutées ci-avant, de même que leur implication tectoniques dans la formation de DNT nous ont conduit à proposer un modèle en deux phases.

Premier stade, de 7 à 3,2 Ma : les observations effectuées sur les réseaux de drainages nous ont permis d'identifier et localiser des ruptures de pentes liées aux failles récentes (KPf) et celles qui ne sont pas directement liées aux failles (KPd) montrent que lors de la première étape du soulèvement, alors que la faille de Nguruman se développe, un réseau de drainage de direction E-W est mis en place, avec les KPf fixés le long de la faille bordière. Ces KPfs sont marqués comme futurs KPd (Fig. 4.11). Peu après, les KPf migrent vers l'ouest des KPfs, car la migration des knickpoints en amont et loin des failles bordières prend beaucoup de temps. Nous interprétons ainsi notre observation au niveau de la zone de Nguruman et au niveau du Sonjo (Fig.s 4.5a, 4.6d, 4.7) : ces KPds diffusés correspondent à un première stade de formation de la DNT, se déroulant entre 7 et 3,2 Ma, parallèlement à la formation de NgW, STFZ, OOF et Sambu. L'autre observation est que les systèmes de drainage transverses sont déjà localisés, impliquant un stade précoce du rifting dans le DNT, similaire aux observations de Cowie et al., 2006. À ce stade initial, l'interaction des failles n'est ni complétée ni réalisée, permettant aux rivières de l'arrière-pays (ou hinterlands) d'être reliées en aval par les écarts entre les failles. Ce résultat est en corrélation avec ceux de la modélisation numérique de Cowie et al., 2006, grâce auxquels ils ont montré qu'un réseau de drainage peut être développé en arrière-pays de compartiment inférieur (foot-wall) dans une phase initiale de rifting. Des KPd migrés en amont et des Ksn diffusés ont également été observés dans le domaine méridional du bloc Manyara-Mbulu, correspondant également à un stade précoce de rifting qui se propage dans la partie sud du NTD. Donc, nous proposons que, lors de la première phase de rifting

(7-3.2 Ma), la déformation soit diffusée et distribuée là où le système de drainage NE-SW a été mise en place par la remontée du Crater Highlands. Le système de drainage résultant est en treillis, probablement en raison du système de failles précoces NE-SW souvent décrit au début du rifting, lors duquel des déformations diffuses ont été observées (Cowie et al., 2006). Le soulèvement des cratères (<5,5 Ma) est également suggéré comme étant responsable du changement de direction des réseaux de drainage situés à l'extrémité sud de W8, où les réseaux de drainage situés à l'extrémité nord de CH sont dirigés vers le NW avant de rejoindre le principal affluent Rw8, puis finissent par couler vers la faille de Natron (Fig. 4.7a).

Deuxième phase de3, 2 à 0 Ma) : elle correspond à la situation actuelle de la DNT, où des KPf et KPd observés sont interprétés comme représentant différentes manifestations d'activités de rifting. Les KPf et des valeurs Ksn élevées et localisées au niveau des failles récentes sont le fait qu'ils n'ont pas eu le temps de migrer en amont. Les valeurs de Ksn faible caractérisent des escarpements faibles (< 80) ou moyens (80-500), en particulier dans les Nguruman-Loita, respectivement dans les parties amont et centrale (Fig. 4.5a). Cette variation de Ksn est corrélée aux processus fluviaux sous l'influence d'activités tectoniques. Cette observation est bien nette sur les failles NgE, Sambu et Natron pour la partie nord et une observation similaire a été faite sur les failles d'Eyasi et Manyara dans la partie sud. Ces configurations correspondent à une évolution tardive de rifting où l'interaction de failles est réalisée. Nous proposons que ce stade corresponde à la période s'étendant 3,2 Ma à 0 où le rifting s'est déplacé vers l'est dans la partie nord et s'est localisé sur Eyasi et Manyara dans la partie sud. Cette étape de déformation a déclenché une forte incision dans le foot-wall par exemple Rw1, Rw2, Rw3 (Fig. 4.5a) ou Rw7, Rw8 (Fig. 4.7a). Cet événement aurait pu aussi rajeunir le système de drainage lié à la première phase. Pendant cette phase tardive de rifting on observe aussi un déclenchement de capture dans lequel Rw14 a été capturé et est parallèle aux failles d'Eyasi au lieu de les traverser, ce qui implique que l'activité tectonique était plus rapide que le taux d'incision à l'extrémité sud de la faille d'Eyasi. En outre, ce modèle de capture est également responsable de l'augmentation de la surface de drainage des bassins versants qui est assez petite au pied des failles Eyasi ou Manyara.

Les profils le long des rivières dans lesquelles KPf et KPd ont été analysés dans les deux phases présentées ci-avant sont convexes (Fig.s 4.5f, 4.6d, 4.9e et 4.10d), bien que dans certains cas des profils de rivières étroites soient observés. Ces formes de profil convexe indiquent un système en état transitoire, contrairement aux profils de rivières concaves, normalement attribués aux rivières en équilibre (Mackin, 1948). L'ensemble de ces formes de rivières sont typiques des environnements tectoniquement actifs (Cowie et al., 2006).

6.2 Conclusions

Le rift magmatique du Kenya, branche orientale du REA, est limité à ses extrémités nord et sud par deux dispositifs anormalement larges par rapport à la largeur classique (60 km) de la vallée axiale. Au niveau du rift sud-kenyan (RSK), sujet du présent travail, le fossé axial Magadi-Natron est bordé à l'ouest par le bloc Ol Doinyo Ogol (ODO) qui présente aussi l'originalité d'être limité, en partie, par des failles transverses d'orientation NE-SW, failles distinctes des zones de transfert NW-SE caractérisant la presque totalité du rift kenyan vers le nord. Cette direction structurale NE-SW est largement développée vers le sud, au niveau de la branche occidentale (Eyasi) de la Divergence Nord Tanzanienne (DNT). À ce jour, aucun modèle structural n'a réellement discuté l'origine de la DNT, les hypothèses proposées ne reposant que sur des données géophysiques (Ebinger et al., 1997), géochronologiques (Foster et al., 1997) ou morpho-structurales (Le Gall et al., 2008) et l'ensemble de ces travaux, exclusivement axés sur la DNT, ne prenant jamais en compte le dispositif RSK dont les anomalies structurales pourraient résulter de processus communs, comme envisagé ici en préambule à ce travail de thèse.

L'objectif de cette étude est donc d'intégrer le dispositif rifté RSK dans le cadre élargi de la DNT. Par ailleurs, les travaux antérieurs consacrés au RSK sont eux aussi incomplets car ils négligent systématiquement le bloc ODO, témoins probables des stades précoces du rifting (Muirhead et al., 2016 ; Weinstein et al., 2017; Lee et al., 2018). Notre travail concerne donc la structure et l'évolution tectono-magmatique de l'ensemble du

système RSK, à savoir la vallée axiale Magadi-Natron et le bloc ODO, pendant les 7 derniers Ma.

L'analyse morpho-structurale, basée sur l'interprétation d'imagerie satellitaire SRTM30 (et MNT), a été focalisée à la fois sur le réseau de failles bordières et sur le dispositif de failles intra-rift. Elle a abouti à identifier 2 structures particulières de direction NE-SW, transverses à l'axe du rift : (1) la zone de transfert Sonjo, responsable du décalage dextre de la zone riftée au niveau du bloc ODO et (2) le promontoire de socle Engare-Nairobi (ENS), responsable du rétrécissement de la vallée axiale.

L'étude comparative des profils d'érosion des escarpements de failles bordiers fournit des éléments de chronologie relative qui permettent de différencier 2 stades successifs de mise en place de ces derniers : corrélés aux datations du volcanisme disponibles, elle confirme les 2 épisodes de rifting de7-1,3 Ma et < 1,3 Ma, qui montrent une évolution depuis un système large et non cylindrique (vallée axiale + ODO) vers un dispositif plus focalisé et linéaire (vallée axiale actuelle).

L'étude statistique de certains paramètres (longueur, déplacement) des populations de failles extraites du MNT (>140) nous permet une analyse quantitative de l'extension, à la fois dans l'espace -fossé axial Magadi-Natron versus bloc ODO, ainsi que failles bordières versus failles intra-rift- et dans le temps -stade précoce versus tardif. Ce travail aboutit à des résultats originaux et plus complets que ceux récemment acquis par Muirhead et al. (2016) qui ne concernaient que la vallée axiale et traitaient un nombre de failles moindre. Parmi les résultats intéressants, on retiendra :

- Le stade précoce du rifting (7-1,3 Ma), dominé par la formation du système des failles bordières W/Nguruman-OOF, très segmentées résultant en la formation des basins en hémi-graben proto Magadi-OOB-Natron, reliés via la zone de failles transverses STFZ. Une inversion des données magnétotellurique 2D démontre à l'échelle de la croûte la nature de la faille OOB, alors que la structure atypique de la STFZ se marque à la fois par ses dimensions (40 x 25 km) et par la cinématique de ses failles internes, qui présentent toutes un déplacement important en 'dip-slip' en réponse à un contexte d'extension 3D complexe dans le SKR à ce stade précoce du rift. L'essentiel de l'extension est très focalisé car elle est accommodée par les failles bordières (W/Nguruman-STFZ-OOF), avec un fort gradient NS entre les segments Magadi (forte extension) et OOB-paléo

Natron (plus faible), responsable de la segmentation structurale précoce du dispositif RSK.

- Le stade plus récent (< 1,3 Ma), durant lequel l'extension est plus largement distribuée, avec la mise en place des failles intra-rift qui enregistrent une déformation supérieure à celle accommodée par les failles bordières néo-formées (E/Nguruman-Sambu-Natron).

- L'importance de la faille bordière du bloc ODO (OOF) est démontrée car elle enregistre la plupart de l'extension totale au niveau du dispositif élargi ODO-Natron. Ceci est confirmé par les nouveaux résultats magnétotelluriques, que démontrent le caractère crustal de la faille bordière OOF, séparant des blocs à résistivité contrastée (socle résistant non rifté à l'ouest et croûte plus conductrice au niveau du domaine rifté ODO). Ces résultats sont également conformes aux modélisations géophysiques récentes de Plasman et al. (2017) qui suggèrent un amincissement crustal marqué (quelques km) à la verticale du bloc ODO, et non pas sous la vallée axiale Natron comme prédit.

- La propagation vers le sud du rift précoce, exprimée par la mise en place diachrone du magmatisme depuis le bassin de Magadi (trachytes de Lengitoto d'âge 7 Ma) jusqu'au bassin décalé OOB (basaltes de Salei d'âge 3,5 Ma). Cependant, une initiation plus précoce du rifting (> 7 Ma) est suggérée par la présence de séquences synrift identifiées sous les laves de Lengitoto, et qui sont supposés avoir formée des bassins sédimentaires pré-volcaniques.

- Les changements importants de style du rifting intervenus vers 1,3 Ma s'expriment par la focalisation axiale de la déformation et résultent donc en un transfert de l'activité des failles bordières vers l'est. Cela correspond aux transferts depuis OOF jusqu'à Sambu-Natron, ainsi que de W/Nguruman à E/Nguruman. De manière concomitante, le volcanisme (les trachytes de Magadi) est concentré dans l'hémi-graben étroite et linéaire de Magadi-Natron où les failles longitudinales sont mises en place.

- Les analyses quantitative des populations de failles bordières et intra-rift indiquant que plus de 7 km (>10%) d'extension de la croûte supérieure ont été enregistrés dans le rift pendant 7 Ma. La majorité (>80%) a été principalement accommodée par un déplacement important sur la faille bordière au cours d'un long processus d'évolution des bassins de rift, avec une diminution marquée de l'activité au fil du temps. Etant donné la valeur

moyenne de l'extension (<20%) liée aux failles intra-rift subite par la vallée axiale Magadi-Natron à ce stade récent (<1,3 Ma), cela suggère que : i) les failles intra-rift n'aient pas accommodé l'extension importante sur le RSK lors du transfert des contraintes vers la vallée axiale et ii) il n'existe pas de transition brutale entre un processus précoce où l'essentiel de l'extension est accommodée par les failles bordières et un processus plus jeune où l'extension est exclusivement accommodée par les failles intra-rift. Ces résultats ne correspondent pas avec les modèles cinématiques généralement appliqués à des segments plus évolués dans les rifts magmatiques du Kenya et d'Ethiopie.

- L'histoire du rifting entre le Néogène et le Récent du système RSK : les travaux soulignent la nécessité d'intégrer le stade de la déformation précoce enregistré par le bloc offset OOB afin de ne pas sous-estimer la quantité d'extension enregistrée par la partie méridionale du système RSK (ca 25%).

- Les profils de déplacement de 140 failles syn-rift étudiées, qui montrent que la plupart d'entre elles (85%) sont asymétriques et caractérisent des failles de type 'restricted'. Quand une faille présente une propagation non perturbée par un blocage mécanique, de type 'unrestricted', son profil devient symétrique, en cloche. On en déduit donc que bloc de socle transverse ENS n'a pas bloqué la propagation de la déformation et que le caractère 'restricted' des failles de la vallée axiale est probablement dû aux interactions entre un réseau de failles très dense dans un système très mature.

A l'échelle du dispositif RSK-DNT, l'un des apports de notre travail est de démontrer l'existence d'une très grande discontinuité transverse, NE-SW (ENS-Eyasi), prenant en écharpe l'ensemble du domaine rifté, depuis le promontoire de socle ENS jusqu'à la faille d'Eyasi. Cette structure de 1er ordre est soulignée en surface par des structures synrift (failles, volcans, sismicité), de natures et d'âges divers, et notamment par le segment magmatique 'hors-axe' des Crater Highlands, démontrant ainsi la dimension crustale/lithosphèrique de cette discontinuité, en accord avec les modélisations récentes de fonction récepteur de Plasman et al. (2017).

- Le modèle du rifting appliqué dans cette étude, qui souligne encore le rôle majeur de la structure de premier ordre, la discontinuité ENS-Eyasi, sur les perturbations structurales et magmatiques du système RKS-DNT à la bordure du craton tanzanien. L'influence possible de cette discontinuité sur le décalage dextre précoce du RKS est envisagée de

deux manières différentes, mais plus importante encore est sa réactivation en plusieurs étapes, exprimée par une variété d'événements tectono-magmatiques éventuellement contrôlés par l'état thermique de la croûte/lithosphère. En effet, la tectonique cassante était strictement confinée à ses extrémités (ENS et réseaux de failles d'Eyasi), c'est-à-dire au-delà de l'axe du rift où la croûte était plus froide, alors que des processus magmatiques se déroulaient dans sa partie centrale à travers le rift et la lithosphère la plus chaude. La faille d'Eyasi s'étendant tout le long du craton archéen en contradiction avec le concept d'héritage structurale évoqué précédemment a probablement été déclenchée par l'affaiblissement thermique de la lithosphère lors de la mise en place hors axe du Crater Highland, dès 5 Ma, attribuée aux i) déflexion de produits de fusion de la tête de panache sous la lithosphère rigide du craton et ii) migration à travers la croûte protérozoïque où ils ont été canalisés par les discontinuités NE-SW pour former le segment magmatique transverse des Crater Highland. Ce magmatisme a pu provoquer l'affaiblissement mécanique de la lithosphère, ce qui a pu faciliter la rupture de la croûte et la mise en place précoce de la faille d'Eyasi au niveau d'une sorte de point de nucléation, la faille venant s'enraciner sur des structures protérozoïques héritées. Notre étude met donc en évidence l'importance de l'héritage structural protérozoïque dans l'origine des directions atypiques (NE-SW), tectoniques et magmatiques, du rift RSK-DNT et dans son élargissement anormal.

La densité et la variété du réseau de drainage identifié sur les compartiments de socle soulevé bordant à l'ouest le domaine rifté, depuis le plateau de Loita au nord jusqu'au plateau de Mbulu lié au système d'Eyasi au sud, permettent une étude de leur relation avec les mouvements verticaux liés aux failles bordières. Ce travail original, n'avait jamais été réalisé à ce jour dans la zone d'étude. Notre analyse de réseau de drainage démontre que dans le flanc ouest de la DNT : i) les variations de la diffusion des anomalies KPf et KPd sont en accord avec le rifting en deux stades, comme l'a montré l'étude morpho-structurale (les KPf sont associés aux événements plutôt récents et donc sont localisés au niveau de failles récentes, tandis que les KPd ont migré vers l'amont du système de rivières et sont donc associés aux soulèvements dus au premier stade), ii) la géométrie des rivières, notamment au nord, indique un contrôle structural, ce qui indique un système hors-équilibre, donc encore jeune, iii) la mise en place de la CH a contrôlé

l'orientation des réseaux de drainage au sud de la OOB, indiquant que la partie nord du CH est probablement plus jeune que l'OOB.

6.3 Perspectives

1) A l'échelle régionale du dispositif RSK-DNT, la discontinuité transverse intra-socle ENS-Eyasi est importante dans le modèle proposé dans cet étude. Il serait intéressant de confirmer l'existence de cette discontinuité par des enregistrements géophysiques (MT, sismique, etc) le long de transects orthogonaux à sa trace de surface.

2) D'un point de vue plus thématique, l'influence d'une discontinuité transverse sur la propagation et la géométrie anormales d'un dispositif en extension pourrait faire l'objet de modélisations (expérimentales et numériques). L'une des difficultés serait le caractère ponctuel et intermittent des anomalies thermiques induites par le magmatisme (segment hors-axe des Crater Highlands).

3) L'importance du bloc latéral Ol Doinyo Ogol pour le développement du DNT a été démontrée dans cette étude. Cependant, son développement tectono-magmatiques manque d'une datation précise. Il est donc essentiel de poursuivre les analyses géochimiques et la datation chronologique afin de bien comprendre ce secteur important dans le RSK.

Bibliographie

Bibliographie

Ackermann, R., Schlische, R., 1997. Anticlustering of small normal faults around larger faults, Geology, 25, 12, 1127-1130.

Acosta, V.T., Bande, A., Sobel, E.R., Parra, M., Schildgen, T.F., Stuart, F., Strecker, M.R., 2015. Cenozoic extension in the Kenya Rift from low-temperature thermochronology: links to diachronous spatiotemporal evolution of rifting in East Africa. Tectonics 34, 2367–2386.

Agostini, A., Bonini, M., Corti, G., Sani, F., Manetti, P., 2011. Distribution of Quaternary deformation in the central Main Ethiopian Rift, East Africa: Deformation in the Main Ethiopian Rift. Tectonics, 30, doi.org/10.1029/2010TC002833.

Aki, K., 1979. Characterization of barriers on an earthquake fault. J. Geophys. Res., 84, B11, 6140-6148.

Albaric, J., 2009. Relations entre déformation active, rhéologie et magmatisme dans un rift continental: Etude sismologique de la Divergence Nord-Tanzanienne, Rift Est-Africain. Université de Bretagne occidentale-Brest.

Albaric, J., Deverchère, J., Perrot, J., Jakovlev, A., Deschamps, A., 2014. Deep crustal earthquakes in North Tanzania, East Africa: Interplay between tectonic and magmatic processes in an incipient rift. Geochem. Geophys. Geosyst., 15, 374-394, doi:10.1002/2013GC005027.

Albaric, J., Déverchère, J., Petit, C., Perrot, J., Le Gall, B., 2009. Crustal rheology and depth distribution of earthquakes: Insights from the central and southern East African Rift System. Tectonophysics 468, 28–41. https://doi.org/10.1016/j.tecto.2008.05.021

Albaric, J., Perrot, J., Deverchère, J., Deschamps, A., Le Gall, B., Wambura, R., Petit, C., Tiberi, C., Sue, C., Songo, M., 2010. Contrasted seismogenic and rheological behaviours from shallow and deep earthquake sequences in the North Tanzanian Divergence, East Africa. J. Afr. Earth Sci., 58, 5, 799-811, doi:10.1016/j.jafrearsci.2009.09.005.

Alipoor, R., Poorkermani, M., Zare, M., El Hamdouni, R., 2011. Active tectonic assessment around Rudbar Lorestan dam site, High Zagros Belt (SW of Iran). Geomorphology 128, 1–14. https://doi.org/10.1016/j.geomorph.2010.10.014

Allen, P.A., Densmore, A.L., 2008. Sediment flux from an uplifting fault block. Basin Res. 12, 367–380. https://doi.org/10.1111/j.1365-2117.2000.00135.x

Arun, P.S., Jana, R., Nathawat, M.S., 2005. A Rulebase physiographic characterization of a drought prone watershed applying remote sensing and GIS. J. Indian Soc. Remote Sens. 33, 189–201. https://doi.org/10.1007/BF02990035

Atmaoui, N., Hollnack, D., 2003. Neotectonics and extension direction of the Southern Kenya Rift, Lake Magadi area. Tectonophysics 364, 71–83. https://doi.org/10.1016/S0040-1951(03)00051-9

Aulbach, S., Rudnick, R. & McDonough, W., 2008. Lithospheric mantle sources within the East African Rift, Tanzania, Geochim. Cosmochim. Acta Supplement, 72, 37.

Baer, G., Y. Hamiel, G. Shamir, and R. Nof (2008), Evolution of a magma-driven earthquake swarm and triggering of the nearby Oldoinyo Lengai eruption, as resolved by InSAR, ground observations and elastic modeling, East African Rift, 2007, Earth Planet. Sci. Lett., 272(1), 339–352.

Bagdasaryan, G.P., Gerasimovskiy, V.I., Polyakov, A.I., Gukasyan, R.K., 1973. Age of

volcanic rocks in the rift zones of East Africa. Geochemistry International 10, 66–71.

Bahrami, S., 2013. Analyzing the drainage system anomaly of Zagros basins: Implications for active tectonics. Tectonophysics 608, 914–928. https://doi.org/10.1016/j.tecto.2013.07.026

Baker, B.H., 1958. Geology of the Magadi area. Geological Survey of Kenya Report, 42. 81 pp.

Baker, B.H., 1963. Geology of the Area of South of Magadi. pp. 27 Geological Survey of Kenya.

Baker, B., 1986. Tectonics and volcanism of the southern Kenya Rift Valley and its influence on rift sedimentation, Geol. Soc. Lond. Spec. Publ., 25(1), 45–57.

Baker, B.H., Mitchell, J.G., 1976. Volcanic stratigraphy and geochronology of the Kedong- Olorgesaile area and the evolution of the south Kenya rift valley. J. Geol. Soc. Lond. 132, 467–484.

Baker, B., Williams, L., Miller, J., Fitch, F., 1971. Sequence and geochronology of the Kenya rift volcanics. Tectonophysics, 11, 191-215.

Baker, B., Wohlenberg, J., 1971. Structure and Evolution of the Kenya Rift Valley. Nature, 229, 538.

Baker, B.H., Mitchell, J.G., 1976. Volcanic stratigraphy and geochronology of the Kedong-Olorgesaile area and the evolution of the south Kenya rift valley. J. Geol. Soc. Lond. 132, 467–484.

Baker, B., Mitchell, J., Williams, L., 1988, Stratigraphy, geochronology and volcanotectonic evolution of the Kedong-Naivasha-Kinangop region, Gregory Rift Valley, Kenya. J. Geol. Soc., London, 145, 107-116.

Baptiste, V., Tommasi, A., Vauchez, A., Demouchy, S. & Rudnick, R.L., 2015. Deformation, hydration, and anisotropy of the lithosphericmantle in an active rift: Constraints frommantle xenoliths from the North Tanzanian Divergence of the East African Rift, Tectonophysics, 639, 34–55.

Bastow, I., Nyblade, A., Stuart, G., Rooney, T., Benoit, M., 2008. Upper mantle seismic structure beneath the Ethiopian hot spot: Rifting at the edge of the African low-velocity anomaly: Geochem. Geophys. Geosystems, 9, 12, doi.org/10.1029/2008GC002107.

Baudouin, C., Parat, F., Denis, C., Mangasini, F., 2016. Nephelinite lavas at early stage of rift initiation (Hanang volcano, North Tanzanian Divergence). Contrib. Mineral. Petrol., 171, 7, doi 10.1007/s00410-016-1273-5.

Baker, B.H., Williams, L.A.J., Miller, J.A., Fitch, F.J., 1971. Sequence and geochronology of the Kenya rift volcanics. Tectonophysics 11, 191–215. https://doi.org/10.1016/0040-1951(71)90030-8

Baker, B.H., Wohlenberg, J., 1971. Structure and Evolution of the Kenya Rift Valley. Nature 229, 538.

Band, L.E., 1986. Topographic Partition of Watersheds with Digital Elevation Models. Water Resour. Res. 22, 15–24. https://doi.org/10.1029/WR022i001p00015

Benes, V., Davy, P., 1996. Modes of continental lithospheric extension: experimental verification of strain localization processes. Tectonophysics, 254, 69-87.

Beutel, E., van Wijk, J., Ebinger, C., Keir, D., Agostini, A., 2010. Formation and stability

of magmatic segments in the Main Ethiopian and Afar rifts. Earth Planet. Sci. Lett. 293, 225-235.

Bhattacharjee, D., Jain, V., Chattopadhyay, A., Biswas, R.H., Singhvi, A.K., 2016. Geomorphic evidences and chronology of multiple neotectonic events in a cratonic area: Results from the Gavilgarh Fault Zone, central India. Tectonophysics 677–678, 199–217. https://doi.org/10.1016/j.tecto.2016.04.022

Bialas, R., Buck, W., Qin, R., 2010. How much magma is required to rift a continent? Earth Planet. Sci. Lett. 292, 68-78.

Biggs, J., Amelung, F., Gourmelen, N., Dixon, T.H., Kim, S.-W., 2009. InSAR observations of 2007 Tanzania rifting episode reveal mixed fault and dyke extension in an immature continental rift. Geophys. J. Int. 179, 549–558. https://doi.org/10.1111/j.1365-246X.2009.04262.x

Birt, C.S., Maguire, P.K.H., Khan, M.A., Thybo, H., Keller, G.R., Patel, J., 1997. The influence of pre-existing structures on the evolution of the southern Kenya Rift Valley — evidence from seismic and gravity studies. Tectonophysics 278, 211–242. https://doi.org/10.1016/S0040-1951(97)00105-4

Bonini, M., Souriot, T., Boccaletti, M., Brun, J.P., 1997. Successive orthogonal and oblique extension episodes in a rift zone: Laboratory experiments with application to the Ethiopian Rift. Tectonics, v. 16, p. 347-362, doi: 10.1029/96TC03935.

Bosworth, W., 1987. Off-axis volcanism in the Gregory rift, east Africa: Implications for models of continental rifting. Geology 15, 397. https://doi.org/10.1130/0091-7613 (1987)15<397: OVITGR>2.0.CO; 2

Boulton, S.J., Whittaker, A.C., 2009. Quantifying the slip rates, spatial distribution and evolution of active normal faults from geomorphic analysis: Field examples from an oblique-extensional graben, southern Turkey. Geomorphology 104, 299–316. https://doi.org/10.1016/j.geomorph.2008.09.007

Brazier, R.A., Nyblade, A.A., Florentin, J., 2005. Focal mechanisms and the stress regime in NE and SW Tanzania, East Africa: Focal mechanisms in NE and SW Tanzanian. Geophys. Res. Lett. 32,. https://doi.org/10.1029/2005GL023156.

Brun, J. –P., 1999. Narrow rifts versus wide rifts: inferences for the mechanics of rifting from laboratory experiments. Philos. Trans. R. Soc. Lond. Ser. Math. Phys. Eng. Sci. 357, 695–712. https://doi.org/10.1098/rsta.1999.0349

Buck, W.R., 2006. The role of magma in the development of the Afro-Arabian Rift System. Geol. Soc. Lond. Spec. Publ. 259, 43–54. https://doi.org/10.1144/GSL.SP.2006.259.01.05

Buck, W.R., 2004. 1. Consequences of Asthenospheric Variability on Continental Rifting, in: Karner, G.D., Taylor, B., Driscoll, N.W., Kohlstedt, D.L. (Eds.), Rheology and Deformation of the Lithosphere at Continental Margins. Columbia University Press, New York Chichester, West Sussex, pp. 1–30. https://doi.org/10.7312/karn12738-002

Buck, W.R., 1991. Modes of continental lithospheric extension. J. Geophys. Res. Solid Earth 96, 20161–20178. https://doi.org/10.1029/91JB01485

Bull, W.B., McFadden, L.D., 1977. Tectonic geomorphology north and south of the Garlock Fault, California.

Burbank, D.W., Anderson, R.S., 2012. Tectonic geomorphology, 2nd ed. ed. J. Wiley & Sons, Chichester, West Sussex ; Hoboken, N.J.

Burgmann, R., Pollard, D.D., Martel, S.J., 1994. Slip distributions on faults: effects of

Stress gradients, inelastic deformation, heterogeneous host-rock stiffness, and fault interaction. J. Struct. Geol. 16, 1675-1690.

Burrough, P.A., McDonnell, R.A., 1998. Creating continuous surfaces from point data. In: Burrough, P.A., Goodchild, M.F., McDonnell, R.A., Switzer, P., Worboys, M. (Eds.), Principles of Geographic Information Systems. Oxford University Press, Oxford, UK.

Calais, E., d'Oreye, N., Albaric, J., Deschamps, A., Delvaux, D., Déverchère, J., Ebinger, C., Ferdinand, R.W., Kervyn, F., Macheyeki, A.S., Oyen, A., Perrot, J., Saria, E., Smets, B., Stamps, D.S., Wauthier, C., 2008. Strain accommodation by slow slip and dyking in a youthful continental rift, East Africa. Nature 456, 783-787.

Calais, E., Ebinger, C., Hartnady, C., Nocquet, J.M., 2006. Kinematics of the East African Rift from GPS and earthquake slip vector data. Geol. Soc. Lond. Spec. Publ. 259, 9–22. https://doi.org/10.1144/GSL.SP.2006.259.01.03

Cardon, H., 1999. Me´canisme de propagation des re´seaux de failles: l'exemple du Rift Gregory (Kenya). University Claude Bernard, Lyon.

Cartwright, J.A., Trudgill, B.D., Mansfield, C.S., 1995. Fault growth by segment linkage: an explanation for scatter in maximum displacement and trace length data from the Canyonlands Grabens of SE Utah. J. Struct. Geol. 17, 1319–1326.

Cerling, T., Powers, D., 1977. Paleorifting between the Gregory and Ethiopian Rifts. Geology, 5, 441-444.

Chapman, G., Lippard, S., Martyn, J., 1978. The stratigraphy and structure of the Kamasia Range, Kenya Rift Valley. J. Geol. Soc., London, 135, 265-281.

Cheng, K.-Y., Hung, J.-H., Chang, H.-C., Tsai, H., Sung, Q.-C., 2012. Scale independence of basin hypsometry and steady state topography. Geomorphology 171–172, 1–11. https://doi.org/10.1016/j.geomorph.2012.04.022

Cheng, Y., He, C., Rao, G., Yan, B., Lin, A., Hu, J., Yu, Y., Yao, Q., 2018. Geomorphological and structural characterization of the southern Weihe Graben, central China: Implications for fault segmentation. Tectonophysics 722, 11–24. https://doi.org/10.1016/j.tecto.2017.10.024

Chiasera, B., Rooney, T., Girard, G., Yirgu, G., Grosfils, E., Ayalew, D., Mohr, P., Zimbelman, J., Ramsey, M., 2018. Magmatically-assisted off-rift extension-the case for broadly distributed strain accommodation. Geosphere, 14, 4, 1544-1563.

Chorowicz, J., 1989. Transfer and transform fault zones in continental rifts: examples in the Afro-Arabian rift system. Implications of crust breaking. J. Af. Earth Sci., 8, 203-214.

Chorowicz, J., 1990. Dynamics of the different basin-types in the East African rift. J. Afr. Earth Sci. Middle East 10, 271–282. https://doi.org/10.1016/0899-5362(90)90060-R

Chorowicz, J., Sorlien, C., 1992. Oblique extensional tectonics in the Malawi Rift, Africa. Geol. Soc. Am. Bull. 104, 1015–1023. https://doi.org/10.1130/0016-7606(1992)104<1015:OETITM>2.3.CO;2

Clark, M.K., Schoenbohm, L.M., Royden, L.H., Whipple, K.X., Burchfiel, B.C., Zhang, X., Tang, W., Wang, E., Chen, L., 2004. Surface uplift, tectonics, and erosion of eastern Tibet from large-scale drainage patterns: Surface uplift, Tectonics and Erosion of the Eastern Tibet. Tectonics 23, n/a-n/a. https://doi.org/10.1029/2002TC001402

Corti, G., 2008. Control of rift obliquity on the evolution and segmentation of the main Ethiopian rift. Nat. Geosci. 1, 258–262. https://doi.org/10.1038/ngeo160

Corti, G., 2009. Continental rift evolution: From rift initiation to incipient break-up in the Main Ethiopian Rift, East Africa. Earth-Sci. Rev. 96, 1-53.

Corti, G., 2012, Evolution and characteristics of continental rifting: Analog modelling-inspired view and comparison with examples from the East African Rift System. Tectonophysics, 522-523, 1-33.

Corti, G., Bonini, M., Conticelli, S., Innocenti, F., Manetti, P., Sokoutis, D., 2003. Analogue modelling of continental extension: a review focused on the relations between the patterns of deformation and the presence of magma. Earth-Sci. Rev. 63, 169–247. https://doi.org/10.1016/S0012-8252(03)00035-7

Corti, G., Philippon, M., Sani, F., Keir, D., Kidane, T., 2013a. Re-orientation of the extension direction and pure extensional faulting at oblique rift margins: comparison between the Main Ethiopian Rift and laboratory experiments. Terra Nova 25, 396–404. https://doi.org/10.1111/ter.12049

Corti, G., Sani, F., Philippon, M., Sokoutis, D., Willingshofer, E., Molin, P., 2013b. Quaternary volcano-tectonic activity in the Soddo region, western margin of the Southern Main Ethiopian Rift: VOLCANO-TECTONIC ACTIVITY AT SODDO. Tectonics n/a-n/a. https://doi.org/10.1002/tect.20052

Courtillot, V.E., Renne, P.R., 2003. On the ages of flood basalt events. Comptes Rendus Geosci. 335, 113–140. https://doi.org/10.1016/S1631-0713(03)00006-3

Coussement, C., Gente, P., Rolet, J., Tiercelin, J.-J., Wafula, M., Buku, S., 1994. The North Tanganyika hydrothermal fields, East African Rift system: Their tectonic control and relationship to volcanism and rift segmentation. Tectonophysics 237, 155–173. https://doi.org/10.1016/0040-1951 (94)90252-6

Cowie, P.A., Attal, M., Tucker, G.E., Whittaker, A.C., Naylor, M., Ganas, A., Roberts, G.P., 2006. Investigating the surface process response to fault interaction and linkage using a numerical modelling approach: Surface process response to fault interaction and linkage. Basin Res. 18, 231–266. https://doi.org/10.1111/j.1365-2117.2006.00298.x

Cowie, P.A., Scholz, C.H., 1992. Physical explanation for the displacement-length relationship of faults using a post-yield fracture mechanics model. J. Struct. Geol. 14, 1133–1148.

Cowie, P.A., Scholz, C.H., 1992. Displacement-length scaling relationship for faults: data synthesis and discussion. J. Struct. Geol., 14 (10), 1149-1156.

Cox, R.T., 1994. Analysis of drainage-basin symmetry as a rapid technique to identify areas of possible Quaternary tilt-block tectonics: An example from the Mississippi Embayment. Geol. Soc. Am. Bull. 106, 571. https://doi.org/10.1130/0016-7606(1994)106<0571:AODBSA>2.3.CO;2

Craig, T.J., Jackson, J.A., Priestley, K., McKenzie, D., 2011. Earthquake distribution patterns in Africa: their relationship to variations in lithospheric and geological structure, and their rheological implications: Earthquake distribution patterns in Africa. Geophys. J. Int. 185, 403–434. https://doi.org/10.1111/j.1365-246X.2011.04950.x

Crossley, R., 1979. The Cenozoic stratigraphy and structure of the western part of the Rift Valley in southern Kenya. J. Geol. Soc. 136, 393–405. https://doi.org/10.1144/gsjgs.136.4.0393

Crossley, R., 1979. The Cenozoic stratigraphy and structure of the western part of the Rift Valley in southern Kenya. J. Geol. Soc., London, 136 (4), 393-405.
Daly, M.C., Chorowicz, J., Fairhead, J.D., 1989. Rift basin evolution in Africa: the influence of reactivated steep basement shear zones. Geol. Soc. Lond. Spec. Publ. 44, 309–334. https://doi.org/10.1144/GSL.SP.1989.044.01.17
Dawson, J.B., 1992. Neogene tectonics and volcanicity in the North Tanzania sector of the Gregory Rift Valley: contrasts with the Kenya sector. Tectonophysics 204 (1-2), 81-83.
Dawson, J. B. 2008. The Gregory Rift Valley and Neogene–Recent Volcanoes of Northern Tanzania. Geological Society, London, Memoirs, 33.
Dawers, N.H., Anders, M.H., Scholz, C.H., 1993. Growth of normal faults: displacement–length scaling. Geology, 21, 1107-1110.
Dawers, N.H., Anders, M.H., 1995. Displacement-length scaling and fault linkage. J. Struct. Geol., v. 17, p. 607-614, doi: 10 .1016 /0191-8141 (94)00091.
Delcaillau, B., Carozza, J.-M., Laville, E., 2006. Recent fold growth and drainage development: The Janauri and Chandigarh anticlines in the Siwalik foothills, northwest India. Geomorphology 76, 241–256. https://doi.org/10.1016/j.geomorph.2005.11.005
Delvaux, D., Barth, A., 2010. African stress pattern from formal inversion of focal mechanism data. Tectonophysics 482, 105–128. https://doi.org/10.1016/j.tecto.2009.05.009
Densmore, A.L., 2004. Footwall topographic development during continental extension. J. Geophys. Res. 109. https://doi.org/10.1029/2003JF000115
Densmore, A.L., Dawers, N.H., Gupta, S., Allen, P.A., Gilpin, R., 2003. Landscape evolution at extensional relay zones: Landscape evolution at relay zones. J. Geophys. Res. Solid Earth 108. https://doi.org/10.1029/2001JB001741
Doser, D.I., Yarwood, D.R., 1994. Deep crustal earthquakes associated with continental rifts. Tectonophysics 229, 123–131. https://doi.org/10.1016/0040-1951(94)90008-6
Driese, S.G., Ashley, G.M., 2016. Paleoenvironmental reconstruction of a paleosol catena, the Zinj archeological level, Olduvai Gorge, Tanzania. Quat. Res. 85, 133–146. https://doi.org/10.1016/j.yqres.2015.10.007
Duffy, O.B., Bell, R.E., Jackson, C.A.-L., Gawthorpe, R.L., Whipp, P.S., 2015. Fault growth and interactions in a multiphase rift fault network: Horda Platform, Norwegian North Sea. J. Struct. Geol. 80, 99–119. https://doi.org/10.1016/j.jsg.2015.08.015
Dunbar, J.A., Sawyer, D.S., 1989. How preexisting weaknesses control the style of continental breakup. J. Geophys. Res. 94, 7278. https://doi.org/10.1029/JB094iB06p07278
Ebinger, C., 2005. Continental break-up: The East African perspective. Astron. Geophys. 46, 2.16-2.21. https://doi.org/10.1111/j.1468-4004.2005.46216.x
Ebinger, C., Djomani, Y.P., Mbede, E., Foster, A., Dawson, J.B., 1997. Rifting archaean lithosphere: the eyasi-manyara-natron rifts, east africa. J. Geol. Soc. 154, 947–960.
Ebinger, C.J., Casey, M., 2001. Continental breakup in magmatic provinces: An Ethiopian example. Geology 29, 527. https://doi.org/10.1130/0091-7613(2001)029<0527: CBIMPA>2.0.CO; 2

Ebinger, C.J., Deino, A.L., Drake, R.E., Tesha, A.L., 1989. Chronology of volcanism and rift basin propagation: Rungwe Volcanic Province, East Africa. J. Geophys. Res. Solid Earth 94, 15785–15803. https://doi.org/10.1029/JB094iB11p15785

Ebinger, C.J., Deino, A.L., Tesha, A.L., Becker, T., Ring, U., 1993. Tectonic controls on rift basin morphology: Evolution of the northern Malawi (Nyasa) Rift. J. Geophys. Res. Solid Earth 98, 17821–17836. https://doi.org/10.1029/93JB01392

Ebinger, C., Djomani, Y.P., Mbede, E., Foster, A., Dawson, J.B., 1997. Rifting archaean lithosphere: the eyasi-manyara-natron rifts, east africa. J. Geol. Soc. 154, 947–960.

Ebinger, C.J., Sleep, N.H., 1998. Cenozoic magmatism throughout east Africa resulting from impact of a single plume. Nature 395, 788–791

Ebinger, C.J., Yemane, T., Harding, D.J., Tesfaye, S., Kelley, S., Rex, D.C., 2000. Rift deflection, migration, and propagation: Linkage of the Ethiopian and Eastern rifts, Africa. Geol. Soc. Am. Bull. 112, 163–176. https://doi.org/10.1130/0016-7606(2000)112<163:RDMAPL>2.0.CO;2

El Hamdouni, R., Irigaray, C., Fernández, T., Chacón, J., Keller, E.A., 2008. Assessment of relative active tectonics, southwest border of the Sierra Nevada (southern Spain). Geomorphology 96, 150–173. https://doi.org/10.1016/j.geomorph.2007.08.004

Eliet, P.P., Gawthorpe, R.L., 1995. Drainage development and sediment supply within rifts, examples from the Sperchios basin, central Greece. J. Geol. Soc. 152, 883–893. https://doi.org/10.1144/gsjgs.152.5.0883

Elkhrachy, I., 2017. Vertical accuracy assessment for SRTM and ASTER Digital Elevation Models: A case study of Najran city, Saudi Arabia. Ain Shams Eng. J. https://doi.org/10.1016/j.asej.2017.01.007

Ellis, Densmore, Anderson, 1999. Development of mountainous topography in the Basin Ranges, USA. Basin Res. 11, 21–41. https://doi.org/10.1046/j.1365-2117.1999.00087.x

Fairhead, J., Mitchell, J., Williams, L., 1972. New K/Ar determinations on rift volcanics of S. Kenya and their bearing on age of rift faulting. Nature Physic. Scien., 238, 66-69.

Fletcher, A., Abdelsalam, M., Emishaw, L., 2018. Lithospheric controls on the rifting of the Tanzanian craton at the Eyasi basin, Eastern branch of the East African rift system. Tectonics, 37, 9, 2818-2832.

Flint, J.J., 1974. Stream gradient as a function of order, magnitude, and discharge. Water Resour. Res. 10, 969–973. https://doi.org/10.1029/WR010i005p00969

Flores-Prieto, E., Quénéhervé, G., Bachofer, F., Shahzad, F., Maerker, M., 2015. Morphotectonic interpretation of the Makuyuni catchment in Northern Tanzania using DEM and SAR data. Geomorphology 248, 427–439. https://doi.org/10.1016/j.geomorph.2015.07.049

Foster, A., Ebinger, C., Mbede, E., Rex, D., 1997. Tectonic development of the northern Tanzanian sector of the East African Rift System. J. Geol. Soc. 154, 689–700.

Freeman, T.G., 1991. Calculating catchment area with divergent flow based on a regular grid. Comput. Geosci. 17, 413–422. https://doi.org/10.1016/0098-3004 (91)90048

Fritz, H., Tenczer, V., Hauzenberger, C., Wallbrecher, E., Muhongo, S., 2009. Hot granulite Nappes-Tectonic styles and thermal evolution of the Proterozoic granulite belts in East Africa. Tectonophysics, 477, 3-4, 160-173.

Frostick, L.E., Reid, I.A.N., 1989. Climatic versus tectonic controls of fan sequences: lessons from the Dead Sea, Israel. J. Geol. Soc. 146, 527–538. https://doi.org/10.1144/gsjgs.146.3.0527

Furman, T., 2007. Geochemistry of East African Rift basalts: An overview. J. Afr. Earth Sci. 48, 147–160. https://doi.org/10.1016/j.jafrearsci.2006.06.009

Gawthorpe, R.L., Hurst, J.M., 1993. Transfer zones in extensional basins: their structural style and influence on drainage development and stratigraphy. J. Geol. Soc. 150, 1137–1152. https://doi.org/10.1144/gsjgs.150.6.1137

Gawthorpe, R.L., Leeder, M.R., 2008. Tectono-sedimentary evolution of active extensional basins. Basin Res. 12, 195–218. https://doi.org/10.1111/j.1365-2117.2000.00121.x

Geoffroy, L., 1998. Diapirisme et extension intraplaque: cause ou conséquence? Comptes Rendus Académie Sci. - Ser. IIA - Earth Planet. Sci. 326, 267–273. https://doi.org/10.1016/S1251-8050(97)86817-6

George, R., Rogers, N., Kelley, S., 1998. Earliest magmatism in Ethiopia: Evidence for two mantle plumes in one flood basalt province. Geology 26, 923. https://doi.org/10.1130/0091-7613 (1998)026<0923: EMIEEF>2.3.CO; 2

Giletycz, S., Loget, N., Chang, C.-P., Mouthereau, F., 2015. Transient fluvial landscape and preservation of low-relief terrains in an emerging orogen: Example from Hengchun Peninsula, Taiwan. Geomorphology 231, 169–181. https://doi.org/10.1016/j.geomorph.2014.11.026

Gloaguen, R., 2000. Analyse quantitative de l'extension continentale par imagerie satellitale optique et radar. Application au rift sud-kenyan.Unpublished PhD Thesis, University of Brest, 200 p.

Green, W., Achauer, U., Meyer, R., 1991. A three-dimensional seimic image of the crust and upper mantle beneath the Kenya rift. Nature, 354, 199-203.

Grijalva, A., Nyblade, A., Homman, K., Accardo, N., Gaherty, J.B., Ebinger, C., et al., 2018. Seismic evidence for plume-and craton-influenced upper mantle structure beneath the Northern Malawi rift and the Rungwe volcanic province, East Africa. Geochem. Geophys. Geosyst., 19, 10, 3980-3994.

Hautot, S., Tarits, P., Whaler, K., Le Gall, B., Tiercelin, J.-J., Le Turdu, C., 2000. Deep structure of the Baringo Rift Basin (central Kenya) from three-dimensional magnetotelluric imaging: Implications for rift evolution. J. Geophys. Res. Solid Earth 105, 23493–23518. https://doi.org/10.1029/2000JB900213

Hayward, N.J., Ebinger, C.J., 1996. Variations in the along-axis segmentation of the Afar Rift system. Tectonics 15, 244–257. https://doi.org/10.1029/95TC02292

Henry, W.J., Mechie, J., Maguire, P.K.H., Khan, M.A., Prodehl, C., Keller, G.R., Patel, J., 1990. A Seismic Investigation of the Kenya Rift Valley. Geophys. J. Int. 100, 107–130. https://doi.org/10.1111/j.1365-246X.1990.tb04572.x

Hentati, I., Zairi, M., Dhia, H., 2008. Hydrotools Outil pour la modélisation et l'extraction d'un réseau hydrologique.

Howard, A.D., 1994. A detachment-limited model of drainage basin evolution. Water Resour. Res. 30, 2261–2285. https://doi.org/10.1029/94WR00757

Howard, A.D., 1967. Drainage analysis in geologic interpretation: a summation. Am. Assoc. Pet. Geol. Bull. 2246–2259.

Huerta, A.D., Nyblade, A.A., Reusch, A.M., 2009. Mantle transition zone structure beneath Kenya and Tanzania: more evidence for a deep-seated thermal upwelling in the mantle. Geophys. J. Int. 177, 1249–1255. https://doi.org/10.1111/j.1365-246X.2009.04092.x

Hurtrez, J.-E., Lucazeau, F., Lavé, J., Avouac, J.-P., 1999. Investigation of the relationships between basin morphology, tectonic uplift, and denudation from the study of an active fold belt in the Siwalik Hills, central Nepal. J. Geophys. Res. Solid Earth 104, 12779–12796. https://doi.org/10.1029/1998JB900098

Ibs-von Seht, M., Blumenstein, S., Wagner, R., Hollnack, D., Wohlenberg, J., 2001. Seismicity, seismotectonics and crustal structure of the southern Kenya Rift - new data from the Lake Magadi area. Geophys. J. Intern., 146 (2), 439-453.

Isaac, G., 1965. The stratigraphy of the Peninj Beds and the provenance of the Natron Australopithecine mandible. Quaternaria 7, 101-130.

Isaac, G.L., Curtis, G.H., 1974. Age of early Acheulian industries from Peninj Group, Tanzania. Nature 249, 624-627.

Isola, I., Mazzarini, F., Bonini, M., Corti, G., 2014. Spatial variability of volcanic features in Early-stage rift settings: the case of the Tanzania Divergence, East African rift system. Terra Nova, 26, 6, 461-468.

Jackson, J., Leeder, M., 1994. Drainage systems and the development of normal faults: an example from Pleasant Valley, Nevada. J. Struct. Geol. 16, 1041–1059.

Jackson, J.A., White, N.J., Garfunkel, Z., Anderson, H., 1988. Relations between normal-fault geometry, tilting and vertical motions in extensional terrains: an example from the southern Gulf of Suez. J. Struct. Geol. 10, 155–170.

Jana, R., Reshmidevi, T.V., Arun, P.S., Eldho, T.I., 2007. An enhanced technique in construction of the discrete drainage network from low-resolution spatial database. Comput. Geosci. 33, 717–727. https://doi.org/10.1016/j.cageo.2006.06.002

Jenson, S. K. and Domingue, J. O.: Extracting topographic structures from digital elevation data from geographic information system analysis, Photogramm. Eng. Rem. S., 54, 1593–1600,1988.

Jordan, G., 2003. Morphometric analysis and tectonic interpretation of digital terrain data: a case study. Earth Surf. Process. Landf. 28, 807–822. https://doi.org/10.1002/esp.469

Joseph Mathew, M., 2016. Geomorphology and Morphotectonic Analysis of north Borneo. Lorient.

Kampunzu, A.B., Bonhomme, M.G., Kanika, M., 1998. Geochronology of volcanic rocks and evolution of the Cenozoic Western Branch of the East African Rift System. J. Afr. Earth Sci. 26, 441–461. https://doi.org/10.1016/S0899-5362 (98)00025-6

Kattenhorn, S.A., 2004. Strike-slip fault evolution on Europa: evidence from tailcrack geometries. Icarus 172, 582–602. https://doi.org/10.1016/j.icarus.2004.07.005

Katumwehe, A.B., Abdelsalam, M.G., Atekwana, E.A., 2015. The role of pre-existing Precambrian structures in rift evolution: The Albertine and Rhino grabens, Uganda. Tectonophysics 646, 117–129. https://doi.org/10.1016/j.tecto.2015.01.022

Keen, C.E., 1985. The dynamics of rifting: deformation of the lithosphere by active and passive driving forces. Geophys. J. Int. 80, 95–120. https://doi.org/10.1111/j.1365-246X.1985.tb05080.x

Keir, D., Bastow, I., Corti, G., Mazzarini, F., Rooney, T., 2015. The origin of along-rift variations in faulting and magmatism in the Ethiopian Rift. Tectonics, 34, 3, 464-477.

Keir, D., C. Ebinger, E. Daly, G. Stuart, P. Maguire, A. Ayele, 2006. Strain

accommodation by magmatism and faulting as rifting proceeds to breakup: Seismicity of the northern Ethiopian rift. J. Geophys. Res., 111, B05314, doi:10.1029/2005JB003748.

Keir, D., Bastow, I.D., Pagli, C., Chambers, E.L., 2013. The development of extension and magmatism in the Red Sea rift of Afar. Tectonophysics 607, 98–114. https://doi.org/10.1016/j.tecto.2012.10.015

Keller, E.A., Pinter, N., 2002. Active tectonics: earthquakes, uplift, and landscape, 2nd ed. ed, Books in the Prentice Hall earth science series. Prentice Hall, Upper Saddle River, N.J.

Keranen, K., Klemperer, S.L., 2008. Discontinuous and diachronous evolution of the Main Ethiopian Rift: Implications for development of continental rifts. Earth Planet. Sci. Lett. 265, 96–111. https://doi.org/10.1016/j.epsl.2007.09.038

Keranen, K., Klemperer, S.L., Gloaguen, R., EAGLE Working Group, 2004. Three-dimensional seismic imaging of a protoridge axis in the Main Ethiopian rift. Geology, v. 32, p. 949-952, doi:10.1130/G20737.1.

Keranen, K.M., Klemperer, S.L., Julia, J., Lawrence, J.F., Nyblade, A.A., 2009. Low lower crustal velocity across Ethiopia: Is the Main Ethiopian Rift a narrow rift in a hot craton?: MAIN ETHIOPIAN RIFT-A NARROW RIFT IN A HOT CRATON? Geochem. Geophys. Geosystems 10, n/a-n/a. https://doi.org/10.1029/2008GC002293

Kinabo, B.D., Hogan, J.P., Atekwana, E.A., Abdelsalam, M.G., Modisi, M.P., 2008. Fault growth and propagation during incipient continental rifting: Insights from a combined aeromagnetic and Shuttle Radar Topography Mission digital elevation model investigation of the Okavango Rift Zone, northwest Botswana: FAULT GROWTH AND PROPAGATION IN RIFTS. Tectonics 27, n/a-n/a. https://doi.org/10.1029/2007TC002154

Kim, Y.S, Sanderson, D.J., 2005. The relationship between displacement and length of faults: a review. Earth Sci. Rev., 68, 317-34.

Kiram E. Lezzar,1 Jean-Jacques Tier, 2002. Control of normal fault interaction on the distribution of major Neogene sedimentary depocenters, Lake Tanganyika, East African rift. AAPG Bull. 86. https://doi.org/10.1306/61EEDC1A-173E-11D7-8645000102C1865D

King, B., 1978. Structural evolution of the Gregory rift valley. In: Bishop, W. (Ed.), Geological Background to Fossil Man, 6, Geol. Soc., London, 29-45.

Kirby, E., Whipple, K.X., 2012. Expression of active tectonics in erosional landscapes. J. Struct. Geol. 44, 54–75. https://doi.org/10.1016/j.jsg.2012.07.009

Kirby, E., X. Whipple, K., 2001. Quantifying differential rock uplift rates via stream profi le analysis: Geology. Geology 29.

Kirby, S.H., Kronenberg, A.K., 1987. Rheology of the lithosphere: Selected topics. Rev. Geophys. 25, 1219. https://doi.org/10.1029/RG025i006p01219

Koptev, A., Burov, E., Calais, E., Leroy, S., Gerya, T., Guillou, L. Cloetingh, S., 2016. Contrasted continental rifting via plume-craton interaction : Applications to Central East African rift. Geoscience Frontiers, 7, 2, 221-236.

Koptev, A., Calais, E., Burov, E., Leroy, S., Gerya, T., 2015. Dual continental rift systems generated by plume–lithosphere interaction. Nat. Geosci. 8, 388.

Koptev, A., Cloetingh, S., Gerya, T., Calais, E., Leroy, S., 2018. Non-uniform splitting of a single mantle plume by double cratonic keels: Insights into the origin of central and southern East African Rift System. Terra Nova, 30, 2, 125-134.

KRISP Working Group, 1991. The Kenya rift: pure shear extension above a mantle

plume. Nature, 345, 223-227.
Kusznir, N.J., Park, R.G., 1987. The extensional strength of the continental lithosphere: its dependence on geothermal gradient, and crustal composition and thickness. Geol. Soc. Lond. Spec. Publ. 28, 35–52. https://doi.org/10.1144/GSL.SP.1987.028.01.04
Lague, D., 2014. The stream power river incision model: evidence, theory and beyond: Stream power incision model. Earth Surface Process Landform. 39, 38–61. https://doi.org/10.1002/esp.3462
Lambert, C., Muirhead, J.D., Ebinger, C.J., Tiberi, C., Roecker, S., Ferdinand-Wambura, R., Kianji, G., and Mulibo, G., 2014, Lower crustal seismicity, volatiles, and evolving strain fields during the initial stages of cratonic rifting: American Geophysical Union, Fall Meeting 2014, abs. T53B-4678.
Last, R.J., Nyblade, A.A., Langston, C.A., Owens, T.J., 1997. Crustal structure of the East African Plateau from receiver functions and Rayleigh wave phase velocities. J. Geophys. Res. Solid Earth 102, 24469–24483. https://doi.org/10.1029/97JB02156
Lee, H., Fischer, T., Muirhead, J., Ebinger, C., Kattenhorn, S., Sharp, Z., Kianji, G., Sano, Y.,Takahata, N., 2017. Incipient rifting accompanied by the release of subcontinental lithospheric mantle volatiles in the Magadi and Natron basin, East Africa. J. Volcanol. Geotherm. Res., doi:10.1016/j.jvolgeores.2017.03.017.
Leeder, M.R., Jackson, J.A., 1993. The interaction between normal faulting and drainage in active extensional basins, with examples from the western United States and central Greece. Basin Res. 5, 79–102.
Le Gall, B., Tiercelin, J.J., Richert, J.P., Gente, P., Sturchio, N.C., Stead, D., Le Turdu, C., 2000. A morphotectonic study of an extensional fault zone in a magma-rich rift: The Baringo Trachyte fault system, central Kenya Rift. Tectonophysics, v. 320, p. 87-106, doi: 10 .1016/S0040 -1951 (00)00069X.
Le Gall, B., Gernigon, L., Rolet, J., Ebinger, C., Gloaguen, R., Nilsen, O., Dypvik, H., Deffontaines, B., Mruma, A., 2004. Neogene-Holocene rift propagation in central Tanzania: Morphostructural and aeromagnetic evidence from the Kilombero area. Geol. Soc. Am. Bull. 116, 490–510.
Le Gall, B., Nonnotte, P., Rolet, J., Benoit, M., Guillou, H., Mousseau-Nonnotte, M., Albaric, J., Déverchère, J., 2008. Rift propagation at craton margin: distribution of faulting and volcanism in the North Tanzanian Divergence (East Africa) during Neogene times. Tectonophysics 448, 1-19.
Le Gall, B., Vétel, W., Morley, C.K., 2005. Inversion tectonics during continental rifting: The Turkana Cenozoic rifted zone, northern Kenya: Inversion Tectonics in Rift context. Tectonics 24, n/a-n/a. https://doi.org/10.1029/2004TC001637
Leseane, K., Atekwana, Estella A., Mickus, K.L., Abdelsalam, M.G., Shemang, E.M., Atekwana, Eliot A., 2015. Thermal perturbations beneath the incipient Okavango Rift Zone, northwest Botswana: THERMAL ANOMALY BELOW THE OKAVANGO RIFT. J. Geophys. Res. Solid Earth 120, 1210–1228. https://doi.org/10.1002/2014JB011029
Le Turdu, C., Richert, J.P., Xavier, J.-P., Renaut, R.W., Tiercelin, J.-J., Rolet, J., Lezzar, K.E., Coussement, C., 1999. Influence of preexisting oblique discontinuities on the geometry and evolution of extensional fault patterns: Evidence from the Kenya Rift using SPOT imagery. In Morley, C.K., ed., Geoscience of Rift Systems. Evolution of East Africa. Am. Assoc. Petrol. Geol. Studies in Geology 44, p. 173-191.

Lezzar, K., Tiercelin, J.J., Cohen, A., Reynolds, D., Le Gall, B., Scholz, C., 2002. Control of normal fault interaction on the distribution of major Neogene sedimentary depocenters, Lake Tanganyika, East African rift. AAPG. Bull., 86, 1027-1059.

Lister, G.S., Etheridge, M.A., Symonds, P.A., 1986. Detachment faulting and the evolution of passive continental margins. Geology 14, 246. https://doi.org/10.1130/0091-7613(1986)14<246:DFATEO>2.0.CO;2

Long, R.E., Backhouse, R.W., 1976. The Structure of the Western Flank of the Gregory Rift. Part II. The Mantle. Geophys. J. Int. 44, 677–688. https://doi.org/10.1111/j.1365-246X.1976.tb00300.x

Macdonald, R., 1994. Petrological evidence regarding the evolution of the Kenya Rift Valley. Tectonophysics 236, 373–390. https://doi.org/10.1016/0040-1951 (94)90185-6

Macdonald, R., Williams, L.A.J., Gass, I.G., 1994. Tectonomagmatic evolution of the Kenya rift valley: some geological perspectives. J. Geol. Soc. 151, 879–888. https://doi.org/10.1144/gsjgs.151.5.0879

Macheyeki, A., Delvaux, D., De Batist, M., Mruma, A., 2008. Fault kinematics and tectonic stress in the seismically active Manyara-Dodoma Rift segment in Central Tanzania- Implications for the East African Rift. J. Af. Earth Sc., 51, 4, 163-188.

Macintyre, R.M., Mitchell, J.G., Dawson, J.B., 1974. Age of Fault Movements in Tanzanian Sector of East African Rift System. Nature 247, 354–356. https://doi.org/10.1038/247354a0

Mackin, J. H. (1948), Concept of the graded river, Geol. Soc. Am. Bull., 59 (5), 463 (512), doi:10.1130/0016-7606(1948)59.

Mahmood, S.A., Gloaguen, R., 2012. Appraisal of active tectonics in Hindu Kush: Insights from DEM derived geomorphic indices and drainage analysis. Geosci. Front. 3, 407–428. https://doi.org/10.1016/j.gsf.2011.12.002

Mana, S., Furman, T., Carr, M.J., Mollel, G.F., Mortlock, R.A., Feigenson, M.D., Turrin, B.D., Swisher, C.C., 2012. Geochronology and geochemistry of the Essimingor volcano: Melting of metasomatized lithospheric mantle beneath the North Tanzanian Divergence zone (East African Rift). Lithos 155, 310–325. https://doi.org/10.1016/j.lithos.2012.09.009

Mana, S., Furman, T., Turrin, B., Feigenson, M., Swisher, C., 2015. Magmatic activity across the East African North Tanzanian Divergence Zone. J. Geol. Soc., London, 172, 368.

Mandlburger, G., Hauer, C., Höfle, B., Habersack, H., and Pfeifer, N.: Optimisation of LiDAR derived terrain models for river flow modelling, Hydrol. Earth Syst. Sci., 13, 1453–1466, 2009, http://www.hydrol-earth-syst-sci.net/13/1453/2009/.

Manega, P.C. 1993. Geochronology, geochemistry and isotopic study of the Plio-Pleistocene hominid sites and the Ngorongoro Volcanic Highland in northern Tanzania. PhD thesis, University of Colorado.

Manighetti, I., King, G., Sammis, C., 2004. The role of off-fault damage in the evolution of normal faults. Earth Planet. Sci. Lett., 217, 399-408.

Marín, D., Escalona, A., Grundvåg, S.-A., Nøhr-Hansen, H., Kairanov, B., 2018. Effects of adjacent fault systems on drainage patterns and evolution of uplifted rift shoulders: The Lower Cretaceous in the Loppa High, southwestern Barents Sea. Mar. Pet. Geol. 94, 212–229. https://doi.org/10.1016/j.marpetgeo.2018.04.009

Martz, L.W., Garbrecht, J., 1998. The treatment of flat areas and depressions in automated drainage analysis of raster digital elevation models. Hydrol. Process. 12, 843–855.

https://doi.org/10.1002/(SICI)1099-1085(199805)12:6<843::AID-HYP658>3.0.CO;2-R

Mayer, L., 1990. Introduction to quantitative geomorphology: an exercise manual. Prentice McConnell, R., 1972. Geological development of the rift system of eastern Africa. Geol., Soc. Am., Bull., 83, 2549-2572.

McClay, K., Dooley, T., Whitehouse, P., Mills, M., 2002. 4-D evolution of rift systems:insights from scaled physical models. AAPG. Bull., 86, 935-959.

McConnel, R.B., 1972. Geological development of the rift system of Eastern Africa. Geological Society America Bulletin 83, 2549–2572.

McHenry, L. J., Luque, L., Gomez, J., Diez-Martın, F., 2011. Promise and pitfalls for characterizing and correlating the zeolitically altered tephra of the Pleistocene Peninj Group, Tanzania. Quat. Res., 75(3), 708-720.

McHenry, L.J., Mollel, G.F., Swisher, C.C., 2008. Compositional and textural correlations between Olduvai Gorge Bed I tephra and volcanic sources in the Ngorongoro Volcanic Highlands, Tanzania. Quat. Int. 178, 306–319. https://doi.org/10.1016/j.quaint.2007.01.004

McIntyre, R., Mitchell, J., Dawson, J., 1974. Age of fault movements in the Tanzanian sector of the East African Rift system. Nature, 247, 354-356.

McKenzie, D., 1978. Some remarks on the development of sedimentary basins. Earth Planet. Sci. Lett. 40, 25–32.

Mechie, J., Keller, G.R., Prodehl, C., Gaciri, S., Braile, L.W., Mooney, W.D., Gajewski, D., Sandmeier, K.-J., 1994. Crustal structure beneath the Kenya Rift from axial profile data. Tectonophysics 236, 179–200. https://doi.org/10.1016/0040-1951(94)90176-7

Merle, O., Michon, L., 2001. The formation of the West European rift: a new model as exemplified by the Massif Central area.Bulletin de la Socie´te´ Ge´ologique de France 172 (2), 213–221.

Michon, L., Sokoutis, D., 2005. Interaction between structural inheritance and extension direction during graben and depocentre formation: an experimental approach. Tectonophysics, 409, 125-146.

Ministry of Energy and Regional development of Kenya, 1987. Geological map of Kenya, 1:1, 000 000. (Eds) BEICIP, Rueil-Malmaison, France.

Mohr, P., 1983. Volcanotectonic aspects of the Ethiopian Rift evolution. Bull. Cent. Rech. Elf Aquitaine Explor. Prod. 7, 175–189.

Mohr, P., Zanettin, B., 1988. The Ethiopian Flood Basalt Province, in: Macdougall, J.D. (Ed.), Continental Flood Basalts. Springer Netherlands, Dordrecht, pp. 63–110. https://doi.org/10.1007/978-94-015-7805-9_3

Möller, A., Mezger, K., Schenk, V., 2000. U-Pb dating of metamorphic minerals: Pan-African metamorphism and prolonged slow cooling of high pressure granulites in Tanzania, East Africa. Precambrian Res., 104, 123-146.

Molin, P., Corti, G., 2015a. Topography, river network and recent fault activity at the margins of the Central Main Ethiopian Rift (East Africa). Tectonophysics 664, 67–82. https://doi.org/10.1016/j.tecto.2015.08.045

Molin, P., Corti, G., 2015b. Topography, river network and recent fault activity at the margins of the Central Main Ethiopian Rift (East Africa). Tectonophysics 664, 67–82. https://doi.org/10.1016/j.tecto.2015.08.045

Montgomery, D.R., Foufoula-Georgiou, E., 1993. Channel network source representation using digital elevation models. Water Resource Research 29, 3925–3934. https://doi.org/10.1029/93WR02463

Mooney, W.D., Christensen, N.I., 1994. Composition of the crust beneath the Kenya rift. Tectonophysics 236, 391–408.

Morgan, P., Baker, B.H., 1983 (Eds.), Processes of Continental Rifting. Tectonophysics 94, 241–252

Morley, C.K., 1999. AAPG Studies in Geology 44, Chapter 7: Boundary Fault Angle, with Particular Reference to the Lokichar Fault, Turkana Region, Kenya.

Morley, C.., 1999. Marked along-strike variations in dip of normal faults—the Lokichar fault, N. Kenya rift: a possible cause for metamorphic core complexes. J. Struct. Geol. 21, 479–492. https://doi.org/10.1016/S0191-8141(99)00043-7

Morley, C.K., 1999. Patterns of displacement along large normal faults: Implications for basin evolution and fault propagation, based on examples from east Africa. Am. Assoc. Petrol. Geol. Bull., 83, 613-634.

Morley, C.K., 1995. Developments in the structural geology of rifts over the last decade and their impact on hydrocarbon exploration. Geol. Soc. Lond. Spec. Publ. 80, 1–32. https://doi.org/10.1144/GSL.SP.1995.080.01.01

Morley, C., Wescott, W., Stone, D., Harper, R., Wigget, S., Karanja, F., 1992. Tectonic evolution of northern Kenya Rift. J. Geol. Soc., 149, 333-348.

Mosley, P., 1993, Geological evolution of the late Proterozoic Mozambique Belt of Kenya. Tectonophysics, 221, 223-250.

Mruma, A., Ernst, R., Soderland, U., 2014. Evidence for ca. 1.775 Ma large igneous province (LIP) in the Tanzanian Craton. Abst., 25th Coll. Af. Geol., Dar es Salaam, Tanzania, p. 9.

Mugisha, F., Ebinger, C., Strecker, M., Pope, D., 1997. Two-stage rifting in the Kenya Rift: Implications for half-graben models. Tectonophysics, 278, 61-81.

Muirhead, J.D., Kattenhorn, S.A., Lee, H., Mana, S., Turrin, B.D., Fischer, T.P., Kianji, G., Dindi, E., Stamps, D.S., 2016. Evolution of upper crustal faulting assisted by magmatic volatile release during early-stage continental rift development in the East African Rift. Geosphere 12, 1670–1700. https://doi.org/10.1130/GES01375.1

Muirhead, J.D., Kattenhorn, S., Lee, H., Fischer, T., Mana, S., Turrin, B., Kianji, G., Dindi, E., Stamps, D., 2016. Evolution of upper crustal faulting assisted by magmatic volatile release during early-stage continental rift development in the East African Rift. Geosphere, 12, 1670, doi:10.1130/GES01375.1.

Muirhead, J.D, Kattenhorn, S.A., 2018. Activation of preexisting transverse structures in an evolving magmatic rift in East Africa. J. Struct. Geol., 106, 1-18.

Muirhead, J.,Lachlan, J., Wright, C., Sholz, C., 2019. Rift evolution in regions of low magma input in East Africa. Earth Planet. Sc., Lett., 506, 332-346.

Mukul, Manas, Srivastava, V., Mukul, Malay, 2017. Out-of-sequence reactivation of the Munsiari thrust in the Relli River basin, Darjiling Himalaya, India: Insights from Shuttle Radar Topography Mission digital elevation model-based geomorphic indices. Geomorphology 284, 229–237. https://doi.org/10.1016/j.geomorph.2016.10.029

Mulibo, G.D., Nyblade, A.A., 2016. The seismotectonics of Southeastern Tanzania: Implications for the propagation of the eastern branch of the East African Rift. Tectonophysics 674, 20–30. https://doi.org/10.1016/j.tecto.2016.02.009

Nicol, A., Walsh, J.J., Watterson, J., Gillespie, P.A., 1996. Fault size distributions–are they really power-law? J. Struct. Geol., 18 (2/3), 191–197.

Nicol, A., Watterson, J., Walsh, J.J., Childs, C., 1996. The shapes, major axis orientations and displacement patterns of fault surfaces. J. Struct. Geol. 18, 235–248.

Nonnotte, P., 2007. Etude volcano-tectonique de la zone de Divergence Nord Tanzanienne (Terminaison Sud du Rift Kenyan). Caractérisation pétrologique et géochimique du volcanisme récent (8 Ma-Actuel) et du manteau source. Contraintes de mise en place. Thèse de Doctorat, Université de Bretagne Occidentale, Brest.

Nonnotte, P., Guillou, H., Le Gall, B., Benoit, M., Cotten, J., Scaillet, S., 2008. New K-Ar age determinations of Kilimanjaro volcano in the North Tanzanian diverging rift, East Africa. J. Volcan. Geoth. Res., 173 (1-2), 99-112.

Nyamai, C., Mathu, E., Opiyo-Akech, N., Wallbrecher, E., 2004. A reappraisal of the geology, geochemistry, structures and tectonics of the Mozambique belt in Kenya, east of the rift system. https://doi.org/10.1016/S1342-937X(05)70517-7

Nyblade, A.A., Langston, C.A., 1995. East African earthquakes below 20 km depth and their implications for crustal structure. Geophys. J. Int. 121, 49–62. https://doi.org/10.1111/j.1365-246X.1995.tb03510.x

Nyblade, A.A., Langston, C.A., Last, R.J., Birt, C., Owens, T.J., 1996. Seismic experiment reveals rifting of craton in Tanzania. Eos Trans. Am. Geophys. Union 77, 517. https://doi.org/10.1029/96EO00339

O'Callaghan, J.F., Mark, D.M., 1984. The extraction of drainage networks from digital elevation data. Comput. Vis. Graph. Image Process. 28, 323–344. https://doi.org/10.1016/S0734-189X(84)80011-0

O'Donnell, J., Adams, A., Nyblade, A., Mulibo, G., Tugume, F., 2013. The uppermost mantle shear wave velocity structure of eastern Africa from rayleigh wave tomography: constraints on rift evolution. Geophys. J. Int., 194, 2, 961-978.

Özsayın, E., 2016. Relative tectonic activity assessment of the Çameli Basin, Western Anatolia, using geomorphic indices. Geodin. Acta 28, 241–253. https://doi.org/10.1080/09853111.2015.1128180

Park, Y., Nyblade, A.A., 2006. P-wave tomography reveals a westward dipping low velocity zone beneath the Kenya Rift. Geophys. Res. Lett. 33. https://doi.org/10.1029/2005GL025605

Paslick, C., Halliday, A., James, D., Dawson, J., 1995. Enrichment of the continental lithosphere by OIB melts: Isotopic evidence from the volcanic province of northern Tanzania. Earth Planet., Sci., Lett., 130, 109-126.

Pasteels, P., Villeneuve, M., De Paepe, P., Klerkx, J., 1989. Timing of the volcanism of the southern Kivu province: implications for the evolution of the western branch of the East African Rift system. Earth Planet. Sci. Lett. 94, 353–363. https://doi.org/10.1016/0012-821X (89)90152-0

Paul W Hare, Thomas W Gardner, 1985. Geomorphic indicators of vertical neotectonism along converging plate margins, Nicoya Peninsula, Costa Rica. Tecton. Geomorphol. 75–104.

Peacock, D.C.P., 1991. Displacements and segment linkage in strike-slip fault zones. J. Struct. Geol., 13, 1025-1035.

Peacock, D.C.P., Price, S.P., Whitham, A.G., Pickles, C.S., 2000. The World's biggest relay ramp: Hold With Hope, NE Greenland. J. Struct. Geol. 22, 843–850. https://doi.org/10.1016/S0191-8141 (00)00012-2

Peacock, D.C.P., Sanderson, D.J., 1991. Displacements, segment linkage and relay ramps in normal fault zones. J. Struct. Geol., 13, 721–733.

Petit, C., Ebinger, C., 2000. Flexure and mechanical behavior of cratonic lithosphere: Gravity models of the East African and Baikal rifts. J. Geophys. Res. Solid Earth 105, 19151–19162. https://doi.org/10.1029/2000JB900101

Philippon, M., Corti, G., Sani, F., Bonini, M., Balestrieri, M.-L., Molin, P., Willingshofer, E., Sokoutis, D., Cloetingh, S., 2014. Evolution, distribution, and characteristics of rifting in southern Ethiopia: rifting in southern Ethiopia. Tectonics 33, 485–508. https://doi.org/10.1002/2013TC003430

Phillips, D., Matchan, E.L., 2013. Ultra-high precision 40Ar/39Ar ages for Fish Canyon Tuff and Alder Creek Rhyolite sanidine: New dating standards required? Geochim. Cosmochim. Acta 121, 229–239. https://doi.org/10.1016/j.gca.2013.07.003

Pik, R., Marty, B., Hilton, D.R., 2006. How many mantle plumes in Africa? The geochemical point of view. Chem. Geol. 226, 100–114. https://doi.org/10.1016/j.chemgeo.2005.09.016

Pike, R.J., Wilson, S.E., 1971. Elevation-relief ratio, hypsometric integral, and geomorphic area-altitude analysis. Geol. Soc. Am. Bull. 82, 1079–1084.

Plasman, M., 2017. Rupture lithosphérique continentale dans le Rift Est Africain Apport de l'inversion conjointe. Université de Bretagne occidentale-Brest.

Plasman, M., Tiberi, C., Ebinger, C., Gautier, S., Albaric, J., Peyrat, S., Déverchère, J., Le Gall, B., Tarits, P., Roecker, S., Wambura, F., Muzuka, A., Mulibo, G., Mtelela, K., Msabi, M., Kianji, G., Hautot, S., Perrot, J., Gama, R., 2017. Lithospheric low-velocity zones associated with a magmatic segment of the Tanzanian Rift, East Africa. Geophys. J. Int. 210, 465–481. https://doi.org/10.1093/gji/ggx177

Pollard, D.D., Segall, P., 1987. Theoretical displacements and stresses near fractures in rock: with applications to faults, joints, veins, dikes, and solution surfaces. In: Atkinson, B.K. (Ed.), Fracture Mechanics of Rock. Acad. Press, London, pp. 277-349.

Pouclet, A., Bellon, H., Bram, K., 2016. The Cenozoic volcanism in the Kivu rift: Assessment of the tectonic setting, geochemistry, and geochronology of the volcanic activity in the South-Kivu and Virunga regions. J. Afr. Earth Sci. 121, 219–246. https://doi.org/10.1016/j.jafrearsci.2016.05.026

Prodehl, C., Ritter, J.R.R., Mechie, J., Keller, G.R., Khan, M.A., Jacob, B., Fuchs, K., Nyambok, I.O., Obel, J.D., Riaroh, D., 1997. The KRISP 94 lithospheric investigation of southern Kenya — the experiments and their main results. Tectonophysics 278, 121–147. https://doi.org/10.1016/S0040-1951 (97)00098-X

Ramsey, L.A., Walker, R.T., Jackson, J., 2008. Fold evolution and drainage development in the Zagros mountains of Fars province, SE Iran. Basin Res. 20, 23–48. https://doi.org/10.1111/j.1365-2117.2007.00342.x

Renne, P.R., Balco, G., Ludwig, K.R., Mundil, R., Min, K., 2011. Response to the comment by W.H. Schwarz et al. on "Joint determination of 40K decay constants and 40Ar∗/40K for the Fish Canyon sanidine standard, and improved accuracy for 40Ar/39Ar geochronology" by P.R. Renne et al. (2010). Geochim. Cosmochim. Acta 75, 5097–5100. https://doi.org/10.1016/j.gca.2011.06.021

Renne, P.R., Deino, A.L., Hilgen, F.J., Kuiper, K.F., Mark, D.F., Mitchell, W.S., Morgan, L.E., Mundil, R., Smit, J., 2013. Time Scales of Critical Events Around the

Cretaceous-Paleogene Boundary. Science 339, 684–687. https://doi.org/10.1126/science.1230492
Ring, U., 1994. The influence of preexisting structure on the evolution of the Cenozoic Malawi rift (East African rift system). Tectonics 13, 313–326.
Ritsema, J., Nyblade, A.A., Owens, T.J., Langston, C.A., VanDecar, J.C., 1998. Upper mantle seismic velocity structure beneath Tanzania, east Africa: Implications for the stability of cratonic lithosphere. J. Geophys. Res. Solid Earth 103, 21201–21213. https://doi.org/10.1029/98JB01274
Rogers, N., Macdonald, R., Fitton, J.G., George, R., Smith, M. & Barreiro, B., 2000. Two mantle plumes beneath the East African rift system: Sr, Nd and Pb isotope evidence from Kenya Rift basalts, Earth planet. Sci. Lett., 176(3), 387–400.
Rooney, T., Bastow, I., Keir; D., Mazzarini, F., Movsesian, E. et al., 2014. The protracted development of focused magmatic intrusion during continental rifting. Tectonics, 33, 6, 875-897.
Rosendahl, B.R., 1987. Architecture of Continental Rifts with Special Reference to East Africa. Annu. Rev. Earth Planet. Sci. 15, 445–503. https://doi.org/10.1146/annurev.ea.15.050187.002305
Royden, L., G. Sclater, J., P. Von Herzen, R., 1980. Continental Margin Subsidence and Heat Flow: Important Parameters in Formation of Petroleum Hydrocarbons.
Ruppel, C., 1995. Extensional processes in continental lithosphere. J. Geophys. Res. Solid Earth 100, 24187–24215. https://doi.org/10.1029/95JB02955
Santillan, J.R., Makinano-Santillan, M., 2016. Vertical accuracy assessment of 30-m Resolution Alos, Aster, and SRTM Global Dems over Northeeastern Mindanao, Philipines. ISPRS - Int. Arch. Photogramm. Remote Sens. Spat. Inf. Sci. XLI-B4, 149–156. https://doi.org/10.5194/isprsarchives-XLI-B4-149-2016
Sarafian, E., Evans, R.L., Abdelsalam, M.G., Atekwana, E., Elsenbeck, J., Jones, A.G., Chikambwe, E., 2018. Imaging Precambrian lithospheric structure in Zambia using electromagnetic methods. Gondwana Res. 54, 38–49. https://doi.org/10.1016/j.gr.2017.09.007
Saria, E., Calais, E., Stamps, D.S., Delvaux, D., Hartnady, C.J.H., 2014. Present-day kinematics of the East African Rift. J. Geophys. Res. Solid Earth 119, 3584–3600. https://doi.org/10.1002/2013JB010901
Schäuble H. (2003). HydroTools 1.0 for Arcview 3.x: hydrological analysis of small and large watersheds. Institute of Applied Geosciences Technical University of Darmstadt. 13 p.
Shackleton, R.M., 1993. Tectonics of the lower crust: a view from the Usambara Mountains, NE Tanzania. J. Struct. Geol., 15, 663-671.
Sherrod, D., Magigita, M., Kwelwa, S., 2013. Geologic map of Oldonyo Lengai and surroundings, Arusha region, United Republic of Tanzania. U.S. Geol. Surv. Open-File Report 2013-1306, 1:50,000, 50 p.
Scholz, C.H., Cowie, P.A., 1990. Determination of total strain from faulting using slip-measurements. Nature 346, 837-839.
Schumm, S.A., 1956. Evolution of drainage systems and slopes in Badlands at Perth Amboy, New Jersey. Geol. Soc. Am. Bull. 67, 597. https://doi.org/10.1130/0016-7606 (1956)67[597: EODSAS] 2.0.CO; 2
Schwanghart, W., Scherler, D., 2014. Short Communication: TopoToolbox 2 – MATLAB-based software for topographic analysis and modeling in Earth surface sciences. Earth Surf. Dyn. 2, 1–7. https://doi.org/10.5194/esurf-2-1-2014

Seeber, L., Gornitz, V., 1983. River profiles along the Himalayan arc as indicators of active tectonics. Tectonophysics 92, 335–367.

Sikes, N.E., Ashley, G.M., 2007. Stable isotopes of pedogenic carbonates as indicators of paleoecology in the Plio-Pleistocene (upper Bed I), western margin of the Olduvai Basin, Tanzania. J. Hum. Evol. 53, 574–594. https://doi.org/10.1016/j.jhevol.2006.12.008

Sippel, J., Meessen, C., Cacace, M., Mechie, J., Fishwick, S., Heine, C., Scheck, M., Strecker, M., 2017. The Kenya rift revisited: insights into lithospheric strength through data-driven 3D gravity and thermal modelling. J. Geophys. Res., Solid Earth, 8, 1, 45-81.

Smets, B., Kervyn, M., d'Oreye, N., Kervyn, F., 2015. Spatio-temporal dynamics of eruptions in a youthful extensional setting: Insights from Nyamulagira Volcano (D.R. Congo), in the western branch of the East African Rift. Earth-Sci. Rev. 150, 305–328. https://doi.org/10.1016/j.earscirev.2015.08.008

Smith, M., 1994. Stratigraphic and structural constraints on mechanisms of active rifting in the Gregory Rift, Kenya. Tectonophysics 236, 3–22. https://doi.org/10.1016/0040-1951(94)90166-X

Smith, M, Mosley, P, 1993. Crustal heterogeneity and basement influence on the development of the Kenya Rift, East Africa. Tectonics 591–606.

Snyder, N.P., 2000. Landscape response to tectonic forcing: Digital elevation model analysis of stream profiles in the Mendocino triple junction region, northern California. Geol. Soc. Am. Bull. 14.

Spiegel, C., Kohn, B.P., Belton, D.X., Gleadow, A.J.W., 2007. Morphotectonic evolution of the central Kenya rift flanks: Implications for late Cenozoic environmental change in East Africa. Geology 35, 427. https://doi.org/10.1130/G23108A.1

Stab, M., Bellahsen, N., Pik, R., Quidelleur, X., Ayalew, D., and Leroy, S. (2015). the role of magmatism and segmentation in the structural evolution of the afar rift. In EGU General Assembly Conference Abstracts, volume 17, page 5705. 13, 317

Stamps, D.S., Calais, E., Saria, E., Hartnady, C., Nocquet, J.-M., Ebinger, C.J., Fernandes, R.M., 2008. A kinematic model for the East African Rift. Geophys. Res. Lett. 35. https://doi.org/10.1029/2007GL032781

Strahler, A.N., 1957. Quantitative analysis of watershed geomorphology. Trans. Am. Geophys. Union 38, 913. https://doi.org/10.1029/TR038i006p00913

Sung, Q.-C., Chen, Y.-C., 2004. Self-affinity dimensions of topography and its implications in morphotectonics: an example from Taiwan. Geomorphology 62, 181–198. https://doi.org/10.1016/j.geomorph.2004.02.012

Thomas, R., Spencer, C., Bushi, A., Baglow, N., Boniface, N., de Kock, G., et al., 2016. Geochronology of the central Tanzania craton and its southern and eastern orogenic margins. Precambrian Res., 277, 47-67.

Thybo, H., Maguire, P., Birt, C., Perchuc, E., 2000. Seismic reflectivity and magmatic underplating beneath the Kenya Rift. Geophys. Res. Lett., 27, 2745-2748.

Tommasi, A., Vauchez, A., n.d. Continental rifting parallel to ancient collisional belts: an e¡ect of the mechanical anisotropy of the lithospheric mantle. Earth Planet. Sci. Lett. 12.

Trudgill, B., Underhill, J.R., 2002. Introduction to the structure and stratigraphy of rift systems. AAPG Bull. 86, 931–934.

Turcotte, D.L., Emerman, S.H., 1983. Mechanisms of Active and Passive Rifting, in: Developments in Geotectonics. Elsevier, pp. 39–50. https://doi.org/10.1016/B978-0-444-42198-2.50010-9

Vauchez, A., Dineur, F. & Rudnick, R., 2005. Microstructure, texture and seismic anisotropy of the lithospheric mantle above a mantle plume: insights from the Labait volcano xenoliths (Tanzania), Earth planet. Sci. Lett., 232(3), 295–314.

Versfelt, J., Rosendahl, B.R., 1989. Relationships between pre-rift structure and rift architecture in Lakes Tanganyika and Malawi, East Africa. Nature 337, 354–357. https://doi.org/10.1038/337354a0

Vetel, W., Le Gall, B., 2006. Dynamics of prolonged continental extension in magmatic rifts: the Turkana Rift case study (North Kenya). Geol. Soc. Lond. Spec. Publ. 259, 209–233. https://doi.org/10.1144/GSL.SP.2006.259.01.17

Vetel, W., Le Gall, B., Johnson, T.C., 2004a. Recent tectonics in the Turkana Rift (North Kenya): an integrated approach from drainage network, satellite imagery and reflection seismic analyses. Basin Res. 16, 165–181. https://doi.org/10.1046/j.1365-2117.2003.00227.x

Vétel, W., Le Gall, B., Walsh, J.J., 2005. Geometry and growth of an inner rift fault pattern: the Kino Sogo Fault Belt, Turkana Rift (North Kenya). J. Struct. Geol. 27, 2204–2222. https://doi.org/10.1016/j.jsg.2005.07.003

Vieux, B.E., 1993. DEM Aggregation and Smoothing Effects on Surface Runoff Modeling. J. Comput. Civ. Eng. 7, 310–338. https://doi.org/10.1061/ (ASCE) 0887-3801(1993)7:3(310)

Walsh, J., Bailey, W., Childs, C., Nicol, A., Bonson, C.., 2003. Formation of segmented normal faults: a 3-D perspective. J. Struct. Geol. 25, 1251–1262. https://doi.org/10.1016/S0191-8141 (02)00161-X

Walsh, J.J., Watterson, J., 1988. Analysis of the relationship between displacements and dimensions of faults. J. Struct. Geol., v. 10, p. 239-247, doi: 10.1016/0191-8141 (88)90057-0.

Weeraratne, D.S., Forsyth, D.W., Fischer, K.M., Nyblade, A.A., 2003. Evidence for an upper mantle plume beneath the Tanzanian craton from Rayleigh wave tomography: Mantl plume beneath Tanzanian Craton. J. Geophys. Res. Solid Earth 108. https://doi.org/10.1029/2002JB002273

Weinstein, A., Oliva, S.J., Ebinger, C.J., Roecker, S., Tiberi, C., Aman, M., Lambert, C., Witkin, E., Albaric, J., Gautier, S., Peyrat, S., Muirhead, J.D., Muzuka, A.N.N., Mulibo, G., Kianji, G., Ferdinand-Wambura, R., Msabi, M., Rodzianko, A., Hadfield, R., Illsley-Kemp, F., Fischer, T.P., 2017. Fault-magma interactions during early continental rifting: Seismicity of the Magadi-Natron-Manyara basins, Africa: Magmatic Rift seismicity. Geochem. Geophys. Geosystems 18, 3662–3686. https://doi.org/10.1002/2017GC007027

Wernicke, B., 1985. Uniform-sense normal simple shear of the continental lithosphere. Can. J. Earth Sci. 22, 108–125. https://doi.org/10.1139/e85-009

Wheeler, W., Rosendahl, B., 1994. Geometry of the Livingstone mountains border fault, Nyasa (Malawi) rift, East Africa. Tectonics 13, 303-312.

Whipple, K.X., Tucker, G.E., 1999. Dynamics of the stream-power river incision model: Implications for height limits of mountain ranges, landscape response timescales, and research needs. J. Geophys. Res. Solid Earth 104, 17661–17674. https://doi.org/10.1029/1999JB900120

Wichura, A., Bousquet, R., Oberhänsli, R., Strecker, M., Trauth, M., 2010. Evidence for Middle Miocene uplift of the East African Plateau. Geology, 38, 6, 543-546.

Willgoose, G., 1994. A statistic for testing the elevation characteristics of landscape simulation models. J. Geophys. Res. Solid Earth 99, 13987–13996. https://doi.org/10.1029/94JB00123

Wilson, M., 1993. Magmatism and the geodynamics of basin formation. Sediment. Geol. 86, 5–29. https://doi.org/10.1016/0037-0738(93)90131-N

Wobus, C., Whipple, K.X., Kirby, E., Snyder, N., Johnson, J., Spyropolou, K., Crosby, B., Sheehan, D., 2006. Tectonics from topography: Procedures, promise, and pitfalls, in: Special Paper 398: Tectonics, Climate, and Landscape Evolution. Geological Society of America, pp. 55–74. https://doi.org/10.1130/2006.2398 (04)

Wood, D.A., Zal, H.J., Scholz, C.A., Ebinger, C.J., Nizere, I., 2017. Evolution of the Kivu Rift, East Africa: interplay among tectonics, sedimentation and magmatism. Basin Res. 29, 175–188. https://doi.org/10.1111/bre.12143

Wright, T. J., Ebinger, C., Biggs, J., Ayele, A., Yirgu, G., Keir, D., Stork, A., 2006. Magma-maintained rift segmentation at continental rupture in the 2005 Afar dyking episode. Nature, 442(7100), 291-294, doi:10.1038/nature04978.

Wu, H., Pollard, D., 1995. An experimental study of the relationship between joint spacing and l ayer thickness. J. Struct. Geol., 17; 887-905.

Yang, W., Hou, K., Yu, F., Liu, Z., Sun, T., 2010. A novel algorithm with heuristic information for extracting drainage networks from raster DEMs. Hydrol. Earth Syst. Sci. Discuss. 7, 441–459. https://doi.org/10.5194/hessd-7-441-2010

Zernitz, E.R., 1932. Drainage patterns and their significance. J. Geol. 40, 498–521.

Ziegler, P.A., Cloetingh, S., 2004. Dynamic processes controlling evolution of rifted basins. Earth-Sci. Rev. 64, 1–50. https://doi.org/10.1016/S0012-8252(03)00041-2

Annexes

Annexes

Au cours de ce travail, j'ai réalisé un certain nombre d'analyses qui n'ont pu être présenté dans les chapitres principaux de cette thèse. Je présente ici quelques documents supplémentaires incluant des informations complémentaires sur les méthodologies, les analyses ainsi que certains résultats. J'ai subdivisé ces annexes en 4 thèmes principaux : a) analyse morphostructurale, b) analyse de l'extension du rift (analyse de faille), c) analyse des réseaux de drainage et d) l'article publié par M. Plasman (Plasman et al., 2017) pour lequel nous avons contribué dans l'acquisition et pour la partie structurale.

Annexe A. Analyse morpho-structurale

Dans cette section, on présente les profiles topographiques utilisés pour l'analyse morpho-structurale réalisée pendant cette thèse. Ces profils sont rangés selon leur position géographique en 6 sections, comme suivant, i) 12 profils E-O dans la vallée axiale Magadi – Natron, ii) 4 profils N-S dans la zone de Magadi-Natron montrant l'évolution topographique de la vallée axiale du rift, iii) des profils au niveau du Oldoinyo Ogol montrant l'évolution morpho structurale du bloc Olgoinyo Ogol, iv) les profils de Engare Nairobi, v) ceux du Ngorongoro et vi) ceux de Eyasi – Manyara.

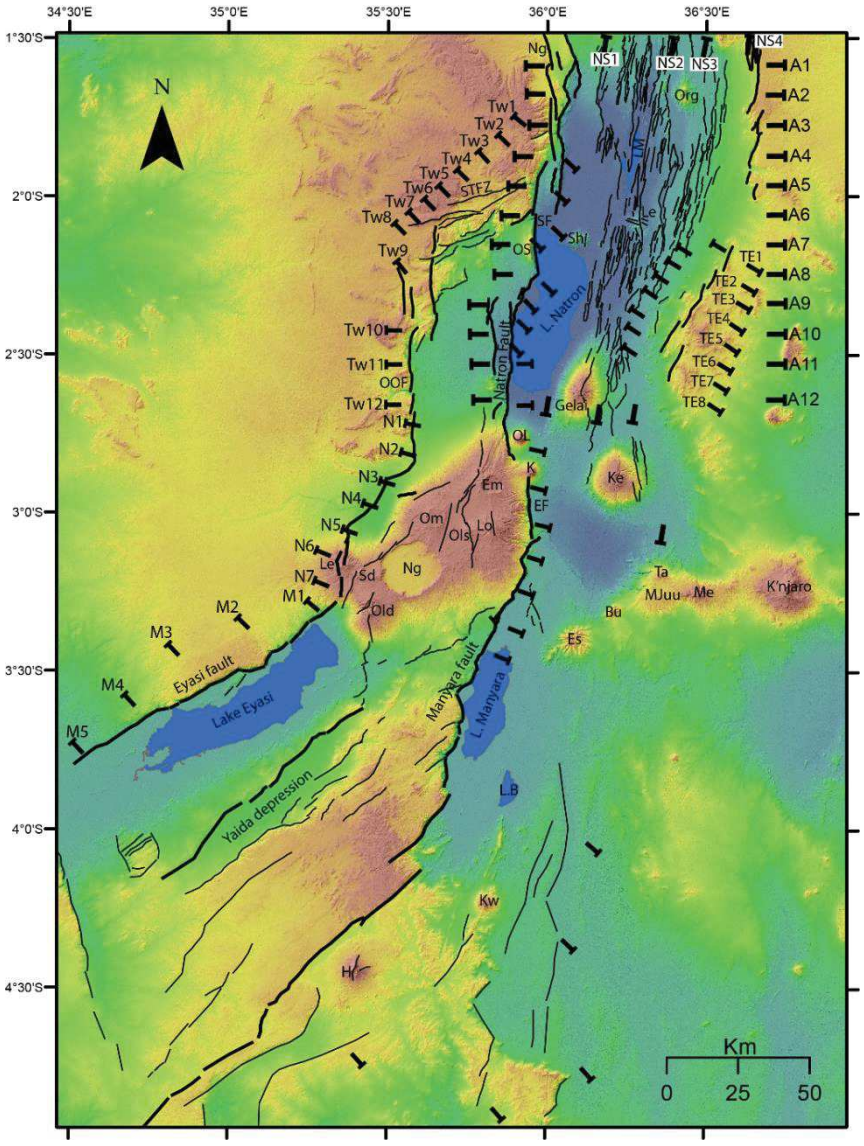

Fig.A. Localisation de l'ensemble des profils topographiques réalisés durant cette thèse.

A. I. Profils E-O au niveau de Magadi – Natron

Ces profils présentent les évolutions topographiques et structurales principales dans la vallée de Magadi – Natron,

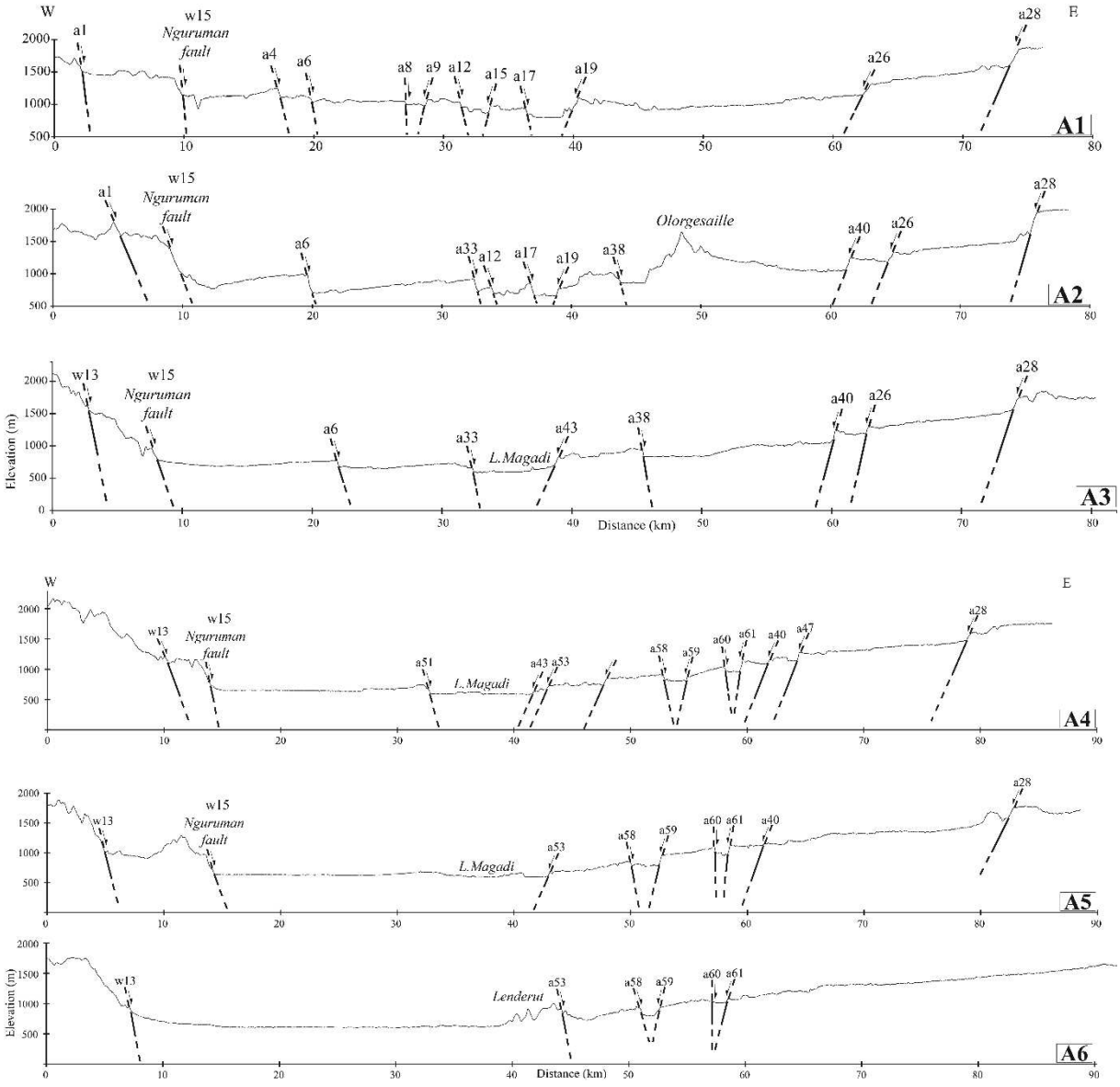

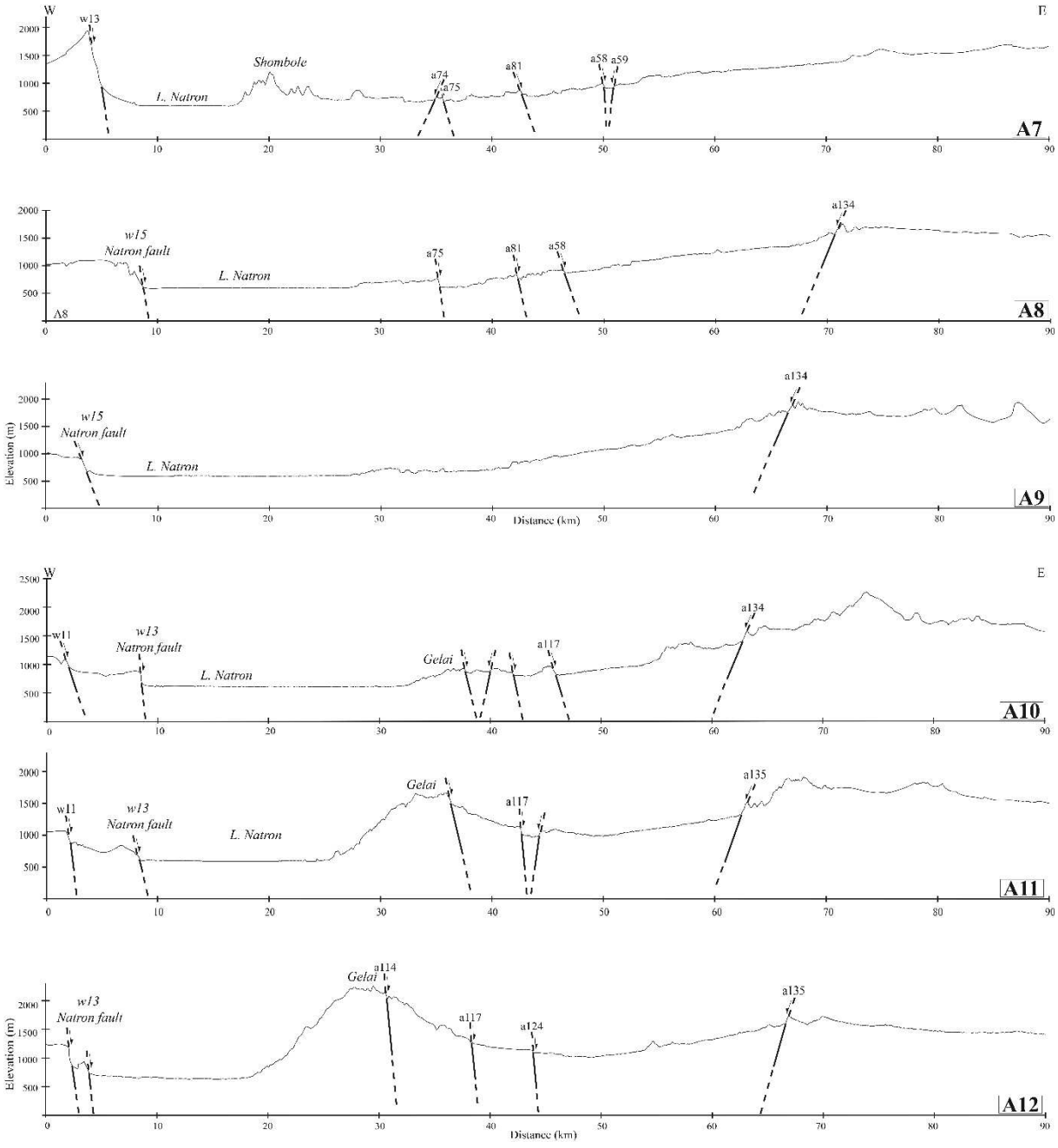
W
E
w13
Shombole
L. Natron
a74
a75
a81
a58
a59
A7
a134
w15
Natron fault
a75
a81
a58
L. Natron
A8
A8
a134
w15
Natron fault
L. Natron
A9
Elevation (m)
Distance (km)
W
E
w11
w13
Natron fault
L. Natron
Gelai
a117
a134
A10
Gelai
a135
w11
w13
Natron fault
L. Natron
a117
A11
a114
Gelai
a135
w13
Natron fault
a117
a124
A12
Elevation (m)
Distance (km)

A. II. N-S Magadi-Natron (4 profils N-S)

Ces profils topographiques N-S représentent la topographie générale de la vallée de Magadi – Natron ainsi que l'influence des volcans.

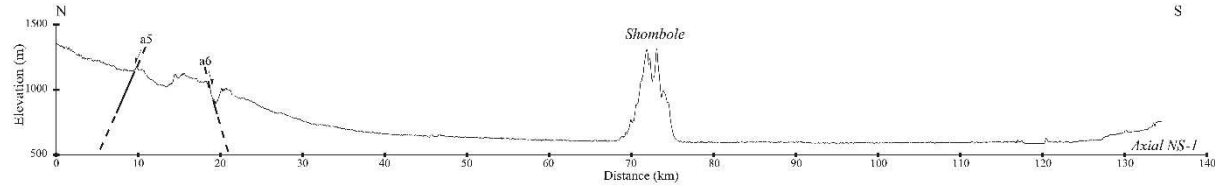

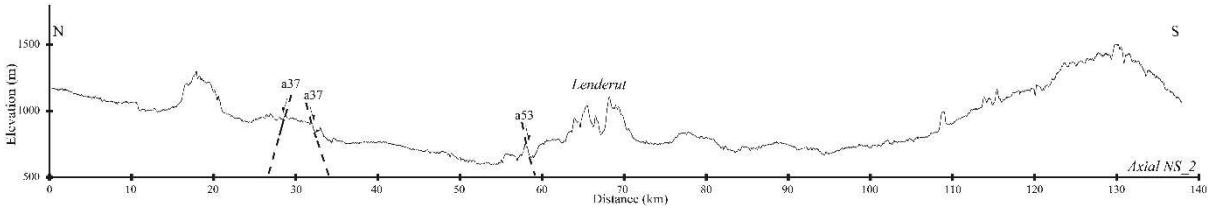

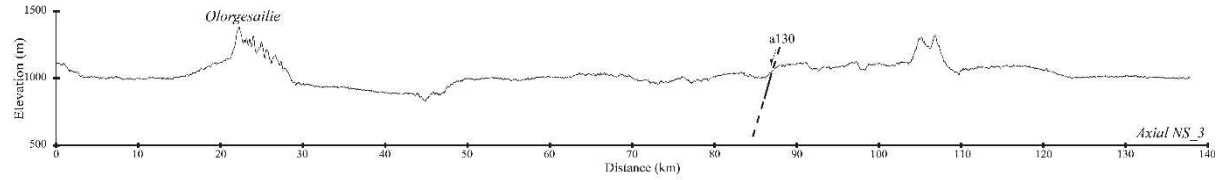

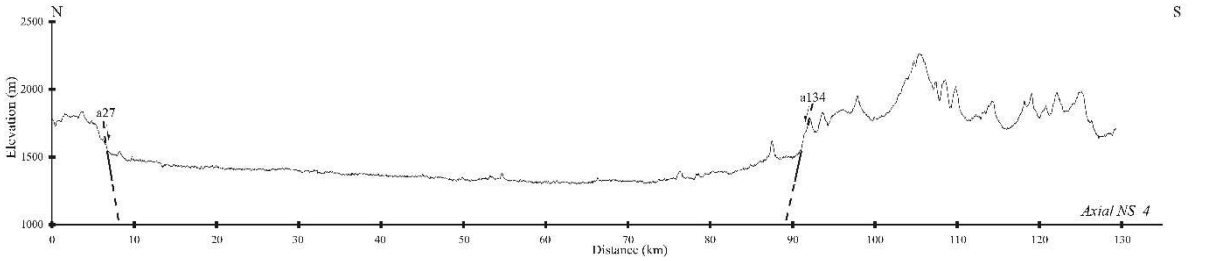

A. III. Profils de l'Oldoinyo Ogol

Ces 12 profils topographiques orientés NO-SE et E-O sont localisés dans la zone de transfert de faille de Sonjo (STFZ) traversant le bloc de l'Oldoinyo Ogol. Ils montrent les structures principales de la STFZ et le bloc de l'Oldoinyo Ogol.

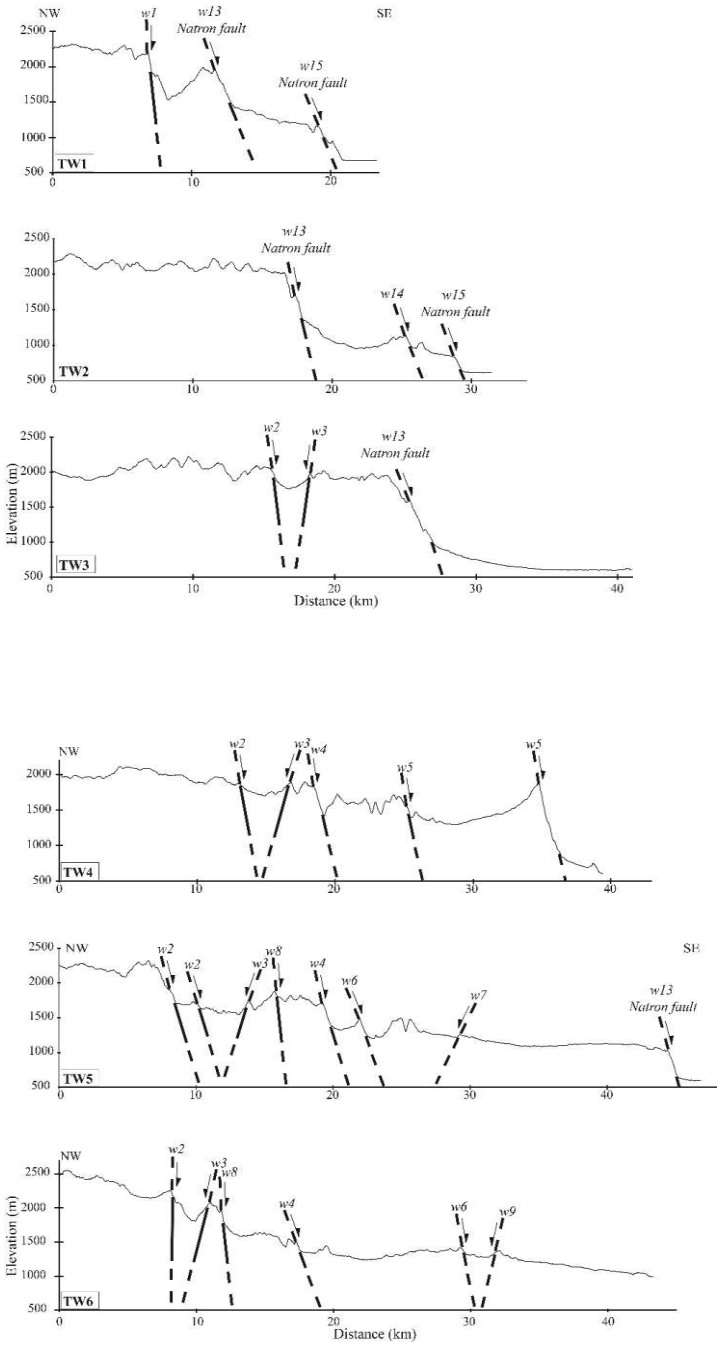

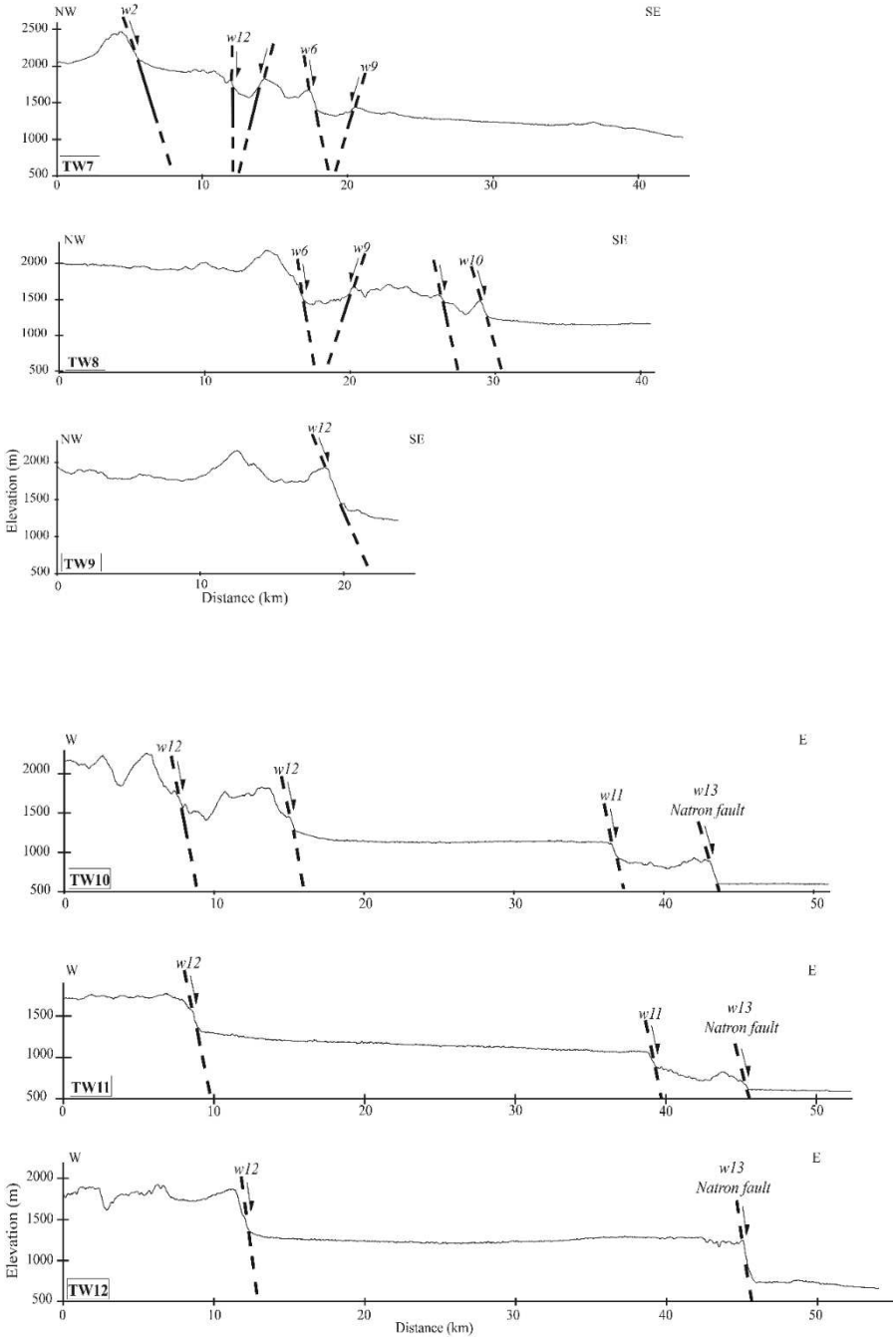

A. IV. Profils de la zone d'Engare Nairobi

Ce sont 8 profils topographiques NO-SE localisés dans les collines de l'Engare Nairobi ou les failles de Magadi-Natron ne se propagent pas. Ces failles sont majoritairement localisées dans la couverture mobile Protérozoïque avec très peu de failles.

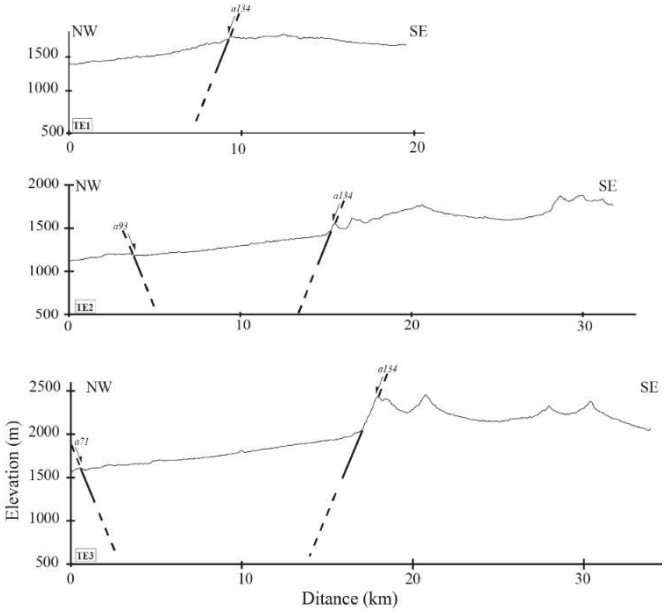
NW
SE
a134
1500
1000
500
TE1
0
10
20
2000
a93
TE2
30
2500
a71
TE3
Elevation (m)
Ditance (km)

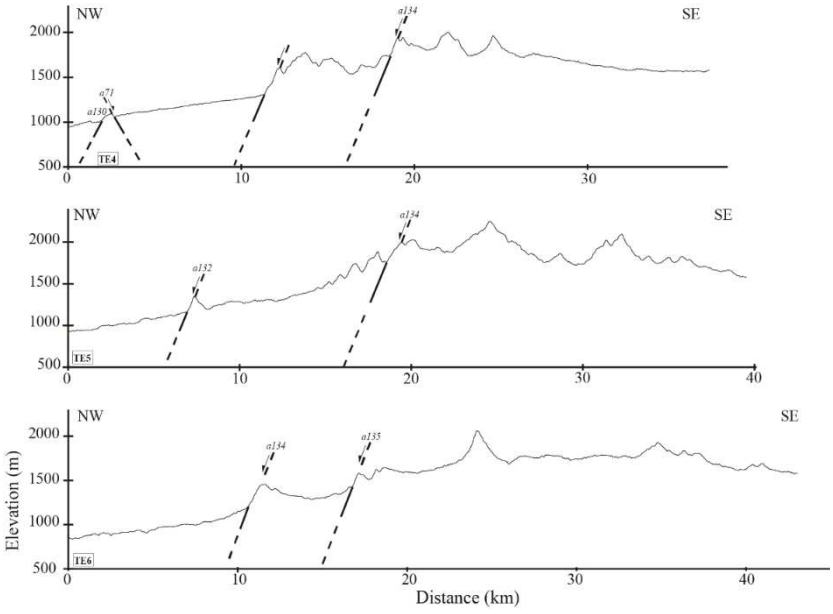
NW
SE
a134
a71
a130
TE4
a132
TE5
a135
TE6
Elevation (m)
Distance (km)

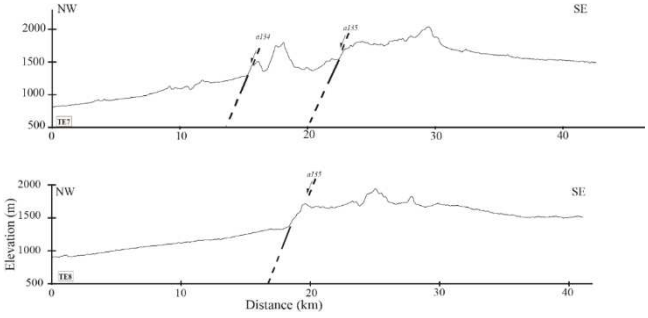
NW
SE
a134
a135
TE7
TE8
Elevation (m)
Distance (km)

A. V. Profils du Ngorongoro

Ces profils NO-SE, à travers la zone volcanique du Ngorongoro, montrent les tendances topographiques et structurale principales de cette zone élevée.

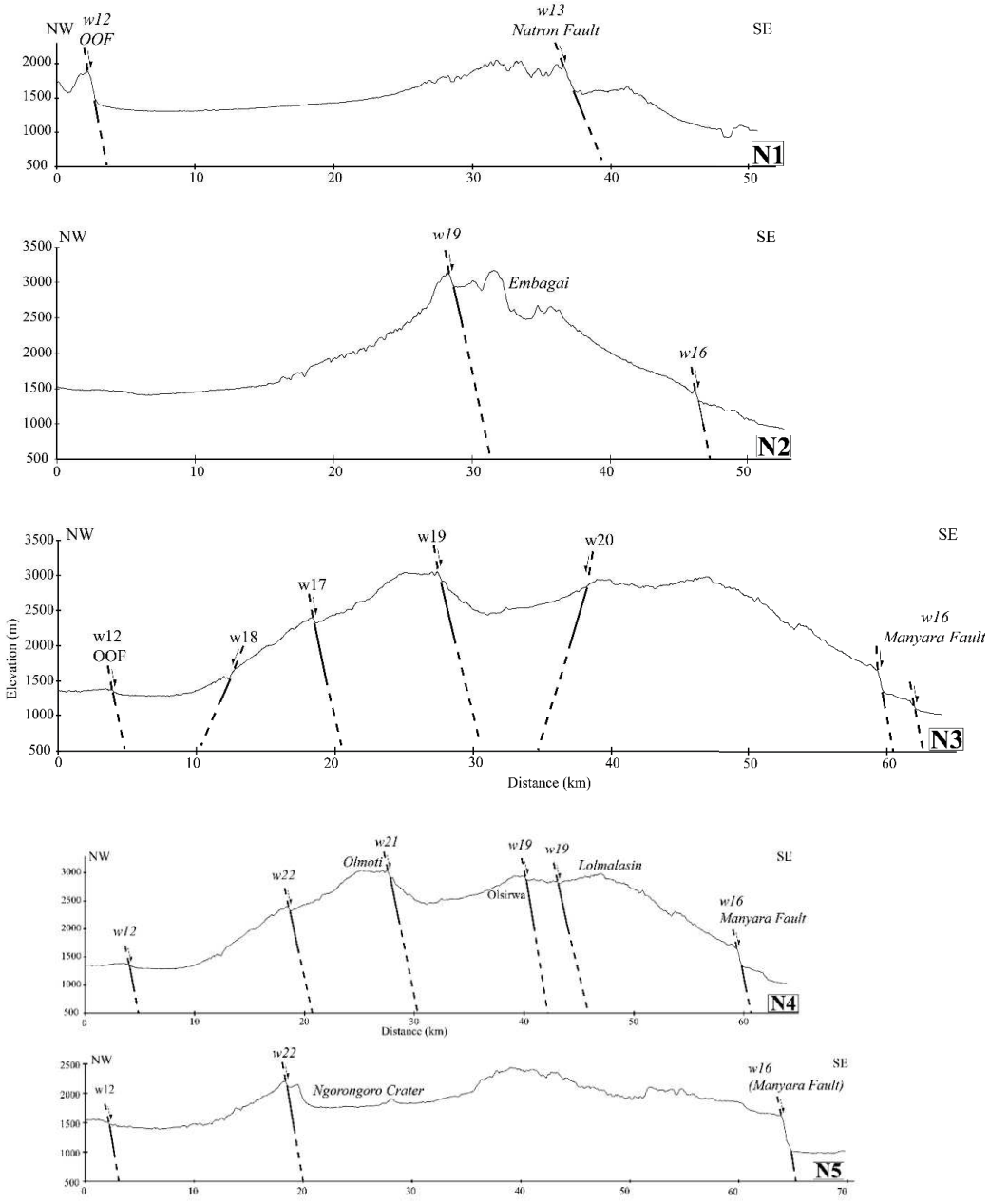

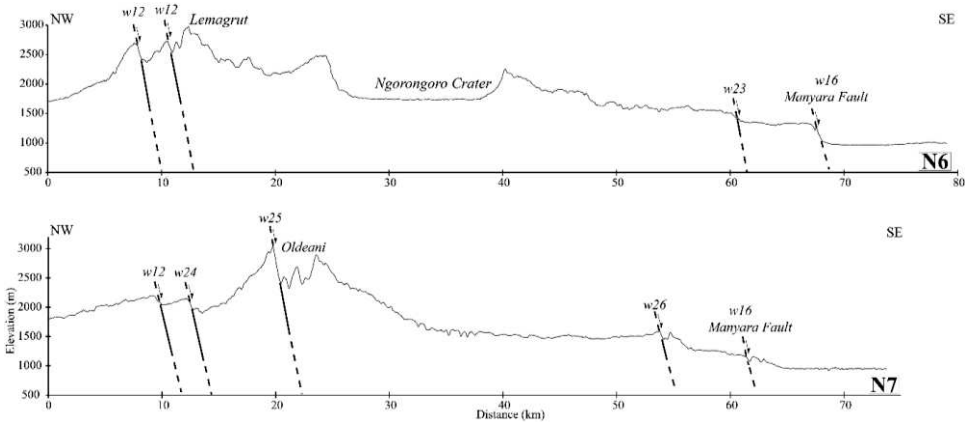

A. VI. Eyasi – Manyara

Ces profils montrent les tendances topographique et structurale au niveau de l'escarpement d'Eyasi, du plateau de Mbulu et de l'escarpement de Manyara.

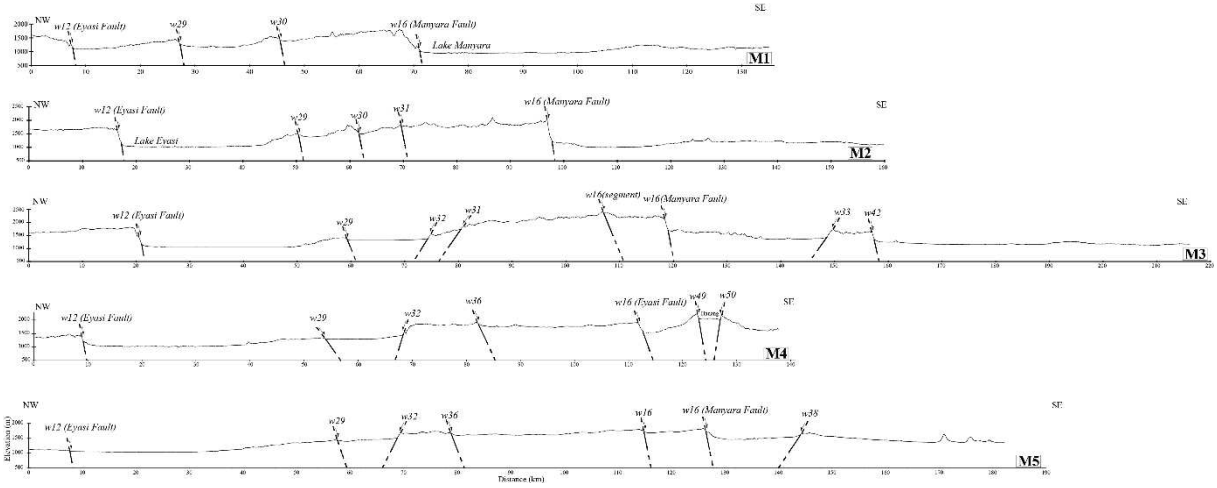

Annexe B. Analyse de l'extension du rift (analyses de failles)

Dans cette section on présente des documents utilisé pour l'analyse des failles présentée dans la thèse. La plupart de ces documents montre une propagation anormale du rift ainsi qu'un héritage structural dans le rift Sud Kenya, tandis que les autres documents ont été utilisé pour mieux comprendre la structure générale de la DNT particulièrement dans les zones stratégiques incluant Ngorongoro, Eyasi et Manyara

Annexe B. I. Tableau des valeurs maximales échantillonnées pour le déplacement vertical, horizontal, le nombre de segments de chaque faille, sa longueur et direction.

Fault Name	No. segments	L (km)	Facing	Max. throw (m)	Max. heave (m)	Dmax (m)
A4	2	8.9	E	147	84.9	169.7
A5	1	6.4	W	56	32.3	63.5
A6	6	38.8	E	310	179.0	358.0
A7	2	12.3	W	83	47.9	95.8
A8	4	18.4	E	142	82.0	164.0
A9	2	19.4	W	90	52.0	103.9
A10	3	13.6	E	123	71.0	142.0
A11	1	11.2	W	84	48.5	97.0
A12	2	18.3	E	235	135.7	271.4
A13	1	4.2	E	81	46.8	93.5
A14	2	7.3	E	73	42.1	84.3
A15	2	17.1	W	120	69.3	138.6
A16	3	15.7	E	78	45.0	90.1
A17	7	29.2	E	225	129.9	259.8
A18	4	11.9	W	160	92.4	184.8
A19	2	22.6	W	210	121.2	242.5
A20	3	13.8	W	150	86.6	173.2
A21	1	10.7	E	190	109.7	219.4
A22	2	9.8	E	120	69.3	138.6
A23	1	8.7	E	101	58.3	116.6
A24	2	13.2	W	202	116.6	233.2
A25	1	7.8	E	48	27.7	55.4
A26	3	30.2	W	230	132.8	265.6
A27	1	12.1	W	217	125.3	250.6
A28a	4	28.5	W	482	278.3	556.6
A28b	2	8.4	W	393	226.9	453.8

A28c	2	16.9	W	270	155.9	311.8
A28d	1	5.3	W	257	148.4	296.8
A29	2	5.9	E	70	40.4	80.8
A30	1	5.1	E	22.5	13.0	26.0
A31	2	11.5	E	156	90.1	180.1
A32	2	7.7	E	42	25.4	50.8
A33	4	22.6	E	222	128.2	256.3
A34	2	8	W	117	67.5	135.1
A35	1	7.1	W	88	50.8	101.6
A36	1	7.4	W	150	86.6	173.2
A37	2	19.8	E	111	64.1	128.2
A38	4	27.9	E	410	236.7	473.4
A39	1	13.6	E	110	63.5	127.0
A40	2	45.2	W	192	110.9	221.7
A41	3	11.3	E	112	64.7	129.3
A42	1	19.8	E	49	28.3	56.6
A43	1	28.6	W	153	88.3	176.7
A44	1	6.8	W	101	58.3	116.6
A45	1	6.7	W	125	72.2	144.3
A46	1	4.3	W	238	137.4	254.0
A47	2	22.7	W	135	77.9	155.9
A48	1	6.6	W	105	60.6	121.2
A49	2	12.5	W	49	28.3	56.6
A50	2	5.8	W	132	76.2	152.4
A51	4	20.6	E	160	92.4	184.8
A52	2	6.7	W	36	20.8	41.6
A53	3	39.7	W	155	89.5	179.0
A54	1	9	E	49	28.3	56.6
A55	3	11.1	E	47	27.1	54.3
A56	1	12.6	W	103	59.5	118.9
A57	1	9.9	W	42	24.2	48.5
A58	8	48	E	170	98.1	196.3
A59	5	35.8	W	201	116.0	232.1
A60	4	33.2	E	135	77.9	155.9
A61	3	36.2	W	180	103.9	207.8
A62	4	8.9	E	76	43.9	87.8
A63	1	10.7	W	56.5	32.6	65.2
A64	4	17.7	E	230	132.8	265.6
A65	8	21.3	W	92	53.1	106.2
A66	3	20	W	122	70.4	140.9
A67	3	19	E	29	16.7	33.5
A68	1	4.2	W	30	17.3	34.6
A69	1	5.8	E	63	36.4	72.7
A70	1	4.4	W	57	32.9	65.8

A71	9	34.1	E	68	39.3	78.5
A72	1	4.6	W	205	118.4	236.7
A73	2	13.5	E	75	43.3	86.6
A74	3	15	W	110	63.5	127.0
A75	6	23.7	E	219	126.4	252.9
A76	1	11.6	E	30	17.3	34.6
A77	2	7.1	W	85	49.1	98.1
A78	4	13.3	E	104	60.0	120.1
A79	2	6	E	59	34.1	68.1
A80	4	16.6	W	70	40.4	80.8
A81	4	19.5	E	128	73.9	147.8
A82	1	2.5	SW	90	52.0	103.9
A83	2	6.3	SW	163	94.1	188.2
A84	1	4.9	SW	161	93.0	185.9
A85	2	5	E	164	94.7	189.4
A86	1	3.1	W	65	37.5	75.1
A87	3	4.4	E	19.5	21.4	42.7
A88	2	8.6	W	138	79.7	159.3
A89	2	4.8	E	44	25.4	50.8
A90	1	3.5	W	111	64.1	128.2
A91	1	6	E	42	24.2	48.5
A92	1	5.7	W	35	20.2	40.4
A93	2	9.7	E	36	20.8	41.6
A94	4	19.7	W	62	35.8	71.6
A95	2	15	E	37	21.4	42.7
A96	3	19.8	E	90	52.0	103.9
A97	2	8.3	E	35	20.2	40.4
A98	1	7	W	60	34.6	69.3
A99	1	3.5	W	73	42.1	84.3
A100	1	6.5	W	23.5	13.6	27.1
A101	2	10.8	W	115	66.4	132.8
A102	1	5.2	W	55	31.8	63.5
A103	5	8.5	E	104	60.0	120.1
A104	1	3.1	W	79	45.6	91.2
A105	2	5.7	E	59	34.1	68.1
A106	2	5.2	W	120	69.3	138.6
A107	3	10	E	42	24.2	48.5
A108	2	10.7	E	64	37.0	73.9
A109	1	4.2	W	54	31.9	65.8
A110	1	2.4	E	53	30.6	61.2
A111	1	9.5	W	105	60.6	121.2
A112	1	9.3	E	52	30.0	60.0
A113a	1	7.3	E	70	40.4	80.8
A113b	1	5.5	E	87	50.2	100.5

A114a	1	4.4	E	39	22.5	45.0
A114b	1	6.7	E	109	62.9	125.9
A114c	2	16.8	E	217	125.3	250.6
A114d	1	8.3	E	245	141.5	282.9
A115	2	9.9	E	155	89.5	179.0
A116	2	11.5	W	110	63.5	127.0
A117	9	49.4	E	176	101.6	203.2
A118	1	7.4	E	54	31.2	62.4
A119	1	12.3	W	79	45.6	91.2
A120	1	14.3	E	62	35.8	71.6
A121	2	11.7	W	43.1	24.9	49.8
A122	1	6.1	E	35	20.2	40.4
A123	2	10.2	E	42	24.2	48.5
A124a	1	9.7	E	72	41.6	83.1
A124b	1	12.8	E	87	50.2	100.5
A125	2	6.8	W	49	28.3	56.6
A126	2	23.2	E	179	103.3	206.7
A127	2	7.3	W	40	23.1	46.2
A128	1	15.7	E	116	67.0	133.9
A129	1	7.1	E	250	144.3	288.7
A130	1	8.3	W	97	56	112
A131	1	10.8	E	55	31.8	63.5
A132	1	4.3	W	165	95.3	190.5
A133	1	7.9	W	301	173.8	347.6
A134	4	42.8	W	645	372.4	744.8
A135	1	13.3	W	500	288.7	577.4

Annexe B. II.

Les profils des traces de 140 failles. Ces profils de failles montrent la nature de la propagation de la faille ainsi que la direction dans laquelle la propagation est limitée. Il y a 3 formes principales de propagation de faille comme discuté dans cette thèse. Ces profils de faille comprennent les failles non restreintes, celles uniquement restreintes à leur extrémité nord et celles à leur extrémité sud.

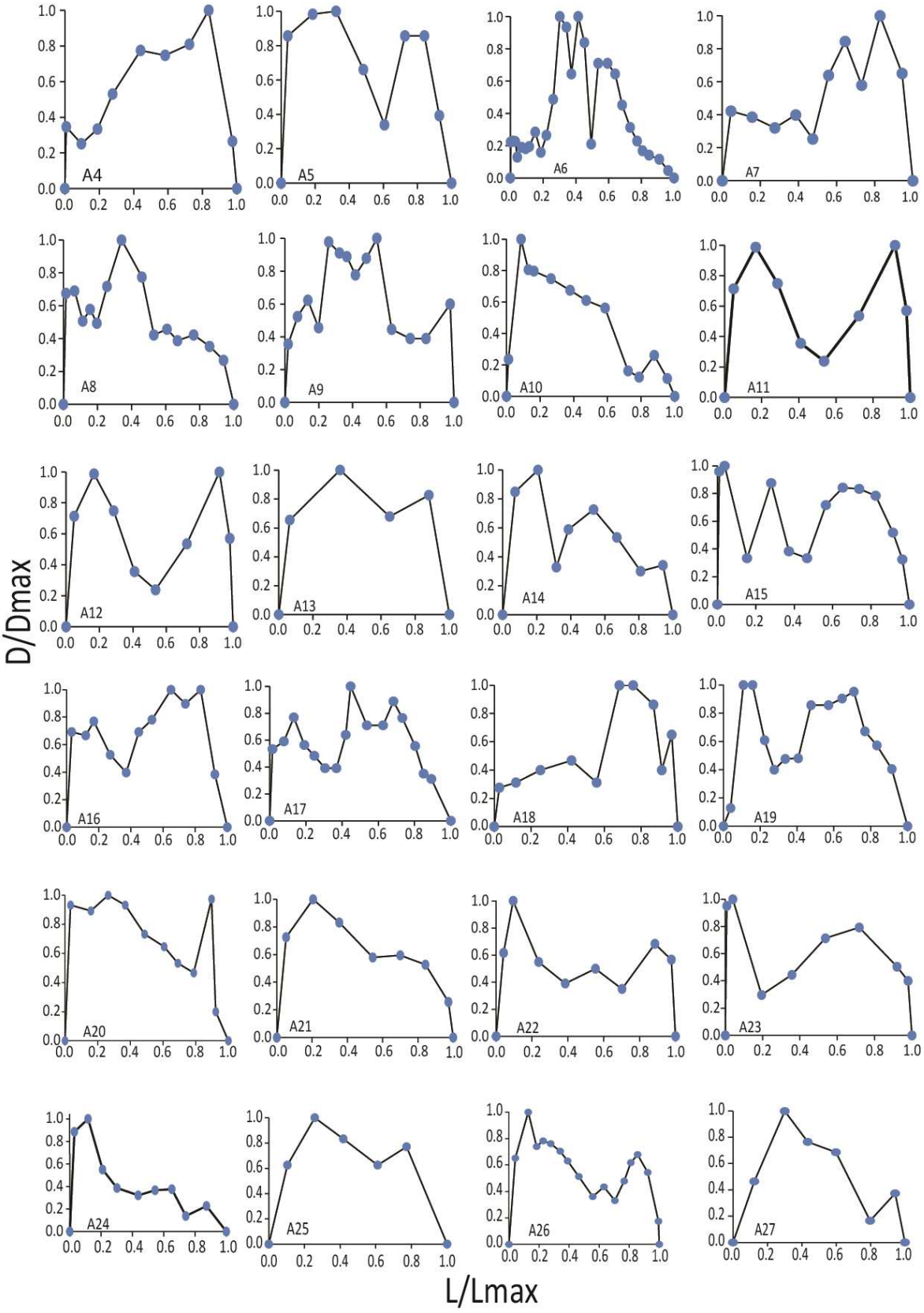
A4
A5
A6
A7
A8
A9
A10
A11
A12
A13
A14
A15
A16
A17
A18
A19
A20
A21
A22
A23
A24
A25
A26
A27
D/Dmax
L/Lmax

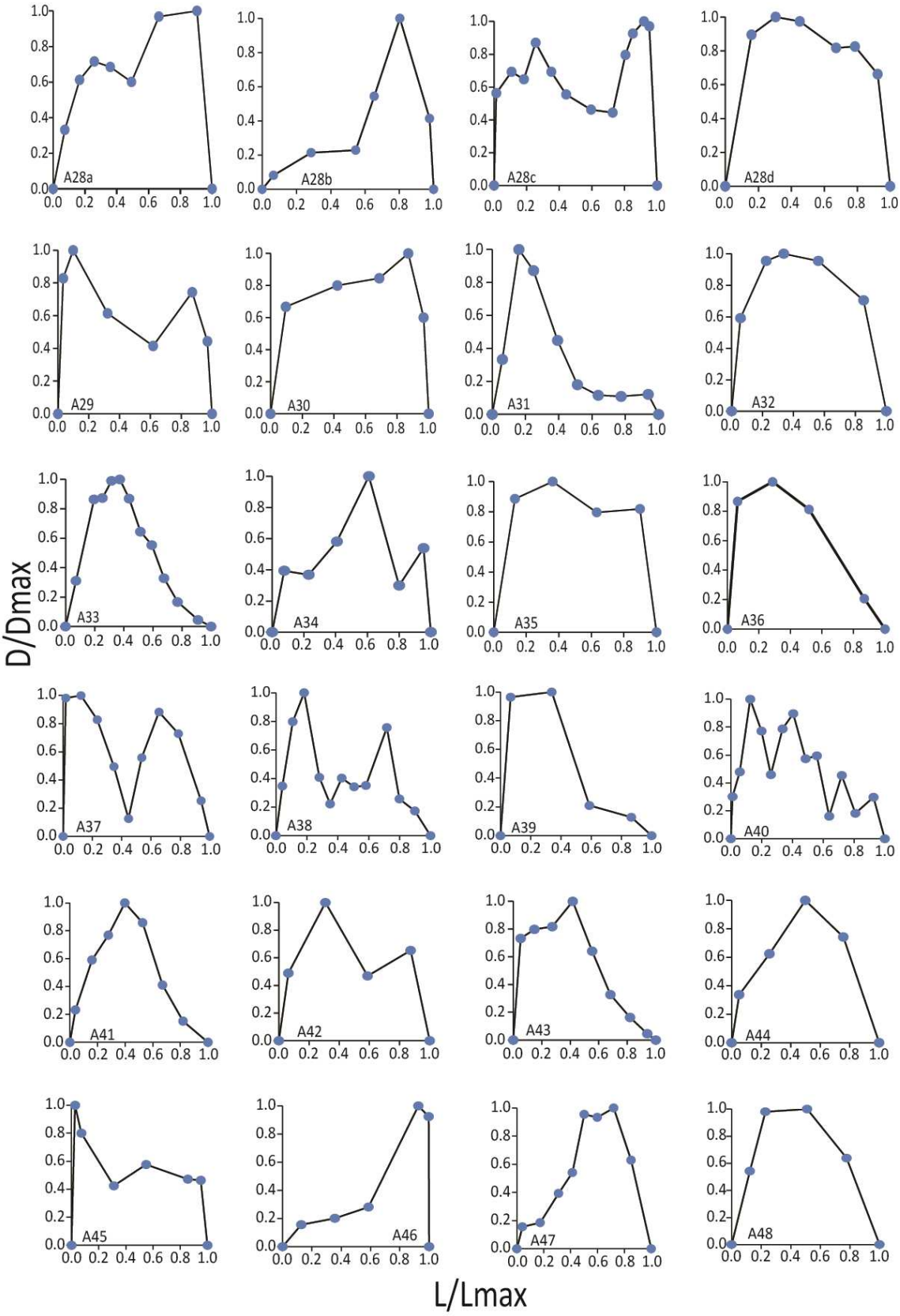
A28a
A28b
A28c
A28d
A29
A30
A31
A32
A33
A34
A35
A36
A37
A38
A39
A40
A41
A42
A43
A44
A45
A46
A47
A48
D/Dmax
L/Lmax

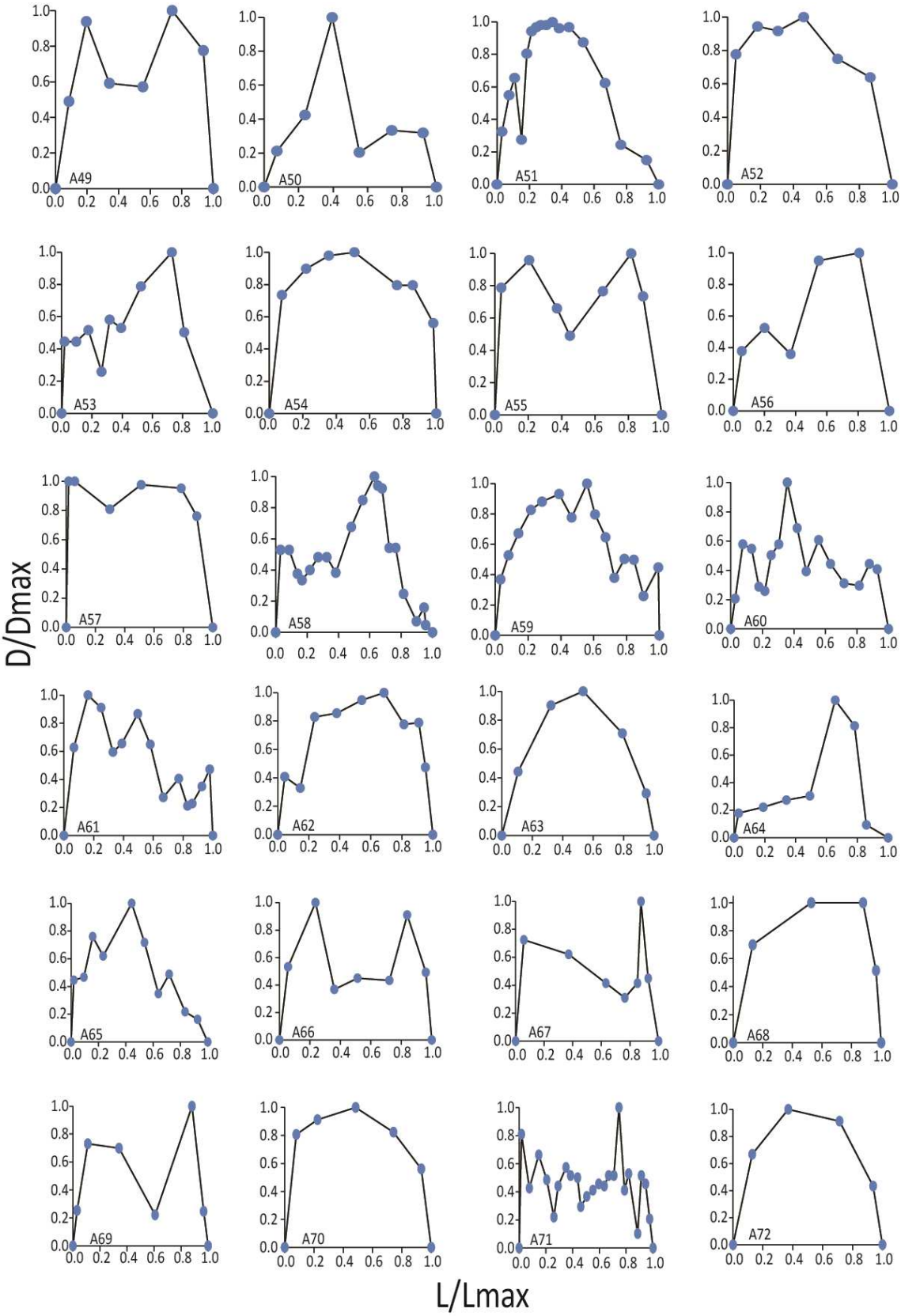
A49
A50
A51
A52
A53
A54
A55
A56
A57
A58
A59
A60
A61
A62
A63
A64
A65
A66
A67
A68
A69
A70
A71
A72
D/Dmax
L/Lmax

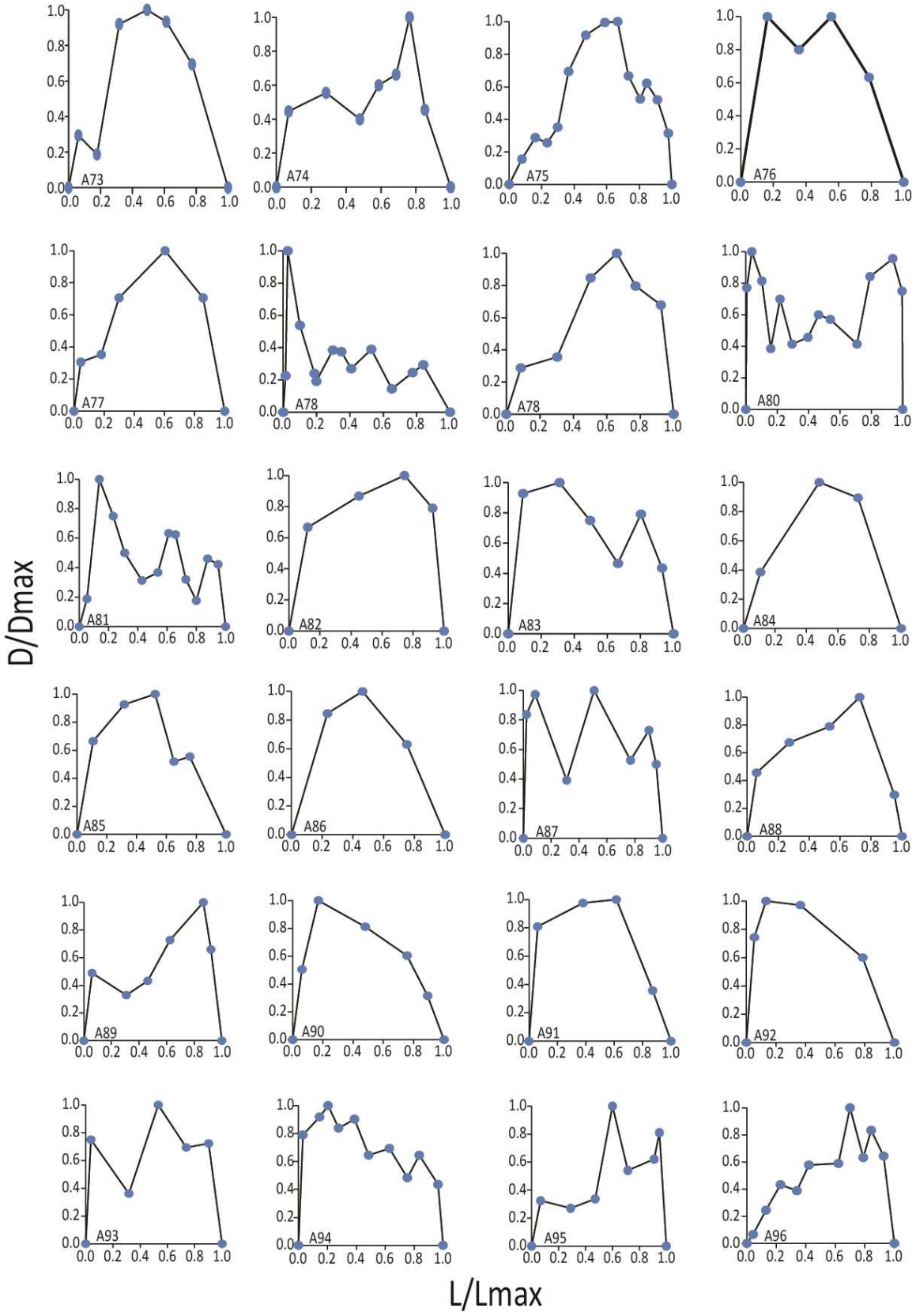
A73
A74
A75
A76
A77
A78
A78
A80
A81
A82
A83
A84
A85
A86
A87
A88
A89
A90
A91
A92
A93
A94
A95
A96
D/Dmax
L/Lmax

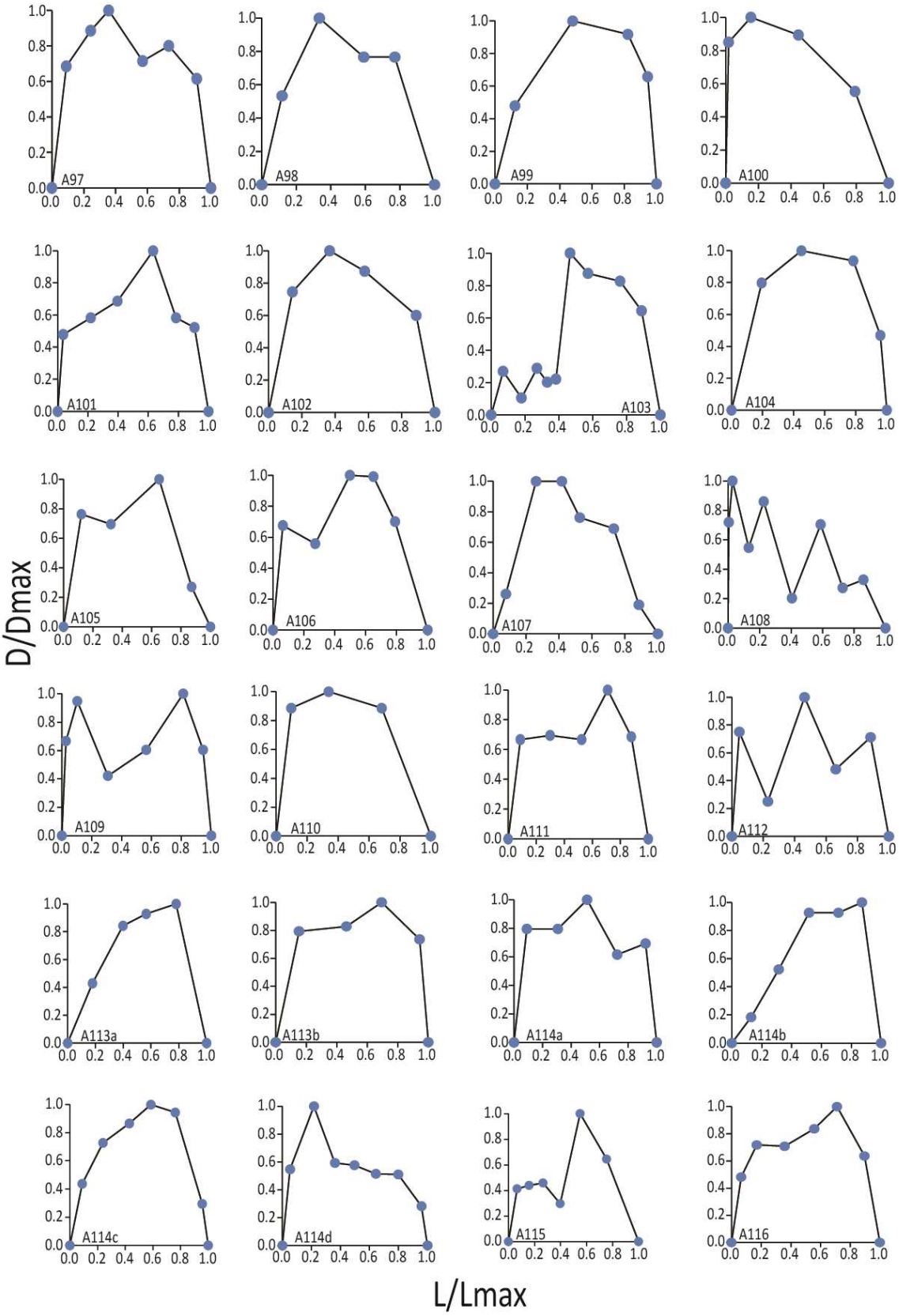
A97
A98
A99
A100
A101
A102
A103
A104
A105
A106
A107
A108
A109
A110
A111
A112
A113a
A113b
A114a
A114b
A114c
A114d
A115
A116
D/Dmax
L/Lmax

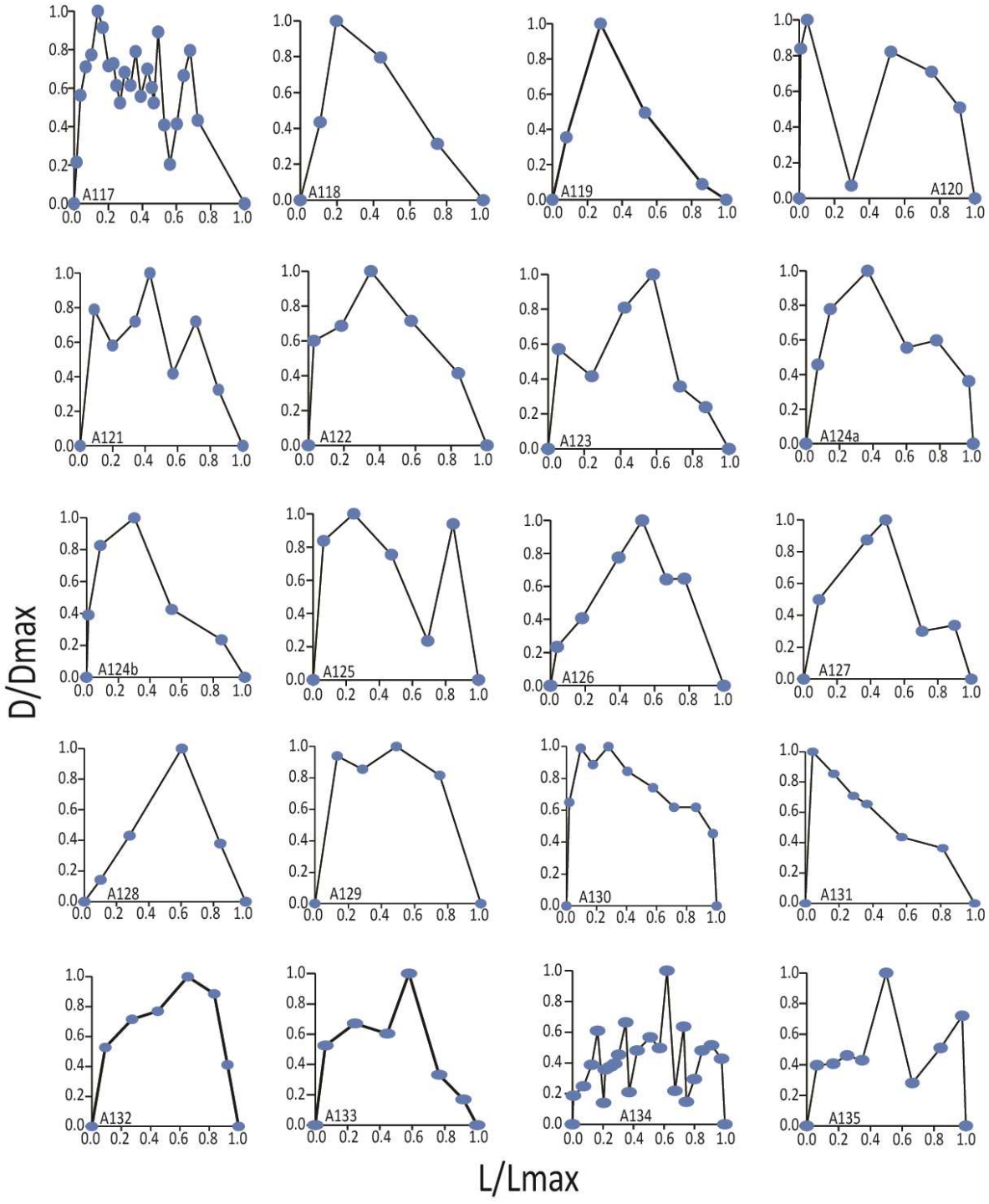

Annexe B. III. Analyse statistique des profils de faille en fonction de leur longueur.
Ce tableau représente la relation entre la longueur des failles et le type de profil de faille. Il est montré ici que la majorité des failles sont dans la gamme des 5-20km ou la plupart sont restreintes à leurs deux extrémités.

Fault classes (orders)	Number of faults & %	Restricted faults			Unrestricted
		N	S	N-S	
0-5 km	Total faults 18	1	4	12	1
	% of faults within class	5.6	22.2	66.7	5.6
5-10 km	Total faults 53	8	8	31	6
	% of faults within class	15.1	15.1	58.5	11.3
10-20 km	Total faults 47	9	5	28	5
	% of faults within class	19.1	10.6	59.6	10.6
> 20 km	Total faults 22	2	2	14	4
	% of faults within class	9.1	9.1	63.6	18.2

Annexe B.IV. Analyse des failles dans la zone volcanique du Ngorongoro avec la position des profils topographiques analysés.

Cette annexe représente les failles et volcans principaux des chaînes volcaniques du Ngorongoro sur une carte topographique. Les localisations des profils topographiques sont aussi représentées.

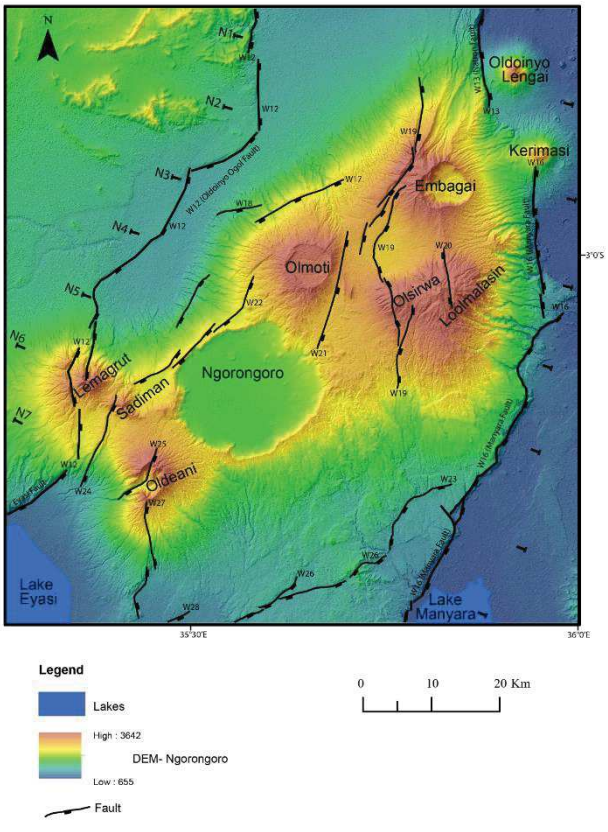

Annexe B. V. Analyse des failles de la zone d'Eyasi – Manyara avec leurs positions pour l'analyse topographique.

Cette annexe montre les principales structures tectoniques de l'escarpement d'Eyasi, du plateau de Mbulu et de l'escarpement de Manyara.

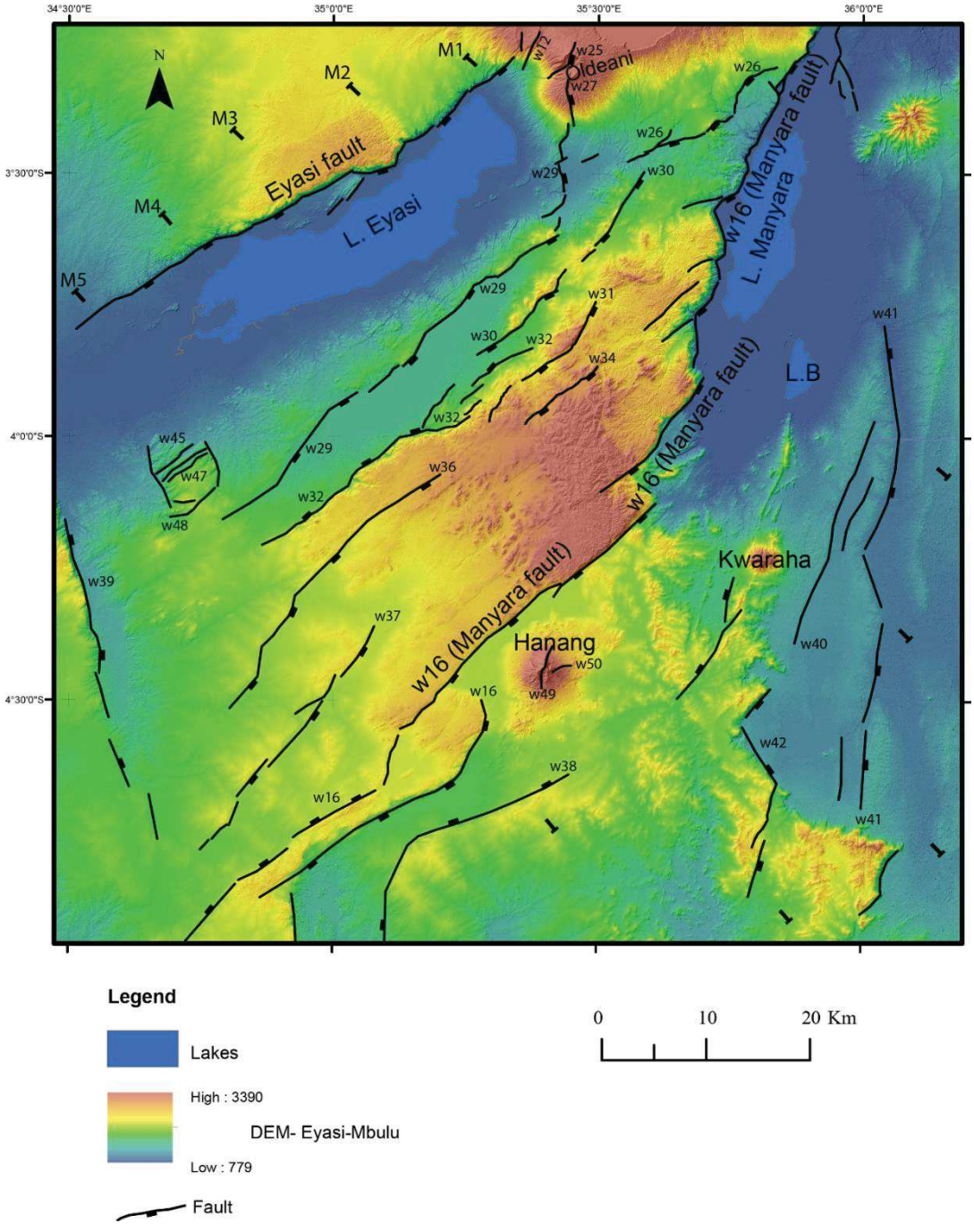

Annexe B) VI. Représentation des lois de distribution à la fois exponentielles et de puissance.

a) Lois de distribution du Sud Kenya et Nord Tanzanie. On a utilisé les valeurs de longueur de faille et leur fréquence cumulative pour déterminer la loi de distribution a laquelle obéissent les failles de Magadi – Natron. On a représenté les lois exponentielles et de puissance lorsque R^2 montre que ces failles obéissent à une loi exponentielle.

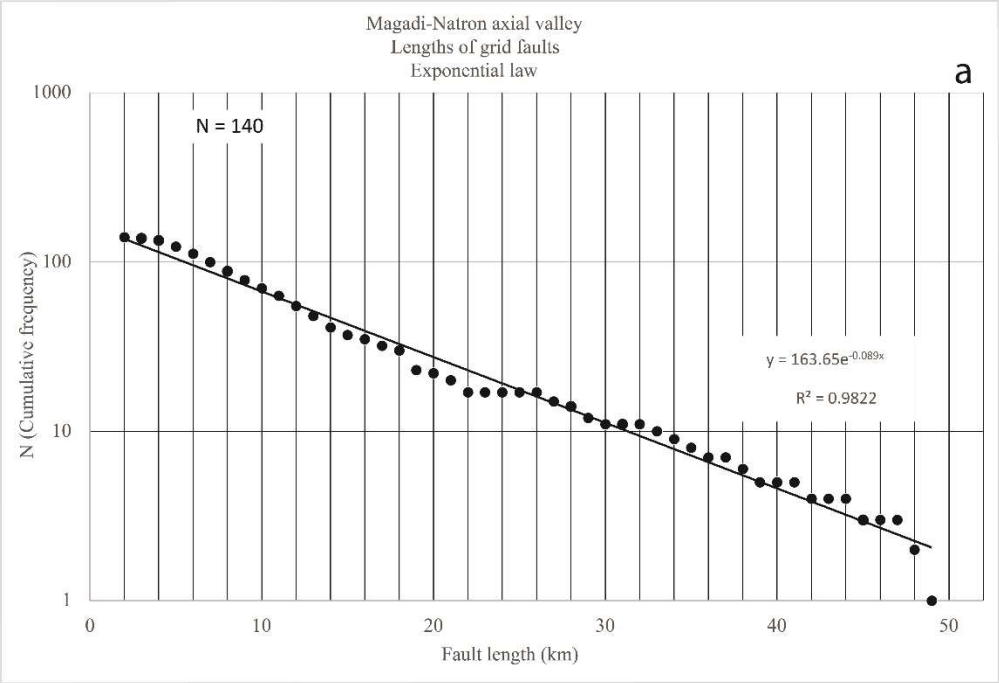

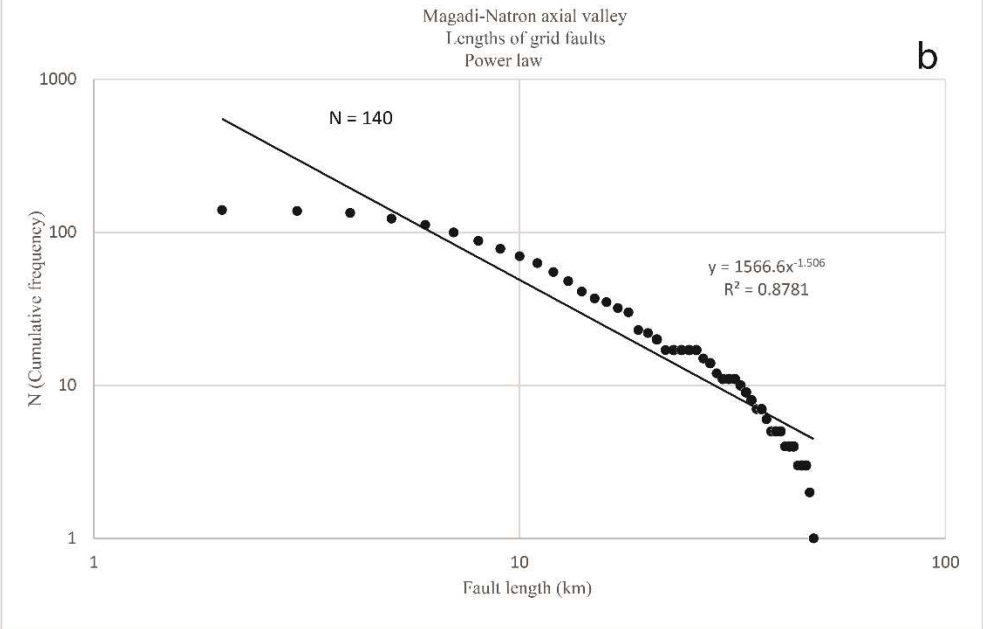

b) Lois de distribution du flanc ouest de la divergence (blocs du Oldoinyo Ogol - Eyasi-Manyara) De la même façon, nous avons étudié les lois pour lesquelles les failles situées dans le secteur du bloc d'Oldoinyo Ogol jusqu'à l'escarpement d'Eyasi obéissent. Comme pour les failles de Magadi – Natron, ces failles obéissent aussi à une loi exponentielle.

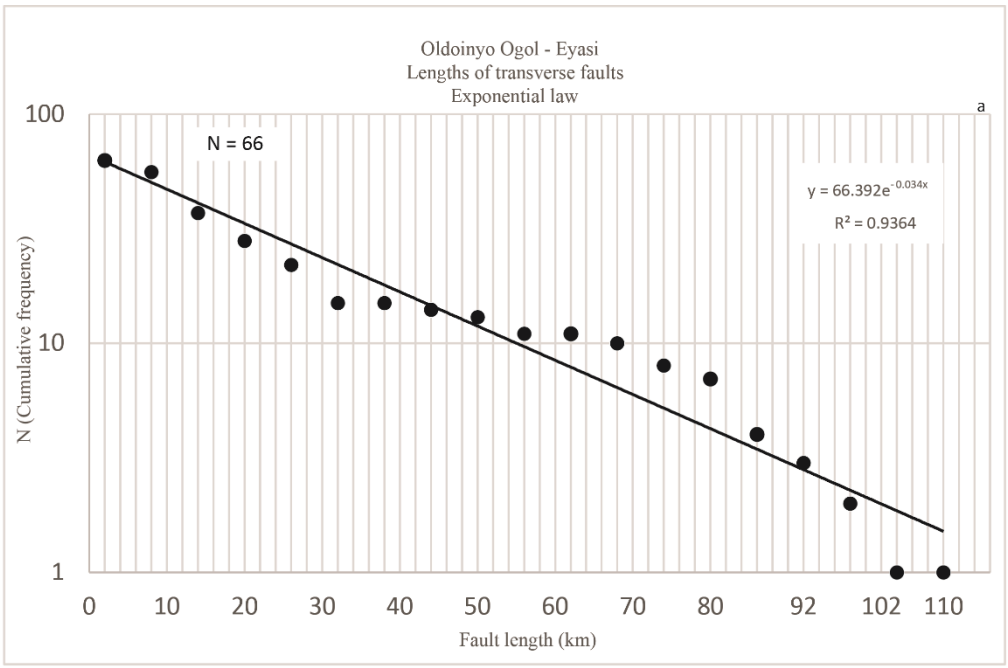

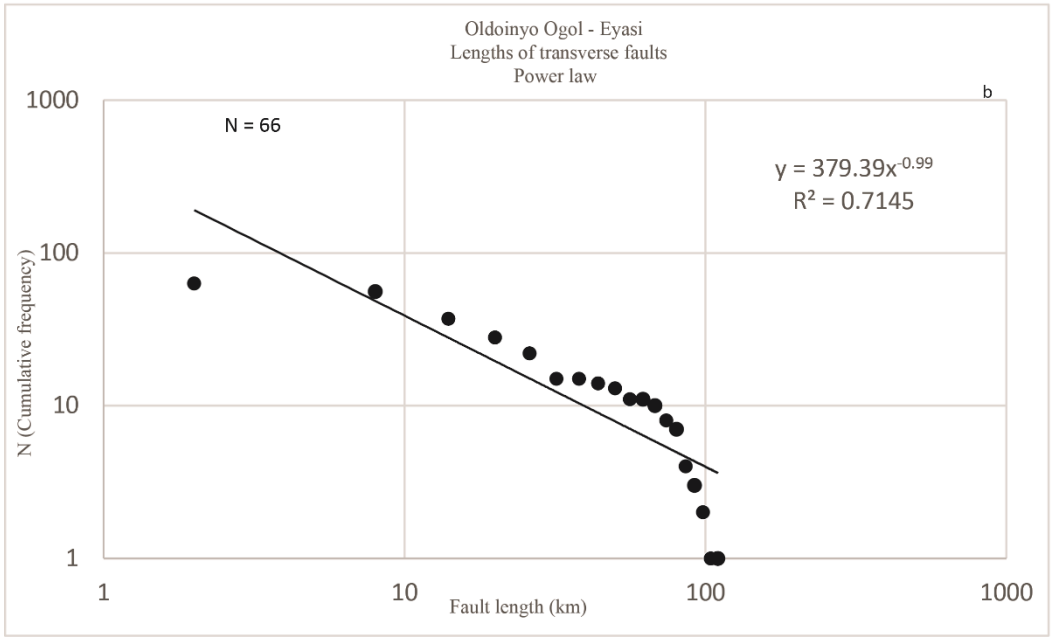

Annexe C. Analyse du réseau de drainage

Dans cette section on présente les annexes pour les analyses des réseaux de drainage. On présente les résultats et tableau des analyses morphométriques n'ayant pas été présenté dans la thèse. On a rangé ces annexes dans l'ordre suivant : i) tableau montrant les principaux bassins versants et les rivières associées, ii) quelques photo de terrain, iii) la méthode d'analyse des courbes hypsométriques et les principaux résultats, iv) une carte de l'hypsométrie intégrée v) la méthodologie du rapport largeur du fond de la vallée sur hauteur de la vallée (VF) et les résultats principaux, vi) la table d'indice des pentes et vii) une carte de la distribution spatiale du facteur d'asymétrie (AF).

Annexe C. I. Tableau des principaux bassins versants et rivières associées

Ce tableau représente certains bassins versants sélectionnés, leur surface, et les principales rivières qui couvrent les 25 études de bassins versants réalisées durant cette thèse.

Water catchment	**Catchment area (km2)**	**Associated main structure/domain**	**River**	**River name**
W1	721	Nguruman	Rw1	Ewaso Ngiro
W2	240	Nguruman	Rw2	Ewaso Ngiro
W3	265	Nguruman	Rw3	Ewaso Ngiro?
W4	78	Nguruman	Rw4	Ewaso Ngiro?
W5	170	Nguruman	Rw5	Pagasi
W6	1695	Natron	Rw6	Pinyinyi (Peninj)
W7	70	Natron	Rw7	Pinyinyi

W8	7552	Natron/Oldoinyo Ogol	Rw8	Sanjan
W9	42	Eyasi escarpment	Rw9	Sirwa
W10	106	Eyasi escarpment	Rw10	Embaruwai
W11	88	Eyasi escarpment	Rw11	Enjeku Enaisho
W12	504	Eyasi escarpment	Rw12	Engarusi
W13	228	Eyasi escarpment	Rw13	Lukala
W14	1414	Eyasi escarpment	Rw14	Sayu
W15	1172	Eyasi basin/Mbulu domain	Rw15	Mbarai
W16	2519	Eyasi basin/Mbulu domain	Rw16	Yaeda
W17	5353	Eyasi basin/Mbulu domain	Rw17	Melagwashi
W18	239	Manyara escarpment	Rw18	Msasa
W19	46	Manyara escarpment	Rw19	Ndala
W20	69	Manyara escarpment	Rw20	Bagayo
W21	238	Manyara escarpment	Rw21	Geyesago
W22	27	Manyara escarpment	Rw22	Yambi

W23	167	Manyara escarpment	Rw23	Magara
W24	215	Manyara escarpment	Rw24	Dangalo
W25	267	Manyara escarpment	Rw25	Gichami

Annexe C.II. Les escarpements de faille au niveau de Natron.

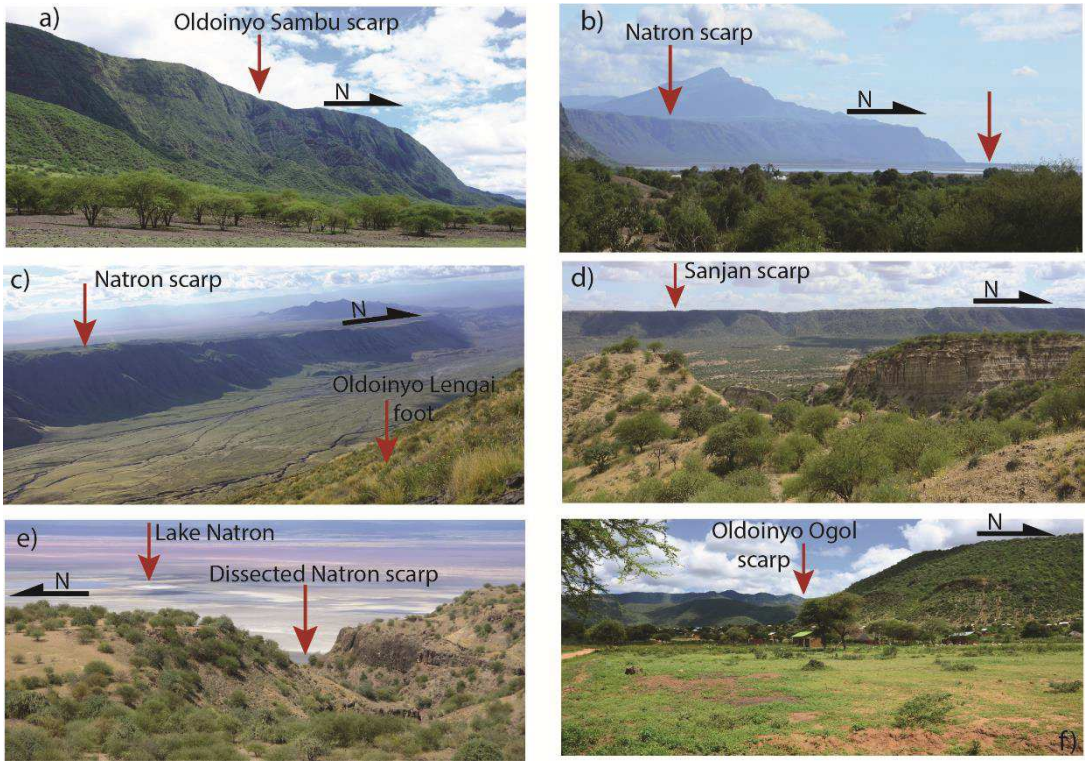

Fig. C.II. Escarpements de failles observés durant la campagne de terrain dans la DNT : a) extrémité sud de l'escarpement du Oldoinyo Sambu qui est la continuation de l'escarpement de Nguruman, b) extrémité nord de l'escarpement de Natron, c) extrémité sud de l'escarpement de Natron, localisé au bord du volcan Oldoinyo Lengai, d) escarpement Sanjan localisé à l'est de la faille de Natron, e) escarpement de Natron et f) l'escarpement du Oldoinyo Ogol.

Annexe C. III. Méthode d'analyse des courbes hypsométriques et les principaux résultats

- Méthode de détermination des courbes hypsométriques

L'hypsométrie est la mesure de la relation entre la zone de partage des eaux et l'altitude (Mukul et al., 2017; Strahler, 1957). Dans un bassin drainant, la courbe hypsométrique représente la proportion relative de la zone de partage des eaux au-dessous ou au-dessus d'une altitude donnée (Pérez-Peña et al., 2009; Schumm, 1956; Strahler, 1957). C'est la courbe de surface – altitude (Fig. R5) qui est utilisée pour caractériser le relief topographique dans les bassins drainants ou la comparaison entre les différents bassins (Pérez-Peña et al., 2009). Les valeurs d'altitude et de surface sont extraites des données DEM et les courbes hypsométriques sont calculées en utilisant la méthodologie proposée par Pérez-Pena et al. (2009). On utilise ensuite le code libre CalHypso disponible en open source GIS pour QGIS 2.18.4, et sur https://github.com/geolovic/Calhypso, pour calculer et représenter les courbes hypsométriques.

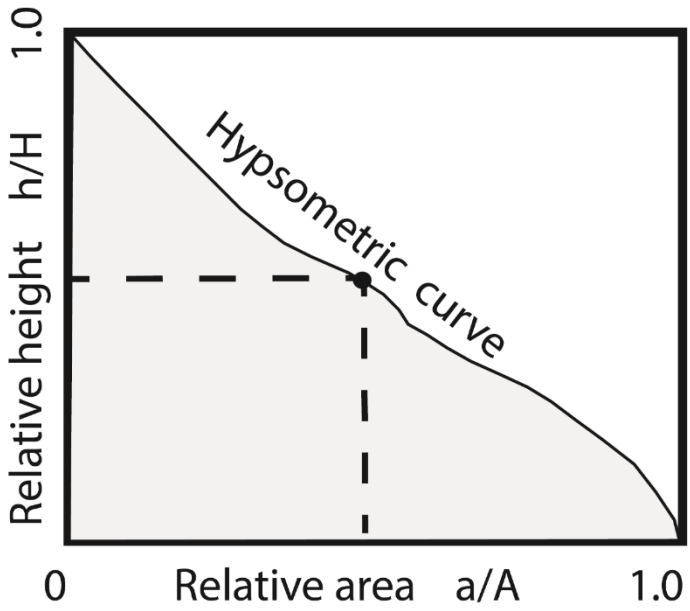

Fig. C.III. Représentation schématique d'une courbe hypsométrique (modifiée d'après Bull and McFadden, 1977; Keller and Pinter, 2002; Özsayın, 2016 et les références à l'intérieur).

- Principaux résultats de la méthode des courbes hypsométriques.

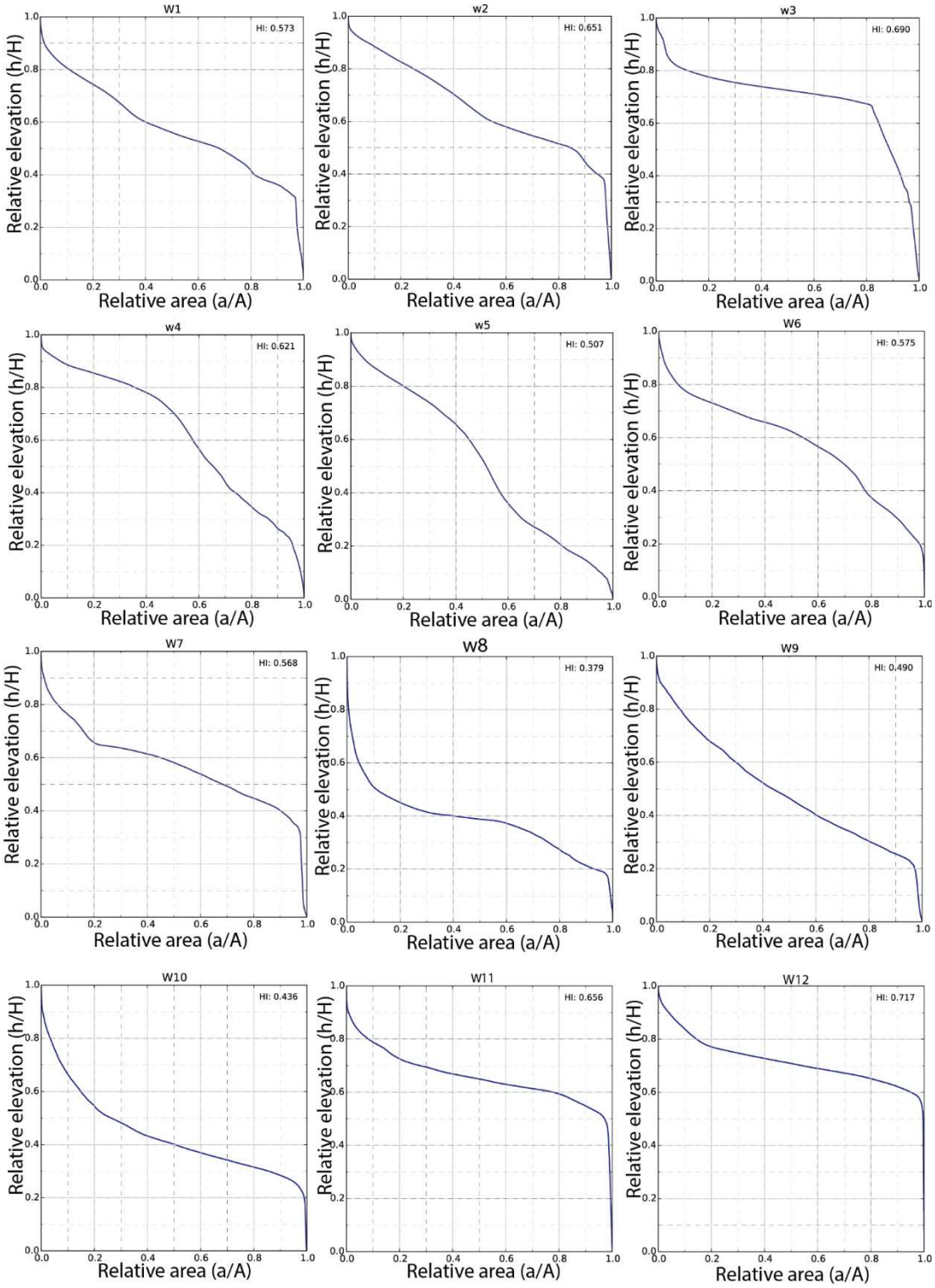

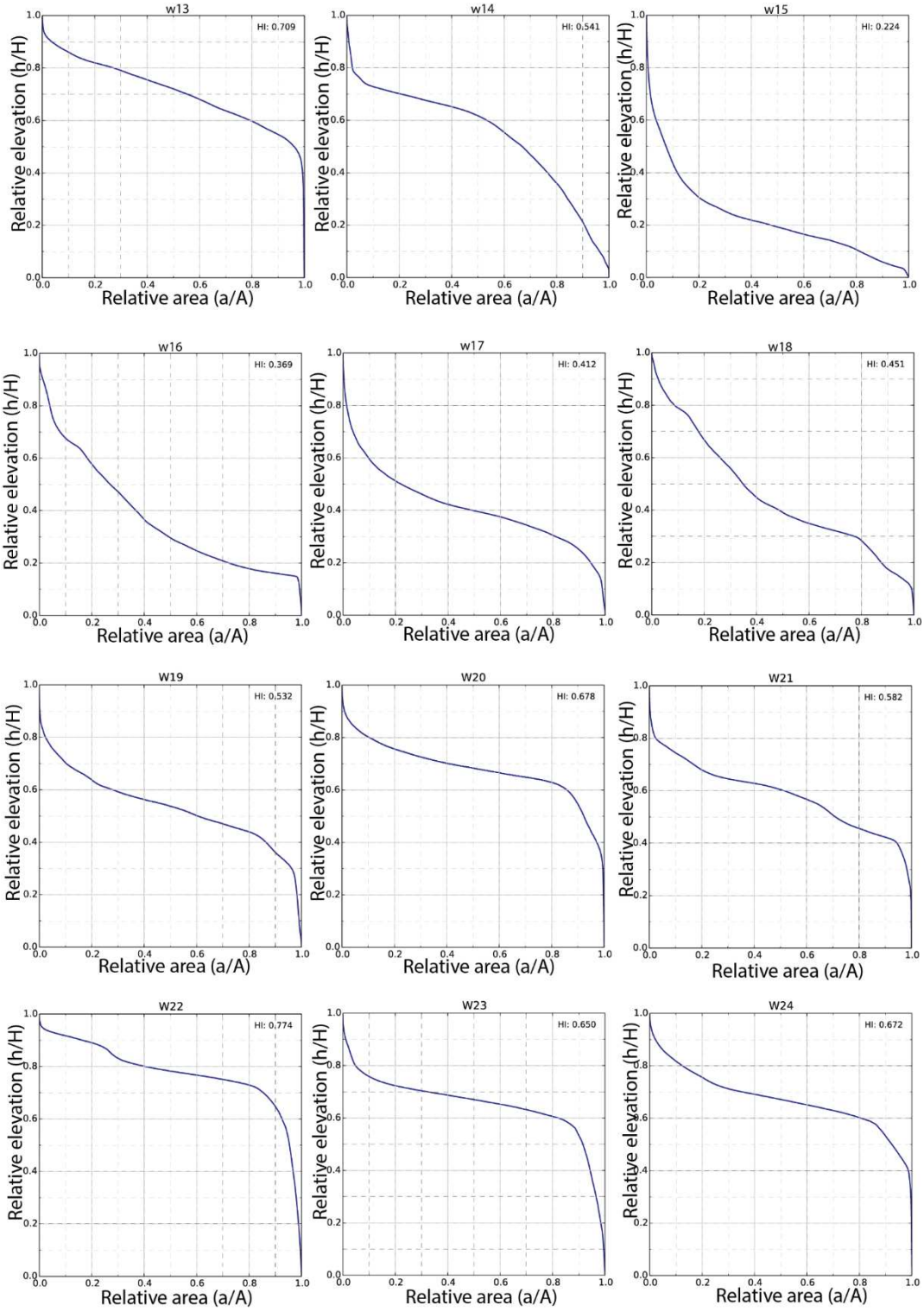
w13
HI: 0.709
w14
HI: 0.541
w15
HI: 0.224
w16
HI: 0.369
w17
HI: 0.412
w18
HI: 0.451
W19
HI: 0.532
W20
HI: 0.678
W21
HI: 0.582
W22
HI: 0.774
W23
HI: 0.650
W24
HI: 0.672
Relative elevation (h/H)
Relative area (a/A)

Annexe C. IV. La distribution spatiale l'hypsométrie (HI)

Cette carte représente la distribution spatiale de l'hypsométrie (HI) présenté dans la thèse. Les classes ont les incisions de rivière suivante : Classe 1 (HI > 0,; fortement incisé) ; Classe 2 (0.4 ≤ HI ≤ 0.5 modérément incisé) ; et classe 3 (HI < 0.4 ; faiblement incisé)

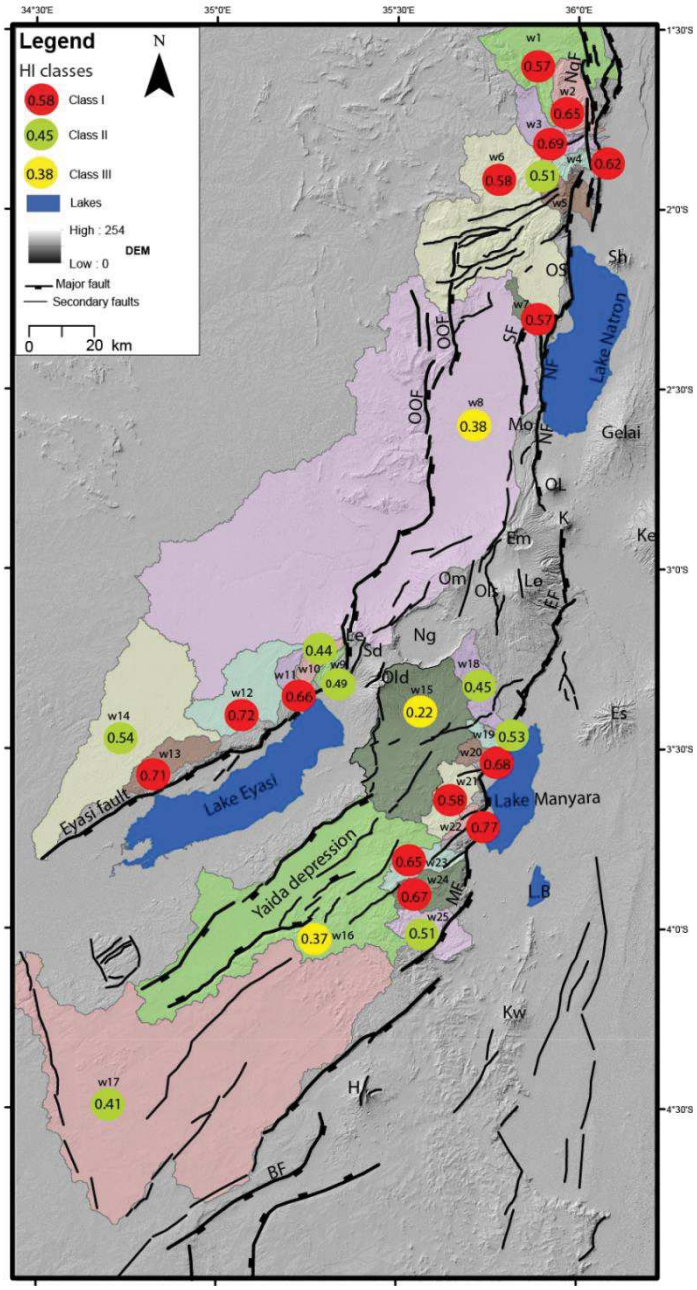

Fig. C.IV. Carte de la distribution spatiale l'hypsométrie (HI)

Annexe C. V. Méthode du rapport entre largeur du fond de la vallée et hauteur de la vallée (VF) et les résultats principaux

- Méthode VF

L'état d'incision d'une rivière est déterminé par le calcul du rapport entre la largeur du fond de la rivière et sa hauteur (VF) (fig . C.V). VF est calculé par (Bull, W.B, 1978; Bull and McFadden, 1977) :

$$VF = 2Vfw/ [(Eld – Esc) + (Erd – Esc)]$$

Ou Vfw est la largeur du fond de la vallée, Eld est l'altitude de la ligne de partage des eaux sur le coté gauche de la vallée, Erd est l'altitude du coté droit et Esc l'altitude moyenne du fond de la vallée. On a utilisé les données d'ASTER DEMs de 25 bassins versants au sein desquels des coupes transverses ont été réalisées à partir de 25 rivières principales. Les mesures ont été faites à une distance comprise en 1 et 2 km de l'embouchure, selon sa nature.

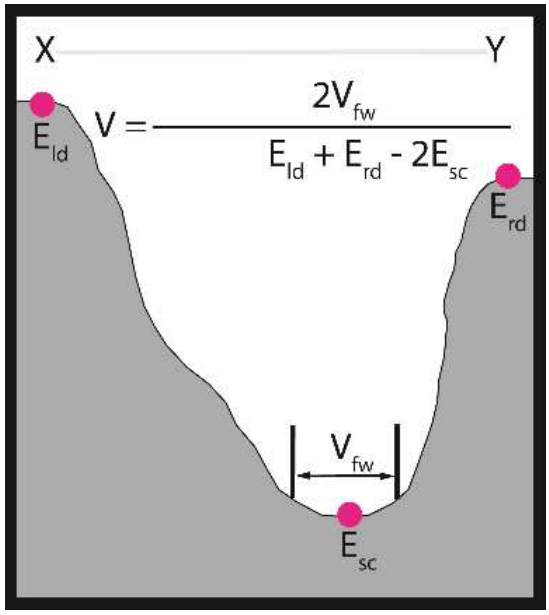

Fig. C.V. Méthode de calcule du rapport largeur du fond de la vallée sur hauteur de la vallée (VF) (modifié d'après Bull and McFadden, 1977; Keller and Pinter, 2002; Özsayın, 2016 et les références associées).

➢ Résultats

Les résultats ont été classés en 3 classes similaires à la classification de Cheng et al., 2018, selon a) classe 1 (Vf < 0.5; fort); classe 2 (0.5≤ Vf < 1.0; modéré); classe 3 (Vf ≥1.0; relativement faible) (tableau dessous).

Catchment	Major escarpment	Rw	River name	Vf	Class
W1	Nguruman	Rw1	Ewaso Ngiro	0.20	1
W2	Nguruman	Rw2	Ewaso Ngiro	0.14	1
W3	Nguruman	Rw3	Ewaso Ngiro?	0.28	1
W4	Nguruman	Rw4	Ewaso Ngiro?	0.38	1
W5	Nguruman	Rw5	Pagasi	1.28	3
W6	Natron	Rw6	Pinyinyi (Peninj)	0.40	1
W7	Natron	Rw7	Pinyinyi (Peninj)?	0.59	2
W8	Natron	Rw8	Sanjan	0.58	2
	Oldoinyo Ogol	Rw8bc	Sanjan	0.87	2
	Oldoinyo Ogol	Rw8d	Sanjan	0.38	1
	Oldoinyo Ogol	Rw8e	Sanjan	3.77	3
W9	Eyasi escarpment	Rw9	Sirwa	0.50	2
W10	Eyasi escarpment	Rw10	Embaruwai	2.44	3
W11	Eyasi escarpment	Rw11	Enjeku Enaisho	0.57	2
W12	Eyasi escarpment	Rw12	Engarusi	0.43	1
W13	Eyasi escarpment	Rw13	Lukala	0.65	2
W14	Eyasi escarpment	Rw14	Sayu	2.17	3
W15	Eyasi basin/Mbulu domain	Rw15	Mbarai	**NA**	
W16	Eyasi basin/Mbulu domain	Rw16	Yaeda		
W17	Eyasi basin/Mbulu domain	Rw17	Melagwashi		
W18	Manyara escarpment	Rw18	Msasa	0.65	2
W19	Manyara escarpment	Rw19	Ndala	0.42	1
W20	Manyara escarpment	Rw20	Bagayo	0.21	1
W21	Manyara escarpment	Rw21	Geyesago	0.69	2
W22	Manyara escarpment	Rw22	Yambi	0.23	1
W23	Manyara escarpment	Rw23	Magara	0.20	1
W24	Manyara escarpment	Rw24	Dangalo	0.35	1
W25	Manyara escarpment	Rw25	Gichami	0.24	1

Annexe C. VI. Tableau de valeur des indices de raideur

Ce tableau présente un résumé de l'analyse des indices de raideur normalisés (Ksn). Ce tableau est complémentaire aux résultats présentés dans l'analyse de drainage de la thèse.

K_{sn} values			
Water catchment	**Minimum**	**Maximum**	**Average**
W1	0	1457	55
W2	12	1119	87
W3	-18	881	88
W4	13	312	103
W5	10	339	90
W6	3	1526	60
W7	14	415	53
W8	-42	2434	35
W9	10	331	87
W10	16	755	63
W11	6	852	51
W12	0	1496	26
W13	-2	882	35
W14	-6	225	20
W15	-1	470	41
W16	-1	681	26
W17	-13	529	21
W18	1	197	57
W19	13	420	50
W20	4	326	39
W21	-1	585	46
W22	0	524	116
W23	2	405	65
W24	-2	1478	64
W25	1	904	63

Annexe C.VII. Carte de la distribution spatiale du facteur d'asymétrie (AF)

Le facteur d'asymétrie AF est un indice qui décrit l'état de basculement d'un bassin. 50 est une valeur neutre, il n y a pas ou peu de basculement du bassin (Cheng et al., 2018; El Hamdouni et al., 2008). Les interprétations tectoniques de AF sont faites en utilisant

la valeur absolue |AF-50| comme dans El Hamdouni et al., (2008) pour ensuite adopter la classification de Cheng et al. (2018) : Classe 1 (|AF-50| ≥ 15; bassin fortement basculé); classe 2 (7 ≤ |AF-50| < 15; modérément basculé); et classe 3 (|AF-50| < 7; relativement peu basculé).

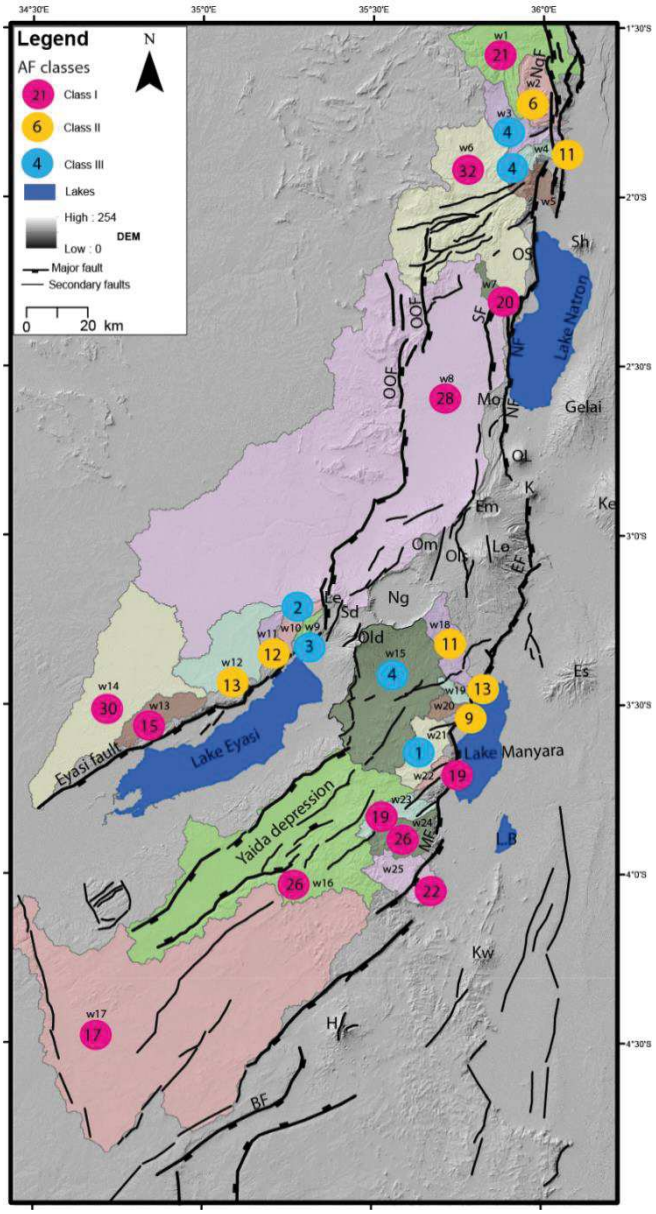

Fig. C.VII : Distribution du AF dans la DNT

Annexe D. Lithospheric low-velocity zones associated with a magmatic segment of the Tanzanian Rift, East Africa (Plasman et al., 2017).

Geophysical Journal International

Geophys. J. Int. (2017) **210,** 465–481
Advance Access publication 2017 May 1
GJI Seismology

doi: 10.1093/gji/ggx177

Lithospheric low-velocity zones associated with a magmatic segment of the Tanzanian Rift, East Africa

M. Plasman,[1] C. Tiberi,[2] C. Ebinger,[3] S. Gautier,[2] J. Albaric,[4] S. Peyrat,[2] J. Déverchère,[1] B. Le Gall,[1] P. Tarits,[1] S. Roecker,[5] F. Wambura,[6] A. Muzuka,[7] G. Mulibo,[6] K. Mtelela,[6] M. Msabi,[6] G. Kianji,[8] S. Hautot,[9] J. Perrot[1] and R. Gama[6]

[1]*IUEM, UMR Géosciences Océan, Plouzané, France. E-mail: matthieu.plasman@gmail.com*
[2]*Géosciences Montpellier, UMR*5243*, Université de Montpellier, Montpellier Cedex* 5*, France*
[3]*University of Rochester, Rochester, NY, USA*
[4]*Université de Franche-Comté, Besançon, France*
[5]*Rensselaer Polytechnic Institute, Troy, NY, USA*
[6]*University of Dar es Salaam, Dar es Salaam, Tanzania*
[7]*Nelson Mandela Institute, Arusha, Tanzania*
[8]*University of Uppsala, Uppsala, Sweden*
[9]*IMAGIR sarl, Brest, France*

Accepted 2017 April 28. Received 2017 March 28; in original form 2016 October 27

SUMMARY

Rifting in a cratonic lithosphere is strongly controlled by several interacting processes including crust/mantle rheology, magmatism, inherited structure and stress regime. In order to better understand how these physical parameters interact, a 2 yr long seismological experiment has been carried out in the North Tanzanian Divergence (NTD), at the southern tip of the eastern magmatic branch of the East African rift, where the southward-propagating continental rift is at its earliest stage. We analyse teleseismic data from 38 broad-band stations *ca.* 25 km spaced and present here results from their receiver function (RF) analysis. The crustal thickness and Vp/Vs ratio are retrieved over a *ca.* 200 × 200 km^2 area encompassing the South Kenya magmatic rift, the NTD and the Ngorongoro-Kilimanjaro transverse volcanic chain. Cratonic nature of the lithosphere is clearly evinced through thick (up to *ca.* 40 km) homogeneous crust beneath the rift shoulders. Where rifting is present, Moho rises up to 27 km depth and the crust is strongly layered with clear velocity contrasts in the RF signal. The Vp/Vs ratio reaches its highest values (*ca.* 1.9) beneath volcanic edifices location and thinner crust, advocating for melting within the crust. We also clearly identify two major low-velocity zones (LVZs) within the NTD, one in the lower crust and the second in the upper part of the mantle. The first one starts at 15–18 km depth and correlates well with recent tomographic models. This LVZ does not always coexist with high Vp/Vs ratio, pleading for a supplementary source of velocity decrease, such as temperature or composition. At a greater depth of *ca.* 60 km, a mid-lithospheric discontinuity roughly mimics the step-like and symmetrically outward-dipping geometry of the Moho but with a more slanting direction (NE–SW) compared to the NS rift. By comparison with synthetic RF, we estimate the associated velocity reduction to be 8–9 per cent. We relate this interface to melt ponding, possibly favouring here deformation process such as grain-boundary sliding (EAGBS) due to lithospheric strain. Its geometry might have been controlled by inherited lithospheric fabrics and heterogeneous upper mantle structure. We evidence that crustal and mantle magmatic processes represent first order mechanisms to ease and locate the deformation during the first stage of a cratonic lithospheric breakup.

Key words: Time-series analysis; Continental tectonics: extensional; Africa; Crustal imaging.

1 INTRODUCTION

Breaking up a continental lithosphere still remains a complex and debated process. The strength of cratonic lithosphere is higher than the tectonic driving forces, implying that magmatism and pre-existing heterogeneities are important in strain localization during early rifting stage (e.g. Bott 1992; Ebinger & Sleep 1998; Buck 2004; Koptev *et al.* 2015). The seismically and volcanically

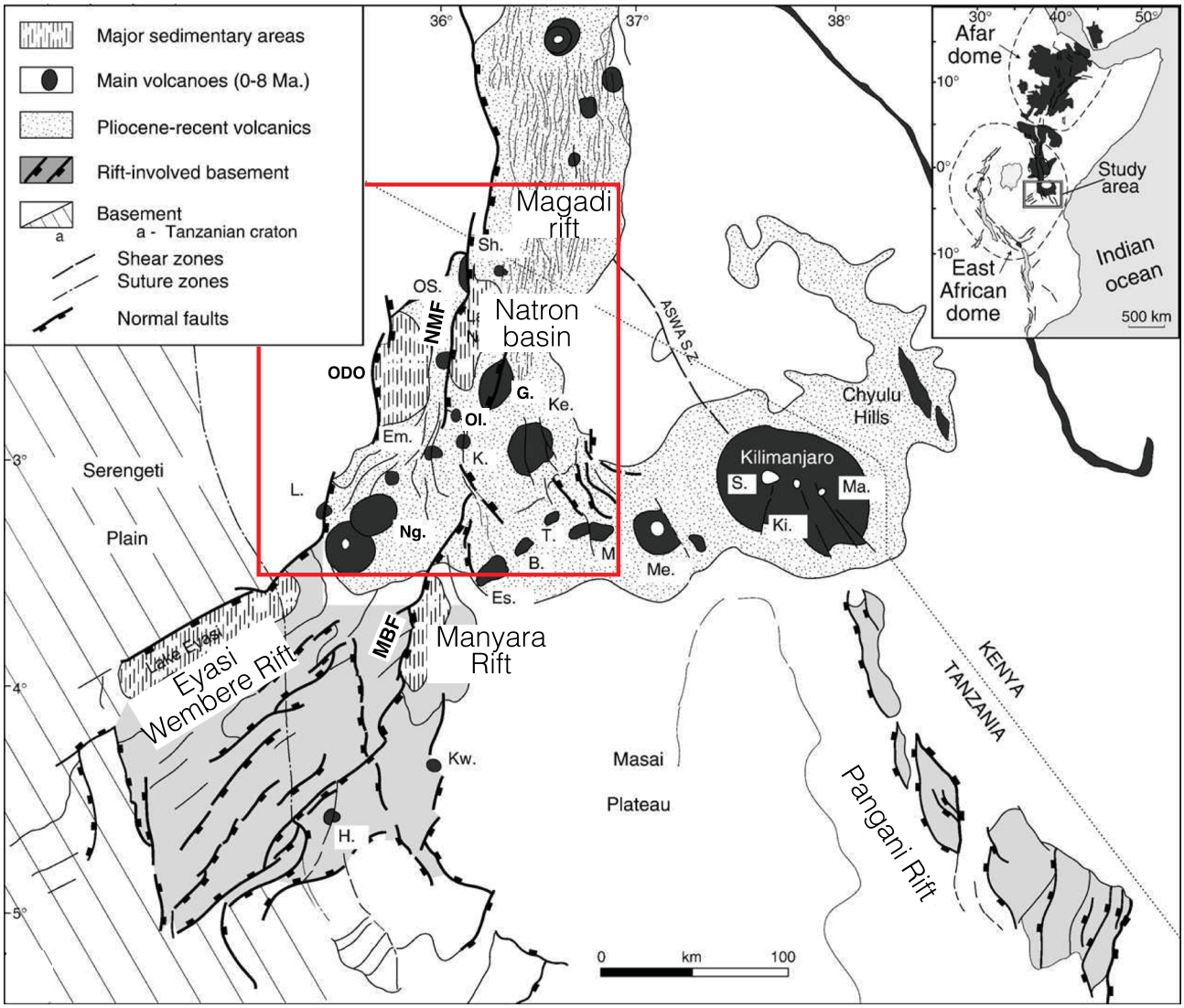

Figure 1. Structural map of the North Tanzanian Divergence with the main magmatic features (dark areas) and tectonic faults (black front lines: MBF, Manyara border fault; NMF, Natron border fault; ODO, Ol Doinyo Ogol). The red rectangle delimits the area of this study (see Fig. 2a for more details). Volcanoes: B., Burko; Em., Embagai; Es., Essimingor; G., Gelai; H., Hanang; K., Kerimasi; Ke., Ketumbeine; Ki., Kibo; Kw., Kwaraha; L., Lemagrut; M., Monduli; Ma., Mawenzi; Me., Meru; Ng., Ngorongoro; Ol., Oldoinyo Lengai; OS., Ol Donyo Sambu; P., Pello. (modified from Le Gall *et al.* 2008).

active East African rift (EAR) system includes sectors where rifting initiates in thick, strong cratonic lithosphere (e.g. Ritsema *et al.* 1998; Petit & Ebinger 2000; Vauchez *et al.* 2005). The rift runs over almost 3000 km, from Afar to offshore Mozambique, transecting Archaean to Palaeozoic orogenic belts and Permo-Triassic to Paleogene rift zones (Fig. 1). The rift evolution is influenced by one or two mantle plumes emplaced prior or synchronously to the rifting process (Ebinger & Sleep 1998; Rogers *et al.* 2000). Their signature is imaged seismically (e.g. Ritsema *et al.* 1999) and detected through elevated He3/He4 ratios (Hilton *et al.* 1999; Pik *et al.* 2008). The youngest stage of continental break-up occurs in North Tanzania, ahead of the eastern branch where the rift interacts with a strong cratonic lithosphere (Le Gall *et al.* 2008). This region provides unprecedented opportunities to evaluate models of continental lithospheric rift initiation and magmatic modification processes.

In order to shed light on the processes involved in continental breakup, we focus our analysis on the North Tanzanian Divergence (NTD) where the eastern branch of the EAR splits into three distinct arms : the Eyasi-Wembere, Manyara and Pangani rift (Fig. 1). This area is the location of a major change both in the structural expression of the rift (Dawson 1992; Foster *et al.* 1997; Le Gall *et al.* 2008) and in magmatic behaviour (Nonnotte *et al.* 2008; Muirhead *et al.* 2015; Lee *et al.* 2016). Imaging lithospheric structures is one major step to understand the interactions between mantle rheology, magmatism, tectonics and inherited structures in this rifted area. Previous studies focused in this specific region were either local tomography restricted to the crustal structures (Albaric *et al.* 2014), or teleseismic analyses on a too large scale to reach a sufficient lateral resolution for detailed lithospheric discontinuities (Ritsema *et al.* 1998; Priestley & McKenzie 2006).

We have conducted a temporary seismological experiment for 2 yr in the NTD area in order to record passive seismicity (CoLiBrEA & CRAFTI projects). We took advantage of this new and original data set to present new images of the 3D architecture of the crust and uppermost mantle in the NTD.

Here we present a receiver function (RF) analysis applied on the 38 seismological stations deployed over a *ca.* 200 × 200 km^2 area in the NTD (Fig. 2). The RF method has for long proved

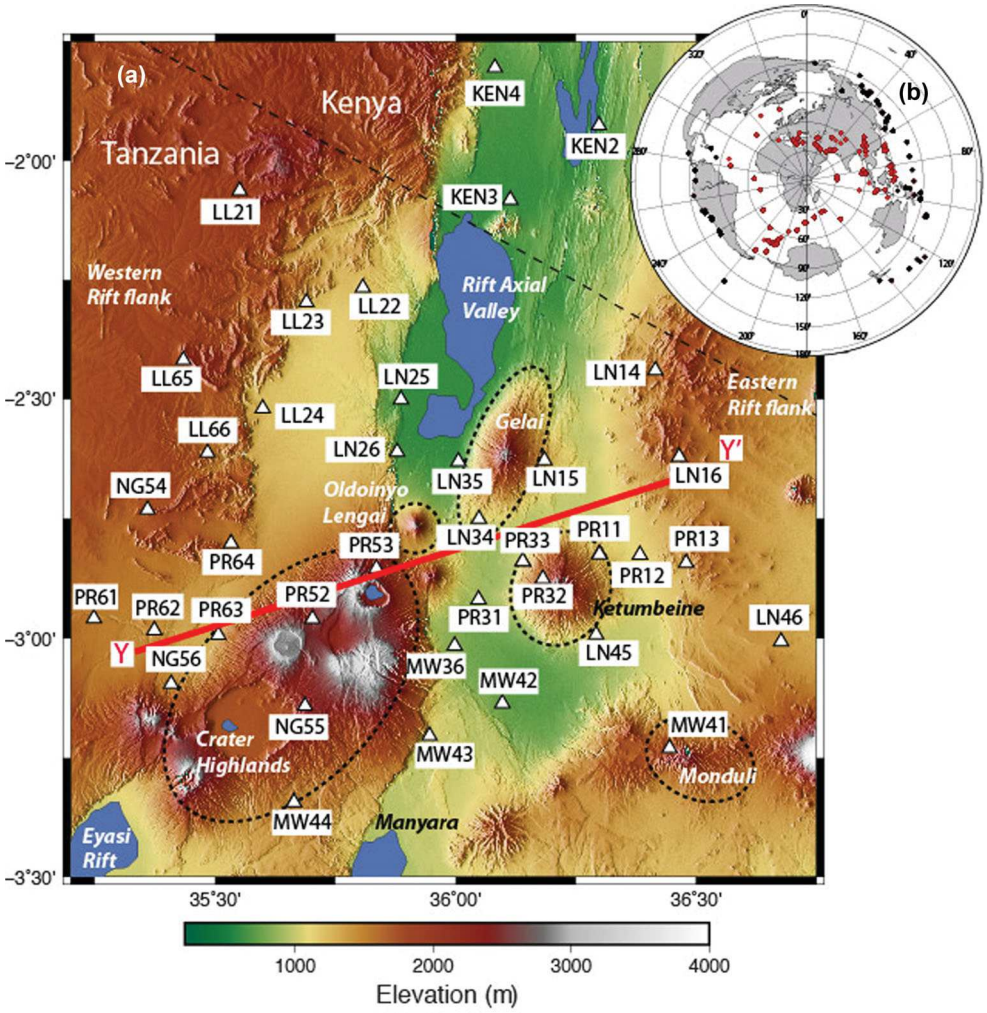

Figure 2. Inset a: location and names of the 38 seismological stations in the NTD in 2013 and 2014 over a topographic map of the region (SRTM3). The main structural features discussed in the text are indicated, and the YY' profile shows the orientation of the block diagram (Fig. 15). Inset b: azimuthal distribution of *P* (red) and PP (black) events used for the receiver functions.

its ability to image crustal and/or mantle interfaces (e.g. Langston 1977). Based on the conversion of seismic phases (Ps) on interfaces lying at depth beneath the seismic recorder, this approach provides either a velocity profile or a layer thickness coupled with a Vp/Vs ratio. We first performed an H–k stacking inversion in order to retrieve the overall crustal thickness and Vp/Vs variations. This allows us to identify the location of rifting within the crust, and to investigate the crustal composition variation due to magmatism. Second, we used forward models to explore in more details crustal and mantle structures. Our results are then discussed in terms of magmatism, anisotropy and crustal/mantle modification during a continental breakup.

2 GEOLOGICAL SETTING

The eastern branch of the EAR formed along the eastern side of the deeply rooted Archaean Tanzanian craton (Fig. 1). Rifting initiated at *ca.* 25 My in the Turkana region, but faulting and magmatism in the Magadi-Natron-Manyara area initiated less than 7 My ago (Baker 1986; Mana *et al.* 2012), where they appear to have been co-eval (Foster *et al.* 1997; Le Gall *et al.* 2008). Rifting initiated in Pan-African lithospheric domains which imparted a strong N-S fabric to crustal rocks (Smith & Mosley 1993; Le Gall *et al.* 2008). The NE-trending Eyasi-Wembere rift arm cross-cuts the east of the suture of the Pan-African-Archaean boundary and continues further SW across the deeply rooted craton. From geodetic data, direction of plate separation in East Africa are estimated at 4 mm yr^{-1} in an approximately E-W direction (Saria *et al.* 2014).

Crust and mantle xenolith data indicate that Archaean mantle lithosphere underlies thin-skinned thrusts of the Pan-African orogen and that much of the Natron-Manyara rift zone formed above Archaean mantle lithosphere (Vauchez *et al.* 2005; Aulbach *et al.* 2008; Baptiste *et al.* 2015). Last *et al.* (1997) and Dugda *et al.* (2005) provide constraints on crustal structures south and north of our study area, respectively. Last *et al.* (1997) found no change in crustal thickness crossing the Archaean-Proterozoic boundary through the central Manyara rift. Dugda *et al.* (2005) find slightly thicker crust in the Pan-African belt (39–42 km) than beneath the Tanzania craton (37–38 km). Their Vp/Vs ratios estimates (1.7–1.78) are indicative of little crustal modification outside the rift zone. Crustal velocities and thicknesses are well constrained in the Magadi rift zone by the KRISP project refraction line that shows significant crustal variation (*ca.* 10 km) beneath the central rift valley (Birt *et al.* 1997). Recorded seismicity occurs throughout the region, with relatively deep lower crustal earthquakes beneath the

Manyara basin (Albaric *et al.* 2009; Mulibo & Nyblade 2009; Craig *et al.* 2011; Albaric *et al.* 2014), and beneath the Natron basin (Lee *et al.* 2016,Weinstein *et al.*, submitted).

Our study mainly focuses on the lithospheric structure beneath the N–S trending Magadi, Natron, and Manyara basins and surrounding uplifted flanks (Fig. 1). The western flank of the Manyara basin is cross-cut by NE-trending faults and eruptive centres of the seismically active 'Crater Highlands' area which includes a number of Pliocene-Recent eruptive centres (Dawson 1992; Muirhead *et al.* 2015), at the western extremity of the Ngorongoro-Kilimanjaro transverse volcanic axis (Nonnotte *et al.* 2008; Mana *et al.* 2015) (Fig. 1). Mana *et al.* (2015) document a northeastward migration of magmatism from the Eyasi area from about 5.9 My to 0.5 My, with a main pulse of activity occurring at about 2.3 My. Ol Doinyo Lengai (Fig. 1) is an active carbonatitic volcano lying in the rift valley near the tip of the Manyara border fault. A sequence of damaging earthquakes, dike intrusion, and eruption at Ol Doinyo Lengai volcano in 2007 documents ongoing activity (Baer *et al.* 2008; Calais *et al.* 2008). The source of the dike that intruded the flank of Gelai volcano in the central Natron basin was assumed to be from an active magma chamber beneath Gelai, but the youngest lava flows here have been dated at ∼1 My (Mana *et al.* 2015; Muirhead *et al.* 2015). Prior to this study, it was unclear whether magma chambers do occur beneath volcanoes.

3 RECEIVER FUNCTION ANALYSIS

3.1 Data processing

To investigate the crustal and upper mantle structure below the NTD, we analysed data recorded during the CoLiBrEA and CRAFTI twin multidisciplinary projects (French ANR and US NSF projects, respectively). A temporary seismic network of 38 broad-band stations was deployed from January 2013 to December 2014 in the Magadi-Natron-Manyara rift basins and their flanks (Fig. 2a). Each site consisted of a Reftek recorder connected to a STS2, Trillium 120, Trillium Compact, 3T or 40T sensor. The equipment was connected to a GPS antenna and power was supplied by a battery reloaded by solar panels. We selected events with magnitude greater than 5.5 to ensure a good signal-to-noise ratio. Both *P*- and *PP*-events were used to provide a wide range of back azimuths by selecting events with epicentral distances between 30°–90° (P) and 90°–180° (PP) (Fig. 2b).

We first rotated the three-component seismograms from the geographical system (ZNE) into radial, transverse and vertical components (ZRT) and then applied a Butterworth band-pass filter between 0.08 and 0.8 Hz. The radial and transverse RFs were computed from an iterative time-domain deconvolution on a 50 s time window (10 s before *P* or *PP* arrival time and 40 s after) with a Gaussian width of 2.5 s (Ligorría & Ammon 1999). The radial RFs were selected based on a least squares misfit criterion. The recovered radial component should at least reproduce 90 per cent of the initial one. This threshold dropped to 80 per cent for stations with a lack of records (instrumental problems) in order to ensure a sufficient number of data to widen the back azimuthal coverage (PR12 and PR13, Fig. 2a). Following this procedure, we obtained between 17 and 107 individual RFs per station (Table 1). The RFs present a high signal-to-noise ratio and a clear Ps conversion phase at the Moho at about 5 s after the first *P* peak taken as the time origin for the RFs (Fig. 3). The first multiple (PpPs) is clearly observed at *ca.* 15 s, and some intermediate phases are also present either before or after 5 s.

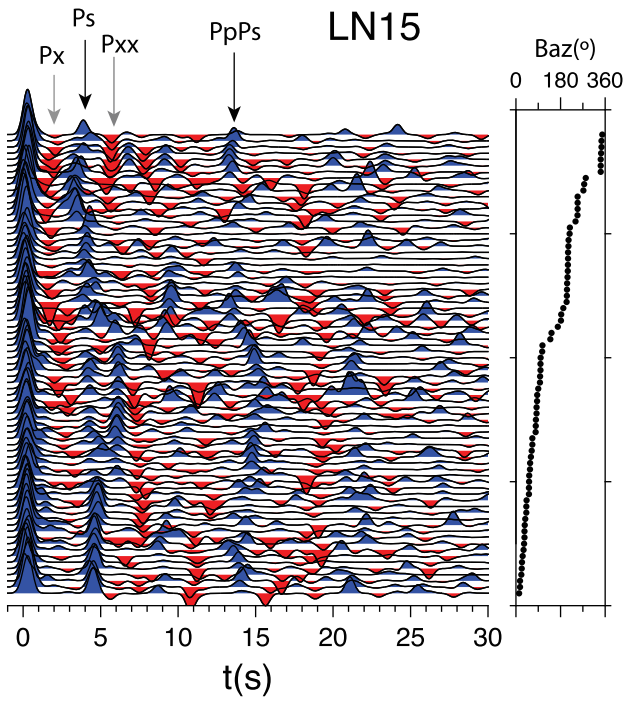

Figure 3. Radial receiver function at station LN15 organized by increasing backazimuth. The approximate arrival time for *P* to *S* conversion at the Moho (Ps) and its first multiple (PpPs) are indicated by the black arrows. Time arrivals for an Intracrustal negative phase conversion (Px) and for a mantle one (Pxx) are marked by grey arrows.

The clarity and strong amplitude of the Ps and PpPs conversion phases justify to apply the now classically used (H-k) stacking inversion to determine first order Moho depth and Vp/Vs ratio (Zhu & Kanamori 2000). However, this method fails to characterize dipping or anisotropic interfaces and second order conversions with weaker multiples. Our Rfs present both intracrustal and mantle conversion phases (Fig. 3, Px and Pxx, respectively), the latter showing an azimuthal dependency. We constrained those second order features with direct modelling, allowing for velocity inversions, anisotropy and dipping interfaces (Frederiksen & Bostock 2000).

3.2 Inversion

In receiver function analysis there is an inherent trade-off between crustal thickness (H) and Vp/Vs ratio (k). The stacking grid search technique in the H-k domain reduces this trade-off by combining the *P* to *S* conversion (Ps) with its two multiples (Zhu & Kanamori 2000). For each station Ps theoretical arrival times, its first (PpPs) and second multiples (PpSs+PsPs) are calculated for all (H,k) couples in a given range. The RF signal amplitudes at these times are stacked and the maximum of this function corresponds to the most coherent (H,k) combination. This method assumes purely horizontal interfaces, isotropic medium and an average crustal *P*-wave velocity (Zhu & Kanamori 2000). In our case, we extracted the mean crustal *P*-wave velocity for each station from Albaric *et al.* (2014) velocity model (Table 1). We defined H and k to initially range between [20–50 km] and [1.6–2.0], respectively. These boundaries correspond to common values found in these types of rift (e.g. Dugda *et al.* 2005).

Finally we controlled the impact of each phase (Ps and its two main multiples) on the results in the objective function computation by setting a weight for each ones. Most RFs show a very

Table 1. Moho depth and Vp/Vs ratio (k) results from the H-k stacking method for all seismic stations. The mean crustal *P*-wave velocity used for each station is taken from Albaric *et al.* (2014). We have an average of 67 events processed per station (46 P-RF and 21 PP-RF), with a mean Moho depth of 35.9 km and an average Vp/Vs of 1.77. The reported error is deduced from the bootstrap algorithm and corresponds to the maximum value of either Evp or Eb (see the text for explanation). Stations also proceeded with a direct modelling are followed with a star (Frederiksen & Bostock 2000).

Location	Station name	Longitude (E)	Latitude (N)	Number of RF	Vp (km s^{-1})	Moho depth (km)	Vp/Vs ratio	Error in depth (km)	Error in Vp/Vs
Eastern edge	LN14*	36.41543	−2.43945	82	6.68	37.0	1.74	1.7	0.011
	LN16*	36.46476	−2.62067	81	6.71	40.9	1.64	1.7	0.014
	LN46*	36.6767	−3.0070	102	6.64	36.8	1.71	1.6	0.019
	PR13*	36.47917	−2.84255	17	6.67	36.8	1.71	3.1	0.040
Western edge	LL21*	35.551	−2.06273	49	6.2	33.16	1.73	1.7	0.026
	LL22	35.5989	−2.5195	42	6.70	36.57	1.73	2.5	0.031
	LL23	35.69	−2.2969	101	6.43	34.5	1.71	1.6	0.009
	LL24	35.8072	−2.2662	53	6.67	34.4	1.74	1.4	0.025
	LL65*	35.43399	−2.41797	82	6.67	35.6	1.75	1.5	0.025
	LL66*	35.48424	−2.61226	80	6.70	38.3	1.68	1.6	0.010
	NG54*	35.35953	−2.73156	97	6.68	37.3	1.7	1.5	0.017
	PR61*	35.24780	−2.95860	95	6.66	39.4	1.71	1.8	0.009
	PR64*	35.53311	−2.80144	60	6.67	39.2	1.67	1.8	0.013
Crater Highlands	MW44	35.6638	−3.3437	72	6.64	40.3	1.71	1.7	0.013
	NG55	35.6870	−3.1418	71	6.64	37.6	1.86	1.9	0.036
	NG56	35.4086	−3.0960	107	6.63	40.3	1.88	3.5	0.067
	PR52	35.70235	−2.95929	42	6.61	31.7	1.90	4.7	0.121
	PR53	35.83537	−2.85378	37	6.58	35.7	1.73	3.0	0.062
	PR62*	35.37356	−2.98336	101	6.66	36.6	1.81	1.8	0.038
	PR63*	35.50668	−2.99326	89	6.64	38.8	1.83	1.7	0.014
Rift valley	KEN2	36.2873	−1.9184	48	6.4	28.0	1.79	6.8	0.061
	KEN3	36.11898	−2.0932	51	6.42	30.0	1.83	1.4	0.048
	KEN4*	36.05358	−1.7840	45	6.41	37.1	1.67	1.7	0.034
	LN15*	36.18465	−2.62788	76	6.63	35.4	1.76	1.5	0.038
	LN25	35.8864	−2.50062	78	6.64	36.0	1.67	1.5	0.023
	LN26	35.87848	−2.61038	66	6.62	29.3	1.94	3.7	0.066
	LN34	36.0485	−2.75104	87	6.60	34.3	1.74	1.6	0.143
	LN35	36.00595	−2.63044	80	6.67	37.1	1.67	1.5	0.026
	LN45	36.2921	−2.9927	58	6.63	35.7	1.76	1.6	0.019
	MW36	35.9981	−3.0158	52	6.64	33.7	1.88	1.3	0.031
	MW41	36.4448	−3.2305	58	6.64	31.8	1.97	2.3	0.059
	MW42	36.1011	−3.04	45	6.45	33.6	1.85	1.4	0.016
	MW43	35.9459	−3.2046	42	6.45	36.2	1.70	2.0	0.049
	PR11*	36.29912	−2.82314	71	6.66	37.9	1.66	1.5	0.069
	PR12	36.38330	−2.82528	30	6.67	36.2	1.72	2.2	0.040
	PR31	36.04759	−2.919	85	6.61	34.3	1.87	1.5	0.027
	PR32	36.18132	−2.87539	47	6.60	35.7	1.79	1.6	0.017
	PR33	36.13952	−2.83913	63	6.60	35.7	1.75	1.6	0.010

clear Ps Moho conversion around 4-5 s with a notable first multiple around 15-16 s (Fig. 3), allowing for a reduction of possible (H.k) couple. The second multiple (at ∼20 s) is hardly notable in our case, certainly due to destructive interference with other multiple layers. After several tests, we finally chose 0.6, 0.3 and 0.1 to be our preferred weighting factors for the 3 phases. We then identified the best couple (H,k) from the stacking functions (Fig. 4) and estimated the associated error from the bootstrap method (Efron & Tibshirani 1994). This error computation allows to quantify the widening of the objective function due to an azimuthal dependency, a complex geometry interface or noisy data. Following Tiberi *et al.* (2007), two errors were computed: one to account for the scattering of the data set (Eb) and the second to consider the crustal *P*-wave velocity uncertainty (Evp). For Eb error, we computed a standard deviation and the 95 per cent ellipse error from 200 subsets of data processed with the H-k stacking method (Fig. 5). For velocity uncertainty, we randomly chose 200 crustal Vp values between 6 and 7 km s^{-1} and reprocessed the whole data set for those values. The final error reported in Table 1 is the maximum value of either Eb or Evp.

3.3 Forward modelling

Zhu & Kanamori (2000) method cannot account for dipping interfaces, anisotropic layers and often fails to characterize intracrustal or mantle interfaces due to their weaker multiples. One third of our stations still presents intracrustal and mantle conversions, as well as a strong back-azimuthal variation for the mantle phase (see for example LN15 Fig. 3). In order to investigate more precisely the lithospheric structure, we used the forward technique proposed by Frederiksen & Bostock (2000) that offers the opportunity to account

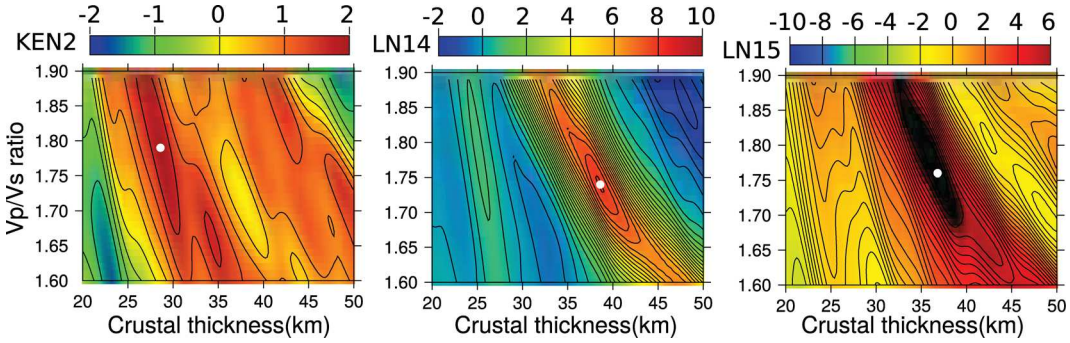

Figure 4. Crustal thickness (H) versus Vp/Vs ratio diagrams from the H–k stacking method for three stations (KEN2, LN14 and LN15, see Fig. 2a for location). White points represent the maximum of the stacking function. The colour bar represents the amplitude of each stacking function.

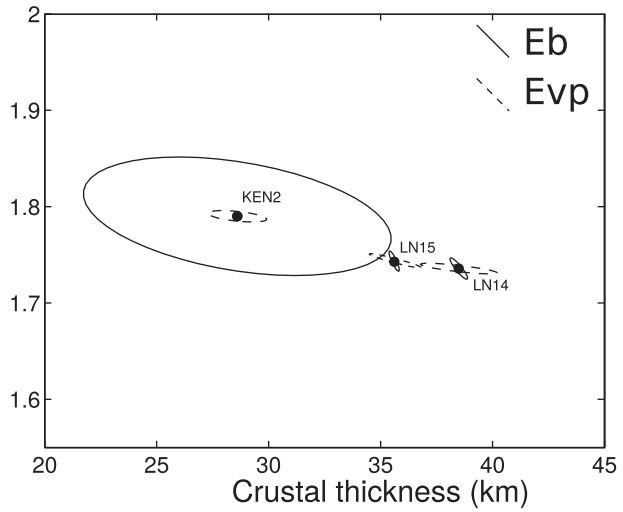

Figure 5. Eb (plain line) and Evp (dashed line) error ellipses for KEN2, LN14 and LN15 obtained from the bootstrap analysis (see Fig. 4 for the H–k stacking method results). Eb is the error accounting for data scattering and Evp reflects the *P*-wave velocity uncertainty.

for several interfaces, as well as anisotropy and dipping interfaces when suspected. We applied this technique on stations with clear intracrustal and/or mantle conversions (Table 1). We computed both the radial and transverse components of the RFs to maximize the information about the intracrustal and mantle interfaces (e.g. Jones & Phinney 1998). We constrained the starting model with Moho and Vp/Vs estimates from our H–k stacking. Then we progressively added complexity by introducing additional layers, dipping interfaces and/or anisotropy. The resulting radial and transverse RFs are then visually compared to the observed ones.

4 RESULTS

4.1 General features

We first applied the grid search stacking method of Zhu & Kanamori (2000) to our complete receiver function set (Table 1). The average errors on Moho depth and Vp/Vs ratio are ±2 km and ±0.03, respectively. The largest values are observed for stations exhibiting Ps azimuthal variation. This is the case for KEN2 site (Fig. 2a and Table 1) which combines this feature with a small number of events and thus presents the largest error in crustal thickness (∼7 km, Fig. 5). The results are visually summarised in Fig. 6.

The computed Moho depth in the NTD ranges between 28 and 41 km with the highest values located beneath the shoulders of the rift. With a mean value of 37 km (±1.3 km) for Moho depth beneath the rift shoulders (Eastern and Western edges, Fig. 6 and Table 1), our results depict slightly lower values than those from Last *et al.* (1997) and Julià *et al.* (2005), which show a mean Moho interface at 38-42 km depth, at a broader scale. Since our study area is more restricted and our network samples many different geological units, we thus claim for more details and lateral variability in our results. For the western flank, the crustal thickness decreases from south (∼38 km near Ngorongoro) to north (∼34.8 km), but remains thicker on average than the eastern flank (36±1.7 km). Both flanks are associated with the lowest Vp/Vs ratio (1.66 to 1.73).

In contrast with the two flanks, a thinner crust is observed in the rift axial valley (∼34 ±2 km) associated with a higher Vp/Vs (1.75–1.81). The highest Vp/Vs values (>1.85) are spatially associated with stations closed to volcanic structures: LN26 (Ol Doinyo Lengai), MW41 (Monduli), PR31, MW36 and MW42 (Ketumbeine) (Figs 2a and 6). The NTD Vp/Vs values are close to the ones estimated in the Albertine rift (Gummert *et al.* 2015) but never overtake the extreme values in Main Ethiopian rift (Stuart *et al.* 2006).

4.2 3D local Moho features

On the eastern edge, stations LN14, LN16, LN46, PR13 present a clear Ps peak at 5 s which weakens or even disappears for a restricted back azimuth range (for example LN14 on Fig. 7). This is associated with a very weak signal on the transverse component and no periodic behaviour. This pattern is thus unlikely produced by crustal anisotropy or a dipping Moho. Alternatively, we assign the absence of Moho signature to a very local structure. Events coming from these azimuths (between N100°E and N200°E) may have travelled through either a low-velocity upper mantle or a fast lower crust which both possibly reduce the impedance at the Moho in a restricted area. Events coming from other back azimuths show a clear Ps conversion with no or only weak intracrustal signal, suggesting a rather homogeneous crust (see for example LN14 in Fig. 7).

Stations located on the Crater Highlands (PR52, PR53, PR62, PR63, PR64, NG56, NG55, Fig. 2a) exhibit a clear disturbance in the Moho Ps conversion with a back azimuth dependency (Fig. 8). The conversion weakens or even splits for some events and is also present on the transverse component. This pattern is restricted to the volcanic edifices, and is coupled with little variation in crustal thickness over the area (Fig. 6). In order to detect any correlation with geological features, we have reported the piercing points for

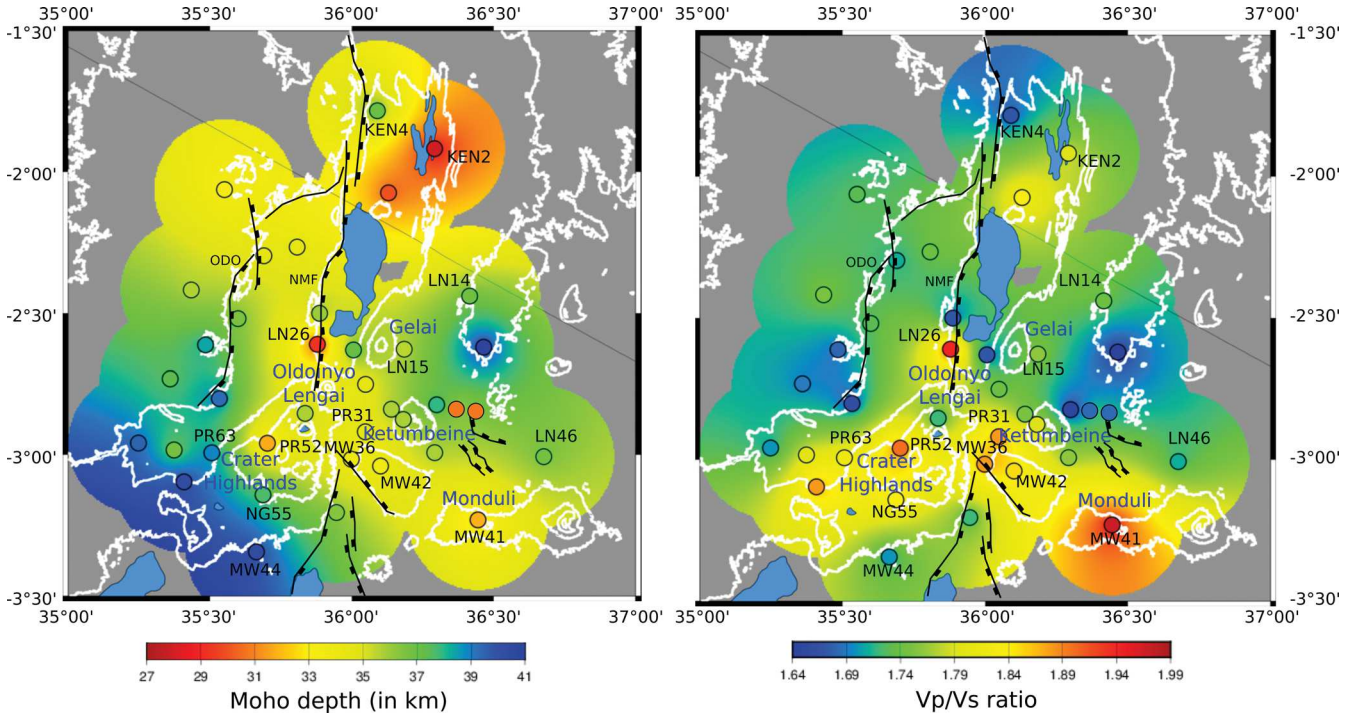

Figure 6. Crustal model of Moho depth (left) and Vp/Vs ratio (right). Small circles represent the seismic stations (see Fig. 2a for names). The background values of the map are interpolated through ~25 km radius circle around each station. The radius of the circle corresponds to the mean distance between each station and its piercing points computed at its Moho depth. Areas without data are grey tint. White lines represent topographic contours. We add the main volcanic and tectonic (black lines) structures and name of some of the stations on which we focus during the study (NMF, Natron master fault; ODO, Ol Doinyo Ogol).

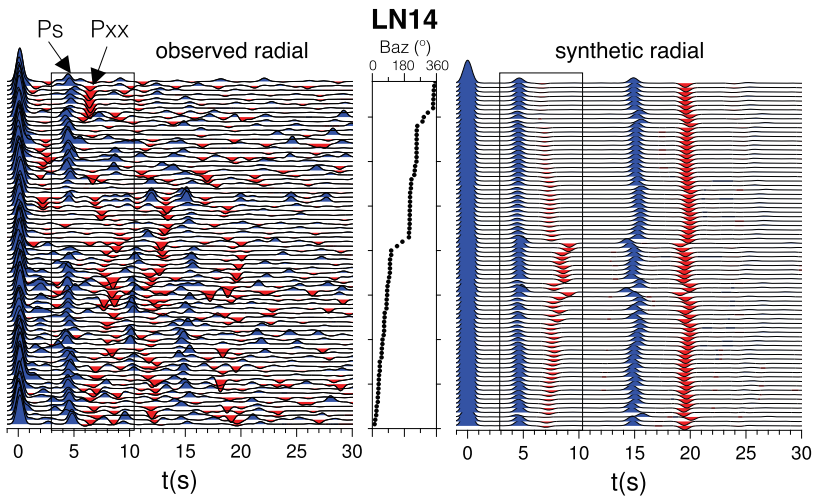

Figure 7. Left: observed radial RFs for LN14 organized by increasing backazimuth (Baz). Converted phases at the Moho (Ps, positive) and at the mantle discontinuity (Pxx, negative) are labelled. Right: corresponding synthetic radial RFs computed with Frederiksen & Bostock (2000) method. The model is composed of a 39 km thick crust (Vp = 6.68 km s^{-1}, Vp/Vs = 1.74), an upper mantle layer (30 km thick, Vp = 8.1 km s^{-1}, Vp/Vs = 1.8), and an LVZ with Vp = 7.4 km s^{-1}, Vp/Vs = 1.8, a dip angle of 30° and a strike of N40°.

the concerned stations at the Moho depth over the Vp/Vs ratio map (Fig. 9a). RFs with a disturbed Ps conversion (double or wider peak, disappearance, ...) significantly differ in location from those with a clear Moho signal and correspond to higher Vp/Vs ratio areas (>1.80, Fig. 9b). On a roughly East-West profile, the Ps disturbance is also associated with the occurrence of a negative Px conversion within the crust (Fig. 9c). Those patterns typically reflect 3-D variations of the Moho geometry and crustal structures, most likely related to the Crater Highlands and volcanic edifices inner system.

4.3 Intracrustal interfaces

A distinct signal waveform that discriminates the stations is the presence or absence of intracrustal converted phases (before ~5 s and noted Px, Fig. 3). For example, LN14 does not exhibit any strong converted phases within the crust (Fig. 7) whereas KEN4 presents a clear negative peak around 3 s (Fig. 10). The sedimentary layer in North Tanzania and South Kenya basins is estimated to be *ca.* 3.5 km thick (Birt *et al.* 1997; Ebinger *et al.* 1997) and cannot be

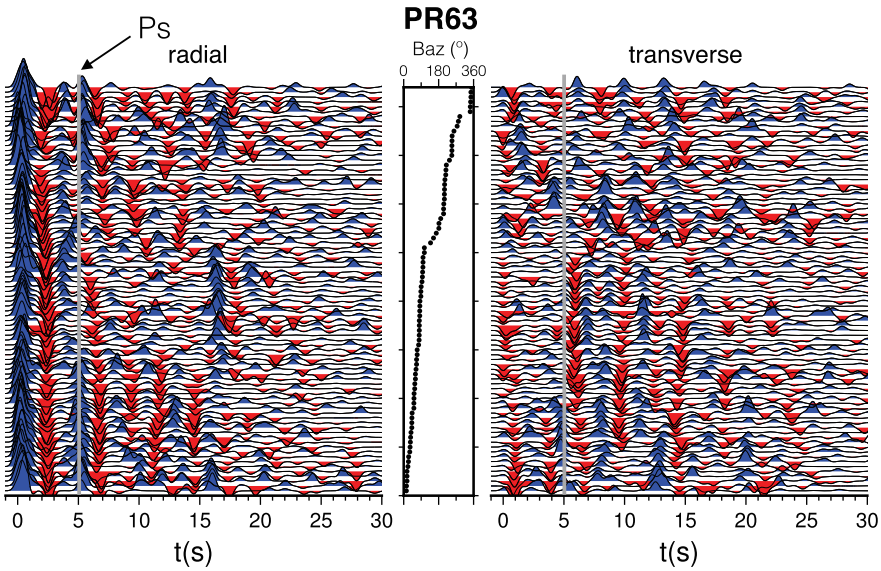

Figure 8. Observed radial (left) and transverse (right) RFs for station PR63, located near the Ngorongoro volcano. The RFs are organized by increasing back azimuth (Baz). The grey line indicates the location of the Ps phase around 5 s.

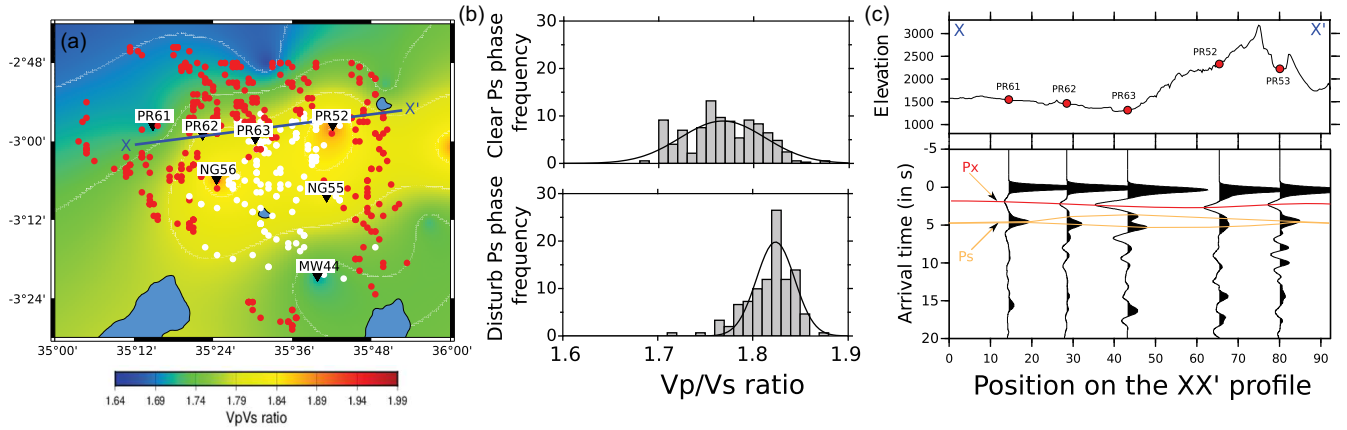

Figure 9. Insert a : seismic piercing points at Moho depth superimposed on the Vp/Vs map zoomed in the Crater Highlands area (Fig. 6). The red points are piercing points with a clear and regular Moho signature in the RFs, while white points are piercing points associated with disturbed Ps peak within the RFs. Insert b: distribution of Vp/Vs ratio according to the quality of the Ps peak (clear on top, disturbed at bottom). Insert c: stacked RFs for stations located on the Crater Highlands along the XX' profile (insert a).

responsible for such feature. In order to explain the strong negative conversion Px observed (Fig. 3), one would expect at least 10 km of sediment thickness (Guo *et al.* 2015). It can rather be related to the upper bound of a low-velocity zone (LVZ) near 15 km depth as it is confirmed by modelling receiver functions for simple crustal models (Fig. 10). The velocity decrease can reach ∼7 per cent and ∼16 per cent for *P*- and *S*-wave, respectively. A similar LVZ in the lower crust is deduced from receiver function analysis in the western branch of REA (Wölbern *et al.* 2010).

We map in Fig. 11 the stations with (1) a clear low-velocity lower crust (red circles), (2) a weak intracrustal phase (orange), and (3) no intracrustal signature (white). The stations exhibiting this intracrustal interface are restricted to the central part of the network and worthy correspond to the location of the low-velocity pattern obtained with a joint ambient noise and arrival time tomography (Roecker *et al.*, submitted). The geometry and contours of this layer are complex and are echoed by a backazimuth dependency for some stations. Particularly, KEN4, LL22 and LN26, located on the edge of the rift basins, all display a fading of this intracrustal negative conversion at ∼2 s for western events (Fig. 10). This characteristic reflects the difference in crustal structure between the flank (Proterozoic basement terranes) and the axis of the rift. Some stations also exhibit a backazimuth dependency for this interface that can come either from a dip or anisotropy (KEN3, LN15, LN35, PR52, PR62, MW43, MW44, NG56). However, the uneven back azimuth distribution, potential interaction with other conversions and poor mutual characteristic between the stations prevent us from discriminating between those two factors by simple direct models.

Stations MW41, MW42, MW43, PR31 and PR32 (Fig. 2a) all present an increasing complexity of the crustal signal with multiple Px conversions and quite high amplitudes on the transverse component (Fig. 12). Direct models for those stations did not lead to a constrained and faithful unique solution due to the high numbers of unknown (9 per layer). This pattern simply enhances the conspicuous complexity and layering of the crust within the axial

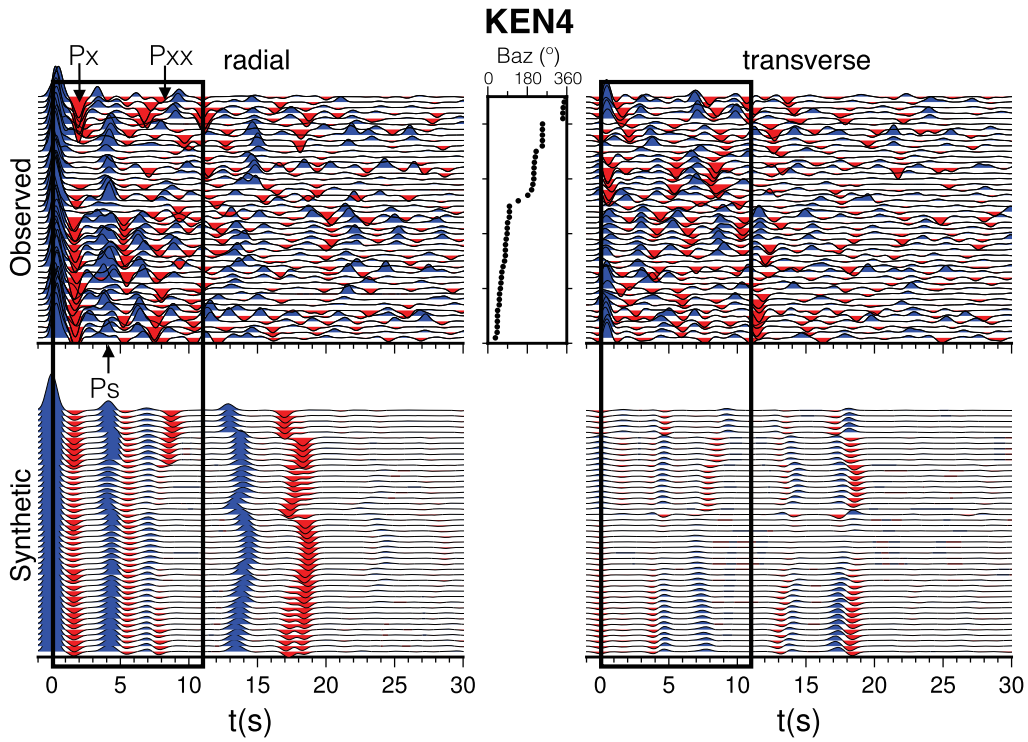

Figure 10. Top: observed radial (left) and transverse (right) RFs for KEN4 organized by increasing backazimuth (baz). Bottom : corresponding synthetic radial (left) and transverse (right) RFs modelled with Frederiksen & Bostock (2000) method. The model includes a 15 km thick upper crust (Vp = 7.0 km s^{-1}, Vp/Vs = 1.70), a 19 km thick LVZ (Vp = 6.5 km s^{-1}, Vp/Vs = 1.91, anisotropy = 8 per cent), an upper mantle layer (Vp = 8.1 km s^{-1}, Vp/Vs = 1.80) and a dipping low velocity mantle zone at 69 km depth dipping N20° with a strike of N220°(Vp = 7.4 km s^{-1}, Vp/Vs = 1.85).

valley. We confidently relate these coherent successive Px peaks to either volcanic features in the neighbourhood of the Ketumbeine (PR32 and PR31), and Monduli (MW41) volcanoes, or the presence of Pliocene-recent sedimentary infill along the rift axis (MW42, MW43).

4.4 Uppermost mantle interface

Most of the stations show a negative phase conversion *ca.* 7 s after the first *P* peak. This conversion (noted Pxx see Fig. 3) is clear even in the absence of intracrustal signal, discarding potential intracrustal multiples (Fig. 7). This negative signal is in agreement with an upper mantle interface displaying a decreasing velocity with depth. We have proceeded to simple direct modelling following the Frederiksen & Bostock (2000) technique to characterize this interface for stations where the peak is clearly expressed (Table 1).

For stations located on the western edge of the rift (LL21, LL65, LL66, NG56, PR61, PR63, PR64, KEN4, Fig. 2a), the arrival time of the negative peak after the Moho Ps conversion is back azimuth-dependent with a 2π period (Fig. 10). The associated interface corresponds to a plane dipping 20°–30° to the west–northwest. The depth of this dipping interface varies between 50 and 75 km, but is systematically associated with a decrease of 6 to 9 per cent in *P*- and *S*-wave velocity, respectively. A quite similar inclined structure is imaged at the eastern stations (LN14, LN16, LN46, PR11, PR13, Fig. 2a), but with an opposite dipping angle (20°–30° to the East). We reported those orientations (strike and dip) over the Vp/Vs map (Fig. 13).

We are fully aware that these models are non-unique, however the dip and the strike of the interface plane are based on the back azimuth dependency and we confidently constrain the value between ±10°. A horizontal mantle interface failed to reproduce the radial observed stacked RFs, whereas a dipping interface better fits the widening of the phase at 7 s (Fig. 14). Moreover the dip, strike and depth of this interface are consistent from one station to another. For PR63 and PR61 for example, the geometry of the dipping interface (30° to the West) is coherent with a depth of ∼48 km under PR63 and 19 km deeper for PR61 (∼67 km, Fig. 13). Finally, the presence of a low-velocity mantle beneath the region is consistent with previous seismological results that demonstrated a marked decrease of surface waves velocity between ∼60 and 100 km depth (Fishwick & Bastow 2011; Weeraratne *et al.* 2003; O'Donnell *et al.* 2013).

5 DISCUSSION

The main structural features of the NTD area, deduced from our RF analysis, are synthesized on the schematic lithospheric-scale block diagram in Fig. 15 (see Fig 2a for the position), and consist as follows:

(i) A relatively deep Moho ranging from 28 to 41 km depth. The thinnest crust is localized in the axial rift valley and corresponds to the most complex and layered signal in the RFs. The thickest crust is observed below the Crater Highlands and beneath Proterozoic mobile belt, where RFs depict a rather homogeneous crustal signal (Fig. 6).

(ii) From East to West, an asymmetric Moho interface with the steepest slope westwards beneath PR63 (Fig. 8).

(iii) A clear low-velocity lower crust in the central part of the network, the top of which lies at 15–18 km depth (Fig. 11). It

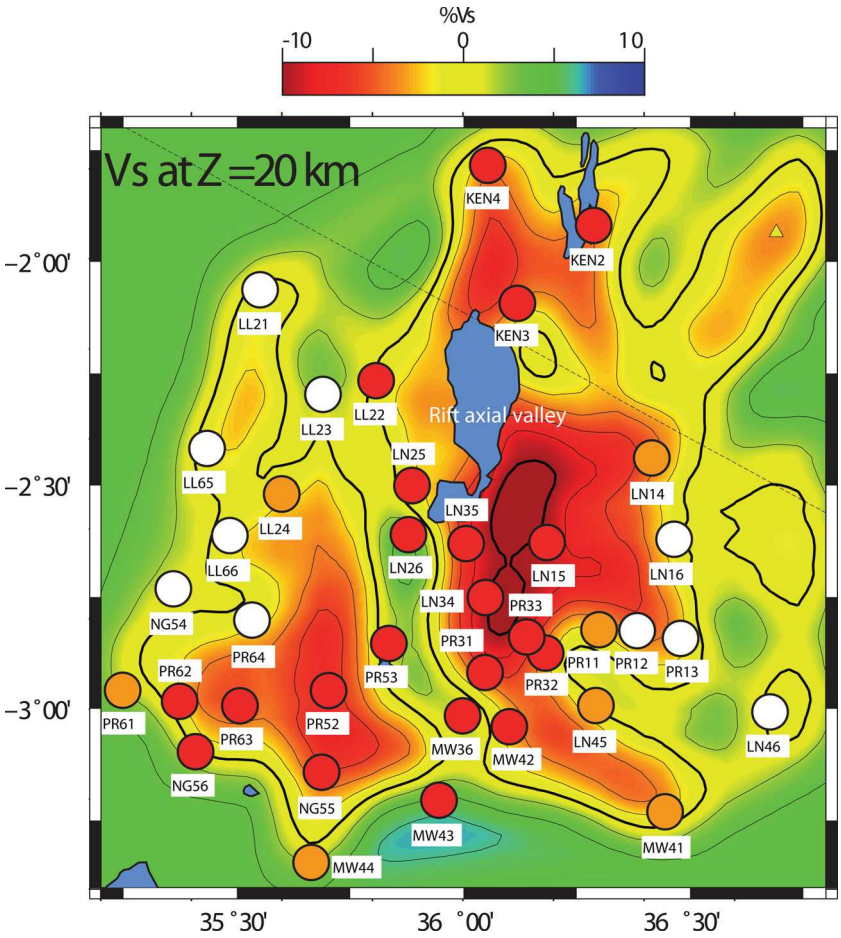

Figure 11. Comparison between intracrustal LVZ in RFs (circles) and local *S*-wave velocity variations (background). Red circles indicate stations with a clear low-velocity lower crust signature on their RF signal, orange ones represent moderate or weak low-velocity signature and white circles are stations with no intracrustal signature in their RFs. The background map is the *S*-wave velocity variations obtained at 20 km depth from a joint surface/body wave inversion (S. Roecker, submitted).

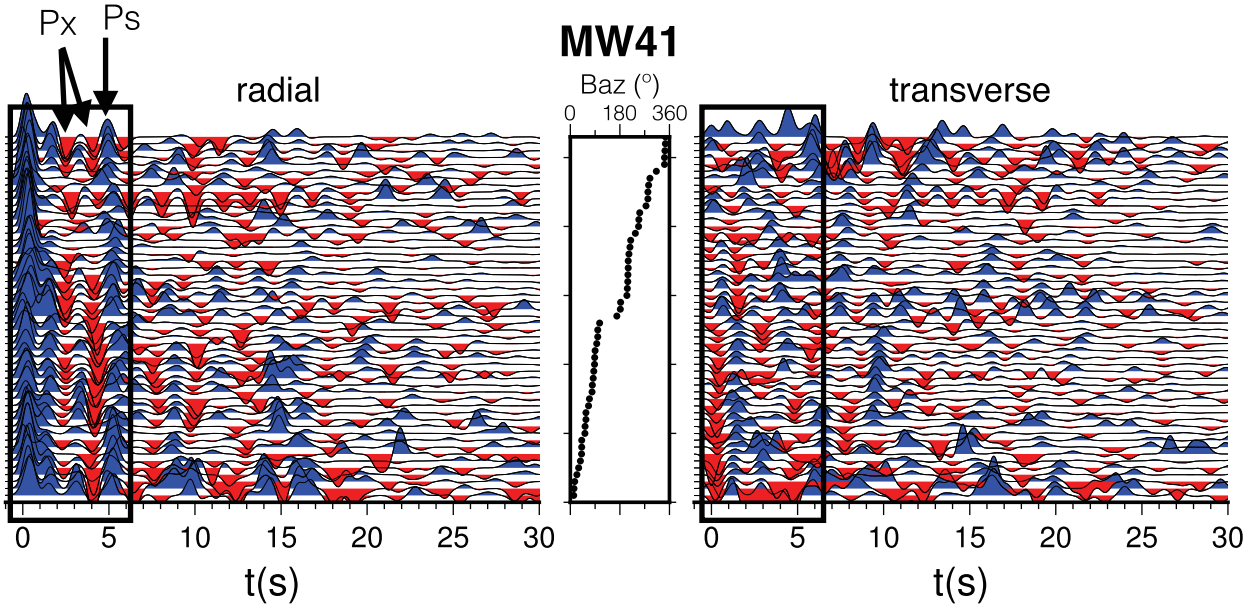

Figure 12. Left: observed radial RFs for MW41 organized by increasing backazimuth (Baz). Right: corresponding observed transverse RFs.

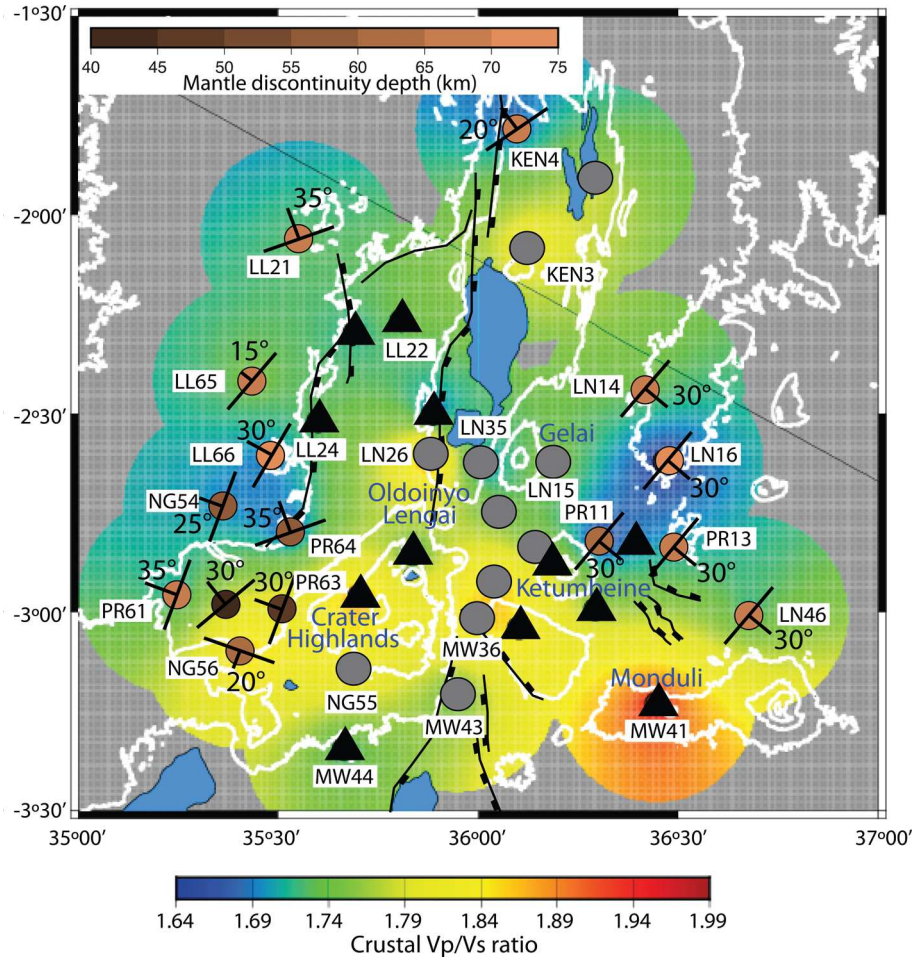

Figure 13. Map of the mid-lithospheric discontinuity delimiting a low velocity underlying mantle deduced from direct modelling (Frederiksen & Bostock 2000). Black triangles represent stations with no detectable mantle interface signature and grey circles represent stations with a mantle interface signature in their RFs, for which no satisfying interface geometry was found due to too global complex signal. Stations for which the geometry of the mantle interface was successfully modelled are represented with brown circles (colour scale representative of the interface depth). The dip angle value is written next to the corresponding station. Background colour map depicts crustal Vp/Vs ratio with topographic contours (white lines).

does not seem to correlate directly with volcanic edifices at the surface and exhibits a complex 3-D geometry.

(iv) Presence of crustal anisotropy in the rift valley and beneath the volcanic edifices.

(v) A low-velocity mantle layer from 60–70 km depth underlying a normal upper mantle. The asymmetrically dipping attitude of this interface is particularly clear in the eastern and western parts of the region, with an SE and NW dip, respectively (Fig. 13).

We will now discussed their meaning in terms of rifting processes in a cratonic lithosphere, tectonic and magmatic mechanisms for the NTD.

5.1 Vp/Vs variations in terms of crustal composition

The Vp/Vs ratio is commonly used to estimate the bulk composition of the crust (e.g. Domenico 1984; Christensen 1996). It usually ranges between 1.6 and 2.0 and is sensitive to rock composition, especially to quartz and feldspar/plagioclase percentage. Vp/Vs ratio usually exhibits low values for felsic composition rocks (1.71 for granite, 1.78 for granodiorite) and increases for mafic rocks (1.84 for gabbro) (Holbrook *et al.* 1992; Zhao *et al.* 2010). The presence of fluids and partial melt are also known to control Vp/Vs ratios, the latter increasing with higher contents (Watanabe 1993).

In our study, the lowest ratios (1.66 to 1.73) are localized beneath the rift flank and coincides with the Archaean crust West of the Crater highlands. They are consistent with previously determined value of ∼1.74 (Last *et al.* 1997; Mollel *et al.* 2008). There is no significant difference between eastern and western flanks, both of them exhibiting values consistent with the presence of cratonic and Proterozoic belt rocks (gneiss or granitoid composition, Harvey 2005).

The stations located in the rift valley and Crater Highlands present higher Vp/Vs values (between 1.75 and 1.81) that coincide with locations of either volcanic edifices, Quaternary sediments and/or interbedded mafic lavas and volcanoclastics (Figs 1 and 6). In the study area, magmatic fluids (e.g. partial melting), water contents and rock composition may equally affect the Vp/Vs values. Moreover it is important to note that our H–k stacking value is only a crustal average and can thus result from different layers interaction, particularly for stations with an intricate crustal signal (e.g. Fig. 10). Direct modelling requires an even higher Vp/Vs ratio restricted in the crustal LVZ for some of the central stations (up to 1.91, Table 2). This result strongly supports the presence of partial melt within the lower crust in the rift valley.

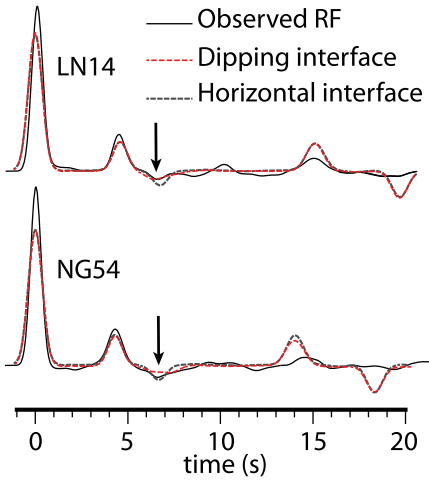

Figure 14. Comparison between observed (continuous black line) and synthetic stacked RF for stations LN14 (upper panel) and NG54 (lower panel). Black dashed line is for the stacked RF signal obtained with a horizontal mantle interface, whereas the red dashed line is for a dipping interface (LN14: dip 30° strike N40°; NG54: dip 25° strike N200°). Black arrow indicates the mantle Pxx converted phase.

Those high Vp/Vs values can however be artefacts from anisotropy or complex structures within the crust (Hammond *et al.* 2014). We strongly suspect anisotropy to be present beneath some of the stations (e.g. MW44 presents strong energy on the transverse component with clear both polarity and amplitude π-periodicity). However it is difficult to quantify in such a complex setting the effect of anisotropy, dipping interfaces, lateral heterogeneities or multiple layering on the Vp/Vs values. We thus consider our results as an upper bound for the Vp/Vs ratio which can be compared with values obtained from independent other methods (i.e. Roecker et al, submitted). Even if overestimated, our Vp/Vs ratios in the Rift valley are indicative of a lower degree of partial melt compared to more mature rifts, which is consistent with an earlier stage of continental breakup (e.g. the Main Central Rift in Ethiopia, Stuart *et al.* 2006; Hammond *et al.* 2011; Keir *et al.* 2011; Reed *et al.* 2014).

5.2 Breaking up a thick crust

Results from H-k stacking analyse show that the Moho evolves from 35–40 km deep beneath the rift flanks up to 28 km in the Rift valley. This crustal thinning is asymmetric, with a steeper slope for its western part (Fig. 15). This steepest gradient coincides with the location of the deeply buried eastern edge of the Tanzanian craton and with the fault-like structure bounding both the Ngorongoro volcanic zone and the Natron half-graben (NNE–SSW-oriented Natron master fault and Ol Doinyo Ogol). We relate this to the Tanzanian Craton influence, which may create a sharper rheological boundary compared to the heterogeneous Proterozoic mobile belt (Le Gall *et al.* 2008). This thinning is comparable in amount to the ~10 km observed in the Main Ethiopian and Kenya rifts (Keller *et al.* 1994; Stuart *et al.* 2006), but does not seem associated to underplating here. Our Ps Moho conversion phases are undoubtedly sharper and do not reflect any gradual velocity contrast contrariwise to the Main Ethiopian Rift, for example (Stuart *et al.* 2006).

We associate the high values of Vp/Vs ratio and the presence of an LVZ in the lower crust to the effect of magmatism, which will ease the breaking up of the lithosphere by intruding partial

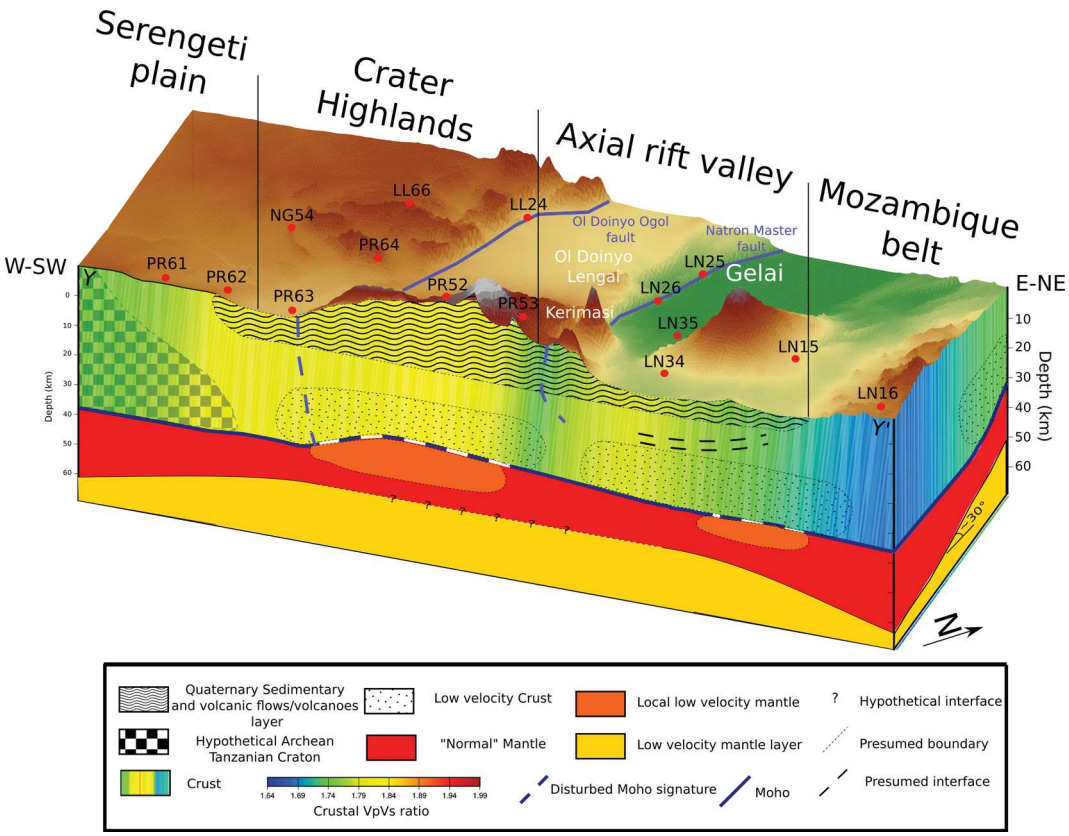

Figure 15. Simplified structural scheme of an ENE-WSW profile (YY' in Fig. 2) of the North Tanzanian Divergence deduced from the receiver functions analysis.

Table 2. Conversion depths and Vp/Vs ration for the crustal low-velocity zone for the most representative stations obtained from Frederiksen & Bostock (2000) direct modelling.

Station	Depth (km)	Vp/Vs
KEN4	15	1.91
LN15	17	1.85
PR11	15	1.86
PR63	18	1.97
PR62	18	1.76

melt in the crust (Buck 2004). If magmatism does not express here by means of mafic underplating, it modifies the crust through two different schemes in the NTD: local connections between mantle and crustal material, and through a broaden lower crust LVZ. First, we interpret the correlation between highest Vp/Vs ratios over the whole Crater Highlands (e.g. ∼1.9 for PR52) and disturbed Ps Moho conversions (Fig. 9) as possible connection or coupling between crust and mantle material. This coupling is less obvious for basaltic shield volcanoes within the axial valley (Gelai and Kitumbeine), where the most disturbed RFs only come from events piercing a region S–SE of Gelai. This region coincides with a strong negative velocity anomaly recently identified in the lower crust (Roecker *et al.*, submitted). The intense and persistent seismicity 8–10 km deep organized in an elliptical (map view) zone between Gelai and Oldoinyo Lengai volcanoes has been interpreted as a magma chamber and sill complex feeding the 2007 Lengai eruption (Baer *et al.* 2008). But our new results indicate a much deeper magma body and feeding than was first inferred from models of InSAR (Calais *et al.* 2008; Biggs *et al.* 2009, 2013).

The weaker correlation between high Vp/Vs ratio and disturbed Ps phase recorded in the axial rift valley may also result from a number of combined factors. First, we used a standard 1-D model (IASP91, Kennett & Engdahl 1991) to calculate the piercing points. The highly heterogeneous crust within the axial valley may lead to mislocated points (Albaric *et al.* 2014, Roecker *et al.*, submitted, Fig. 11). Second, our Vp/Vs estimate results from a computation over the whole RFs, regardless of ray azimuth. Vp/Vs lateral variations for a given station is then limited and may not include all the complexity of the axial valley signal. Lastly, this poor correlation can reflect smaller wavelength structures not detected by our ray distribution and affecting the RFs with less consistency. The lateral influence of the ray over the Fresnel zone has not been taken into account here, and can be responsible for the observed discrepancy. Conversely, the crust and mantle connection beneath the Crater Highlands seems to be wide enough to consistently affect the RF signal over a broader area.

Magmatism further modifies the crust by way of a clear LVZ in the lower crust starting at 15–18 km depth we retrieve beneath the rift axial valley. This decrease of velocity (∼9 per cent for *P* wave and ∼15 per cent for *S* wave) is consistent with the latest crustal tomographic models in the area (Fig. 11, Albaric *et al.*, 2014, Roecker *et al.*, submitted). Stations located between the Crater Highlands and central rift valley (LN25, LN26, PR53, MW36 and MW43) coincide yet with normal to high *S*-wave velocities (Fig. 11). A detailed backazimuthal inspection of those RFs shows that the low-velocity Px phase is only present for events passing through either Ngorongoro or Gelai volcanic areas. Events not coming from those backazimuths depict only little or no intracrustal signatures, highlighting the strong 3-D structure of this layer. Our network distribution permits to reveal the complex 3-D geometry of this LVZ, localized in the Natron rift segment and around the Crater Highlands (Fig. 11) but which does not extend to the Tanzanian Craton (Julià *et al.* 2005). From our RF analysis, we may further argue that the Natron master fault acts like a barrier and prevent this LVZ to go further West. As proposed at a wider scale by Ebinger & Sleep (1998) the spatial distribution of this LVZ may be controlled by inherited crustal structures and crustal thickness variations that might have both acted as a guide or a barrier for the low-velocity pattern.

Previous seismological studies in Tanzania at a broader scale show a similar low velocity layer starting at ∼20 km (Last *et al.* 1997; Julià *et al.* 2005). At the scale of the East African Rift, some segments display similar features (Keranen *et al.* 2009; Tuluka 2010; Wölbern *et al.* 2010; Gummert *et al.* 2015), and more generally low-velocity crustal zones are observed for similar depth in other rifts, such as the Rhine graben (Fuchs *et al.* 1987), Southern Tibet (Cogan *et al.* 1998; Jiang *et al.* 2014) and the Baikal Rift (Mordvinova *et al.* 2007; Basuyau & Tiberi 2011). In most cases, this pattern is attributed to multiple deep processes or features such as partial melting, magmatic chambers, aqueous fluids or even crustal delamination (e.g. Wallner & Schmeling 2011). Simple direct modelling we performed using Frederiksen & Bostock (2000) technique pleads for high Vp/Vs value (∼1.9) restricted within this LVZ (Table 2). We thus interpret this LVZ to be the location for partial melting with a lesser amount than for more mature rift.

5.3 Anisotropic behaviour

Recent seismicity studies (Weinstein *et al.*, submitted), active CO_2 degassing along border faults (Lee *et al.* 2016), and the 2007 dike intrusion (Calais *et al.* 2008; Biggs *et al.* 2009) attest to fluid-filled crustal cracks within the study area, that are likely able to produce anisotropic behaviour recordable by our network (Gerst & Savage 2004; Keir *et al.* 2011; Hammond *et al.* 2014). If some of our stations present backazimuthal dependency clearly imputable to anisotropic crustal structures (e.g. MW44), the transverse component of our RFs is most of the time hardly attributable to only one causing factor (e.g. MW41 on Fig. 12). Dipping interfaces can mix with anisotropy to produce a complex signal on the transverse component (e.g. Jones & Phinney 1998; Wirth & Long 2012). Our H–k stacking and the simple direct models we performed cannot unequivocally distinguish between those factors, given the complexity and numbers of interfaces involved in the observed RF signal. A thoroughly analyse of the signal through more sophisticated methods taking into account phase back-azimuthal variations or polarity change on the transverse component might resolve these ambiguities (Shiomi & Park 2008; Bianchi *et al.* 2010; Park & Levin 2016). Moreover, when present, the transverse component does not systematically show a common behaviour over the whole network, hence being indicative or either different axis of anisotropy, or variation in the dip of the interfaces.

5.4 Upper mantle structure

The modification of the lithosphere by rifting is not restricted to the solely crust, but considerably affects the upper mantle too, as we identified a clear velocity decrease of ∼9 per cent at *ca.* 60 km depth (Fig. 13). Its strong and clear signature on either side of the rift valley advocates for a continuous and high-velocity contrast, even if its presence is not firmly assessed for the very central part of the rift, due to strong interference and multiple phases in the RF signal. We relate this lithospheric LVZ to the velocity decrease recorded at

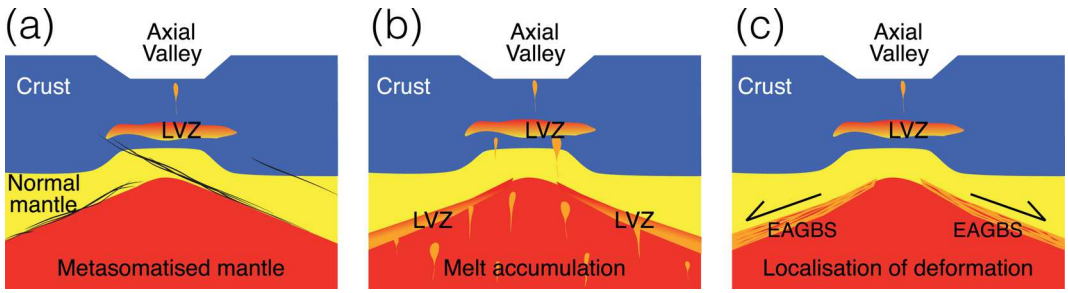

Figure 16. Alternative scenarii to explain the source of the mid-lithospheric discontinuity observed at *ca.* 60–80 km depth. (a) An ascending lithosphere results in a metasomatized mantle restricted by the presence of inherited lithospheric fabrics in the upper part. (b) Accumulated melt at mid-lithospheric depth can explain up to 10 per cent of velocity reduction. (c) Elastically accommodating grain boundary sliding (EABGS) process can take place in the upper part of the mantle, where conditions required for such a process are gathered in a rifting area.

a more regional scale by surface wave tomography at about 70 km associated to a locally high Vp/Vs ratio (1.9) in the volcanic areas (e.g. Weeraratne *et al.* 2003; O'Donnell *et al.* 2013, 2016). Our denser array and the quality of our data bring new insight on this LVZ, in particular on its dipping geometry and depth variation at the scale of the whole NTD. Several processes can be invoked to explain this mantle LVZ beneath the NTD (Fig. 16):

(i) seismic anisotropy, due to either mantle flow (Bagley & Nyblade 2013), lattice-preferred orientation (Tommasi *et al.* 1999) or oriented melting cracks (Holtzman & Kendall 2010) can produce a local change in velocity. Our RF analysis can hardly be conclusive for the presence of azimuthal anisotropy within the lithosphere, and particularly in this LVZ. Recent SKS analyses emphasize the presence of mantle anisotropy (Albaric *et al.* 2014; Ebinger *et al.* 2016), but it barely explains 9 per cent of velocity reduction within the mantle in all directions. We thus plead for the contribution of another main factor.

(ii) a metasomatic alteration of the mantle : This LVZ could evidence the boundary between a metasomatized and a more 'normal' mantle in agreement with Mattsson *et al.* (2013) who showed that the volcanic rocks around the Natron lake and the Engaruka area originate from a metasomatized lithosphere (Fig. 16a). Additional evidence are supplied by mantle xenoliths from Pello Hill and Eledoi areas (south of Gelai volcano) that recorded metasomatism-induced hydration (Baptiste *et al.* 2015). Wölbern *et al.* (2012) invoke a mineralogical alteration of the lower lithosphere by means of metasomatism to explain a similar LVZ at about 70-90 km beneath the Albertine Rift (Western EAR Branch). Ascending asthenospheric melts can produce this alteration of the lithosphere. Inherited structures (craton, Proterozoic fabric) may have restricted the ascent of the asthenosphere and explain the trend and dip of the interface (Fig. 13).

(iii) the presence of a partial melting front (Fig. 16b). Melilititic and nephelinitic rocks from the Natron lake area show degrees of partial melting consistent with melting zones as deep as 60–75 and 75–90 km (Mattsson *et al.* 2013). A melt fraction of 3–6 per cent can reduce seismic velocity by 5–10 per cent in the upper mantle (Olugboji *et al.* 2013), depending on melting body geometry (Faul *et al.* 1994; Takei 2002). Moreover, accumulated melt at mid-lithosphere could feed the LVZ observed at low crustal depth and can be related to the intricate axial valley structure complexity observed in the RFs. However, no evidence for underplating is found within the RFs, which all show very clear Ps conversion at the Moho depth, and a normal upper mantle velocity below this interface, by contrast to patterns typically observed in more mature magmatic rift zones (Stuart *et al.* 2006). In order to fit the observed sharp seismic signature on the RFs, additional processes (viscosity, permeability) are requested to maintain a large melt fraction in a thick layer to produce a recordable seismic signal as observed (Olugboji *et al.* 2013).

(iv) elastically accommodated grain-boundary sliding (EAGBS, Fig. 16c) provides an alternative explanation for a velocity drop at mid lithospheric depth (Karato 2012; Karato *et al.* 2015). At moderate temperatures, grain boundaries weaken and lead to the reduction of the elastic modulus for polycrystalline aggregates (Zener 1941; Kê 1947). The induced velocity decrease and its location in depth will depend on water content, geotherm and grain size. Olugboji *et al.* (2013) show that the reduction of velocity produced by EAGBS is recordable by *P*-receiver functions, depending on the sharpness of the velocity contrast created. This process has already been proposed to explain mid-lithospheric discontinuities (MLD Faul & Jackson 2005; Selway *et al.* 2014) but gradually leads to diffusion creep processes with increasing temperature (Lee *et al.* 2011). EAGBS is then usually restricted to uppermost mantle depth, even if the presence of a secondary phase of low viscosity (e.g. melt) makes the EAGBS predominant at higher temperature (Jackson *et al.* 2006). The velocity drop caused by EAGBS is poorly constrained (Faul & Jackson 2005) and can reach 5 per cent but is sharper when associated to a water content change (e.g. wet mantle Karato 2012). The acute signature observed on our RFs is coherent with a metasomatism-induced hydration (Baptiste *et al.* 2015) which could enhance the EAGBS effect on seismic signal.

Finally, this structure may have a deeper origin and could reflect the interaction between Proterozoic inherited structures and flow from the lower mantle. As proposed by Bagley & Nyblade (2013), lower mantle flow could have strongly influenced the Afro-Arabian rift, and its NE–NNE orientation probably control the tectonic deformation observed at the surface. These flows seem to not necessary correspond to the principal African plume but maybe more to a deflection of this one, preferentially channelled along the east side of the Tanzanian craton (Koptev *et al.* 2015).

6 CONCLUSION

Analysis of receiver functions recorded by a broad-band seismic network in the North Tanzanian Divergence area, eastern branch of the East African rift, provides constraint on the accommodation of strain in a cratonic rifting lithosphere. Moho geometry evidences an asymmetric crustal thinning of about 10 km localized beneath the axial rift valley. The Vp/Vs ratio variations indicate strong modification of crustal composition. The strong correlation between high

Vp/Vs ratio and major volcanic edifices advocates for the presence of magma/fluids within the crust associated with magmatic events. Beneath the rift axial valley, those variations are also controlled by the complex crustal structure and nature of the crust. A first LVZ is detected in the lower crust (15–35 km depth) and results from a combined effect of partial melting for areas where Vp/Vs ratio is high, temperature and rock composition variations. A second low-velocity layer is identified at mid-lithospheric depth (∼60 km) and presents a decrease of up to 9 per cent in velocity. Its geometry and distribution is not restricted to the rift axial valley and can be the product of a melt accumulation within the upper mantle, the raising deflection of asthenospheric and metasomatized material. Alternatively, deformation processes like grain boundary sliding may take place in this thick rifting lithosphere and explain this velocity drop. For both LVZ, we assume Archaean and/or Proterozoic inherited structures to constrain their geometry and extension. No obvious link between the two LVZs at depth has been clearly demonstrated from receiver function analysis alone.

ACKNOWLEDGEMENTS

The seismic instruments were provided by the Incorporated Research Institutions for Seismology (IRIS) through the PASSCAL Instrument Center at New Mexico Tech. Data collected will be available through the IRIS Data Management Center. The facilities of the IRIS Consortium are supported by the National Science Foundation under Cooperative Agreement EAR-1261681 and the DOE National Nuclear Security Administration. We are very grateful for the assistance of RPI graduate student Anastasia Rodzianko, Rochester undergraduate students Eli Witkin, Catherine Lambert, Avery Palardy and Geosciences Montpellier graduate student Nathalie Rasendra in seismic installations and servicing. Work was conducted with approval by the Commission for Science and Technology (Tanzania) and the National Council for Science and Technology (Kenya). We are grateful for logistical support from Tanzania National Parks Commission and to the Ngorongoro National Park. We could not have achieved this work without logistical assistance from primary and secondary school teachers throughout the region, the Masai clans in Kenya and Tanzania, driver-guides from Fortes Tours, the Ngorongoro conservation area, Tanapa and the French Ambassy. Then we want to thank Majura Songo and Sindato Moreto and all the people from CoLiBrEA (ANR-12-JS06-0004) and Crafti (EAR-1261681) projects. We want to deeply thank Prof. J. Park, the editor and one anonymous reviewer for their constructive remarks, which have greatly improved the manuscript.

REFERENCES

Albaric, J., Déverchère, J., Petit, C., Perrot, J. & Le Gall, B., 2009. Crustal rheology and depth distribution of earthquakes: insights from the central and southern East African Rift System, *Tectonophysics,* **468**(1), 28–41.

Albaric, J., Déverchère, J., Perrot, J., Jakovlev, A. & Deschamps, A., 2014. Deep crustal earthquakes in North Tanzania, East Africa: Interplay between tectonic and magmatic processes in an incipient rift, *Geochem. Geophys. Geosyst.,* **15**(2), 374–394.

Aulbach, S., Rudnick, R. & McDonough, W., 2008. Lithospheric mantle sources within the East African Rift, Tanzania, *Geochim. Cosmochim. Acta Supplement,* **72,** 37.

Baer, G., Hamiel, Y., Shamir, G. & Nof, R., 2008. Evolution of a magma-driven earthquake swarm and triggering of the nearby Oldoinyo Lengai eruption, as resolved by insar, ground observations and elastic modeling, East African Rift, 2007, *Earth planet. Sci. Lett.,* **272**(1), 339–352.

Bagley, B. & Nyblade, A.A., 2013. Seismic anisotropy in eastern Africa, mantle flow, and the African superplume, *Geophys. Res. Lett.,* **40**(8), 1500–1505.

Baker, B., 1986. Tectonics and volcanism of the southern Kenya Rift Valley and its influence on rift sedimentation, *Geol. Soc. Lond. Spec. Publ.,* **25**(1), 45–57.

Baptiste, V., Tommasi, A., Vauchez, A., Demouchy, S. & Rudnick, R.L., 2015. Deformation, hydration, and anisotropy of the lithospheric mantle in an active rift: Constraints from mantle xenoliths from the North Tanzanian Divergence of the East African Rift, *Tectonophysics,* **639,** 34–55.

Basuyau, C. & Tiberi, C., 2011. Imaging lithospheric interfaces and 3D structures using receiver functions, gravity, and tomography in a common inversion scheme, *Comput. Geosci.,* **37**(9), 1381–1390.

Bianchi, I., Park, J., Piana Agostinetti, N. & Levin, V., 2010. Mapping seismic anisotropy using harmonic decomposition of receiver functions: An application to northern apennines, italy, *J. geophys. Res.,* **115**(B12), B12317, doi:10.1029/2009JB00700761.

Biggs, J., Amelung, F., Gourmelen, N., Dixon, T.H. & Kim, S.-W., 2009. Insar observations of 2007 Tanzania rifting episode reveal mixed fault and dyke extension in an immature continental rift, *Geophys. J. Int.,* **179**(1), 549–558.

Biggs, J., Chivers, M. & Hutchinson, M.C., 2013. Surface deformation and stress interactions during the 2007–2010 sequence of earthquake, dyke intrusion and eruption in northern Tanzania, *Geophys. J.,* **195,** 16–26.

Birt, C., Maguire, P., Khan, M., Thybo, H., Keller, G.R. & Patel, J., 1997. The influence of pre-existing structures on the evolution of the southern Kenya Rift Valleyevidence from seismic and gravity studies, *Tectonophysics,* **278**(1), 211–242.

Bott, M., 1992. Modelling the loading stresses associated with active continental rift systems, *Tectonophysics,* **215**(1), 99–115.

Buck, W.R., 2004. Consequences of asthenospheric variability on continental rifting, in *Rheology and Deformation of the Lithosphere at Continental Margins,* vol. 62, pp. 1–30, eds Karner, G.D., Taylor, B., Driscoll, N.W. & Kohlstedt, D.L., Columbia University Press.

Calais, E. *et al.*, 2008. Strain accommodation by slow slip and dyking in a youthful continental rift, East Africa, *Nature,* **456**(7223), 783–787.

Christensen, N.I., 1996. Poisson's ratio and crustal seismology, *J. geophys. Res.,* **101**(B2), 3139–3156.

Cogan, M.J. *et al.*, 1998. Shallow structure of the Yadong-Gulu rift, southern Tibet, from refraction analysis of Project INDEPTH common midpoint data, *Tectonics,* **17**(1), 46–61.

Craig, T., Jackson, J., Priestley, K. & McKenzie, D., 2011. Earthquake distribution patterns in Africa: their relationship to variations in lithospheric and geological structure, and their rheological implications, *Geophys. J. Int.,* **185**(1), 403–434.

Dawson, J., 1992. Neogene tectonics and volcanicity in the North Tanzania sector of the Gregory Rift Valley: contrasts with the kenya sector, *Tectonophysics,* **204**(1), 81–92.

Domenico, S.N., 1984. Rock lithology and porosity determination from shear and compressional wave velocity, *Geophysics,* **49**(8), 1188–1195.

Dugda, M.T., Nyblade, A.A., Julia, J., Langston, C.A., Ammon, C.J. & Simiyu, S., 2005. Crustal structure in Ethiopia and Kenya from receiver function analysis: Implications for rift development in eastern Africa, *J. geophys. Res.,* **110**(B1).

Ebinger, C., Djomani, Y.P., Mbede, E., Foster, A. & Dawson, J., 1997. Rifting archaean lithosphere: the eyasi-manyara-natron rifts, east africa, *J. Geol. Soc.,* **154**(6), 947–960.

Ebinger, C., Tiberi, C., Currie, C., van Wijk, J. & Albaric, J., 2016. Rifting an archaean craton: Insights from seismic anisotropy patterns in E. Africa, in *AGU Fall Meeting,* T21F-01.

Ebinger, C.J. & Sleep, N., 1998. Cenozoic magmatism throughout east Africa resulting from impact of a single plume, *Nature,* **395**(6704), 788–791.

Efron, B. & Tibshirani, R.J., 1994. *An Introduction to the Bootstrap,* CRC press.

Faul, U.H. & Jackson, I., 2005. The seismological signature of temperature and grain size variations in the upper mantle, *Earth planet. Sci. Lett.,* **234**(1), 119–134.

Faul, U.H., Toomey, D.R. & Waff, H.S., 1994. Intergranular basaltic melt is distributed in thin, elogated inclusions, *Geophys. Res. Lett.,* **21**(1), 29–32.

Fishwick, S. & Bastow, I.D., 2011. Towards a better understanding of African topography: a review of passive-source seismic studies of the African crust and upper mantle, *Geol. Soc. Lond. Spec. Publ.,* **357**(1), 343–371.

Foster, A., Ebinger, C., Mbede, E. & Rex, D., 1997. Tectonic development of the northern Tanzanian sector of the East African Rift System, *J. Geol. Soc.,* **154**(4), 689–700.

Frederiksen, A. & Bostock, M., 2000. Modelling teleseismic waves in dipping anisotropic structures, *Geophys. J. Int.,* **141**(2), 401–412.

Fuchs, K., Bonjer, K.-P., Gajewski, D., Lüschen, E., Prodehl, C., Sandmeier, K.-J., Wenzel, F. & Wilhelm, H., 1987. Crustal evolution of the Rhinegraben area. 1. exploring the lower crust in the Rhinegraben rift by unified geophysical experiments, *Tectonophysics,* **141**(1–3), 261–275.

Gerst, A. & Savage, M.K., 2004. Seismic anisotropy beneath ruapehu volcano: a possible eruption forecasting tool, *Science,* **306**(5701), 1543–1547.

Gummert, M., Lindenfeld, M., Wölbern, I., Rümpker, G., Celestin, K. & Batte, A., 2015. Crustal structure and high-resolution moho topography across the rwenzori region (albertine rift) from p-receiver functions, *Geol. Soc. Lond. Spec. Publ.,* **420,** SP420–4.

Guo, Z. *et al.*, 2015. High resolution 3-d crustal structure beneath {NE} china from joint inversion of ambient noise and receiver functions using {NECESSArray} data, *Earth planet. Sci. Lett.,* **416,** 1–11.

Hammond, J., Kendall, J.-M., Stuart, G., Keir, D., Ebinger, C., Ayele, A. & Belachew, M., 2011. The nature of the crust beneath the Afar triple junction: Evidence from receiver functions, *Geochem. Geophys. Geosyst.,* **12**(12), Q12004, doi:10.1029/2011GC003738.

Hammond, J., Kendall, J.-M., Wookey, J., Stuart, G., Keir, D. & Ayele, A., 2014. Differentiating flow, melt, or fossil seismic anisotropy beneath Ethiopia, *Geochem. Geophys. Geosyst.,* **15**(5), 1878–1894.

Harvey, P.K., 2005. Petrophysical properties of crystalline rocks, Geological Society of London.

Hilton, D.R., Grönvold, K., Macpherson, C.G. & Castillo, P.R., 1999. Extreme 3 he/4 he ratios in northwest Iceland: constraining the common component in mantle plumes, *Earth planet. Sci. Lett.,* **173**(1), 53–60.

Holbrook, W.S., Mooney, W.D. & Christensen, N.I., 1992. The seismic velocity structure of the deep continental crust, *Cont. Lower Crust,* **23,** 1–43.

Holtzman, B.K. & Kendall, J., 2010. Organized melt, seismic anisotropy, and plate boundary lubrication, *Geochem. Geophys. Geosyst.,* **11**(12), Q0AB06, doi:10.1029/2010GC003296.

Jackson, I., Faul, U., Fitz Gerald, J. & Morris, S., 2006. contrasting viscoelastic behavior of melt-free and melt-bearing olivine: Implications for the nature of grain-boundary sliding, *Mater. Sci. Eng. A,* **442,** 170–174.

Jiang, M., Ai, Y., Zhou, S. & Chen, Y.J., 2014. Distribution of the low velocity bulk in the middle-to-lower crust of southern Tibet: implications for formation of the north–south trending rift zones, *Earthq. Sci.,* **27**(2), 149–157.

Jones, C.H. & Phinney, R.A., 1998. Seismic structure of the lithosphere from teleseismic converted arrivals observed at small arrays in the southern Sierra Nevada and vicinity, California, *J. geophys. Res.,* **103**(B5), 10 065–10 090.

Julià, J., Ammon, C.J. & Nyblade, A.A., 2005. Evidence for mafic lower crust in Tanzania, East Africa, from joint inversion of receiver functions and Rayleigh wave dispersion velocities, *Geophys. J. Int.,* **162**(2), 555–569.

Karato, S.-i., 2012. On the origin of the asthenosphere, *Earth planet. Sci. Lett.,* **321–322,** 95–103.

Karato, S.-i., Olugboji, T. & Park, J., 2015. Mechanisms and geologic significance of the mid-lithosphere discontinuity in the continents, *Nat. Geosci.,* **8,** 509–514.

Kê, T.-s., 1947. Experimental evidence of the viscous behavior of grain boundaries in metals, *Phys. Rev.,* **71**(8), 533–546.

Keir, D., Belachew, M., Ebinger, C., Kendall, J.-M., Hammond, J., Stuart, G., Ayele, A. & Rowland, J., 2011. Mapping the evolving strain field during continental breakup from crustal anisotropy in the Afar depression, *Nat. Commun.,* **2,** 285.

Keller, G. *et al.*, 1994. The East African rift system in the light of KRISP 90, *Tectonophysics,* **236,** 465–483.

Kennett, B. & Engdahl, E., 1991. Traveltimes for global earthquake location and phase identification, *Geophys. J. Int.,* **105**(2), 429–465.

Keranen, K.M., Klemperer, S.L., Julia, J., Lawrence, J.F. & Nyblade, A.A., 2009. Low lower crustal velocity across Ethiopia: Is the main Ethiopian Rift a narrow rift in a hot craton?, *Geochemistry, Geophysics, Geosystems,* **10**(5), Q0AB01, doi:10.1029/2008GC002293.

Koptev, A., Calais, E., Burov, E., Leroy, S. & Gerya, T., 2015. Dual continental rift systems generated by plume-lithosphere interaction, *Nat. Geosci.,* **8**(5), 388–392.

Langston, C.A., 1977. The effect of planar dipping structure on source and receiver responses for constant ray parameter, *Bull. seism. Soc. Am.,* **67**(4), 1029–1050.

Last, R.J., Nyblade, A.A., Langston, C.A. & Owens, T.J., 1997. Crustal structure of the East African Plateau from receiver functions and Rayleigh wave phase velocities, *J. geophys. Res.,* **102**(B11), 24 469–24 483.

Lee, H., Muirhead, J.D., Fischer, T.P., Ebinger, C.J., Kattenhorn, S.A., Sharp, Z.D. & Kianji, G., 2016. Massive and prolonged deep carbon emissions associated with continental rifting, *Nat. Geosci.,* **9,** 145–149.

Lee, L., Morris, S. J.S. & Wilkening, J., 2011. Stress concentrations, diffusionally accomodated grain boundary sliding and the viscoelasticity of polycrystals, *Proc. R. Soc. Lond. A,* **467**(2130), 1624–1644.

Le Gall, B., Nonnotte, P., Rolet, J., Benoit, M., Guillou, H., Mousseau-Nonnotte, M., Albaric, J. & Deverchère, J., 2008. Rift propagation at craton margin.: Distribution of faulting and volcanism in the North Tanzanian Divergence (East Africa) during Neogene times, *Tectonophysics,* **448**(1), 1–19.

Ligorría, J.P. & Ammon, C.J., 1999. Iterative deconvolution and receiver-function estimation, *Bull. seism. Soc. Am.,* **89**(5), 1395–1400.

Mana, S., Furman, T., Carr, M., Mollel, G., Mortlock, R., Feigenson, M., Turrin, B. & Swisher, C., 2012. Geochronology and geochemistry of the Essimingor volcano: melting of metasomatized lithospheric mantle beneath the North Tanzanian Divergence zone (East African rift), *Lithos,* **155,** 310–325.

Mana, S., Furman, T., Turrin, B.D., Feigenson, M.D. & Swisher, C.C., 2015. Magmatic activity across the East African North Tanzanian Divergence Zone, *J. Geol. Soc.,* **172,** 368–389.

Mattsson, H.B., Nandedkar, R.H. & Ulmer, P., 2013. Petrogenesis of the melilititic and nephelinitic rock suites in the Lake Natron–Engaruka monogenetic volcanic field, northern Tanzania, *Lithos,* **179,** 175–192.

Mollel, G.F., Swisher, C.C., Feigenson, M.D. & Carr, M.J., 2008. Geochemical evolution of Ngorongoro Caldera, Northern Tanzania: Implications for crust–magma interaction, *Earth planet. Sci. Lett.,* **271**(1), 337–347.

Mordvinova, V., Deschamps, A., Dugarmaa, T., Dverchre, J., Ulziibat, M., Sankov, V., Artemev, A. & Perrot, J., 2007. Velocity structure of the lithosphere on the 2003 Mongolian-Baikal transect from SV waves, *Izv. Phys. Solid Earth,* **43**(2), 119–129.

Muirhead, J.D., Kattenhorn, S.A. & Le Corvec, N., 2015. Varying styles of magmatic strain accommodation across the East African Rift, *Geochem. Geophys. Geosyst.,* **16**(8), 2775–2795.

Mulibo, G. & Nyblade, A., 2009. The 1994–1995 Manyara and Kwamtoro earthquake swarms: Variation in the depth extent of seismicity in Northern Tanzania, *South Afr. J. Geol.,* **112**(3–4), 387–404.

Nonnotte, P., Guillou, H., Le Gall, B., Benoit, M., Cotten, J. & Scaillet, S., 2008. New k–ar age determinations of Kilimanjaro volcano in the North Tanzanian diverging rift, East Africa, *J. Volcanol. Geotherm. Res.,* **173**(1), 99–112.

O'Donnell, J., Adams, A., Nyblade, A., Mulibo, G. & Tugume, F., 2013. The uppermost mantle shear wave velocity structure of eastern Africa from rayleigh wave tomography: constraints on rift evolution, *Geophys. J. Int.,* **194**(2), 961–978.

O'Donnell, J., Selway, K., Nyblade, A., Brazier, R., El Tahir, N. & Durrheim, R., 2016. Thick lithosphere, deep crustal earthquakes and no melt: a triple challenge to understanding extension in the western branch of the East African Rift, *Geophys. J. Int.,* **204**(2), 985–998.

Olugboji, T.M., Karato, S. & Park, J., 2013. Structures of the oceanic lithosphere-asthenosphere boundary: Mineral-physics modeling and seismological signatures, *Geochem. Geophys. Geosyst.,* **14**(4), 880–901.

Park, J. & Levin, V., 2016. Anisotropic shear zones revealed by backazimuthal harmonics of teleseismic receiver functions, *Geophys. J. Int.,* **207**(2), 1216–1243.

Petit, C. & Ebinger, C., 2000. Flexure and mechanical behavior of cratonic lithosphere: Gravity models of the East African and Baikal rifts, *J. geophys. Res.,* **105**(B8), 19151–19162.

Pik, R., Marty, B., Carignan, J., Yirgu, G. & Ayalew, T., 2008. Timing of East African Rift development in southern Ethiopia: Implication for mantle plume activity and evolution of topography, *Geology,* **36**(2), 167–170.

Priestley, K. & McKenzie, D., 2006. The thermal structure of the lithosphere from shear wave velocities, *Earth planet. Sci. Lett.,* **244**(1), 285–301.

Reed, C.A., Almadani, S., Gao, S.S., Elsheikh, A.A., Cherie, S., Abdelsalam, M.G., Thurmond, A.K. & Liu, K.H., 2014. Receiver function constraints on crustal seismic velocities and partial melting beneath the Red Sea rift and adjacent regions, Afar Depression, *J. geophys. Res.,* **119**(3), 2138–2152.

Ritsema, J., Ni, S., Helmberger, D.V. & Crotwell, H.P., 1998. Evidence for strong shear velocity reductions and velocity gradients in the lower mantle beneath Africa, *Geophys. Res. Lett.,* **25**(23), 4245–4248.

Ritsema, J., van Heijst, H.J. & Woodhouse, J.H., 1999. Complex shear wave velocity structure imaged beneath Africa and Iceland, *Science,* **286**(5446), 1925–1928.

Roecker, S. *et al.*, Subsurface Images of the Eastern Rift, Africa, from the Joint Inversion of Body Waves, Surface Waves, and Gravity: Investigating the Role of Fluids in Early-Stage Continental Rifting. *Geophys. J. Int.,* submitted.

Rogers, N., Macdonald, R., Fitton, J.G., George, R., Smith, M. & Barreiro, B., 2000. Two mantle plumes beneath the East African rift system: Sr, Nd and Pb isotope evidence from Kenya Rift basalts, *Earth planet. Sci. Lett.,* **176**(3), 387–400.

Saria, E., Calais, E., Stamps, D., Delvaux, D. & Hartnady, C., 2014. Present-day kinematics of the East African Rift, *J. geophys. Res.,* **119**(4), 3584–3600.

Selway, K., Ford, H. & Kelemen, P., 2014. The seismic mid-lithosphere discontinuity, *Earth planet. Sci. Lett.,* **414,** 45–57.

Shiomi, K. & Park, J., 2008. Structural features of the subducting slab beneath the kii peninsula, central japan: Seismic evidence of slab segmentation, dehydration, and anisotropy, *J. geophys. Res.,* **113**(B10), B10318, doi:10.1029/2007JB005535.

Smith, M. & Mosley, P., 1993. Crustal heterogeneity and basement influence on the development of the Kenya Rift, East Africa, *Tectonics,* **12**(2), 591–606.

Stuart, G., Bastow, I. & Ebinger, C., 2006. Crustal structure of the northern Main Ethiopian Rift from receiver function studies, *Geol. Soc. Lond. Spec. Publ.,* **259**(1), 253–267.

Takei, Y., 2002. Effect of pore geometry on vp/vs: From equilibrium geometry to crack, *J. geophys. Res.,* **107**(B2), ECV 6-1–ECV 6-12, doi:10.1029/2001JB000522.

Tiberi, C., Leroy, S., D'Acremont, E., Bellahsen, N., Ebinger, C., Al-Lazki, A. & Pointu, A., 2007. Crustal geometry of the northeastern Gulf of Aden passive margin: localization of the deformation inferred from receiver function analysis, *Geophys. J. Int.,* **168**(3), 1247–1260.

Tommasi, A., Tikoff, B. & Vauchez, A., 1999. Upper mantle tectonics: three-dimensional deformation, olivine crystallographic fabrics and seismic properties, *Earth planet. Sci. Lett.,* **168**(1), 173–186.

Tuluka, G.M., 2010. Crustal structure beneath two seismic broadband stations revealed from teleseismic p-wave receiver function analysis in the Virunga volcanic area, Western Rift Valley of Africa, *J. Afr. Earth Sci.,* **58**(5), 820–828.

Vauchez, A., Dineur, F. & Rudnick, R., 2005. Microstructure, texture and seismic anisotropy of the lithospheric mantle above a mantle plume: insights from the Labait volcano xenoliths (Tanzania), *Earth planet. Sci. Lett.,* **232**(3), 295–314.

Wallner, H. & Schmeling, H., 2011. Sensitivity analysis of rift induced delamination with application to Rwenzori Mountains, *Geophys. J. Int.,* **187**(3), 1135–1145.

Watanabe, T., 1993. Effects of water and melt on seismic velocities and their application to characterization of seismic reflectors, *Geophys. Res. Lett.,* **20**(24), 2933–2936.

Weeraratne, D.S., Forsyth, D.W., Fischer, K.M. & Nyblade, A.A., 2003. Evidence for an upper mantle plume beneath the Tanzanian craton from Rayleigh wave tomography, *J. geophys. Res.,* **108**(B9), 2427, doi:10.1029/2002JB002273.

Weinstein, A. *et al.*, Volatile assisted rifting in East Africa: Seismicity of the Magadi-Natron-Manyara basins, Africa. *Geophys. J. Int.,* submitted.

Wirth, E.A. & Long, M.D., 2012. Multiple layers of seismic anisotropy and a low-velocity region in the mantle wedge beneath japan: Evidence from teleseismic receiver functions, *Geochem. Geophys. Geosyst.,* **13**(8), Q08005, doi:10.1029/2012GC004180.

Wölbern, I., Rümpker, G., Schumann, A. & Muwanga, A., 2010. Crustal thinning beneath the Rwenzori region, Albertine rift, Uganda, from receiver-function analysis, *Int. J. Earth Sci.,* **99**(7), 1545–1557.

Wölbern, I., Rümpker, G., Link, K. & Sodoudi, F., 2012. Melt infiltration of the lower lithosphere beneath the tanzania craton and the albertine rift inferred from s receiver functions, *Geochem. Geophys. Geosyst.,* **13**(8), Q0AK08, doi:10.1029/2012GC004167.

Zener, C., 1941. Theory of elasticity of polycrystals with viscous grain boundaries, *Phys. Rev.,* **60,** 906–908.

Zhao, M., Qiu, X., Xia, S., Xu, H., Wang, P., Wang, T.K., Lee, C.-S. & Xia, K., 2010. Seismic structure in the northeastern south china sea: S-wave velocity and vp/vs ratios derived from three-component obs data, *Tectonophysics,* **480**(1), 183–197.

Zhu, L. & Kanamori, H., 2000. Moho depth variation in southern California from teleseismic receiver functions, *J. geophys. Res.,* **105**(B2), 2969–2980.

UNIVERSITE SCIENCES BRETAGNE DE LA MER LOIRE ET DU LITTORAL

UBO Université de Bretagne Occidentale

Titre : **Structure et propagation d'un rift magmatique en bordure de craton : Approche intégrée de la Divergence Nord-Tanzanienne par analyse des populations de failles et du réseau de drainage**

Mots clés : Divergence Nord Tanzanienne, Bloc Oldoinyo Ogol, Propagation du rift, failles intra-rift, extension, soulèvement; drainage, morpho-structural

Résumé : Tout modèle cinématique appliqué à la propagation du rift sud kenyan (RSK) et à sa divergence vers l'ouest au nord de la Tanzanie (DNT) doit nécessairement intégré la vallée axiale Magadi-Natron (études antérieures), mais aussi le bloc soulevé Oldoinyo Ogol (OOB) à l'ouest (ce travail). Notre étude, basée pour l'essentiel sur l'interprétation d'imagerie satellitale SRTM 30 m, nous permet (1) de préciser l'organisation morphostructurale de l'ensemble du RSK, (2) d'identifier 2 systèmes successifs de failles bordières, (3) d'affirmer le rôle majeur de celle d'OlDoinyo Ogol, (4) d'élaborer un modèle de rifting en 2 étapes (7-3 Ma et <3 Ma) et (5) d'attribuer le « shift » latéral du domaine rifté (OOB), puis sa divergence le long de la branche d'Eyasi (DNT) à la présence d'une discontinuité transverse protérozoïque, à laquelle on rapporte aussi le développement précoce et 'hors axe' du segment magmatique des « Crater Highlands », démontrant ainsi l'importance de l'héritage structural sur la cinématique du rifting.
L'analyse quantitative des populations de failles démontre le caractère « restricted » des failles intra-rift et aboutit aussi à préciser l'évolution, dans l'espace et le temps, du taux d'extension, depuis un stade précoce à déformation localisée jusqu'à un stade récent à déformation diffuse (<3 Ma).
L'analyse des réseaux de drainage identifiés sur le compartiment de socle bordant à l'ouest le dispositif RSK-NTD démontre (1) leur contrôle étroit par le dispositif lithologique et tectonique du socle, (2) la nature polyphasée du soulèvement lié aux failles bordières, et (3) le caractère déséquilibré du réseau actuel en cours de soulèvement.

Title: **Structure and propagation of a magmatic rift at the edge of a Craton: Integrated approach of the structure of the North Tanzanian Divergence, East Africa: Analysis of fault populations and drainage network.**

Keywords: North Tanzanian Divergence, Oldoinyo Ogol Block, Rift propagation, Intra-rift faults, Extension, Up-lift, drainage, morphostructural

Abstract: Any kinematic model applied to the southerly-propagating and diverging South Kenya rift (SKR) should necessarily integrate the structure of the Magadi-Natron axial trough (previous studies), but also those of the Oldoinyo Ogol (OOB) offset block to the west. Our work is chiefly based on SRTM 30 m satellite imagery analysis, and allows us (1) to precise the morphostructural arrangement of the entire SKR, (2) to identify 2 successive border faults systems, (3) to emphasize the role of the Ol Doinyo Ogol master fault, (4) to elaborate a 2-stage rift model (7-3 Ma et <3 Ma), and (5) to attribute a key-role to a transverse Proterozoic discontinuity on the lateral shift of the OOB, as well as on the split of the rift into the Eyasi rift arm and on the off-axis location of the early Crater Highlands magmatic segment, hence demonstrating the importance of basement structural inheritance on rift kinematics.

The quantitative analysis of fault populations shows the restricted nature of most intra-rift faults, and leads us to precise the spatio-temporal evolution of extension from a stage of localized strain (border faults) to a stage of diffuse extension (<3 Ma).

From the analysis of the river drainage extracted from the basement uplifted block bounding the rift system to the west, it is assumed that (1) lithological and tectonic basement features exerted a strong control on the river network, (2) fault-related basement uplift is polyphased, and (3) the unsteady nature of the present-day river drainage is due to still active rift-flank uplift in the southern portion of the rift system.